The Thesis Committee for Robert Stevenson Blair

Certifies that this is the approved version of the following thesis:

Finite Element Analysis of Wood Shoring Towers used in Urban Search and Rescue

APPROVED BY
SUPERVISING COMMITTEE:

Supervisor:

Dan L. Wheat

Michael D. Engelhardt

Finite Element Analysis of Wood Shoring Towers used in Urban Search and Rescue

by

Robert Stevenson Blair, B.Arch.E.

Thesis

Presented to the Faculty of the Graduate School of

The University of Texas at Austin

in Partial Fulfillment

of the Requirements

for the Degree of

Master of Science in Engineering

The University of Texas at Austin

December 2012

Dedication

To God, my heavenly Father, by whom and for whom all things were made. Apart from Him I can do nothing.

To my parents, for always being on my side, and whose boundless love and encouragement have shaped who I am today.

Acknowledgements

First, I would like to thank the Department of Homeland Security as well as Protection Engineering Consultants for providing the funding for this project. Serving on the project team has been a remarkable experience.

I would also like to thank professors Dan Wheat, Michael Engelhardt, and Eric Williamson for allowing me to take on this challenging and exciting endeavor. I especially want to convey my gratitude toward professor Dan Wheat for offering his wisdom and personal guidance throughout the entire project. His knowledge and consistent input resulted in significant improvements to my thesis. The finished product is definitely something I will treasure and be proud of from this point forward.

I truly enjoyed working with the talented staff and students at the Ferguson Structural Engineering Laboratory. In particular, I want to thank Eric Shell, whose collaborative personality along with his extensive laboratory and technical expertise ensured that the specimen testing went smoothly.

I am grateful to have worked on this project alongside classmate Scott McCord, whose strong work ethic contributed enormously to the success of the laboratory testing. I would also like to thank fellow graduate student Whitney Lee, who worked diligently on material testing that aided in the development of the finite element models.

My gratefulness for the unconditional love, sacrifice, and support from my family cannot be expressed enough. I am blessed to have such wonderful people in my life who champion me and always teach me to do the right thing. This achievement would not have been possible without them.

Steven Blair

August 2012

Abstract

Finite Element Analysis of Wood Shoring Towers used in Urban Search and Rescue

Robert Stevenson Blair, M.S.E.

The University of Texas at Austin, 2012

Supervisor: Dan Wheat

This thesis focuses on the finite element modeling and analysis of wood shoring towers used by Urban Search and Rescue (US&R) teams during emergency response situations. These shores are constructed on site to provide temporary stabilization to a damaged structure. A high demand exists for experimental testing of the performance of these shores under non-ideal loading conditions, and for possible design modifications that could improve their overall behavior. To respond to this need, a total of thirteen vertical shores of the type laced post (LP) and plywood laced post (PLP) were constructed and tested at the Ferguson Structural Engineering Laboratory (FSEL) in Austin, Texas. The tests conducted on these shores aimed to investigate their performance under purely vertical load as well as various combinations of vertical and lateral loads. Finite element models for eight of the shores tested at FSEL were built and analyzed in Abaqus to compare the computed results with the actual linear elastic response of the shores. Material properties for the posts in each shore were obtained through further material testing at the conclusion of each shore test. Shore members were

assumed to be isotropic. Solid elements were used to model each member, and Cartesian connector elements with a predefined nonlinear stiffness were used to model each nail. In general, the vertical load-displacement response computed from Abaqus exhibited good agreement with the laboratory results for the linear elastic range. The same general modeling scheme was then used to make design changes to the original shores based on observations gained during testing as well as modeling. Each design change was modeled, analyzed, and then compared with the computed results from the original shore design as well as the other design changes. The basis for evaluating the effectiveness of a given shore design involved comparing the bending moment diagrams for each post and the maximum first story nail slips (connector displacements). Recommendations were made for improved shore designs to be verified by experimental testing.

Table of Contents

List of Tables

List of Figures

CHAPTER 1

Introduction

This thesis presents a discussion and analysis of the results from an experimental investigation of Urban Search and Rescue (US&R) emergency wood shoring systems. Also included in this thesis is a detailed presentation of the results from a finite element modeling analysis of these shores as well as shores with alternate designs. This chapter includes a brief background of shoring systems, a statement of the research objectives, and an overview of the testing and modeling conducted.

1.1 BACKGROUND OF US&R WOOD SHORING SYSTEMS

Over the past two decades, catastrophic events across the United States have called for the use of wood shoring systems of the type used by US&R teams. Shores serve the purpose of providing temporary stabilization or support to any structural element that has been compromised by partial or total collapse of the structure (19). During these emergency response situations, a designated team of specially trained firefighters must work quickly to assemble the shoring systems in a safe and reliable manner. Shoring systems not only provide a safe environment for firefighters to rescue victims, but they also help to decrease the potential for further collapse. Although shores can be constructed out of many different structural materials, the shores investigated in this thesis consisted exclusively of wood members with nailed connections.

Since the demand for shoring systems has until recently been slim, there exists a very limited amount of knowledge and previous research in this area. Several emergency management personnel and structures specialists from the Federal Emergency Management Agency (FEMA) and United States Army Corps of Engineers (USACE) US&R groups and the industry have classified testing under non-ideal loading conditions as a major gap in current understanding of shoring systems. In response to the urgent need for research in this area, the Department of Homeland Security (DHS) has requested

that a testing program be conducted to address the issues of combined lateral and vertical loading as well as force-controlled testing.

To begin answering this need, several wood shoring specimens were tested under these non-ideal loading conditions at the Ferguson Structural Engineering Laboratory (FSEL) at the University of Texas at Austin between August and December 2011.

1.2 RESEARCH OBJECTIVES

The first objective of this research was to obtain the vertical load versus vertical displacement response of each shore tested at FSEL under non-ideal loading conditions. Next, all towers except for those involving reversed cyclic loading were modeled in a finite element program to simulate the behavior of the tests. Modeling of the shores had two main objectives. The first of these objectives was to determine the appropriate way to represent the structural behavior of the members and connections that constitute the shores; the second objective was to use the general modeling scheme to make design modifications to the shore models for the purpose of improving the structure's overall behavior. The results from these models would then serve to provide design recommendations for the vertical shores used by the US&R teams in the future.

1.3 OVERVIEW OF TESTING

A total of thirteen vertical shores were constructed and tested at FSEL. All shores consisted of No.1 grade Southern Yellow Pine wood. The first four shores were tested under vertical load only. Each subsequent test consisted of a combination of vertical and lateral loading, but the principle objective was to determine the ultimate vertical load capacity of each shore. Three of the remaining nine tests included reversed cyclic loading under a constant vertical load. Another four of the tests endeavored to capture the loading scenario that occurs when a floor slab in a structure shifts suddenly. To achieve this task, the shore was loaded to its working load of 32 kips, then the top of the shore was displaced laterally 15 inches (the maximum distance allowed by the test setup),

and further loaded vertically to failure. The final two tests conducted were for rapid vertical loading and sustained vertical loading only.

1.4 OVERVIEW OF MODELING

Very complex structures are capable of being analyzed as computer models which, once validated by physical tests or by other means, may be carefully used to extrapolate behavior to scenarios beyond those used in the validation process. Such is the case in this research, where the laboratory specimens were carefully modeled using a combination of measured material properties (where available), and presumed material properties acquired from literature. Modeling of laboratory specimens, which were constructed more scrupulously than may occur in the field, is the starting point for future research.

Modeling of the shores was done in Abaqus CAE 6.11 (2), a general-purpose finite element analysis program that is capable of modeling highly complex linear and nonlinear problems encountered in structural engineering. Each physical test was modeled except the ones involving reversed cyclic loading and load rate effects, since hysteretic behavior of nails and time-dependent behavior of wood exceeded the scope of this thesis. To capture the local behavior surrounding each nail, solid elements were used to model all the members. Although Abaqus allows for orthotropic elasticity, the models consisted solely of elements with isotropic material behavior. This was an acceptable assumption because for these particular shores, longitudinal behavior was much more significant than radial and tangential behavior.

Chapter 2 of this thesis provides additional background on the subject of emergency wood shoring systems used by the US&R teams as well as a literature review pertinent to the modeling of wood systems. A description of the experimental setup is presented in *Chapter 3* and the results from the laboratory tests for several of the shores can be found in *Chapter 4*. *Chapter 5* includes a detailed overview of the finite element modeling setup followed by a presentation of the model results in *Chapter 6*. *Chapter 7* contains an analysis and discussion of the model results from several alternate shore

designs as well as recommendations for design improvements. Conclusions are presented in *Chapter 8*.

CHAPTER 2

Background

A discussion of the background information relevant to the application and modeling of Urban Search and Rescue (US&R) shoring systems is provided in this chapter. In particular, a brief description of the history and application of shoring systems, a description of previous shore testing, and a literature review on finite element modeling of wood structures are presented.

2.1 HISTORY OF URBAN SEARCH AND RESCUE SHORING

The US&R task force, established by the Federal Emergency Management Agency (FEMA) in 1989, utilizes wood shoring towers during rescue operations. When a large-scale event of catastrophic proportions occurs, such as an earthquake, a hurricane, or an act of terrorism, a number of response teams from the US&R task force is immediately sent to the site. These task forces endeavor to combine the abilities of each member and their specialized equipment to search damaged structures for live victims, administer emergency medical care to victims, survey structural hazards for rescue crews, and construct shoring when needed (22). Two structural specialists are assigned to every deployed US&R task force. It is the responsibility of the structural specialists to plan and oversee shoring operations.

As mentioned in *Chapter 1*, shoring serves the purpose of providing temporary stabilization or support to the physically damaged structure. In turn, the towers mitigate the potential for further collapse and allow firefighters to safely enter the structure to rescue victims trapped inside. A proper shoring system contains four main elements: a header, one or more posts, a sole plate, and a lateral bracing system. Each of these fundamental elements contributes to the overall success of a shore. In essence, the most basic purpose of a shore is to collect loads from a damaged area, distribute them vertically through the post system, and then redistribute them to the ground or to other

structural elements (19). Figure 2.1 illustrates the ideal loading principle for a shore as well as some of the basic components of a shore.

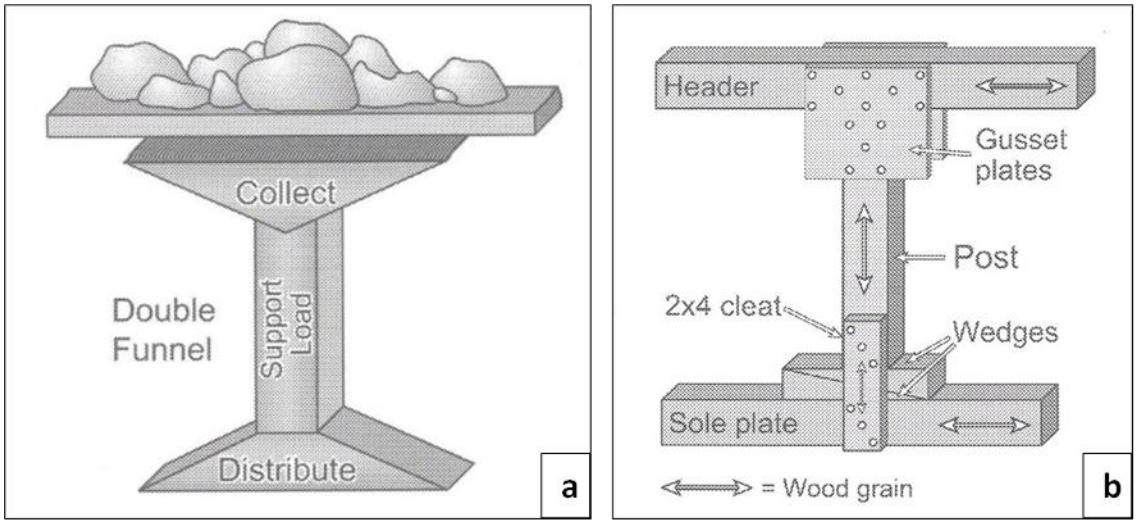

Figure 2.1 (a) Principle of shoring system behavior (b) Shoring system nomenclature [Source: O'Connell 19]

To maintain consistency in shoring construction, a Field Operations Guide (23), simply referred to as the FOG, was published by the USACE. Recent events such as the bombing of the Alfred P. Murrah federal building in Oklahoma City in 1995 and the terrorist attacks on the United States in September 2001 have necessitated the use and study of the performance of shoring systems.

As stated in Section 1.1, the primary objective of this research project was to recommend design modifications that would improve the performance of common vertical shoring systems used by the US&R teams.

2.1.1 Shore Classifications

In the most general sense, shoring systems are grouped into three categories: class 1, class 2, and class 3. Respectively, each shore represents a one-dimensional, two-dimensional, and three-dimensional structure. Obviously, the class three shore offers the most strength and stability. Class 1 shores are typically constructed for very temporary support while class 2 shores are constructed and installed at nearby locations. When

higher loads must be supported, class 2 shores can serve as temporary support while class 3 shores are assembled and erected.

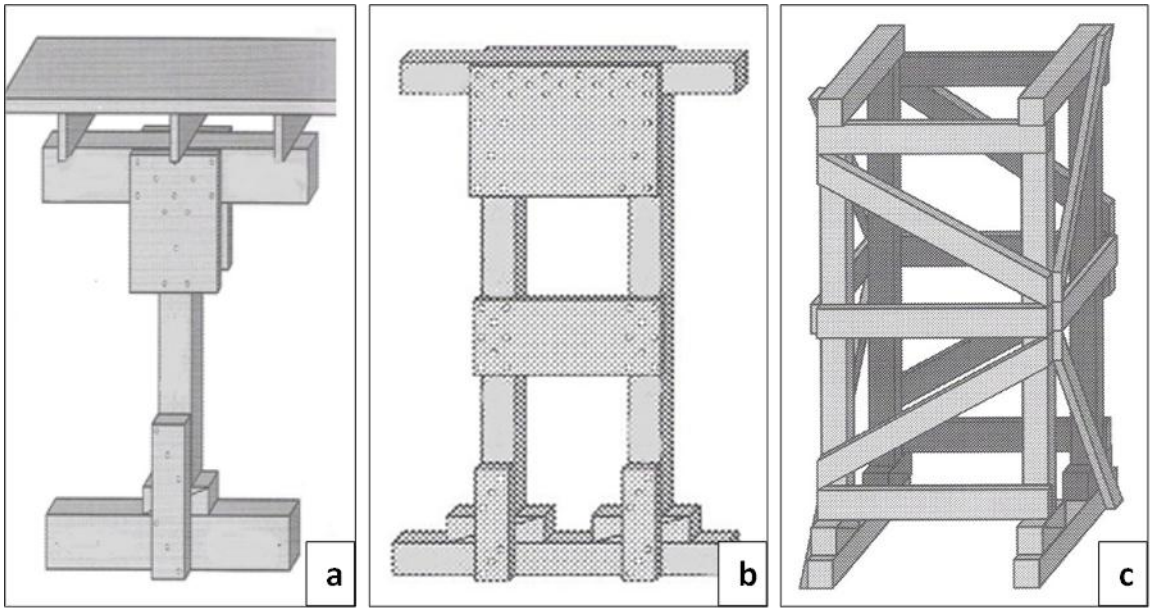

Figure 2.2 Examples of shoring classifications (a) Class 1 shore – Single T (b) Class 2 shore – Double T (c) Class 3 shore – Laced post [Source: O'Connell 19]

2.1.2 Vertical Shores

As stated by O'Connell (19), vertical shores, also known as dead shores, are mainly responsible for carrying the dead load of a collapsed structure. Two of the most commonly used types of vertical shores are the laced post (LP) shore and the plywood laced post (PLP) shore, which are respectively shown in Figures 2.3 and 2.4.

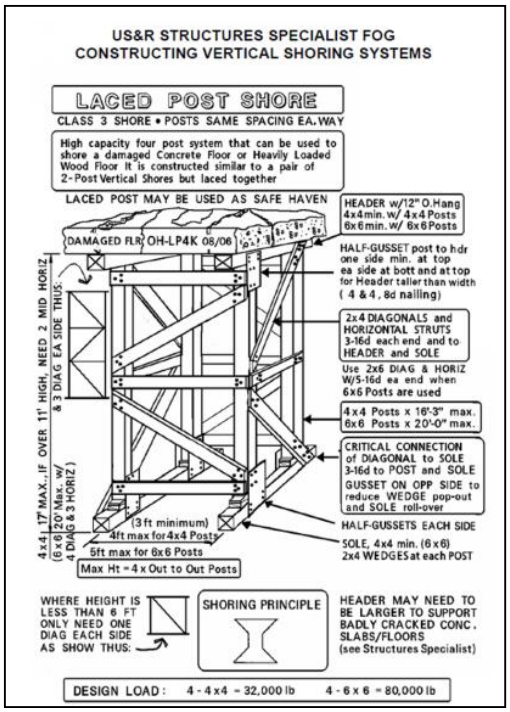

Figure 2.3 Class 3 Laced Post (LP) Shore [Source: USACE FOG 23]

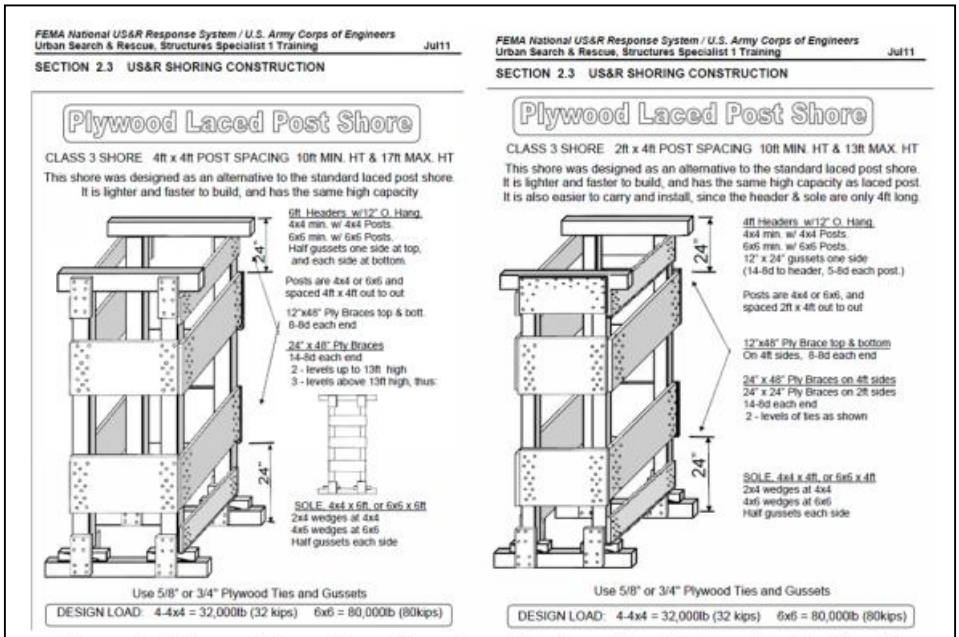

Figure 2.9 Plywood Laced Post Shore Specifications, 4ft x 4ft Base (Left), 2ft x 4ft Base (Right), *(USACE FOG 2011)*

Figure 2.4 Class 3 Plywood Laced Post (PLP) Shore [Source: USACE FOG 24]

Laced post shores are known for providing substantial strength and stability, and can be constructed around any damaged structural element without disturbing it. As such, the laced post shore works quite well as a replacement for bearing walls or columns that have been damaged or destroyed. The plywood laced post shore, which became a standard shore several years after the laced post shore, now serves as an alternate option for the laced post shore. It requires fewer members and has a smaller footprint than the laced post shore. Consequently, these shores are not only lighter than their laced post counterparts, but also quicker and easier to construct. Both types of vertical shores generally use 4x4 posts, although 6x6 posts are sometimes needed if the load to be supported has the potential to be rather large, i.e. for multistory buildings. These types of shores normally are installed below damaged floors, ceilings, or roofs.

2.1.3 Past Shoring Applications

On April 19, 1995 in Oklahoma City, the most devastating act of domestic terrorism occurred on American soil, giving urgent rise to the need for shoring systems. Around 9:02 in the morning, a bomb was detonated in the bed of a truck parked outside of the Alfred P. Murrah federal building, a nine story reinforced concrete structure. The explosion completely destroyed half of the building and caused damage to numerous surrounding structures.

Vertical wood shores were constructed throughout the first and second floors of the collapsed structure. A total of 18 were built, with 16 on the first floor and 2 on the second floor (18). The members that comprised the towers ranged in size from 2x6 to 6x6. Shores erected using 4x4 lumber supported floor slabs that were either damaged or unstable. Figure 2.5 and 2.6 show examples of the various vertical shores installed in the Murrah building's structure. As a result of this catastrophic incident, the FEMA US&R teams began to address the issue of determining a balance between constructed shoring and acceptably engineered shoring.

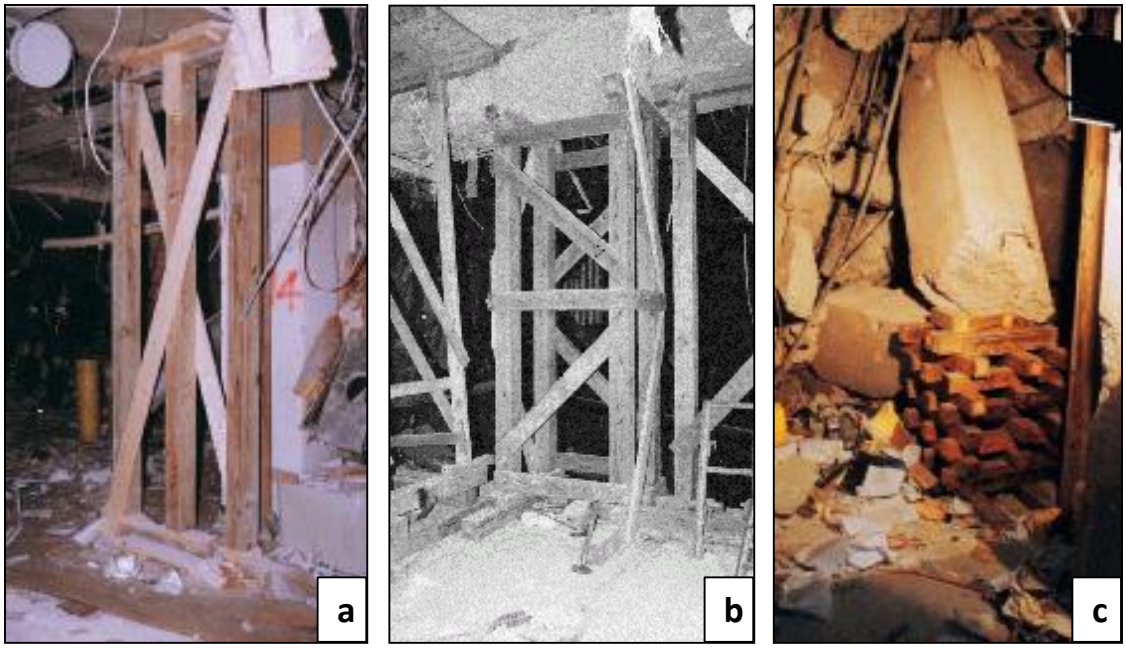

Figure 2.5 Shoring at the Murrah Building in OKC (a) Vertical shore (b) Laced post shore (c) Three tier crib shore [Source: O'Connell 18]

Figure 2.6 Shoring at the Murrah Building in OKC (a) Vertical shore supporting a fractured floor beam (b) Laced post shore with other vertical shores [Source: O'Connell 18]

Another prime example of the application of vertical shoring systems is from the terrorist attacks on the United States on Tuesday September 11, 2001. At approximately 9:38 in the morning, a low-flying Boeing 757 en route to Los Angeles crashed into the west side of the Pentagon in Washington D.C. Immediately, FEMA deployed a total of four US&R task forces to the site of the incident. The impact, coupled with the 30,000 pounds of fuel in the plane, caused an explosion and subsequent fire that destroyed many of the nearby concrete columns and beams.

Upon rigorous inspection and evaluation by structures specialists, it was determined that the structure was unstable and that several crib shores and vertical post shores were needed to support the damaged parts of the structure. As in the case with Oklahoma City, vertical post systems constructed at the Pentagon served to support beams, floor slabs, and overhead debris. They were located strategically in various areas to provide protection to the shoring squads so they could safely access more critical areas that needed the higher capacity crib shores (22). Photos of typical vertical shores in place at the Pentagon are shown in Figure 2.7.

Figure 2.7 Shoring at the Pentagon in Washington D.C. (a) Crib shore (b) Vertical shores constructed near crib shore [Source: Titus 22]

2.2 PREVIOUS SHORE TESTING

In response to the need for better understanding of shore behavior, the FEMA US&R, in cooperation with USACE, launched a series of load tests between May 2001 and May 2010 on laced post shores with various configurations. The results of these tests aimed to demonstrate the vertical load-carrying capacity of the shores, the ability of the fuses to provide warning prior to failure, and the different modes of failure.

The following sections present discussions of the three loading setups used for the aforementioned tests. All tests were conducted at the NASA/AMES Outdoor Aeronautical Research Facility (OARF) in Moffet Field, California.

2.2.1 May 2001 – March 2005

A total of three series of tests were run between May 2001 and March 2005 on 12.5 feet high laced post (LP) specimens. The testing apparatus consisted of a 150 ton bridge crane that was used to lower a 38 kip concrete slab on top of the shores. Next, additional weight, in the form of 12.5 kip pairs of concrete blocks, was added in increments of 25 kips until failure occurred. For every test, failure of the shores occurred during the addition of the third pair of concrete blocks. In turn, the maximum vertical load capacity could only be estimated to lie within the range of 88 kips to 113 kips. Figure 2.8 presents photos of the overall test setup before and after failure of a LP shore.

Figure 2.8 (a) Loading of LP shore using crane (b) Failure of LP shore after addition of third pair of concrete blocks [Source: Hammond 6]

2.2.2 November 2005 – May 2006

Between November 2005 and May 2006, two series of tests were conducted on 13 foot tall LP and PLP specimens. The testing apparatus consisted of four 50-ton hydraulic rams that were used to gradually lower the 38 kip concrete slab on top of the shores. A total of six 12.5 kip pairs of concrete blocks were added to the top of the slab during testing. Unlike the previous tests, the load at any point in time could be calculated. This was accomplished by reading the pressure of the rams and then calculating the corresponding portion of the weight carried by the rams. The remaining portion of the weight was then said to be carried by the shore. Figure 2.9 gives a close-up view of one of the rams used during the tests, and Figures 2.10 and 2.11 show photographs of the shores after failure.

Figure 2.9 (a) Test setup (b) Close-up view of ram [Source: Hammond 6]

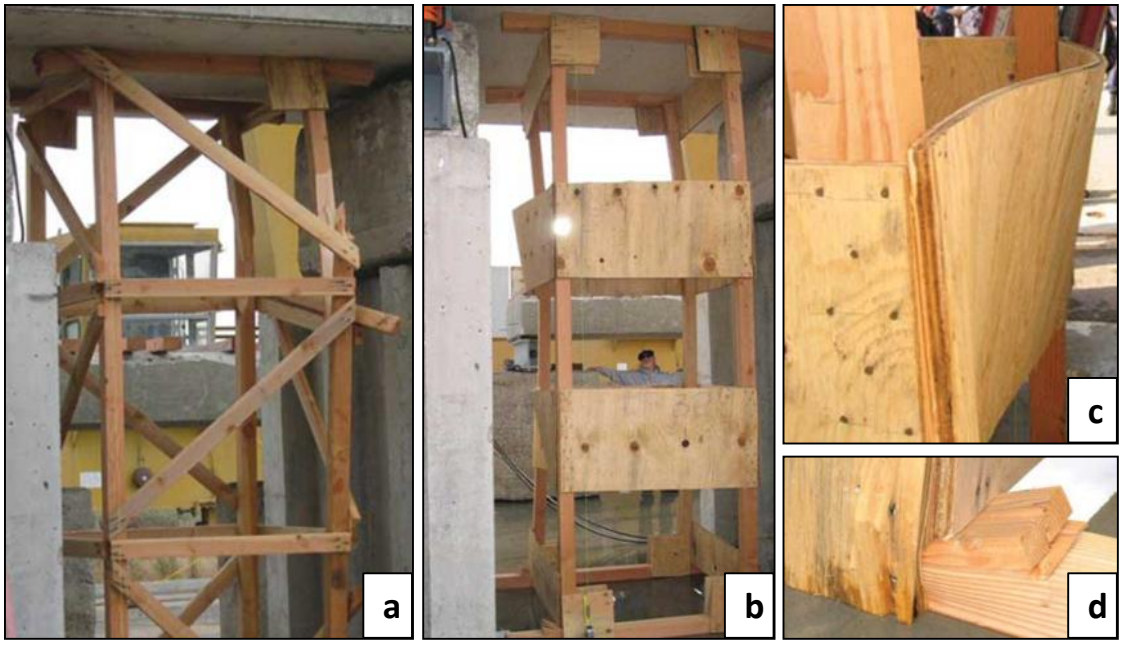

Figure 2.10 (a) LP shore failure (b) PLP shore failure at posts (c) Plywood brace warping in PLP shore (d) Typical wedge cupping at base of shores [Source: Hammond 6]

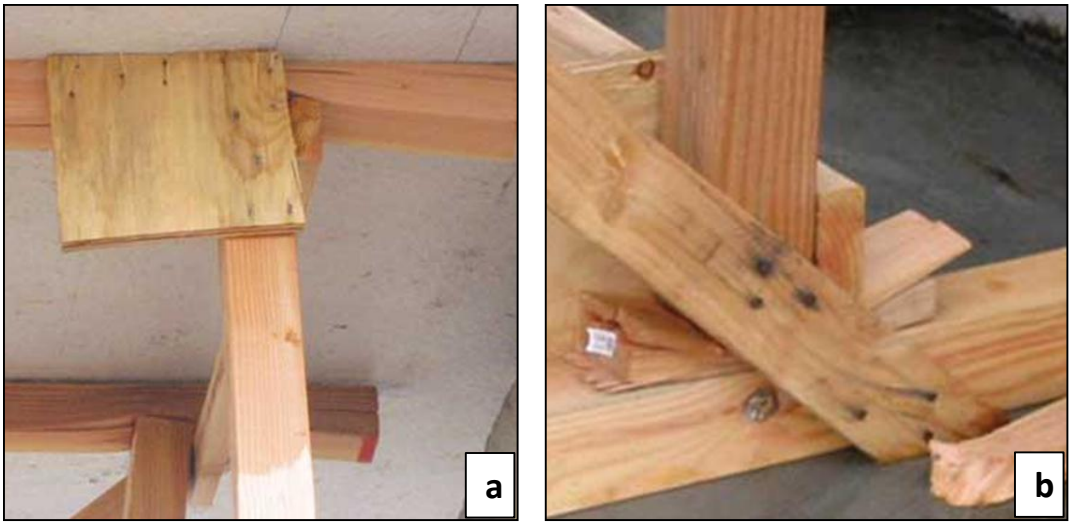

Figure 2.11 (a) Post bearing into header above (b) Wedge cupping at base of shore, [Source: Hammond 6]

2.2.3 May 2007 – May 2010

Most recently, four series of tests were conducted between May 2007 and May 2010 on 12 foot tall LP and PLP specimens. This time, as shown in Figure 2.12, load was applied by having the four 50-ton hydraulic rams slowly lift the floor of the testing apparatus, causing the top of the shore to press against the steel beams above them. This arrangement allowed the load supported by the shores at any point during the tests to be determined by measuring the pressure in the rams. However, since there was no load averaging manifold in these series of tests, there was no way to verify whether or not each post shared an equal amount of load.

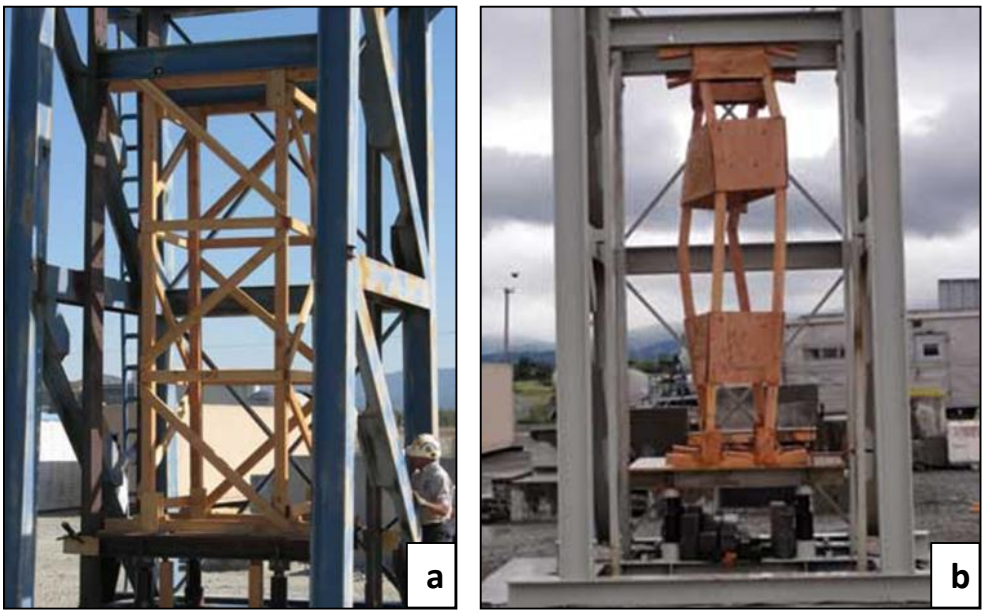

Figure 2.12 (a) Test setup (b) Failure of LP shore [Source: Hammond 6]

Tables 2-1 through 2-3 show the results from each series of tests conducted. Although the tables clearly contain scattered results, a noticeable increase in vertical capacity is seen from the PLP shores tested after 2006.

Table 2-1 Summary of LP shore tests [Source: Hammond 6]

Table 1. LP Shore Tests (2 × 4 or 2 × 6 Lacing)

Shore	Year	Tester	Lacing	Failure	Comments
LP-1	2001	OARF-1	2 × 4	100k	Failed at knots in posts
LP-2	2001	OARF-1	2 × 4	90k+	System failure because of inadequate bracing
LP-11	2004	OARF-1	2 × 4	90k+	Failed at knots in posts
LP-12	2004	OARF-1	2 × 4	90k+	Failed at knots in posts
LP-13	2004	OARF-1	2 × 4	NA	38k load, followed by lateral load test (1.2k max)
LP-21	2005	OARF-1	2 × 6	110k+	Best performance yet
LP-22	2005	OARF-1	2 × 6	90k+	Posts were split prior to test because of excess nailing from standard five 16d nails used for 2 × 6 lacing
LP-23	2005	OARF-1	2 × 6	NA	Pneumatic struts with 2 × 6 lacing. Two cycles of 2-inch lateral with 38k, then end test with no failure
LP-24	2005	OARF-1	2 × 4	100k+	Two cycles of 2-inch lateral with 38k, then vertical load to failure. Very good performance
LP-31	2005	OARF-2	2 × 4	103k	New loading system. Failed at knots in posts
LP-41	2006	OARF-2	2 × 4	103k	New loading system. Failed at knots in posts
LP-51	2007	280k-VT	2 × 4	100k	280k tester. Failed at knots in posts
LP-61	2008	280k-VT	2 × 4	103k	280k tester. Failed at knots in posts

Note: 1k = 1,000 lbs.
Except as noted, shores used 4 × 4-inch posts and 2 × 4 or 2 × 6 lacing.
Source: Table by author.

Test findings.

1. Except for LP-2, all specimens performed as a system with adequate bracing. LP-2 used only one midbrace per side instead of two, which is inadequate for this height.
2. LP systems supported three times the design load prior to failure.
3. Wedge cupping occurred 1.5 to 2.0 times the design load.
4. Header splitting occurred at about 2 times the design load.
5. Properly constructed FEMA LP shores should provide adequate warning of overload, allowing time for mitigation.
6. In most cases, the failures occurred at post knot locations near the intersection of the 2 × lacing with the posts.
7. Deflection (vertical compression of system) was normally less than a ½ inch at design load, and increased to between two and three inches just prior to failure. Most deflection resulted from crushing of the header and sole.

Table 2-2 Summary of 4ft x 4ft PLP shore tests [Source: Hammond 6]

Table 2. PLP Shore Tests (4-foot× 4-foot Layout)

Shore	Year	Tester	Lacing	Failure	Comment
LP-32	2005	OARF-2	2-24" plywood	103k	Failed at post knots, similar to 2 × diagonal tests
LP-42	2006	OARF-2	3-12" ply	83k	Failed in buckling, 12-inch plywood is inadequate
LP-52	2007	280k-VT	2-24" ply	100k	Failed at knots in posts, similar to 2 × diag. tests
LP-53	2007	280k-VT	2-24" ply	88k	Failed at knots in poorest quality posts
LP-62	2008	280k-VT	4-24" ply	115k	Failed at knots in posts. Very good performance
LP-63	2008	280k-VT	5-24" ply	144k	Plywood was too close = impractical

Note: 1k = 1,000 lbs.
Source: Table by author.

Test findings.

1. With one exception (LP-42), all systems failed at the post knot locations near the upper or lower edge of the plywood lacing. Except for LP-42, failure occurred in using 12-inch plywood lacing, indicating that the plywood was too narrow to adequately brace the posts.
2. These PLP systems supported three times the design load prior to failure.
3. Wedge cupping was observed from 1.5 to two times the design load.
4. Header splitting occurred at about two times the design load.
5. PLP shores with 4-foot× 4-foot post layout can be configured to perform as well as standard LP shores.

Table 2-3 Summary of 2ft x 4ft PLP shore tests [Source: Hammond 6]

Table 3. PLP Shore Tests (2-foot × 4-foot Layout)

Shore	Year	Tester	Lacing	Failure	Comment
PLP-31	2005	OARF-2	2-24" ply	88k	Buckling failure
PLP-32	2005	OARF-2	1-24" ply	88k	Buckling failure and re-test to 65k
PLP-41	2006	OARF-2	2-12" ply	65k	Buckling failure and post failure, 12" plywood not good.
PLP-42	2006	OARF-2	3-12" ply	67k	Buckling failure and post failure, 12" plywood not good.
PLP-51	2007	280k-VT	2-24" ply	90k	Failed at poor post with big knot
PLP-61	2008	280k-VT	4-24" ply	85k	Failed at poor post at big knot
PLP-62	2008	280k-VT	1-96" ply	115k	Very good test. Do additional tests
PLP-71, 72	2009	280k-VT	1-96" ply	125k+	5/8" plywood, very good test
PLP-73, 74, 81	2009	280k-VT	1-96" Ply	105k+	1/2" plywood, very good test
PLP-75	2009	280k-VT	1-96" ply	115k	3/4" oriented strand board (OSB), very good test
PLP-76	2009	280k-VT	48"+24"	115k	3/4" ply, (48" + 24", no 96") very good test
PLP-82, 83	2010	280k-VT	48"+24"	115k+	PLP-82=5/8"ply, PLP-83=1/2" ply
PLP-84, 85	2010	280k-VT	2-24" ply	120k+	5/8"ply, spaced near top and bottom of posts

Note: 1k = 1,000 lbs. Source: Table by author.

Test findings.
1. The 2-foot× 4-foot PLP, up to 13 feet high, can be configured to perform as well as the standard LP and the 4-foot × 4-foot PLP.
2. The PLP system can support three times the design load prior to failure.
3. Cupping of the wedges can be observed from 1.5 to two times the design load.
4. Splitting of the headers can be observed at about two times the design load.
5. Deflection was normally less than ½-inch at design load, and increased to between two and 3½ inches just prior to failure. Most of the deflection resulted from the crushing of the header and sole. Deflection increased significantly for loading above 100k, since the headers and soles become crushed to nearly one-half their original height.
6. PLP shores will be proposed as a new FEMA shore.

2.3 LITERATURE REVIEW

A literature review regarding the finite element modeling of wood structures was conducted prior to the modeling of the shores. Based on the behavior of the shores during testing at FSEL, it became evident that the nailed joints were in major part a reason that the shores were able to maintain sufficient structural integrity to carry the vertical and lateral loads seen in the tests. Thus, in order to achieve acceptable correlation between the computer models and the physical tests, the main topic of the following literature discussed involves nailed wood joints. In particular, the literature emphasizes singe-shear dowel type connections in wood joints. The review is divided into two sections: the load-slip behavior of nailed joints and past methods for nailed joint modeling of wood structures. In essence, the first section describes ways of experimentally determining load-slip relationships for nailed joints while the second section outlines how researchers in the past have applied the information from these relationships to finite element models.

2.3.1 Load-slip Behavior of Nailed Joints

Building upon the work of many others before him, Kuenzi (10) formulated an analysis technique for determining the deformation in a single-nailed joint in the linear elastic range. Unlike research done previously, Kuenzi accounted for both joint deformation and permanent distortion of the nail by modeling the nail as a beam on an elastic foundation. This allowed the author to calculate design values for the joints based on expressions he derived using the Winkler model for beams on elastic foundations. Although this model introduced new improvements to the area of nailed joint behavior in wood, it did not consider inelastic behavior of the members or nails. Thus, the results could only be trusted until the wood members reached their proportional limit stress or the nail reached its yield stress.

Wilkinson (28) sought to use the beam on elastic foundation assumption to find a simple theoretical expression for computing stresses and deformations in nailed joints with smooth round nails loaded in single shear. By deriving an expression that could be readily used by engineers, the author hoped to eliminate the need for costly and time-intensive laboratory testing. The expression he obtained, given by Eq. 2-1, assumes the wood members are isotropic (only uses longitudinal modulus of elasticity) and accounts for different wood species, nail sizes, and nail material.

$$\boldsymbol{P = 0.1667 E^{1/4} (\alpha E_l)^{3/4} d^{7/4} \delta} \qquad \textit{Eq. 2-1}$$

$P = Load\ (lbs)$

$E = Nail\ modulus\ of\ elasticity\ (psi)$

$\alpha = Constant\ (in^{-1})$

$E_l = Wood\ modulus\ of\ elasticity\ (psi)$

$d = Fastener\ width\ (in)$

$\delta = Joint\ slip\ (in)$

The calculated slope of the load-slip curve using the equation developed in this study showed good agreement with experimental results. However, near the proportional limit, there were significant differences between the theoretical expression and the test results.

This error was most likely due to the fact that the effects of combined nail and wood interaction were not taken into account.

To bridge the gap between theory and design, Morris (15) proposed a simple linear relationship between lateral load and slip in a nailed wood joint based only on the diameter of the nail. By analyzing the results from load-slip curves from researchers such as Mack (12) and Noren (17) and other various sources, the following equation was suggested for design purposes:

$$\boldsymbol{k = 50{,}000 * d} \qquad \textit{Eq. 2-2}$$

$k = Slip\ modulus\ (lb/in)$

$d = Fastener\ Diameter\ (in)$

Although rather conservative for a given load-slip curve, the above relationship proved to be quite useful in practical applications. Several researchers since this discovery, including Van Dyer (25) and others, have also found that the slip modulus varies directly with the connector diameter.

From a finite element analysis perspective, Foschi (3) was the one of the first to implement a procedure used by several researchers later on regarding the load-slip characteristics of nails. He developed an elasto-plastic finite element model that allowed the nonlinear behavior of the load-slip relationship between steel nails and wood members to be captured. Like Kuenzi (10), his model was based on the theory of beams on elastic foundations. In his approach, he accounted for yielding of the nail in bending as well as the nonlinear bearing behavior of the wood members. Foschi concluded that the theory of beams on elastic foundations did not yield accurate predictions of ultimate loads, but did boast good estimations of initial joint stiffness. The following expressions reveal his findings for a theoretical load-slip relationship for joints fastened with nails known as glulam rivets. The expression given by Eq. 2-3 is for clamped head nails and Eq. 2-4 is for free head nails.

$$\boldsymbol{P = 1,537.72[1.0 - exp(-42.93\Delta)]} \qquad \textit{Eq. 2-3}$$

$$\boldsymbol{P = 1,060.10[1.0 - exp(-29.30\Delta)]} \qquad \textit{Eq. 2-4}$$

$P = Load\ (lbs)$

$\Delta = Joint\ slip\ (in)$

McLain (14) developed a logarithmic expression to describe the load-slip relationships of laterally loaded nailed joints. He conducted several experiments on two-member nailed joints and obtained the load-slip curve for each one. Of all the equations investigated to find a best fit curve to match the data, the following expression was found to yield the highest level of agreement with the experiments:

$$\boldsymbol{P = A * log_{10}(1 + B\Delta)} \qquad \textit{Eq. 2-5}$$

$P = Lateral\ load\ on\ joint\ (lbs)$

$\Delta = Joint\ Deformation\ (in)$

$A, B = Dimensionless\ parameters$

The parameters A and B in Eq. 2-5 are dimensionless coefficients that depend on the specific gravities of the connecting wood members as well as the dynamic modulus of elasticity of the joint components.

In later years, Foschi (4) extended his elasto-plastic analysis to completely model the nonlinear behavior of the load-slip relationship for nailed wood joints. To make this endeavor possible, Foschi modeled the shank as a beam bearing on a nonlinear foundation. Perhaps the most attractive feature of this enhanced model was that the entire load-slip curve as well as the ultimate load of the joint could be computed using only basic properties of the steel in the nail and the bearing characteristics of the wood. After a series of tests, the experimental data from the load-slip curves was fit to an experimental equation involving parameters that varied for different connection types. Results from the tests exhibited good agreement with the finite element model. The equation used to obtain these various parameters which, among others things, considered the shank embedment into the wood, is shown in Eq. 2-6.

$$\boldsymbol{p(w) = (p_o + p_1 w)[1.0 - exp\left(-\frac{kw}{p_o}\right)]} \qquad \textit{Eq. 2-6}$$

$P = Applied\ force\ (lbs/in)$

$P_o = Intercept\ of\ the\ asymptote\ at\ ultimate\ load\ (lbs)$

$P_1 = Modulus\ at\ large\ slips\ (lbs/in)$

$w = Shank\ embedment\ (in)$

$k = Initial\ slip\ modulus\ (lbs/in)$

Thomas and Malhotra (21) proposed a theoretical model to approximate the load-slip behavior of laterally loaded timber joints fabricated with multiple nails. Previously, it was common to assume in design that the capacity of a joint containing multiple fasteners in a row was equal to the product of the number of nails in a row and the lateral capacity of a single nail joint. The authors determined that this design philosophy slightly overestimated joint capacity when a joint contained more than three nails in a row. Therefore, modification factors were suggested to more accurately represent joint stiffness of joints with multiple nails. Furthermore, the results from this investigation showed that the effect of friction on the overall stiffness of multi-nailed joints becomes nearly negligible as the number of nails in a row increases.

Hunt and Bryant (7) improved upon the work of Foschi (4) by modifying the wood-to-nail bearing test setup, which allowed them to account for rotational restraint at the head of the nail. Additionally, the authors took into account the effects of nail head size and shape as well as the grain orientation with respect to loading. Using a finite element analysis as an extension to that of Foschi's (3), the authors confirmed that their theoretical model agreed closely with experimental tests. Their experimental results paved the way for more accurate theoretical predictions of nailed joint behavior to be made over the entire displacement range.

By utilizing a two-dimensional geometric nonlinear analysis, Nishiyama and Ando (16) endeavored to improve the way in which the load-slip curve of nailed wood

joints sheathed with a panel was calculated. The authors modeled the load-slip characteristics through load increments in a finite element analysis. Their model captured the nonlinearity in nail bending with rotational springs at each end of every beam segment of the nail. Also, the authors modeled shank embedment based on the theory of beams on elastic foundations by including a series of closely spaced axial springs along the length of the nail. In this regard, increasing the number of axial springs increased the model accuracy. Results from this study proved that a geometric nonlinear analysis provided relatively better predictions for load-slip curves of nailed wood joints. Moreover, the model results more closely matched experimental tests when the effects of friction and axial force in the nails were included.

According to Section 10.3.6 of the 2005 National Design Specification for Wood Construction (1), the load-slip modulus, γ, for dowel-type fasteners in wood-to-wood connections may be computed using the following exponential equation:

$$\boldsymbol{\gamma = 180,000 * (D)^{1.5}} \qquad \textbf{\textit{Eq. 2-7}}$$

$\gamma = Slip\ modulus\ of\ connection\ (lbs/in)$

$D = Fastener\ diameter\ (in)$

This equation as well as those of Foschi (4) and McLain (14) has been among the most frequently used in modeling nailed wood joints.

2.3.2 Past Methods for Nailed Joint Models

In light of the findings of the aforementioned investigations of load-slip relationships, several approaches for modeling nailed wood joints have been used by researchers. These approaches have been applied to analyze wood floor systems, beams, frames, shear walls, and diaphragms.

To study the effects of the nonlinear stiffness of nails in wood flooring systems, Wheat and Vanderbilt (26) made use of McLain's (14) equation (Eq. 2-5). Their study involved experimental testing of wood joist floor systems fastened with 8d nails followed by verification through finite element analyses in a computer program. The midspan

deflection was recorded from each test. In general, the experimental results agreed well with the computed deflections using the nonlinear model.

Later on, Wheat and Calixto (27) utilized Foschi's (4) expression given by Eq. 2-6 to study its accuracy in computing the response of a nailed two-layered wood member subjected to interlayer slip. The authors employed an energy method to develop the governing nonlinear ordinary differential equations of the member. Good agreement was observed when comparing the computed deflections, interlayer slip, and normal strains to those obtained experimentally.

In a study of the semi-rigid and nonlinear behavior of nailed joints in timber frames, Kermani (9) derived a solution using the stiffness method. A series of piecewise linear relationships, based on the load-slip response of single shear joints loaded laterally, was used to model the rotation of each nailed joint. In essence, the contribution of each nail to the rotational rigidity in each joint was accounted for by multiplying the lateral stiffness of the nail at a given load increment by the square of the fastener's distance to the geometric centroid of the nail group. With the rotational rigidity calculated, the effects of semi-rigid connections at the ends of structural elements were incorporated into the analysis by modifying each element's stiffness matrix. By including the effects of nonlinearity in the analysis, Kermani was able to successfully predict the ultimate carrying capacity of each structure. It should be noted, however, that the author assumed that the center of rotation of each nail remained unchanged throughout both the linear and nonlinear deformations of the frames.

In a study involving sheathing-to-framing connections in wood shear walls and diaphragms, Judd and Fonseca (8) sought to provide a rigorous analytical model that requires neither scaling nor adjustments. Their model represents sheathing-to-framing connections as an oriented pair of nonlinear springs. The use of oriented spring pairs aimed to provide adequate results for cyclic loading, which was not accomplished with a single spring model (Figure 2.13). Previous studies had shown that single spring pair models were subject to potentially significant numerical errors as the ultimate load was reached.

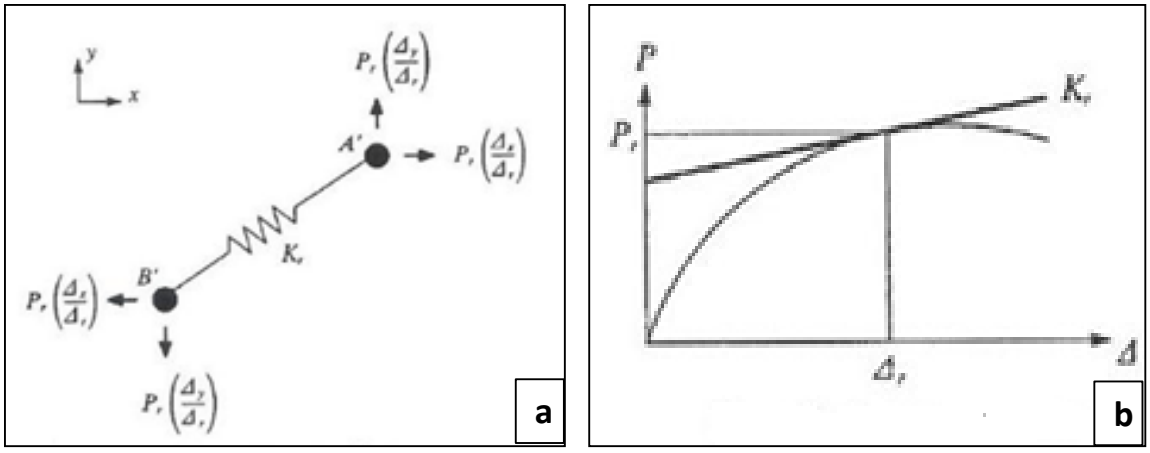

Figure 2.13 Single spring model (a) Element representation (b) Load-slip curve, where Δ_r is the resultant displacement of the joint [Adapted from Judd and Fonseca 8]

As shown in Figure 2.14, a non-oriented spring pair model was tested first in this study, in which the connections were modeled as two orthogonal nonlinear springs. Based on the output, the connection stiffness was overestimated in the nonlinear range. The major cause of this error was due to the fact that one spring was oriented in the fixed global x-direction while the other was oriented in the fixed global y-direction. Consequently, the joint stiffness and force were arbitrary, and they changed relative to the displacement trajectory. This was a crucial error because the actual connection stiffness remained the same regardless of the displacement path.

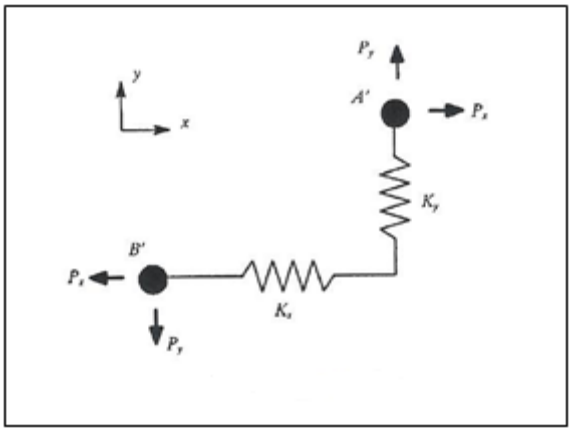

Figure 2.14 Element representation for non-oriented spring pair model [Adapted from Judd and Fonseca 8]

To solve this issue, the authors switched to an oriented spring pair model (Figure 2.15). The connections were modeled as two orthogonal nonlinear springs oriented using the initial displacement trajectory, a schematic of which is shown in Figure 2.16. In turn, the angle change that occurred within the joint during loading was accounted for in the analysis. Also, the element stiffness matrix and nodal force vector were coupled in the x and y directions. As intended, the connection stiffness and forces were functions of the u and v directional displacements. The model has proven to be adequate in monotonic and cyclic analyses. Indeed, the model showed excellent improvements in accuracy for measuring ultimate displacement, ultimate load, and energy absorbed.

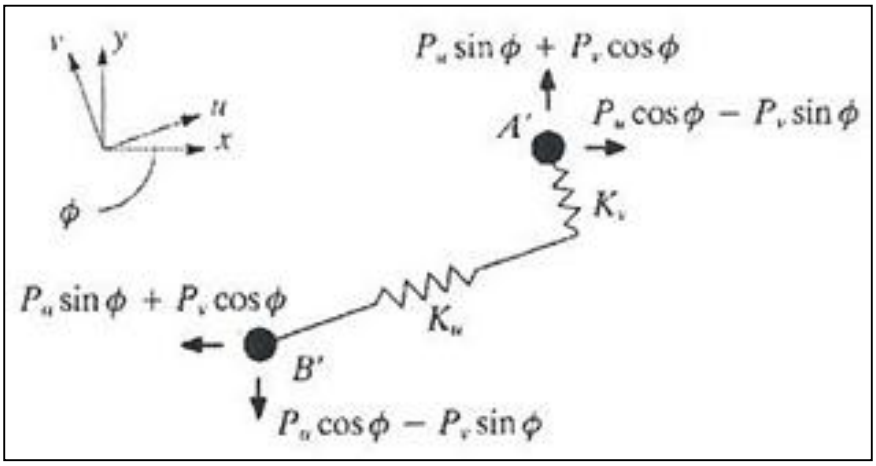

Figure 2.15 Element representation for oriented spring pair model [Adapted from Judd and Fonseca 8]

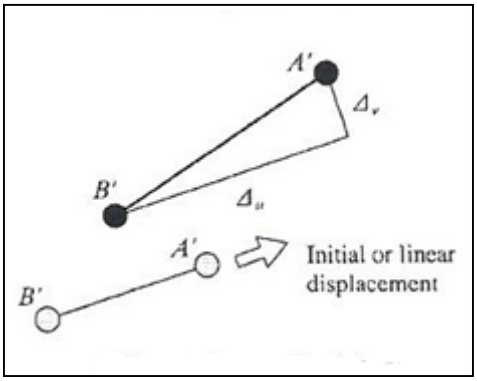

Figure 2.16 Initial displacement trajectory [Adapted from Judd and Fonseca 8]

The finite element modeling procedure utilized for the shores described in this research is explained in *Chapter 5*. A detailed description of the experimental setup utilized to test the shoring specimens is provided next in *Chapter 3*.

CHAPTER 3

Experimental Setup

The following sections contain a description of the overall design and details of the experimental setup used to test the shoring specimens. The topics covered include loading requirements, design of the loading mechanism, and means of instrumentation. It should be noted that the information discussed in this chapter was adapted from the description of the experimental setup by McCord (13). This chapter is included herein to make this document more self-contained.

3.1 LOADING REQUIREMENTS

At the request of the Federal Emergency Management Agency (FEMA) Urban Search and Rescue (US&R), design of the experimental setup had to accommodate several types of non-ideal loading scenarios commonly encountered in real world applications. It was desired that a large portion of the specimens be subjected to a combination of vertical and lateral loading.

3.1.1 Vertical Loading

Since gravity loads are always present on a vertical shore, all tests conducted at Ferguson Structural Engineering Laboratory (FSEL) included the application of vertical loading. The testing protocol called for both load control and displacement control tests.

A load control test involves the gradual application of load at certain increments until failure occurs. In a shore test, the failure is sudden and rapid under vertical load control; the load drops to zero immediately as the structure reaches its ultimate strength. Although this is representative of real world loading on a shore, a load control test limits the amount of data that can be acquired in a laboratory test.

In all but one of the tests, vertical load was applied to the specimens using displacement control. In this type of test, an incremental displacement is induced at the top of the shore, and the corresponding load to obtain that certain displacement is recorded. The load continues to be recorded as the deformation is increased. At certain

deformation levels – even before ultimate strength is reached – the load may drop in order to maintain equilibrium as the deformations increase. At ultimate strength, as deformations are still forced to increase, the load reduces accordingly in a manner consistent with equilibrium requirements. It is impossible to surmise in most practical uses of shores whether a given shore is exposed to a load controlled or deformation controlled scenario.

The output desired from this particular type of loading was the vertical load versus vertical displacement curve for each specimen. However, from an experimental viewpoint, it was of interest to discern if there were major differences in ultimate strengths between the two loading conditions.

In *Chapter 6*, this information is used to verify the accuracy of the finite element model used for this research.

3.1.2 Lateral Loading

As described in *Chapter 2*, US&R has already conducted a large number of vertical loading tests on shoring towers. Although plenty of useful information was obtained from these tests, there existed virtually no data regarding the lateral load capacity of each type of shore. Therefore, it was highly desired that the loading mechanism utilized in this study be capable of providing either a lateral displacement or lateral force to the top of the shore along with the vertical load application in certain tests. To study the behavior of shoring systems during load or deformation reversals, reversed cyclic loading was also included in the testing protocol.

3.1.3 Loading Interface

In emergency response situations, vertical shores are often subjected to unique loading interfaces and boundary conditions. As mentioned previously, a vertical shore is typically constructed beneath a floor slab or beam. To better model the loading interface present in shoring applications, it was desired that the test setup include a floor slab or beam to transfer load onto the top of the shore.

3.1.4 Sloped Loading and Level Loading

As described in the case studies of shoring used for the emergency events in Oklahoma City and at the Pentagon, a severely damaged structure is usually accompanied by a significant loss of overall stability. Of major concern with regard to this issue is the stability of floor systems in the structure. When the stability of a floor system is compromised, it becomes extremely susceptible to various types of movement. At this point, the slab is potentially free to exhibit any of 6 rigid body modes (3 translations and 3 rotations). The slab can displace in the global x, y, or z directions as well as undergo a rigid body rotation about any of these axes. Under the constraints of the testing apparatus used in this study, it was not feasible to capture all of the aforementioned types of motion. Furthermore, several of the safety issues involved in such a test setup presented considerable concern. For example, it was agreed upon that allowing rigid body rotation of the slab during testing would be difficult to achieve while, at the same time, maintaining accurate and safe loading. Due to the high level of uncertainty and risk discussed above, the research team decided that the degrees of freedom for the loading head would be limited to vertical and horizontal displacement in the global directions. In other words, the loading head would not be allowed to tilt or rotate at all during testing. All of the factors mentioned above resulted in the final design of the test setup that was used during each of the tests conducted at FSEL.

3.2 LOADING SYSTEM

This section presents the details and designs with respect to the loading system used for each test specimen. The discussion includes the individual components of the loading apparatus, safety features, and limitations.

3.2.1 Loading Frame and Actuators

A large steel L-frame recycled from a previous research project served as the loading frame for the test setup. The frame was used in conjunction with a thick concrete slab cast specifically for this project. The slab, intended to represent a floor slab in a

structure, was used as the element of load transfer from the frame to the shore. Two wide flange steel sections, welded together at their ends and stiffened throughout with full-length and half-length web stiffeners, made up the form of the L-frame.

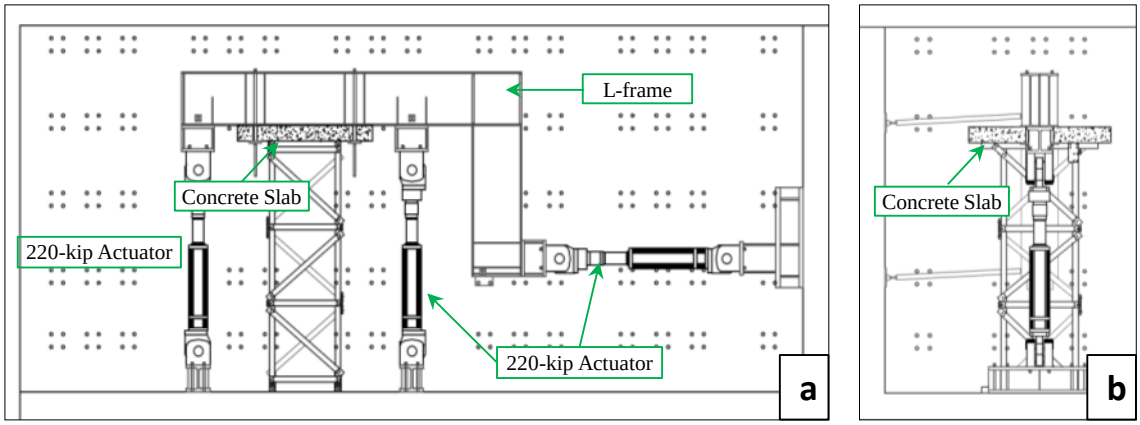

Figure 3.1 (a) Front view of test setup (b) Side view from north
[Adapted from McCord 13]

As shown in Figure 3.1, the loading frame was connected to two vertical MTS hydraulic actuators and one horizontal MTS hydraulic actuator. Each actuator possessed a capacity of 220 kips and a stroke of 30 inches. The vertical actuators were anchored to a thick concrete strong floor while the horizontal actuator was anchored to a concrete reaction wall. The two vertical actuators could be controlled in unison to maintain a level loading head on the shore (Figure 3.2a). The horizontal actuator was used to move the L-frame to left and right in the tests involving lateral load, lateral displacement, and reversed cyclic loading (Figure 3.2b). For the tests involving lateral load, the horizontal actuator induced a lateral displacement on the entire load frame while the L-frame was kept level throughout the test by use of a programmed control loop on the two vertical actuators.

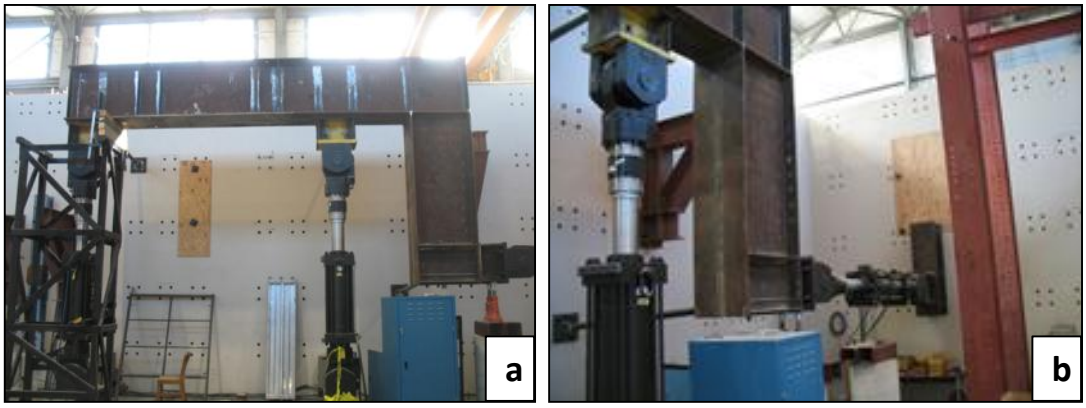

Figure 3.2 (a) Two vertical MTS actuators (b) Horizontal MTS actuator

3.2.2 Concrete Slab Design

The concrete slab served to evenly distribute the load from the loading frame and apply it to the shore. Unlike slabs in practical structures, deflection of the slab during testing was not desired because of the potential inaccuracies it would inflict on the data readings of the overall displacement. Additionally, since it would have been costly and time-consuming to cast a new slab, it was desired to use the same slab for each test. As such, the slab would need to exhibit excellent resistance to cracking and failure under the anticipated loads. Therefore, the slab was intentionally overdesigned in its stiffness and strength for the purpose of enduring multiple tests.

To provide the necessary strength and stiffness to the slab for surviving a series of load tests, 10 ksi concrete was used to cast the slab. Moreover, a substantial amount of longitudinal and transverse reinforcement was placed at the top and bottom sides of the slab. A detailed drawing of the slab and reinforcement can be found in McCord (13).

3.2.3 Safety Features

In any type of laboratory test, one must identify any potential safety hazards and take appropriate measures to eliminate them. One of the key safety precautions in this test setup involved the support of the loading frame. As a result, several safety features were implemented to restrain unwanted movement of the heavy loading arm. A discussion of these components is provided in the sections that follow.

3.2.3.1 Lateral Braces

To prohibit out-of-plane movement and instability of the loading frame, three lateral braces were installed. The braces were anchored to the strong wall behind the test setup. As shown in Figure 3.3, the braces strictly limited the L-frame to lateral movement in the plane of the page.

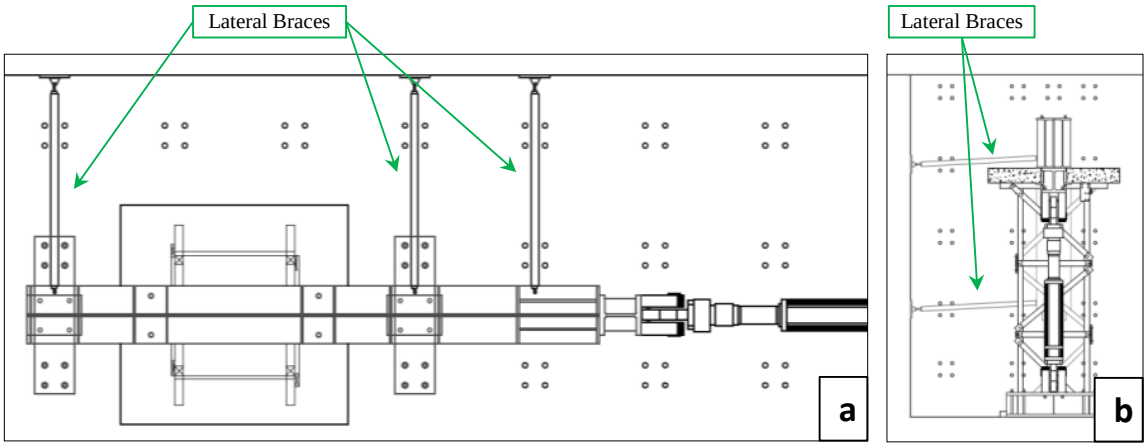

Figure 3.3 (a) Plan view of lateral braces (b) Side view of lateral braces [Adapted from McCord 13]

The lateral braces consisted of a cylindrical steel tube with a ball joint attached at each end. Using the ball joints, each brace was connected to the strong wall and the loading frame with threaded bolts. This arrangement allowed the system to be loosened or tightened simply by turning the cylindrical tube. The strategic location of the lateral braces prevented out-of-plane rotation of the L-frame while providing adequate stability. Photographs of the braces are displayed in Figure 3.4.

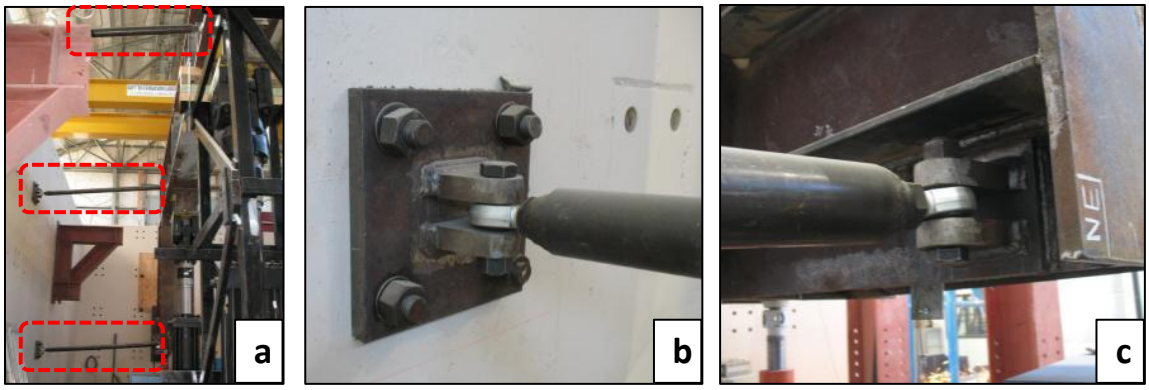

Figure 3.4 (a) All three lateral braces (b) Connection of lateral brace to strong wall (c) Connection of lateral brace to L-frame

3.2.3.2 Safety Shoring

An additional measure taken as a precaution against unwanted movement of the loading frame was the installation of a safety shore. The dead weight alone of the slab and the L-frame was estimated at 26 kips. A major concern was raised regarding the fact that if during testing the actuator pressures were suddenly obstructed, the enormous weight of the frame and slab would cause the actuators to compress the remaining 15 inches of stroke. This large vertical displacement could fracture the lateral supports, ultimately causing failure of the frame. To eliminate the possibility of such an event, a modified safety shore was constructed around the left vertical actuator. This shore, along with two jacks placed under the short leg of the L-frame, served to inhibit unwanted downward deflection of the testing frame. Figure 3.5 displays a schematic drawing and a photograph of this safety shore in the context of the overall test setup.

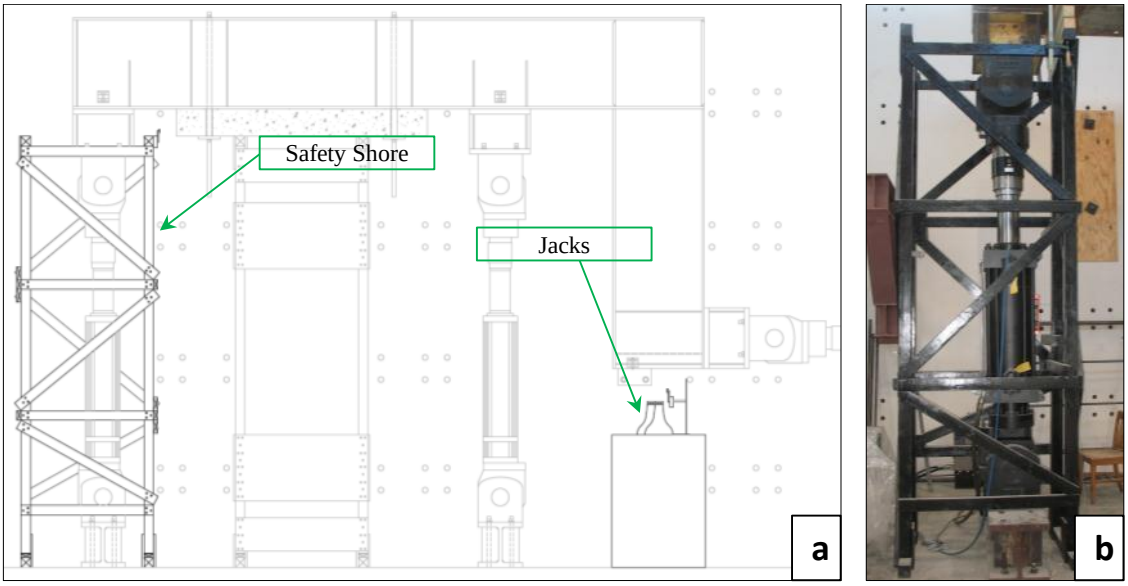

Figure 3.5 (a) Schematic of safety shore location (b) Photograph of safety shore in place [Adapted from McCord 13]

3.2.3.3 Emergency Shutoff Switches

Although the test setup included an emergency shutoff button that would immediately stop actuator movement, two additional shutoff switches were installed to ensure the frame did not exceed the allowable vertical displacement. These two switches, which upon activation would stop the test abruptly, were placed at each end of the L-frame (Figure 3.6).

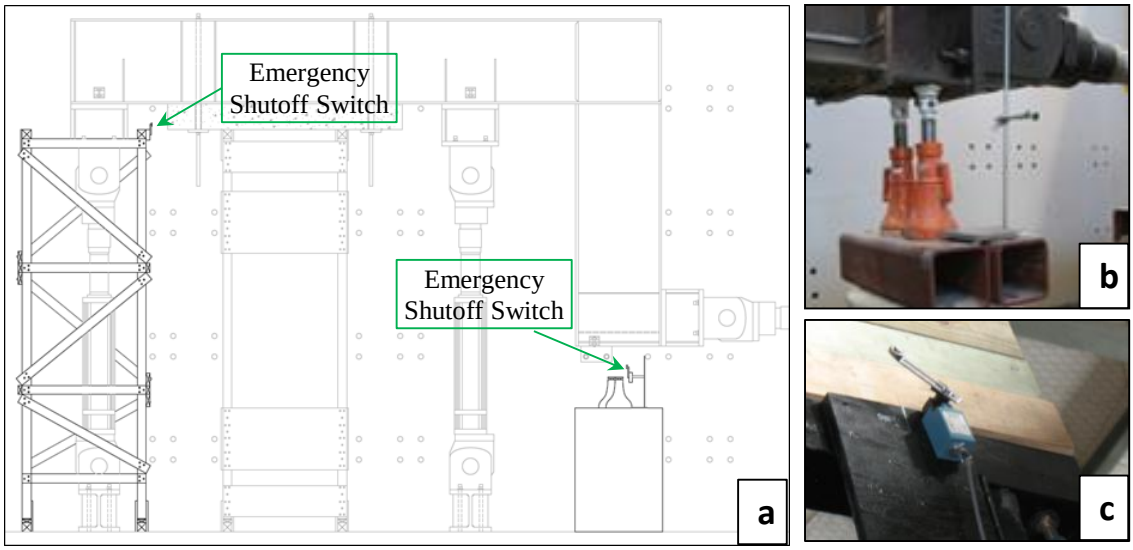

Figure 3.6 (a) Schematic of emergency shutoff switch locations (b) Shutoff switch for south actuator (c) Shutoff switch for north actuator [Adapted from McCord 13]

3.2.4 Additional Test Setup Considerations

The geometry of the testing apparatus limited the shore specimens to an overall height of 13 feet. Fortunately, the testing protocol specified the shores tested at FSEL to be representative of those used in one-story applications. Shorter specimens could be tested by inserting blocking between the soles and the ground, but taller towers would require an arduous process for altering the entire frame.

For the tests involving lateral load and lateral displacement at the top of the shore, seven slip brackets were installed to restrain undesired in-plane movement of the headers and soles. After much discussion, it was decided that slip should indeed be avoided during testing to garner the most accurate and reliable data possible. Using snug tight nuts, the brackets were anchored to the strong floor for restraining the soles and to the slab for restraining the headers (Figure 3.7).

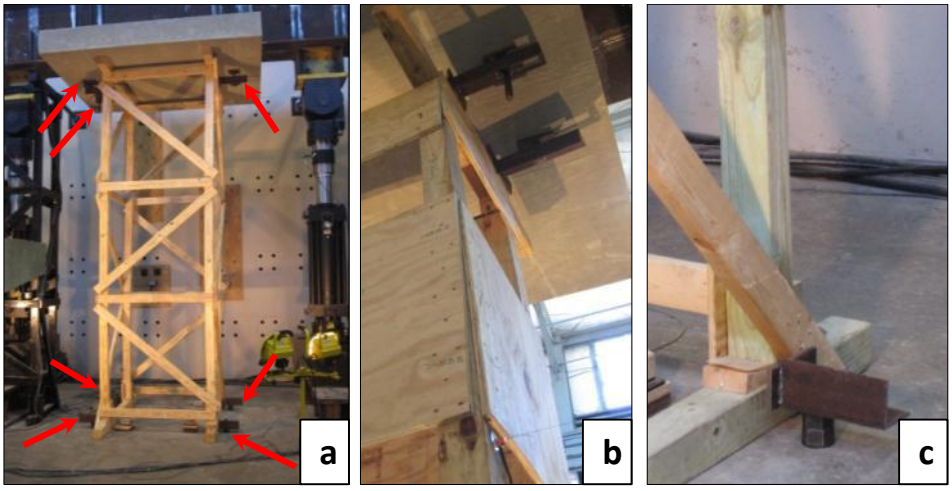

Figure 3.7 Slip brackets (a) Location of all seven (b) Two brackets at the shore header (c) Bracket near the sole of the shore

3.3 INSTRUMENTATION AND DOCUMENTATION

Two primary means of data acquisition were employed to collect data pertaining to the applied on the shores and induced displacement of the shores. This section presents a description of the instrumentation and documentation used for the purpose of collecting data in each test.

3.3.1 Actuator Data

The MTS hydraulic actuators provided the bulk of the data collected in the laboratory tests. Each actuator possessed a load cell and LVDT displacement transducer, which digitally reported data to the data acquisition program. Measurements for vertical displacement, load, and time were taken at regular intervals throughout the tests.

3.3.2 Structural Response Data Collection

String type linear potentiometers, located strategically at various locations for each specimen, provided the secondary means of data acquisition (Figure 3.8). A potentiometer was placed near the top of each post to record the vertical displacement. Poly-coated steel fishing line was used to connect the potentiometers to the top of the

posts. To prevent any obstructions from affecting the steel lines during testing, the potentiometers were offset from the posts using 12 inch cantilevered steel bars attached to each post (Figure 3.8). In order to prevent movement of the potentiometer boxes during loading, steel blocks were used to provide added weight.

Lateral displacements near the immediate joints of the shores were recorded by four potentiometers, two anchored to the strong wall and two anchored to the safety shore. Prior to each test, all the string type linear potentiometers were calibrated and checked for desired performance.

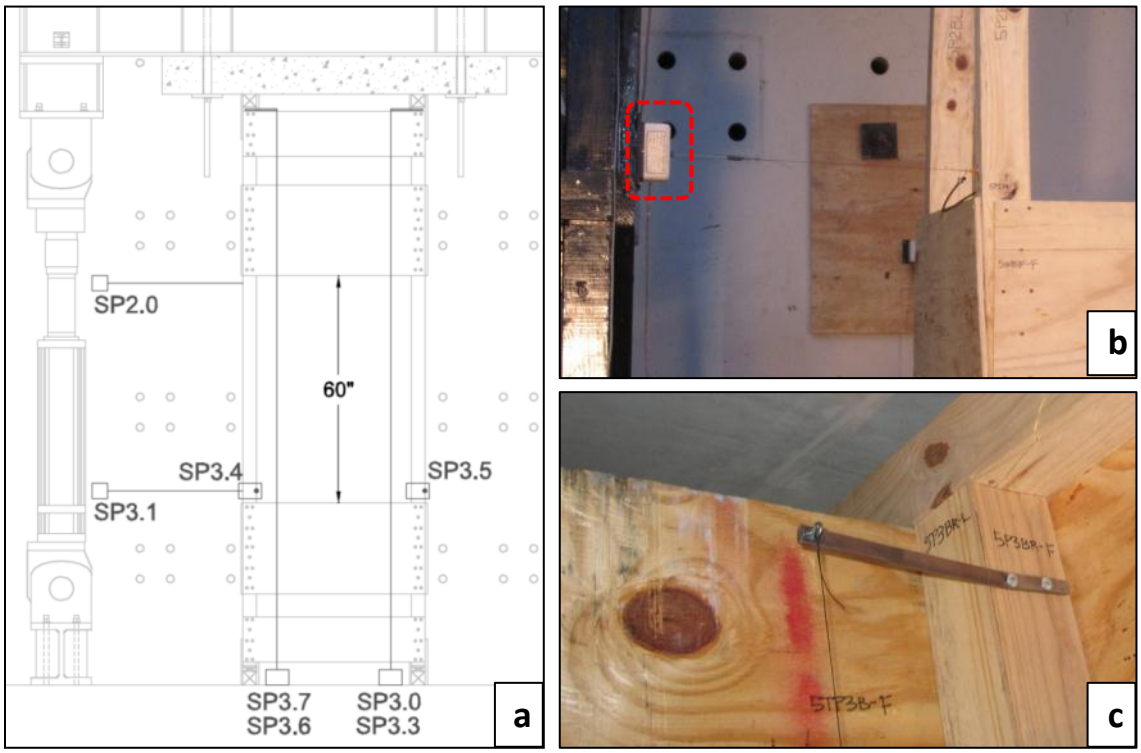

Figure 3.8 (a) Schematic of string potentiometer locations (b) Lateral string potentiometer (c) Attachment of vertical potentiometer to post [Adapted from McCord 13]

3.3.3 Photographic and Video Documentation

Each shore contained a photographic database that documented every single member according to its orientation and location. This library of photos contained

folders of each shore before, during, and after testing for the purpose of making comparisons between areas of the shore prior to and after failure. A member specific identification system was created to organize all photographs in their respective shores. Prior to testing, a five part identification number was written on each face of the every member of the shore. Details for the method of obtaining a nomenclature system for each member are presented in Figure 3.9. Figure 3.10 gives an illustration of a member identification number.

Figure 3.9 Description of nomenclature system for shore members

[Source: McCord 13]

Figure 3.10 Example of shore member label: Shore 1, Wide Brace, Level 1, Front of shore, Front side of member

During testing, digital photographs were taken to document the behavior of each shore from the onset of loading to the last failure of a post. Additional photographs were taken at the end of each test to capture areas of failure or distress, including nail withdrawal. These photographs were then added to the library database of photographs and compared to the pretest photographs for careful investigation of behavior.

Each test was documented by two video cameras that were placed at different locations, making possible the detection of cracking noises as well as post bending.

3.4 TEST MATRIX AND LOADING SCENARIOS

With the exception of one shore (Shore 10), all specimens were constructed with Southern Yellow Pine wood, grade No.1. This particular group of wood species is widely available in most regions of the United States, making it a perfect choice for shoring towers in real world applications. A variety of loading scenarios and designs were investigated. Table 3-1 provides a summary of the governing test matrix, with highlighted rows indicating the shores that were modeled in Abaqus.

Table 3-1 Description of the testing protocol for the shore specimens

TEST MATRIX		
Shore No.	**Shore Type**	**Loading Scenario**
1	PLP*	[A] Vertical Load Only
2	PLP	[A] Vertical Load Only
3	LP	[A] Vertical Load Only
4	LP	[A*] Vertical Load Only (Load-Control)
5	PLP*	[B] Cyclic Loading Under Two Levels of Vertical Load
6	LP	[C] Constant Lateral Displacement (6in), Increasing Vertical Load
7	PLP	[C] Constant Lateral Displacement (6in), Increasing Vertical Load
8	LP	[D] Constant Vertical Load (32kips), Increasing Lateral Displacement
9	PLP	[D] Constant Vertical Load (32kips), Increasing Lateral Displacement
10	LP*	[B] Cyclic Loading Under Two Levels of Vertical Load
11	LP	[B] Cyclic Loading Under Two Levels of Vertical Load
12	PLP	[E] Rapid Vertical Loading Only
13	PLP	[F] Sustained Vertical Load Only (72kips for 8hrs)

LP: Standard Laced Post Shore - SYP No. 1

LP*: Laced Post Shore - SYP No. 2

PLP: 5ft Clear Space Plywood Laced Post Shore

PLP*: 4ft Clear Space Plywood Laced Post Shore

As shown above, Specimens 1-4 were tested under vertical loading only. Evaluation of their results at the end of testing provided insight and guidance for the remaining tests as well as a suitable comparison to the previous tests performed by US&R (*Chapter 2).* In particular, Specimens 3 and 4 were tested to investigate the effects of displacement-controlled loading versus load-controlled testing. Comparison of these results revealed that no significant increase in capacity was afforded by either method. As anticipated, the only noteworthy difference observed between the two methods was the rate at which overall shore failure occurred. In the load-controlled test, the entire shore failed rapidly at an accelerated rate. Once the first failure initiated, it only took a few seconds for the rest of the posts to fail, culminating in the collapse of the tower. This occurred because during a load-controlled test, the load is maintained and increased on the system at a specified rate, meaning that any sudden geometric changes in the structure can result in large descents of the load above in order to maintain its effect. On the other hand displacement-controlled tests maintained a constant rate of

vertical displacement before and after the peak load was reached, allowing each individual shore to fail gradually at a unique load. Therefore, to maximize the amount of knowledge obtained in this study, all remaining tests were conducted using the displacement-controlled method.

The next series of tests (5-11) investigated the combined effects of vertical loading and lateral displacements on both LP and PLP shores. For purposes of comparison between the two types of shores, each specific scenario was conducted on one LP and one PLP specimen. Tests 12 and 13, using vertical load only, were conducted on PLP shores to investigate effects of rate of applied loading on the overall shore capacity.

The subsequent sections provide a description of the loading scenarios involved for the shores discussed in the scope of this thesis. A description of the remaining loading sequences can be found in McCord (13).

3.4.1 Loading Scenario A

This loading scenario subjected the shores to purely vertical load. Shores 1, 2, and 3 were vertically loaded by moving the load frame downward by means of the two vertical MTS actuators while maintaining a horizontally level loading head. Using displacement-controlled loading, vertical displacement was imposed at the top of the shores at a constant rate of 0.2 inches per minute. Lateral movement of the loading frame was not permitted.

Specimen 4, the only one to undergo a load-controlled test, was loaded vertically at a constant rate of 10 kips per minute. Each vertical actuator applied one-half of the total load to the shore, allowing the loading head to remain level throughout the test. Again, the loading frame was restrained from lateral movement during testing. The rate of loading remained the same until the failure of the entire shore had been achieved.

3.4.2 Loading Scenario C

The tests conducted on Specimens 6 and 7 aimed to demonstrate the vertical capacity of a shore with a large initial lateral displacement at the top of the tower prior to the application of loading. Measurements of the average out-of-plumbness of the top of each shore relative to the bottom were taken and recorded prior to testing. At the start of testing, an additional lateral displacement was imposed at the top of the shore in the same direction as the out-of-plumbness, to force its initial imperfection to be 6 inches. For instance, if the shore was initially out-of-plumb 1.5 inches in a certain direction, then the shore was displaced an additional 4.5 inches in the same direction to achieve a total displacement of 6 inches. Afterward, the shore was loaded vertically to failure using a displacement-controlled loading rate of 0.2 inches per minute. No additional lateral movement of the loading frame was allowed.

3.4.3 Loading Scenario D

As a counterpart to the loading scenario C, Specimens 8 and 9 were tested by first applying a constant vertical load of 32 kips (the design capacity of the shore) and then gradually increasing the lateral displacement of the top of the shore at a rate of approximately 0.6 inches per minute. Due to the available stroke length of the horizontal actuator, the maximum allowable lateral displacement for these tests was 15 inches. In the event that a shore did not experience failure prior to reaching the 15 inch lateral displacement limit, vertical load was subsequently increased on the shore until failure.

Laboratory results for the shores tested at FSEL and later modeled in Abaqus can be found in *Chapter 4*.

CHAPTER 4

Test Results

The following chapter contains a detailed summary of several of the shore tests conducted at the Ferguson Structural Engineering Laboratory (FSEL) in Austin, Texas. It should be noted that the content provided in this chapter was adapted from the test results as described by McCord (13). Included in the results for each test is a description of the individual shore behavior during testing, maximum shore capacity, a plot of the vertical load versus vertical deflection, the mode of failure, and supporting photographs. Although 13 tests were performed, the results of only the 8 shores that were modeled and analyzed in the computer after testing are presented in these sections. The nature of certain tests exceeded the scope of the modeling tasks. Therefore, the results for tests involving cyclic lateral loading, rapid vertical loading, and sustained vertical loading were excluded from this chapter. A full summary of the remaining 5 tests (Specimens 5, 10, 11, 12, and 13) is available in McCord (13).

All shores were constructed and tested at FSEL between August and December 2011. Under the supervision and guidance of John O'Connell, a highly experienced shoring instructor for the Fire Department of New York (FDNY), 9 of the 13 shores tested were assembled within 2 work days. Of the 8 shores discussed in the subsequent sections, 4 were laced post (LP) and 4 were plywood laced post (PLP). The LP specimens were constructed with a footprint of 4ft x 4ft, while the PLP specimens were constructed with a 2ft x 4ft footprint. All connections involving 2x4 members and 4x4 posts or headers/soles consisted of 8d sinker nails (12d common) while 16d sinker nails (12d common) were used to connect plywood to 4x4 members. It should be noted that each LP shore contained around 220 nails and each PLP shore contained just over 400 nails. A detailed documentation of the specimen design and construction has been compiled and presented in McCord (13).

As described in Section 3.3, each test consisted of two methods of data acquisition. These included readings taken from each MTS actuator as well as string type

linear potentiometers strategically located throughout the shore. The majority of the data collected and focused on in this chapter came from the MTS load cells and LVDT transducers. Since each vertical actuator kept track of its own pressure, the loads recorded from each were simply combined to obtain the total load applied to the shore at any given time. Additionally, the vertical actuators were programmed to displace vertically the exact same amount. As such, the data from each actuator was averaged and taken as the overall vertical displacement of the shore. It is important to point out that prior to testing, a large gap existed between the bottom of the slab and the top of the shore. At this point, all MTS instrumentation was initialized to give a zero reading. Once the loading frame was lowered to establish contact between the slab and the shore, an apparent initial offset was added to the data. Most of the plots shown in this chapter have been adjusted to minimize this effect and improve the authenticity of the data.

Another helpful piece of information in understanding the output pertains to the initial region of stiffening in several of the load-displacement plots. It has been speculated that two main causes contributed to this phenomenon. First, at the onset of testing, quite a few of the shores had gaps between the soles and the ground. Many of the shores were constructed more than one month prior to being tested and, as a result, changes in the moisture content of the shore members caused many of them to bow. Once loading started, these small gaps allowed for some rigid body motion of the shore until it became tightly wedged between the slab and the ground. Secondly, a number of the shores also contained small gaps between the posts, wedges, and headers. A major reason for this was that the shores were constructed on their sides, making it extremely difficult to maintain a snug interface at each end of the posts. Consequently, under loading, these posts shifted downward against the resistance of nails connecting nearby gussets until they were able to fully bear on the wedges below and the headers above. This region of stiffening will be referred to as the zone of "*system engagement"*. Figure 4.1 illustrates the test stages with respect to the factors discussed above.

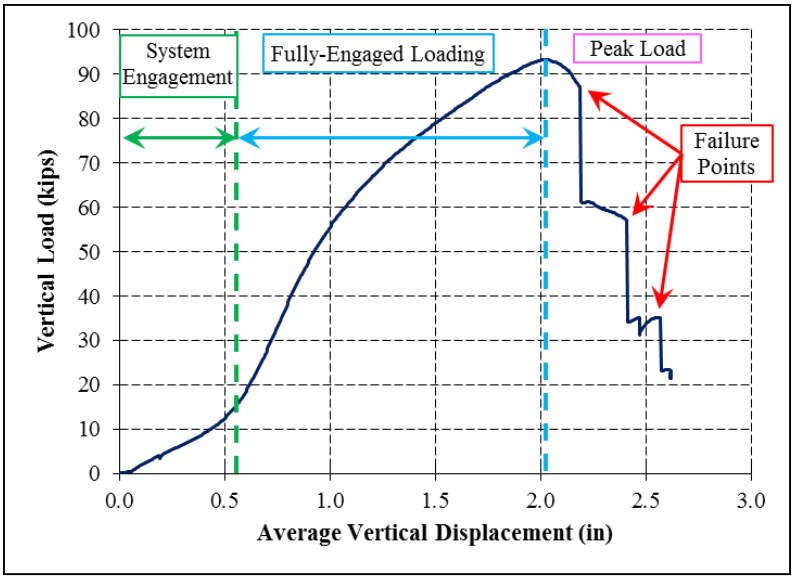

Figure 4.1 Typical loading stages during testing [Adapted from McCord 13]

Following the system engagement zone, the load-displacement curve generally has a region in which the slope is constant, or nearly so, followed by a region with decreasing slope. This region, labeled as the "*fully-engaged loading*" region, results from stiffening of the shoring system as all its elements are fully engaged to resist the applied vertical load. A peak load was attained at the climax of this *fully-engaged* loading region as inelastic behavior of the wood and the loss of single shear stiffness of the connections initiated. The sudden drop in vertical load that occurs shortly after the peak load is attained represents the first failure of the shore. Typically, the first failure came in the form of fracturing of one of the four posts. Intuitively, each subsequent drop in vertical load signifies additional failures in the shore. After the each failure, slight changes in vertical load yielded large changes in vertical displacement. As described in *Chapter 3*, acquiring this unloading portion of the load-displacement curve is only possible through displacement-controlled testing.

As shown in the following sections, the majority of the load-displacement plots from the tests done at FSEL possess similar characteristic regions as those in *Chapter 2*. The information presented in this chapter was used to aid in verification of the finite element model discussed in *Chapter 5.*

4.1 TEST SPECIMEN 1

Table 4-1, shown below, contains details pertaining to the test conducted as well as the condition of the specimen shortly before testing commenced.

Table 4-1 Details for Specimen 1

Specimen 1	
Shore Type	PLP, 4ft Clear Space
Load Scenario	[A] Vertical Only
Test Type	Displacement Control
Loading Rate	0.2 in/min
Lateral Braces Used	NO
Avg Initial Out-of-Plumbness (Top rel. to Bottom)	
L-R (North-South)	3.5 in L
F-B (West-East)	1.6 in R

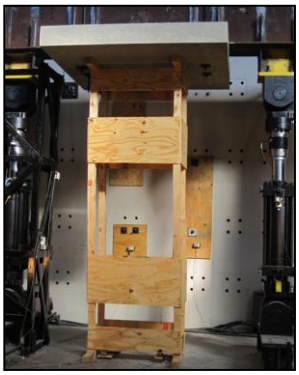

As shown in Table 4-1, this specimen was extremely out-of-plumb in the north-south direction (along the 4-ft dimension of the shore). This out-of-plumbness, likely the result of the shore having sat idle for several weeks, was clearly noticeable prior to testing.

At relatively low vertical load levels (20-30 kips), slight cracking sounds in the wood were observed periodically. As the shore neared its vertical capacity (70 kips and above), these noises increased in frequency and intensity. During loading, audible sounds of the wood creaking and cracking were heard from periods of low loads (20-30 kips) up to failure. Cupping of some of the shore wedges also occurred throughout the test. Figure 4.2 depicts these wedge deformations for PLP Shore 1 at the end of testing.

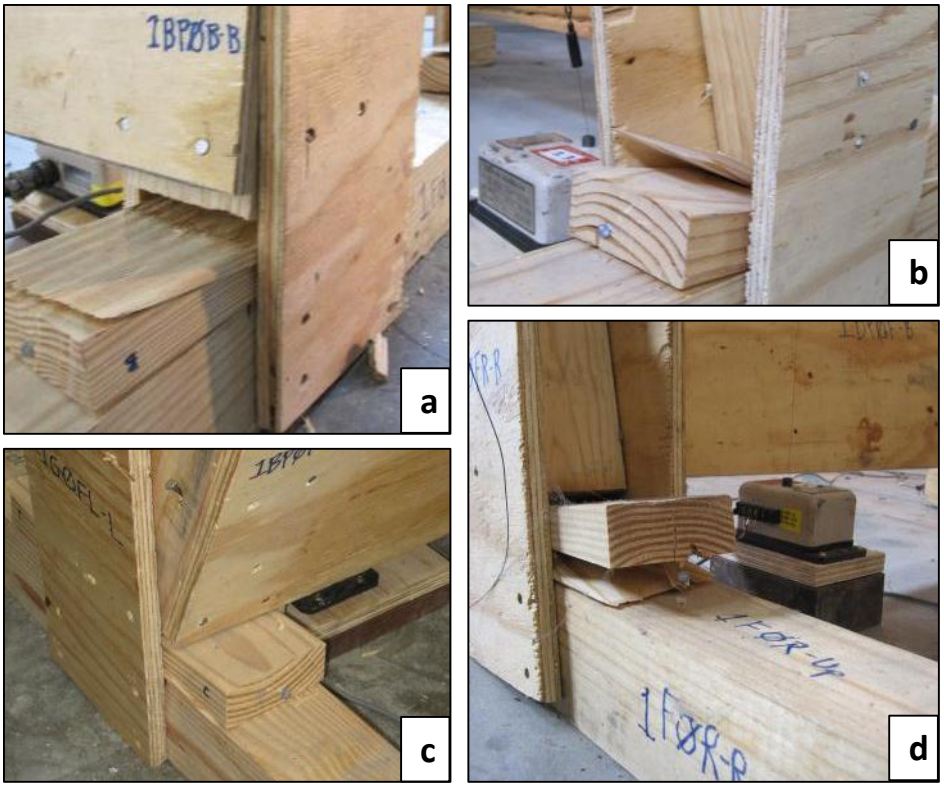

Figure 4.2 Performance of wedges in Test 1 (a) Back-left (b) Back-right (c) Front-left (d) Front-right

The photos in Figure 4.2 show clearly the visible stages of wedge cupping (which began at around 50 kips of vertical load). Interestingly, the two sets of wedges on the right side of the shore exhibited more cupping action than the two sets on the left.

At approximately 82.1 kips, the shore reached its pure vertical load capacity its peak and the load began to decrease. Around this same time, all four posts slowly started to bow outward toward the front. As expected, the area of highest stress appeared to be in the middle un-braced area of the shore. The first failure occurred at a knot in the back right post about halfway between the two intermediate plywood braces. At this same load (65 kips), the front right post cracked around a spike knot just above the lower intermediate brace. This split widened progressively as the load was increased. At approximately 32 kips, the two left posts simultaneously failed at knots. The load-

displacement curve shown in Figure 4.3 illustrates these progressive stages of the test. Photographs provided in Figure 4.4 show some of the failures described.

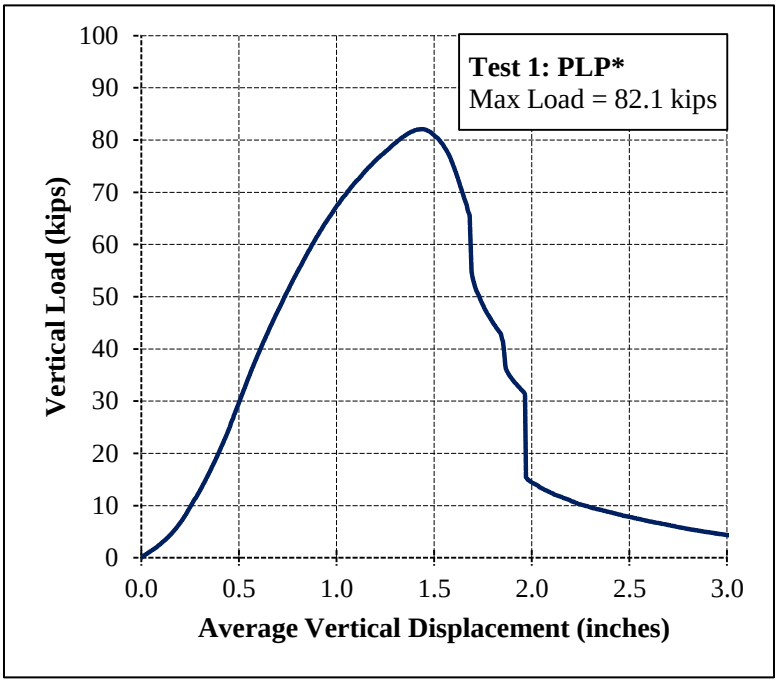

Figure 4.3 Load-Displacement plot for Test 1

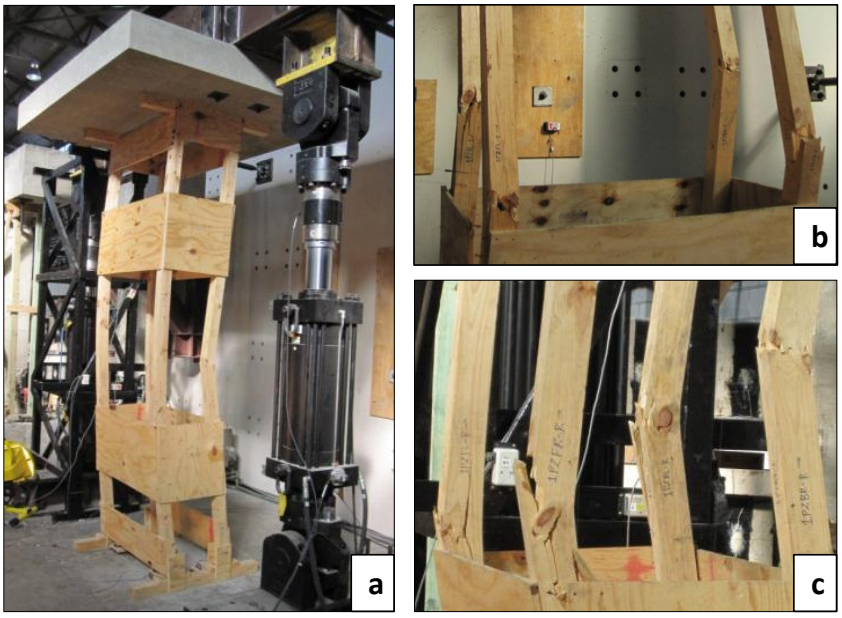

Figure 4.4 Post failures (a) Front-right and back-right (b) All posts (c) All posts

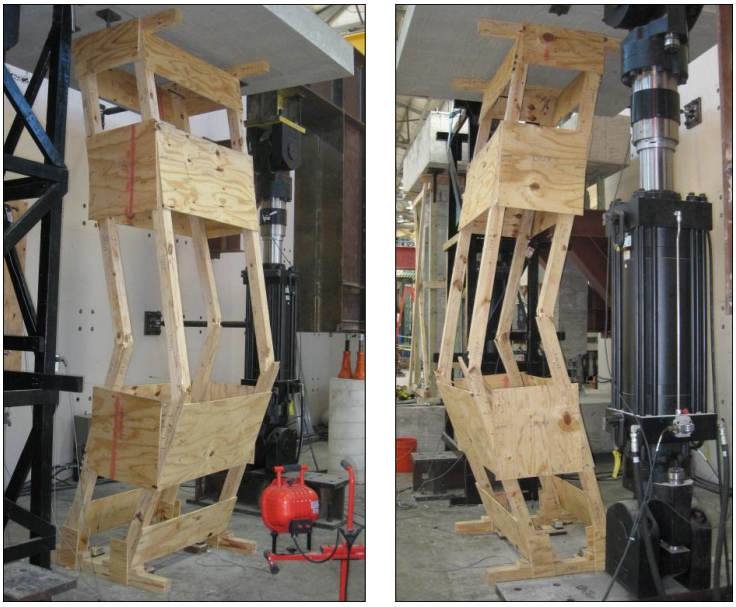

Figure 4.5 Isometric views of final failed condition at end of Test 1

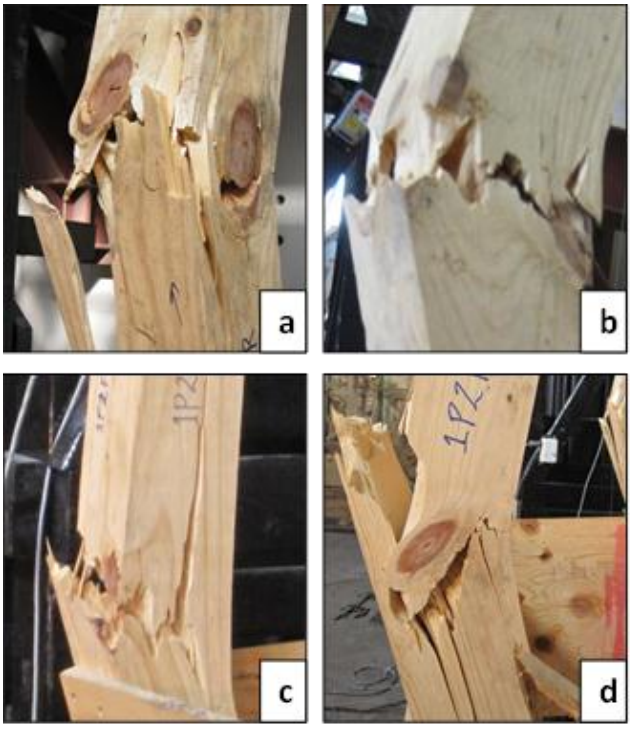

Figure 4.6 Post failures (a) Back-left (b) Back-right (c) Front-left (d) Front-right

No local material failures occurred in any of the plywood members. Instead, nearly all of the plywood members experienced nail withdrawal of some or all nails. Nail

withdrawal became visibly evident as the vertical load neared its peak (70 kips and beyond). This behavior most likely contributed to the decrease in stiffness observed in the load-displacement plot of Figure 4.3. In some cases, the nails pulled cleanly out of the posts but remained attached to the plywood braces, and in others the nails pulled completely through the plywood members while staying attached to the posts. The bent shapes of the nails that exhibited withdrawal were directly related to the direction in which the posts bowed or the plywood brace restrained movement. Some of the nails in the half-gusset plates at the bottom of the shore also pulled through as the posts failed and rotated about the wedges below them. Figure 4.7 illustrates the various types of connection failures in Shore 1.

Figure 4.7 Joint failures (a) Pull-through (b) Withdrawal (c) Post splintering (d) Half-gusset rotation and withdrawal

4.2 TEST SPECIMEN 2

Table 4-2, shown below, contains details pertaining to the test conducted as well as the condition of the specimen shortly before testing commenced.

Table 4-2 Details for Specimen 2

Specimen 2	
Shore Type	PLP, 5ft Clear Space
Load Scenario	[A] Vertical Only
Test Type	Displacement Control
Loading Rate	0.2 in/min
Lateral Braces Used	NO
Avg Initial Out-of-Plumbness (Top rel. to Bottom)	
L-R (North-South)	1.5 in L
F-B (West-East)	1.8 in F

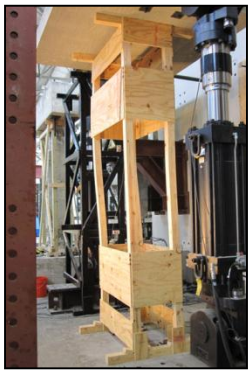

Specimen 2 had similar measurements for the out-of-plumbness in both the east-west and north-south directions. Unlike the previous test, this initial imperfection was not easily noticeable by the naked eye.

Beginning at an axial load of approximately 20 kips, audible creaking and cracking of wood could be heard. As before, these noises increased in magnitude and frequency as the shore reached its vertical capacity. Initial cupping of the wedges started at around 65 kips and continued gradually as the test progressed. In this particular test, each set of four wedges showed uniform and consistent behavior. Figure 4.8 illustrates the performance of the wedges.

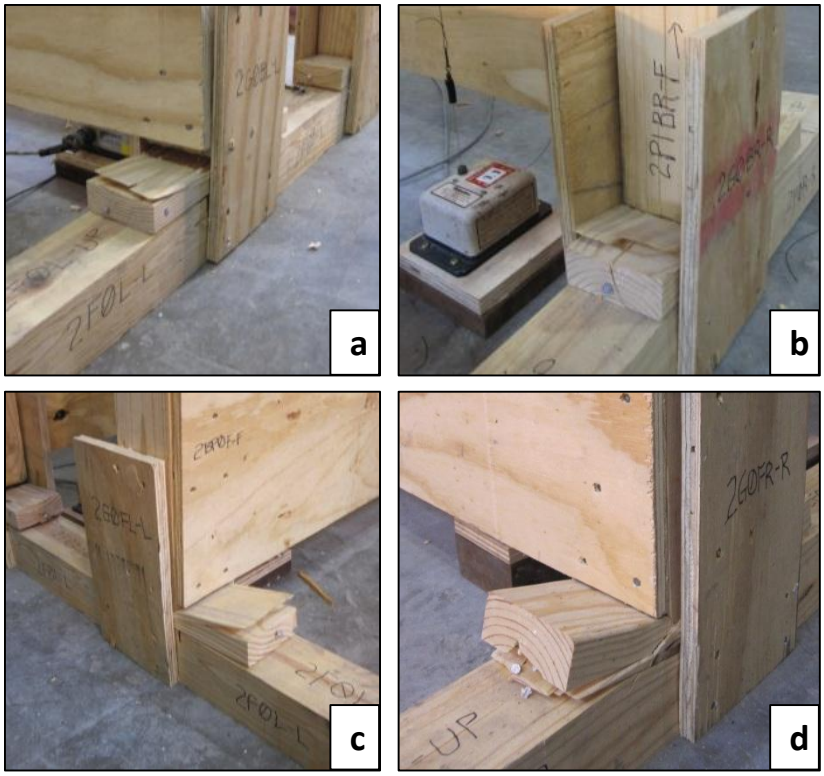

Figure 4.8 Test 2 wedge performance (a) Back-left (b) Back-right (c) Front-left (d) Front-right

At 85 kips, the two posts on the left side of the shore took on an 'S' shape, indicating the presence of double curvature in these members. The vertical capacity was reached at 93.4 kips, after which the load decreased and the first failure occurred. In one instantaneous motion, the back right post experienced a complete failure at two points in its cross section, launching a three foot section forward. Shortly afterward, the back-right post snapped near its center and its intermediate joints, followed by buckling of the front-left post at approximately 34 kips. Surprisingly, the only post that did not buckle (the front-left post) had the highest moisture content reading just before testing. These stages of testing are shown in the load-displacement curve of Figure 4.9.

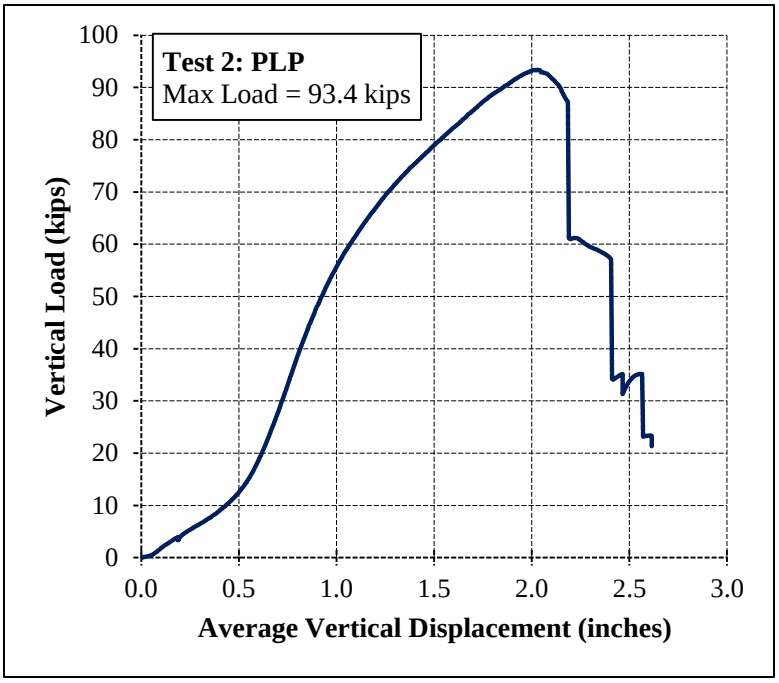

Figure 4.9 Load-displacement plot for Test 2

The following figures (4.10 and 4.11) contain photographs of Test 2 that capture the steps in which the post failures occurred. In light of the unpredictable nature of wood systems, it is interesting to point out that all three failures were unique and did not exhibit the same unidirectional buckling failures as seen in Test 1.

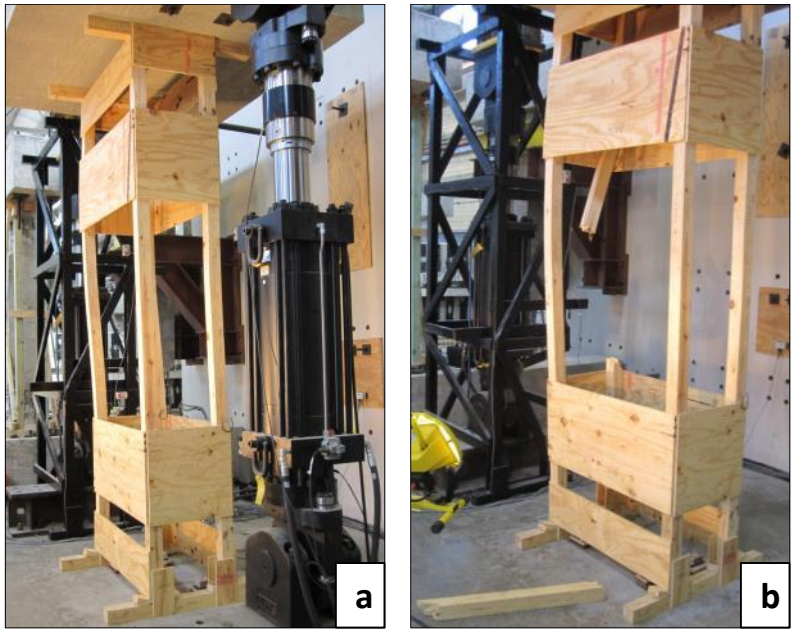

Figure 4.10 Specimen 2 (a) Bending of left posts (b) First failure

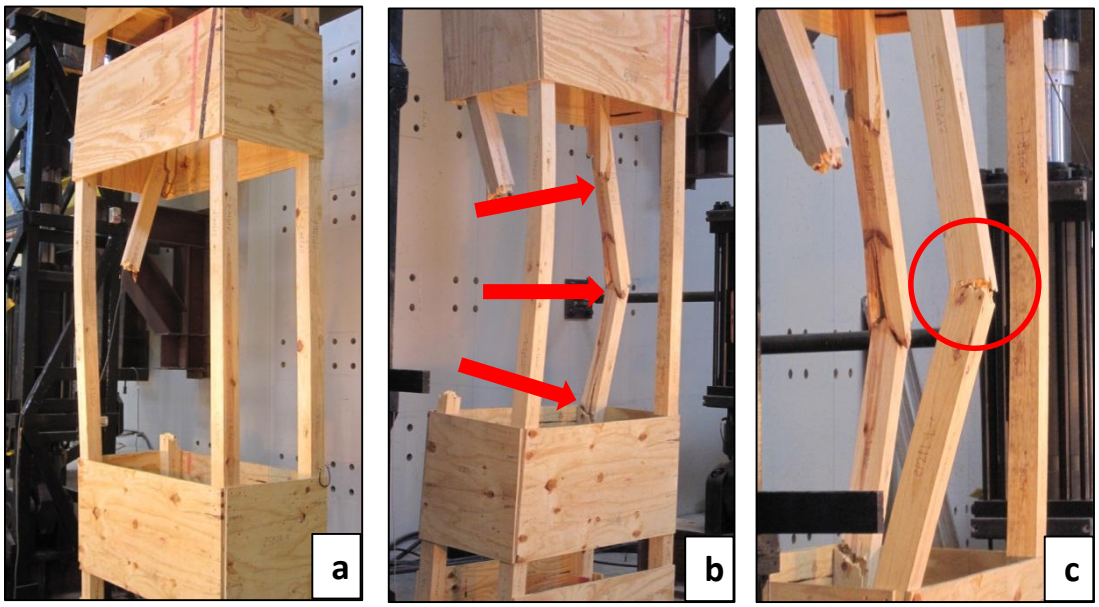

Figure 4.11 Specimen 2 (a) First failure (b) Second failure (c) Third failure

As expected again, all the failures in the posts occurred within the large unbraced length of the shore. However, in contrast to Specimen 1, the failure mechanisms of Specimen 2 did not involve full nail withdrawal of any joints. Apparently, the wood fibers in the posts of Shore 2 were not strong enough to allow significant stresses to be transferred to the plywood braces and cause nail withdrawal. The only evidence of nail withdrawal that occurred in this test came in the form of partial withdrawal of some of the 8d nails in the half-gusset plates and plywood braces (Figure 4.12).

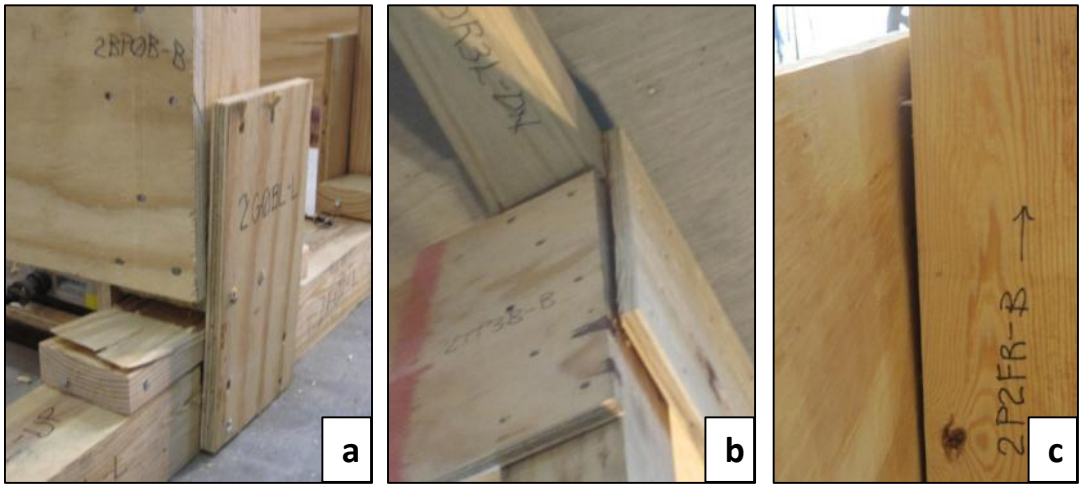

Figure 4.12 Partial nail withdrawal from Test 2 (a) Back-left at sole (b) Back-left at header (c) Front-right at wide brace

4.3 TEST SPECIMEN 3

Table 4-3, shown below, contains details pertaining to the test conducted as well as the condition of the specimen shortly before testing commenced.

Table 4-3 Details for Specimen 3

Specimen 3	
Shore Type	LP
Load Scenario	[A] Vertical Only
Test Type	Displacement Control
Loading Rate	0.2 in/min
Lateral Braces Used	NO
Avg Initial Out-of-Plumbness (Top rel. to Bottom)	
L-R (North-South)	1.6 in L
F-B (West-East)	0.5 in R

The data in Table 4-3 shows that Specimen 3 was nearly plumb in the north-south direction. Incidentally, this was the dominant direction in which buckling occurred in the first two specimens. However, this specimen possessed a considerable amount out-of-plumbness of the top to the left (north). As mentioned at the beginning of this chapter, the LP shores were constructed with a 4ft x 4ft square footprint as opposed to the 2ft x 4ft rectangular footprint of the PLP shores.

The very early stages of wood cracking began as early in the loading process as 17 kips, and increased in frequency and magnitude at load above 50 kips. Cupping of the back-right set of wedges became noticeable at around 50 kips. At about 75 kips, the front two pair of wedges underwent cupping as well. Cupping of the pair of wedges beneath the back-left post occurred slightly at around 50 kips, and progressed an insignificant amount throughout the test. Figure 4.13 depicts the behavior of the wedges.

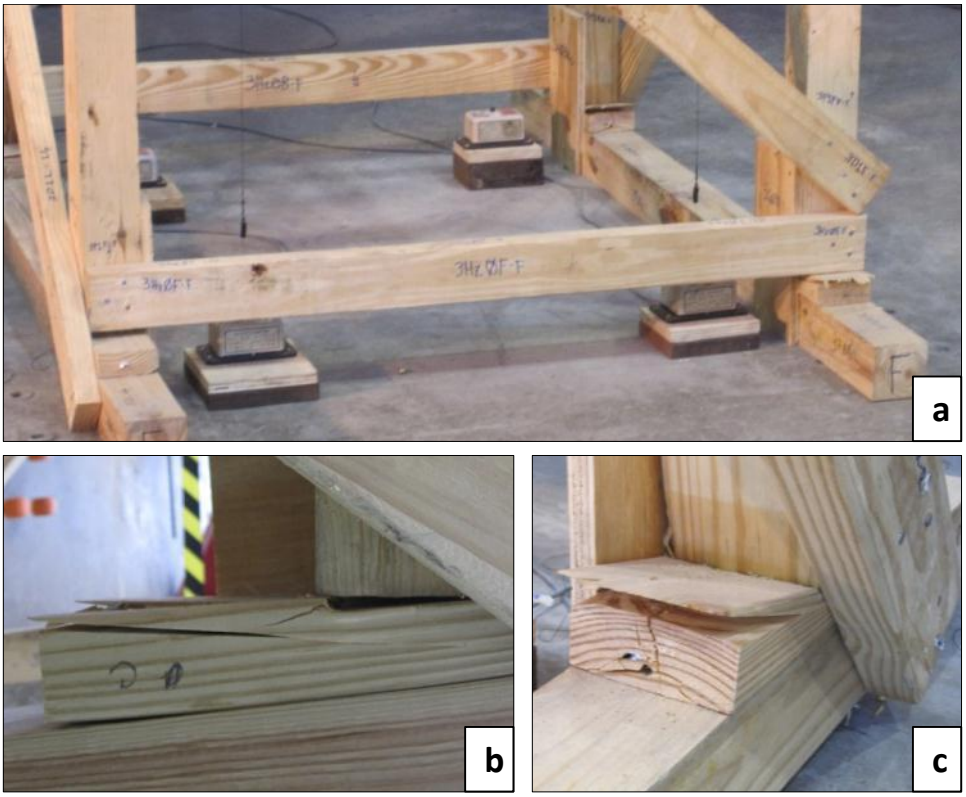

Figure 4.13 Wedge performance in Test 3 (a) Cupping at around 60 kips (b) Back-right wedge at end of test (c) Front-left wedge at end of test

The shore reached its peak load at 85.7 kips, after which the front-right and back-right posts bowed outward significantly to signal their impending failure. As the load decreased to approximately 66 kips, both right posts buckled simultaneously between the first and second shore levels. The front right post failure was marked by splitting of its tension face, followed by propagation of the split longitudinally up the post. Shortly after the level 1 horizontal brace pulled completely out of the back-right post, the back-left post buckled at approximately 46 kips. Lastly, when the test had concluded and only 16 kips remained on the shore, the front-left post failed. Figure 4.14 shows the bowing of the right posts prior to buckling as well as the failures of all four posts. Notice the difference in buckling directions between the back-left post and the other three posts (Figure 4.14d).

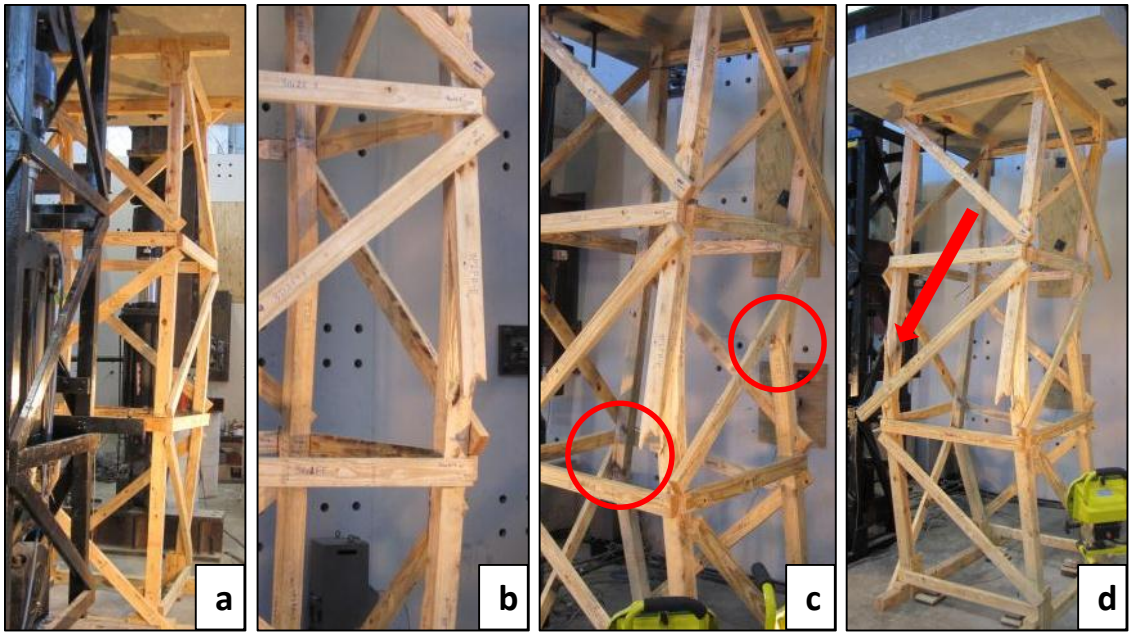

Figure 4.14 Specimen 3 (a) Bowing of front-right post (b) First failure (c) Second failure (d) Third failure

A close-up view of each failed post in Shore 3 can be found in Figure 4.15. Each failure occurred at the location of a knot in the post. The loading stages of Test 3 are documented and displayed by the sudden drops in vertical load after the peak was attained, as shown in the load-displacement plot in Figure 4.16.

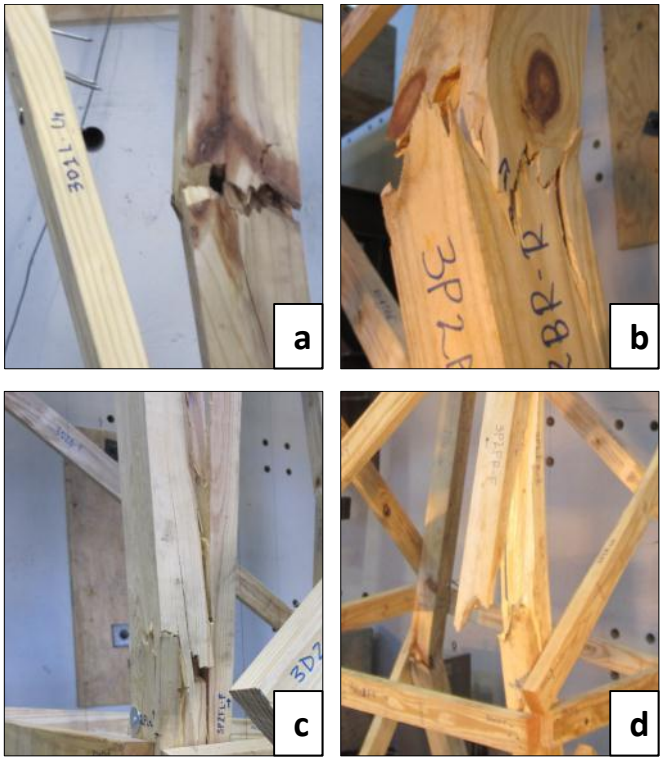

Figure 4.15 Post failures (a) Back-left (b) Back-right (c) Front-left (d) Front-right

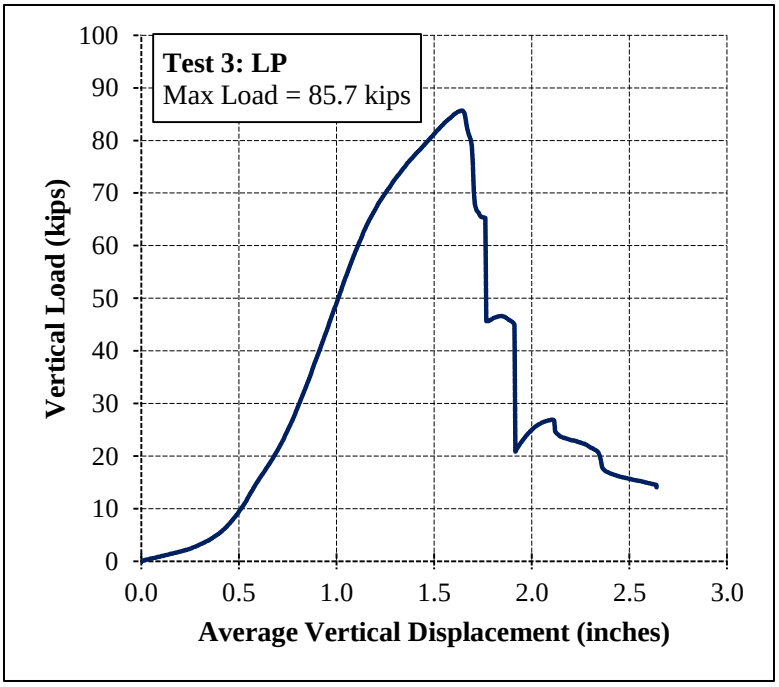

Figure 4.16 Load-displacement plot for Test 3

While no major material failures occurred in the 2x4 braces, several of them experienced nail withdrawal, and thus joint failure. Nail withdrawal failures in this test seemed to result from minor splitting of the brace around a nail, as well as yielding of the steel in the nail itself. The following five joints failed by nail withdrawal: the first level diagonal on left side of shore (3D1-L), the first level diagonal on right side of shore (3D1-R), the first level horizontal on back side of shore (3Hz1-B), the second level diagonal on front side of shore (3D2-F), and the third level diagonal on right side of shore(3D3R). Additionally, partial nail withdrawal was observed at the joint connecting the front-right post to the third level diagonal on the left side of the shore (3D3-L). The following photographs in Figure 4.17 and Figure 4.18 display the locations of the failed braces and also close-up images of typical withdrawal behaviors.

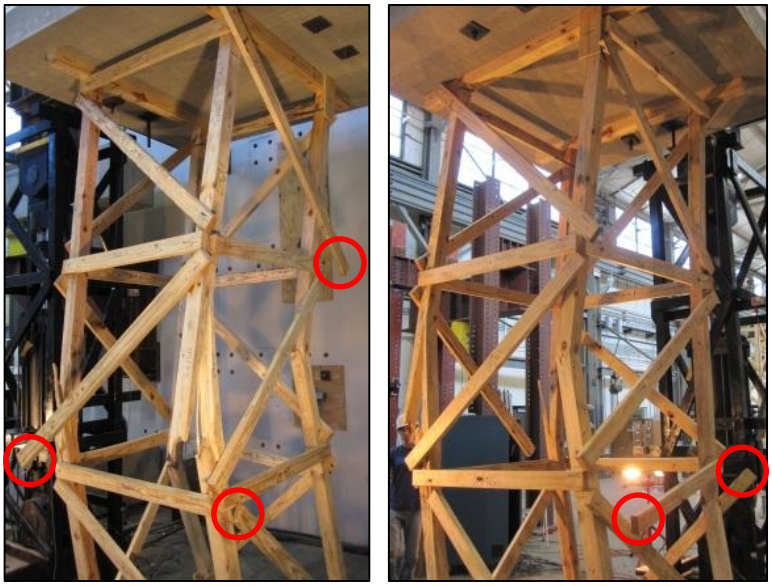

Figure 4.17 Images of the five brace connection failures in Test 3

Figure 4.18 Close-up views of connection failures (a) Partial nail withdrawal (b) Nail-withdrawal from split brace (c) Full nail-withdrawal

4.4 TEST SPECIMEN 4

Table 4-4, shown below, contains details pertaining to the test conducted as well as the condition of the specimen shortly before testing commenced.

Table 4-4 Details for Specimen 4

Specimen 4	
Shore Type	LP
Load Scenario	[A*] Vertical Only
Test Type	Load Control
Loading Rate	10 kips/min Total
Lateral Braces Used	NO
Avg Initial Out-of-Plumbness (Top rel. to Bottom)	
L-R (North-South)	1.3 in L
F-B (West-East)	0.1 in B

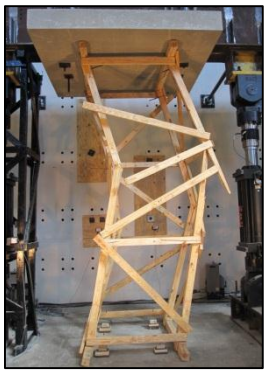

This shore was nearly perfectly plumb in the front-to-back direction and averaged over an inch out-of-plumb in the left-to-right direction. As shown in Table 4-4, vertical load was applied in load-controlled manner at a rate of 5 kips per minute per actuator, producing a total loading rate of 10 kips per minute. In essence, the load applied to the shore was not reduced or removed until complete failure of the structure was realized.

Hardly any audible wood cracks were observed prior to the load reaching roughly 70 kips. These cracking and creaking sounds became louder and more frequent from 85 kips until failure. The wedges cupped only a very small amount throughout the test. In fact, as shown in Figure 4.19, only the back-left set of wedges visibly cupped.

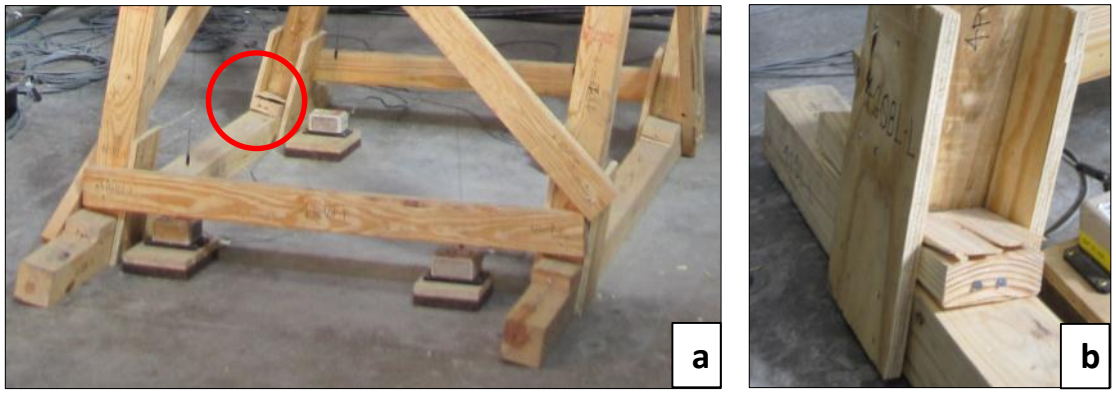

Figure 4.19 Wedge performance in Test 4 (a) Cupping of back-left wedges (b) Close-up

As the shore approached its pure vertical capacity, the two back posts buckled to the right, almost immediately followed by buckling of the front two posts in the same direction. To prevent rapid descent of the slab after shore failure, the emergency stop

button was pushed to halt all testing activity. In stark contrast to the progressive failures of the previous three tests, the failure of all four posts occurred in approximately one second. Undoubtedly, this test was the most destructive. The following figures (Figure 4.20-Figure 4.22) present the load-displacement plot as well as photographs of Test 4.

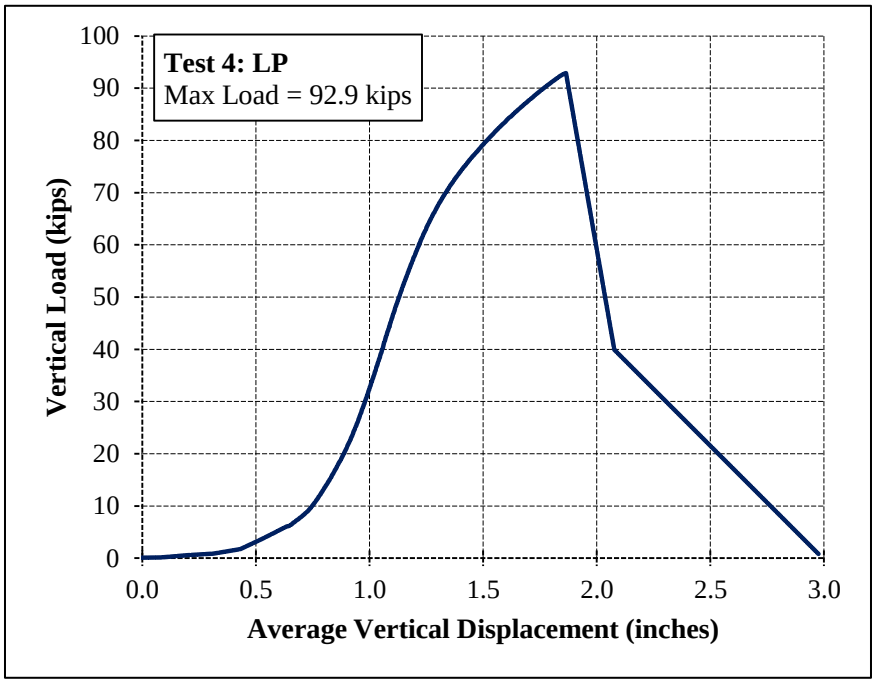

Figure 4.20 Load-displacement plot for Test 4

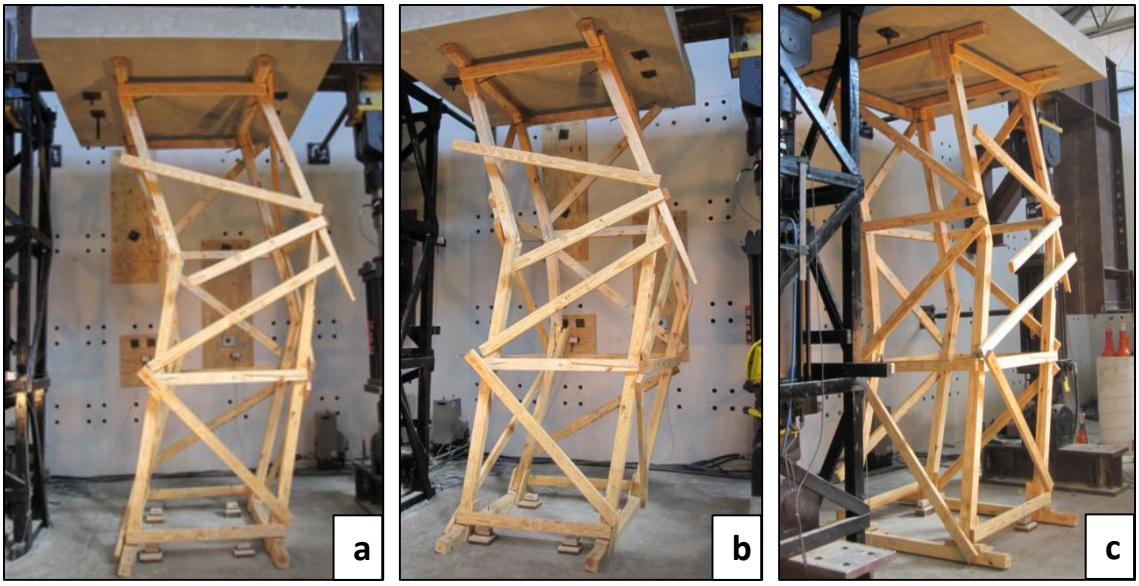

Figure 4.21 Final condition of Specimen 4 (a) Front (b) Isometric from right (c) Isometric from left

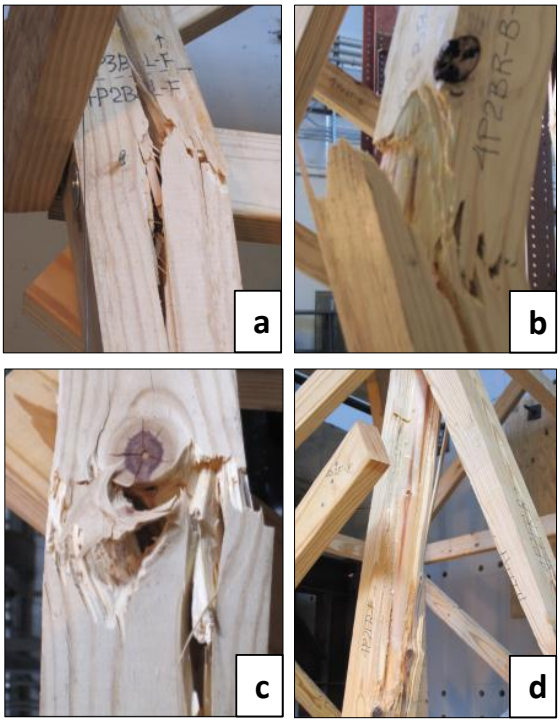

Figure 4.22 Test 4 post failures (a) Back-left (b) Back-right (c) Front-left (d) Front-right

With the buckling action to the right, the majority of the braces on the front and back sides of the shore experienced nail withdrawal at their connections to the posts. It was observed that all nail withdrawal failures consisted of direct nail withdrawal from the posts, and did not include nail pull through by means of a split in the 2x4 brace as seen in Test 3. Nail withdrawal occurred on the following braces: all diagonal braces on the front side of the shore, the second level horizontal brace on the front side (4Hz2F), the first level diagonal on the back side (4D1B) and third level diagonal on the back side (4D3B). Many other horizontal and diagonal braces exhibited partial nail withdrawal. Figure 4.23 shows the locations of all six joints that displayed complete connection failures, and Figure 4.24 presents up-close images of these failures.

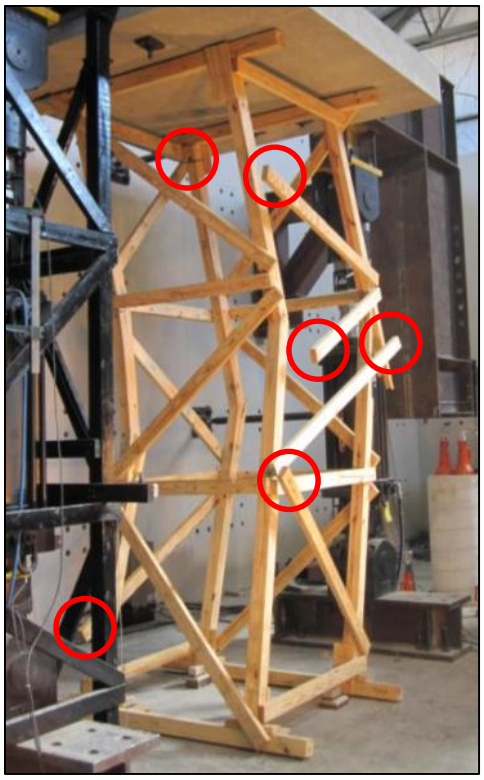

Figure 4.23 Joint failure locations for Specimen 4

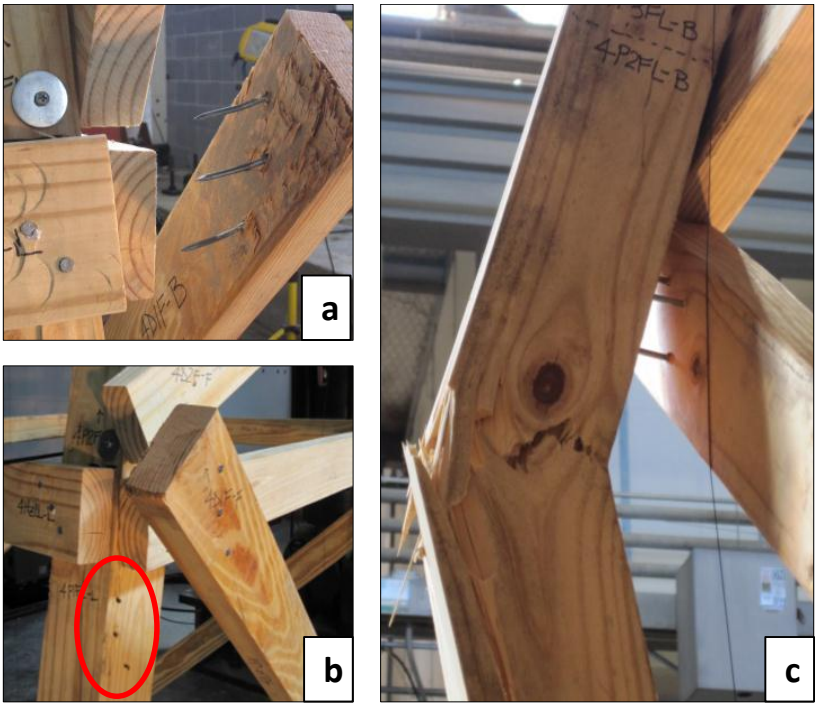

Figure 4.24 Test 4 joint failures (a) Nail-withdrawal (b) Nail-withdrawal holes (c) Partial nail-withdrawal on left side of shore

4.5 TEST SPECIMEN 6

Table 4-5, shown below, contains details pertaining to the test conducted as well as the condition of the specimen shortly before testing commenced.

Table 4-5 Details for Specimen 6

Specimen 6	
Shore Type	LP
Load Scenario	[C] Const Lat Disp, Incr Vert Load
Test Type	Displacement Control
Loading Rate	0.2 in/min
Lateral Braces Used	YES
Avg Initial Out-of-Plumbness (Top rel. to Bottom)	
L-R (North-South)	1.0 in L
F-B (West-East)	0.6 in F

Since this specimen possessed an initial out-of-plumbness of 1 inch to the left, an additional 5 inches of lateral displacement was imposed at the top of the shore to reach a

total value of 6 inches prior to the application of vertical loading. Hardly any cracking in the wood was noticed during loading until approximately 55 kips. This shore achieved its maximum vertical capacity at a load 64.6 kips. As the load reduced, a series of splitting wood sounds announced the failure of wood fibers.

Wedge cupping was virtually nonexistent throughout the test. Splitting of the wedges was also not observed, as was common in other tests. The images in Figure 4.25 show the condition of the wedges at the conclusion of the test.

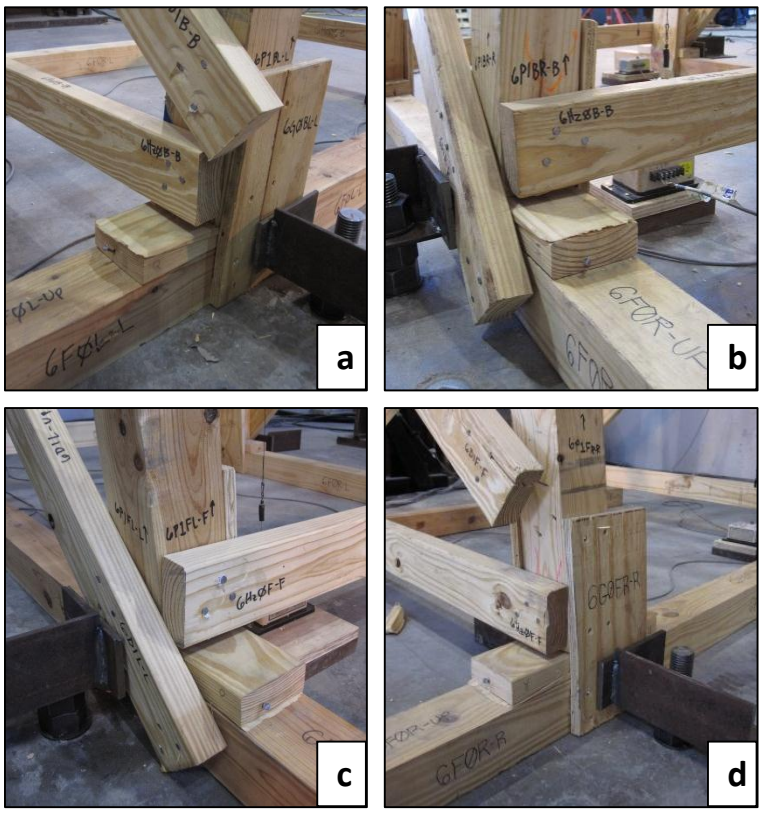

Figure 4.25 Wedge performance in Test 6 (a) Back-left (b) Back-right (c) Front-left (d) Front-right

The first failure consisted of a joint failure of the first level diagonal on the back side of the shore at the back-right post. The nails in the joint gradually withdrew from the post as the shore reached its vertical capacity, freeing the back-right post to undergo considerable bending. The load-displacement plot for this test, shown in Figure 4.26, signifies this joint failure and post buckling by revealing an immediate loss of capacity

after the peak load was reached, followed by stiffening of the shore system as redistribution of the load occurred. As the load reduced, the back-right post finally failed at a vertical load of 41 kips, followed by simultaneous failure of both front posts at 30 kips. Figure 4.27 contains photographs of the various phases of testing.

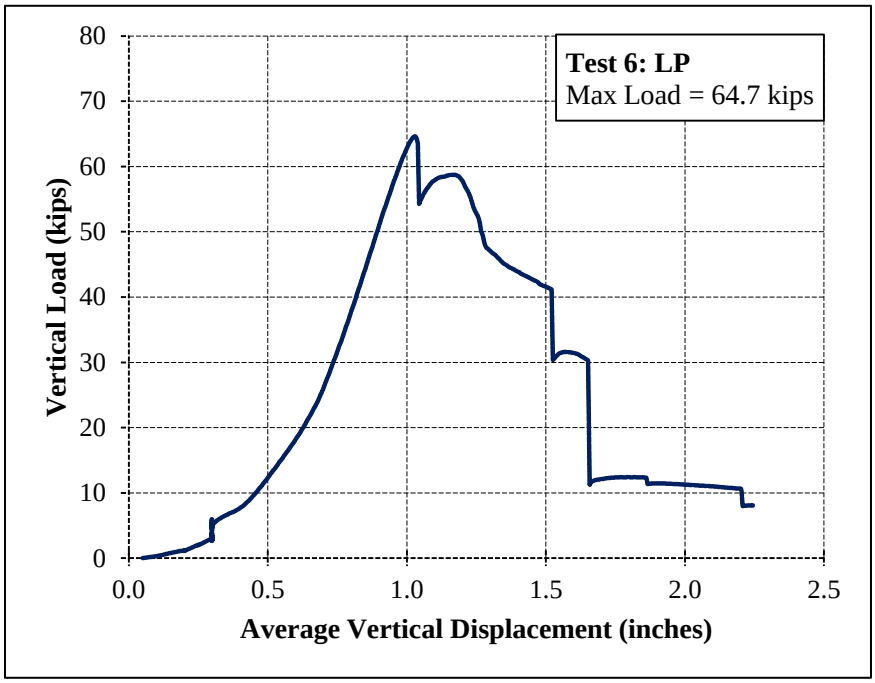

Figure 4.26 Vertical load-displacement plot for Test 6

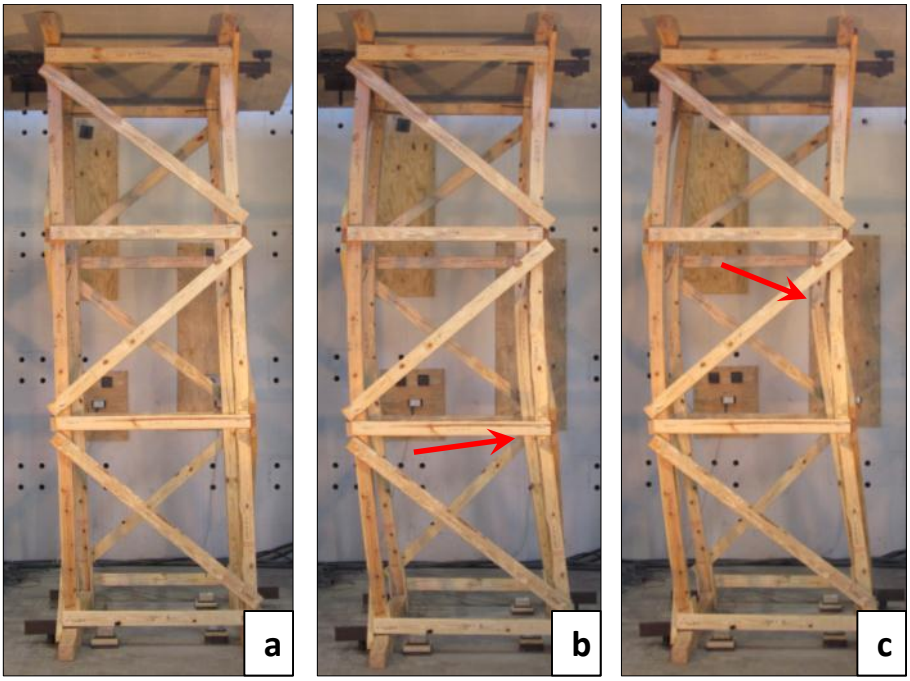

Figure 4.27 Test 6 loading stages (a) Initial 6 inch displacement prior to loading (b) First joint failure (c) Back-right post failure

The failure sequence of each post was captured by the photographs in Figure 4.28. Close up views of these failures can be found in Figure 4.29.

Upon post-test evaluation of the shore, it was discovered that the back-left post experienced a rather long split longitudinally up the post. Figure 4.29a presents a photograph of this split.

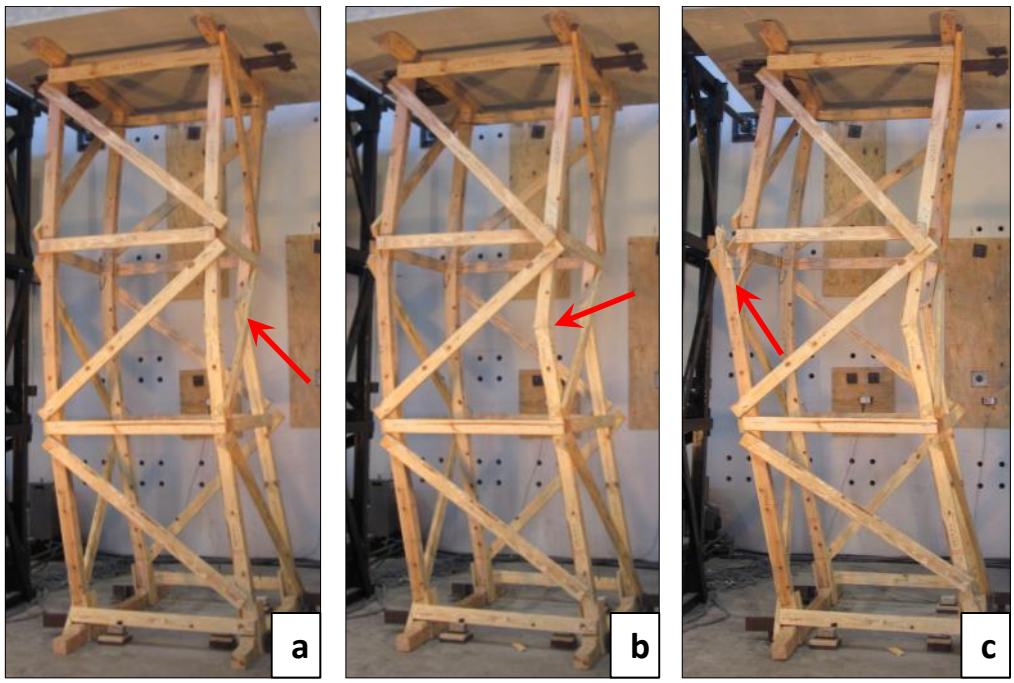

Figure 4.28 Test 6 failure sequence (a) First failure (b) Second failure (c) Third failure

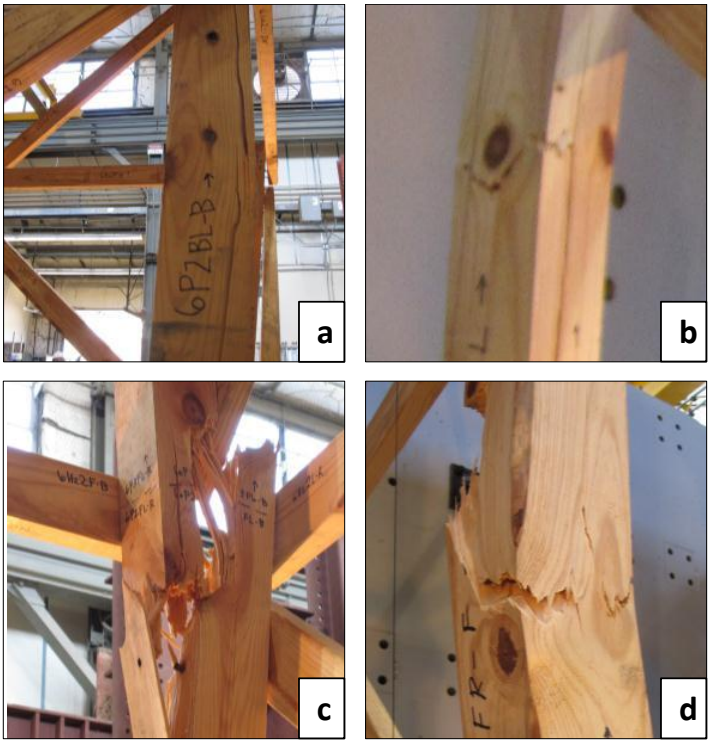

Figure 4.29 Detailed post failures (a) Back-left (b) Back-right (c) Front-left (d) Front-right

A total of three 2x4 braces failed via nail withdrawal from the post (Figure 4.30). Numerous other braces exhibited partial nail withdrawal, most commonly near the post failure locations.

Figure 4.30 Test 6 joint failures involving nail withdrawal

4.6 TEST SPECIMEN 7

Table 4-6, shown below, contains details pertaining to the test conducted as well as the condition of the specimen shortly before testing commenced.

Table 4-6 Details for Specimen 7

Specimen 7	
Shore Type	LP, 5ft Clear Space
Load Scenario	[C] Const Lat Disp, Incr Vert Load
Test Type	Displacement Control
Loading Rate	0.2 in/min
Lateral Braces Used	YES
Avg Initial Out-of-Plumbness (Top rel. to Bottom)	
L-R (North-South)	1.8 in L
F-B (West-East)	FL: 2.25 in B FR: 0.5 in F (Twist)

This specimen had an initial out-of-plumbness of 1.75 inches to the left, and therefore additional 4.25 inches of lateral displacement was applied at the top of the shore to reach a total value of 6 inches prior to the application of vertical loading. This

specimen presented an interesting new challenge: an initial twist in the front-to-back plane. The top of the front-right post leaned 0.5 inches toward the front while the top of the front-left post leaned 2.25 inches toward the back. During initial vertical loading, audible cracking sounds were relatively minor, becoming noticeable at around 45 kips. The sounds increased in noise level and frequency once the vertical load reached roughly 60 kips.

During testing, wedge cupping occurred beneath all four posts. Wedge cupping began at approximately 80 kips, about 72 percent of the observed capacity. Significant crushing of the wedges due to bearing of the posts was also observed in the post-test evaluation, as depicted in Figure 4.31.

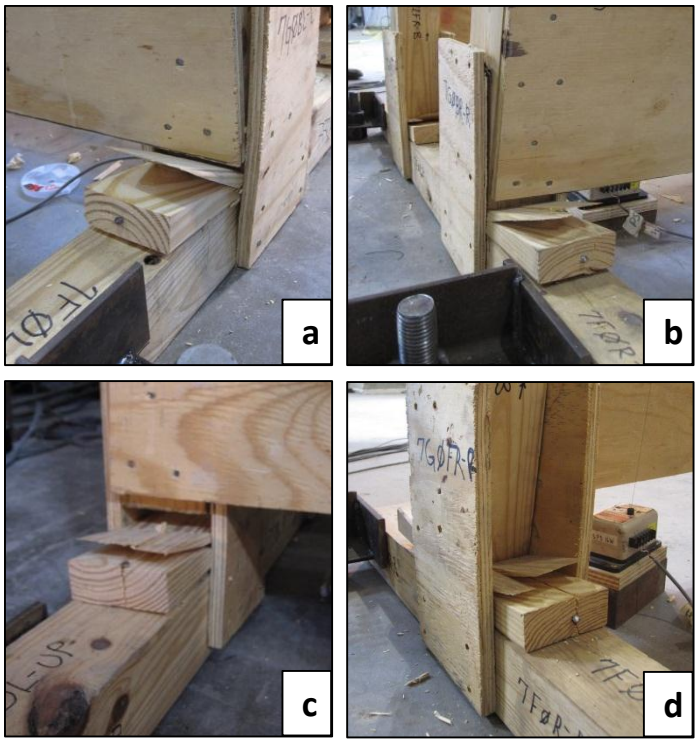

Figure 4.31 Wedge performance for Test 7 (a) Back-left (b) Back-right (c) Front-left (d) Front-right

The shore reached its vertical capacity at 111 kips, after which the load started to reduce gradually. Suddenly, at approximately 88 kips, a 2 foot section of the front-left post fractured and was ejected from the shore. At the same time, the front-right post also

failed by splitting along its back side. The next failure occurred in back-right post just above the second level plywood brace at approximately 36 kips. The final failure consisted of the back-left post at 17 kips by longitudinal splitting along its back side (tension face). Figure 4.32 presents the load-displacement plot for the entire duration of the test.

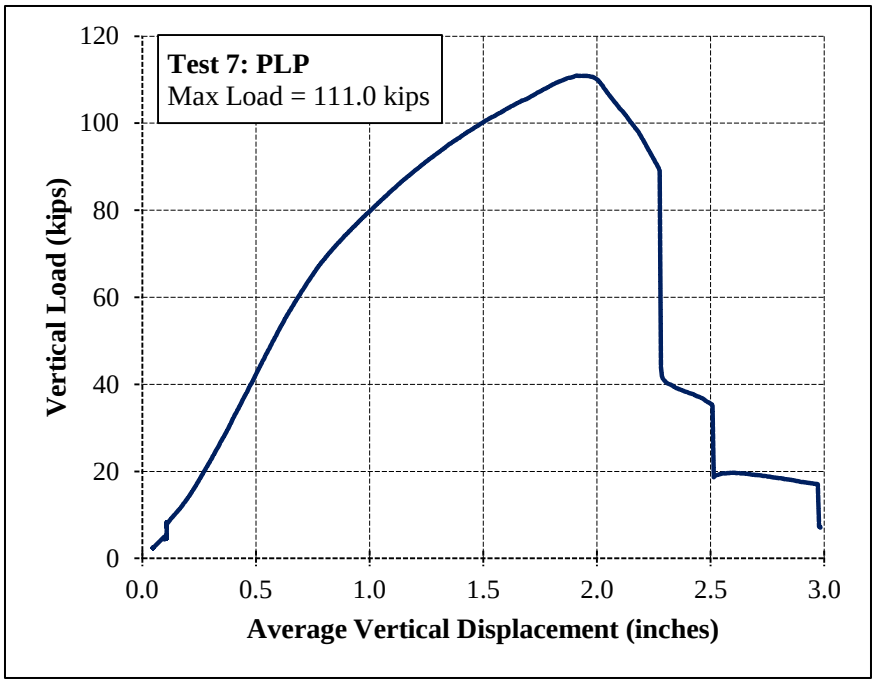

Figure 4.32 Vertical load-displacement plot for Test 7

The following photographs, shown in Figure 4.33 and Figure 4.34, capture the sequence of failure events of the specimen as well as close-up views of each post failure.

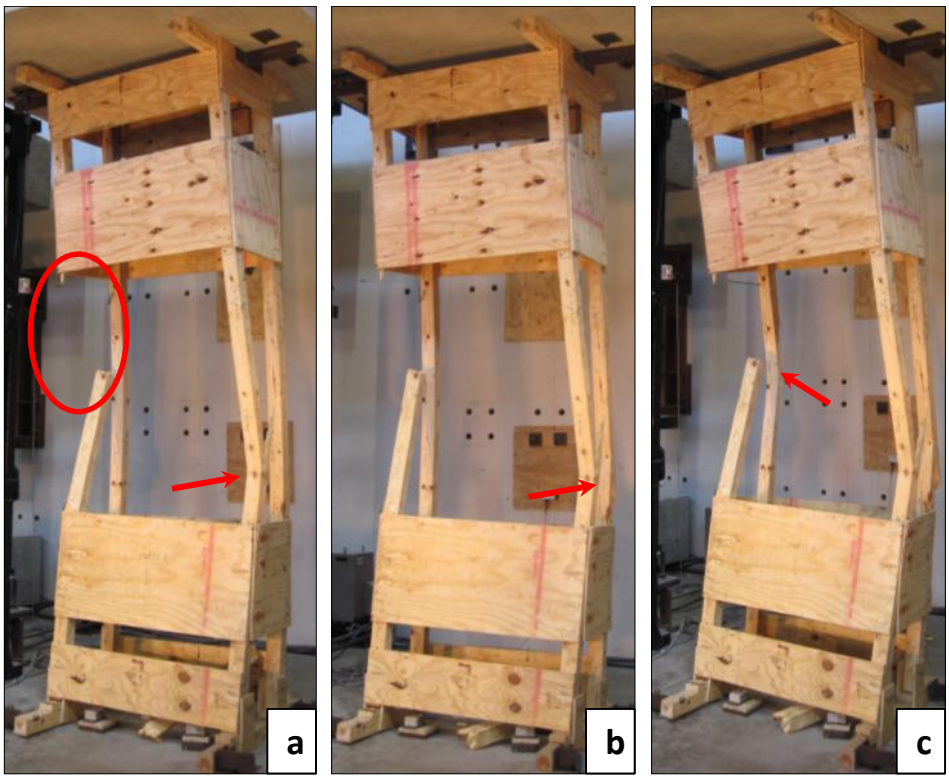

Figure 4.33 Test 7 failure sequence (a) First failure (b) Second failure (c) Third failure

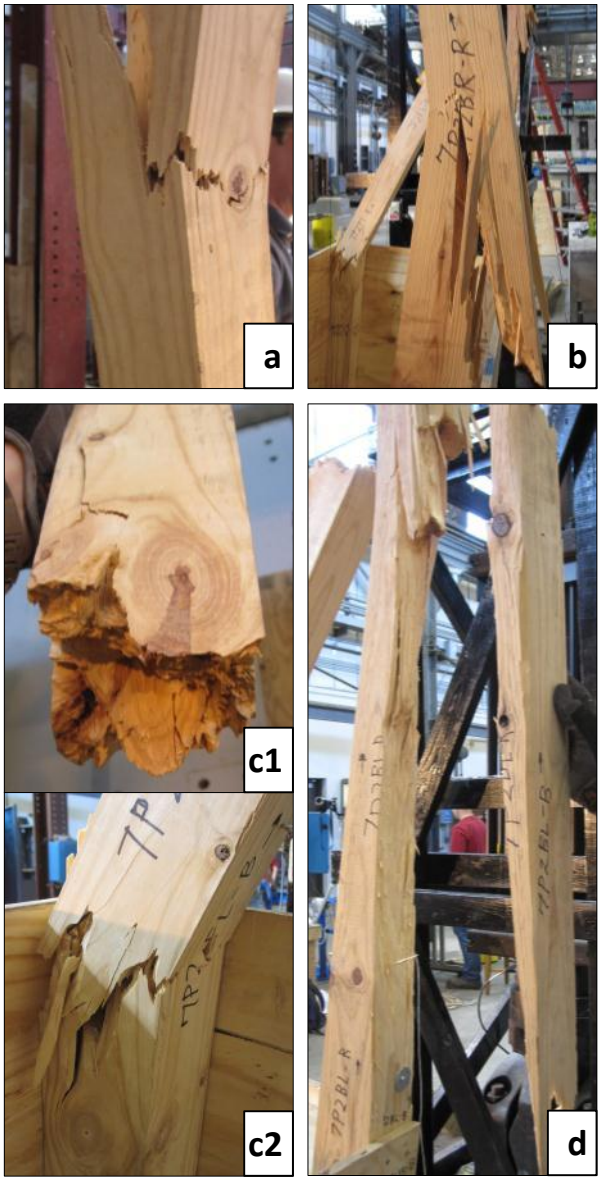

Figure 4.34 Detailed failure photographs (a) Front-right post (b) Back-right post (c1) Top failure of front-left post (c2) Bottom failure of front-left post (d) Back-left post

No significant brace failures occurred during the testing of Specimen 7. In fact, only the regions immediately adjacent to the post failures exhibited any nail withdrawal or tear-out. Figure 4.35 highlights these areas of failure.

Figure 4.35 Notable regions of joint failure for Test 7

As illustrated above, the section of the front-left post that broke off from the shore indicates nail withdrawal did indeed occur during failure. The photographs also provide evidence to conclude nail withdrawal was present on the front-right post just below its failure point. Joint detachment due to nail withdrawal was much more common on the right side of the shore than anywhere else.

4.7 TEST SPECIMEN 8

Table 4-7 contains details pertaining to the test conducted as well as the condition of the specimen shortly before testing commenced.

Table 4-7 Details for Specimen 8

Specimen 8	
Shore Type	LP
Load Scenario	[D] Const Vert Load, Incr Lat Disp
Test Type	Displacement Control
Loading Rate	0.6 in/min
Lateral Braces Used	YES
Avg Initial Out-of-Plumbness (Top rel. to Bottom)	
L-R (North-South)	0.3 in R
F-B (West-East)	0.3 in F

Specimen 8 was loaded vertically to the specified shore design capacity (32 kips), and then laterally displaced to the right while ensuring the 32 kip load stayed unchanged. The tower was relatively plumb in both directions.

Considering the noises prevalent throughout the previous tests, Specimen 8 behaved rather quietly during the test. Only minor to moderate cracking sounds were heard on occasion. The first noticeable cracking sounds in the wood were observed when the shore had been subjected to approximately 13.5 inches of lateral displacement.

No cupping of any of the four pairs of wedges occurred during the lateral displacement phase or vertical loading phase. Figure 4.36 shows the status of the wedges when the shore had reached 15 inches of lateral displacement.

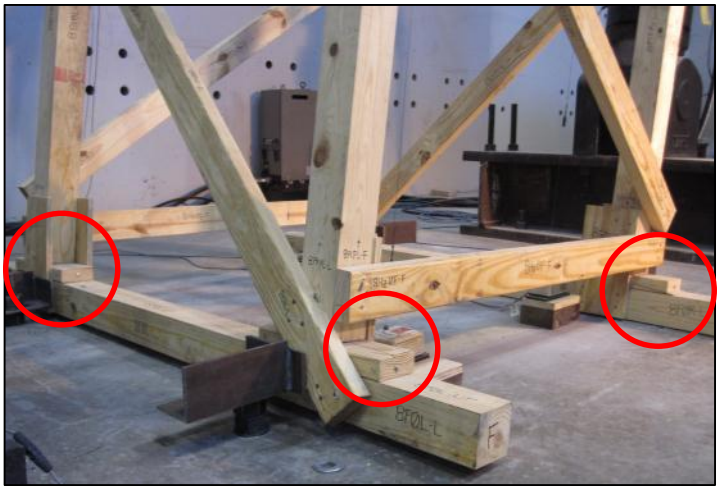

Figure 4.36 Wedge performance for Test 8

While maintaining the constant 32 kip load vertical load, Specimen 8 successfully withstood a total lateral displacement of 15 inches to the right (south). Upon reaching this 15 inch stroke limit of the test frame, the shore was loaded vertically until failure while the lateral displacement remained constant. Shown respectively in Figure 4.37 and Figure 4.38 are the vertical load-displacement curve and lateral load-displacement curve for Test 8. Notice that the vertical load-displacement curve includes both the vertical loading and lateral displacement phases of the test.

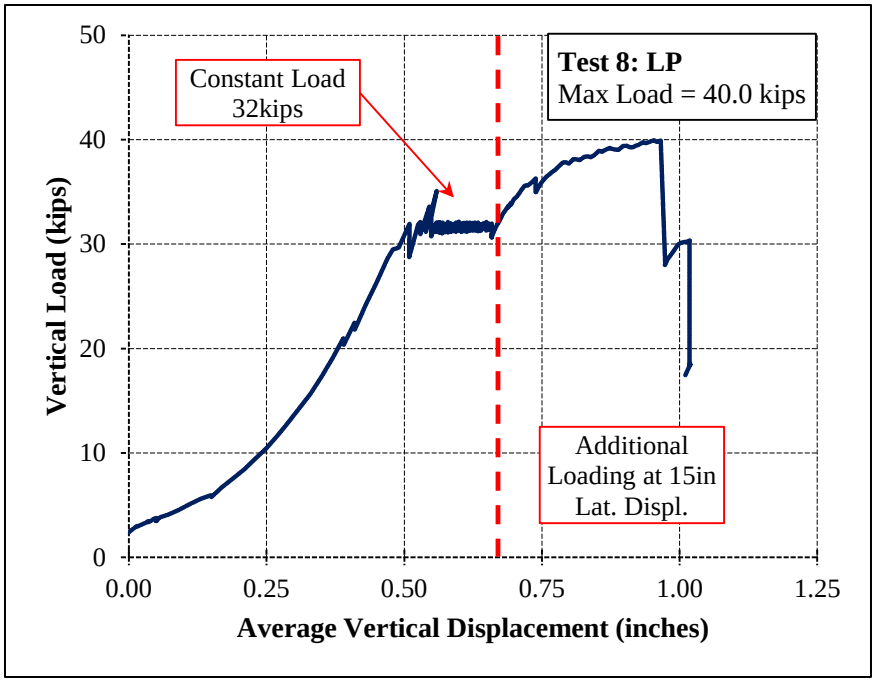

Figure 4.37 Vertical load-displacement plot for Test 8

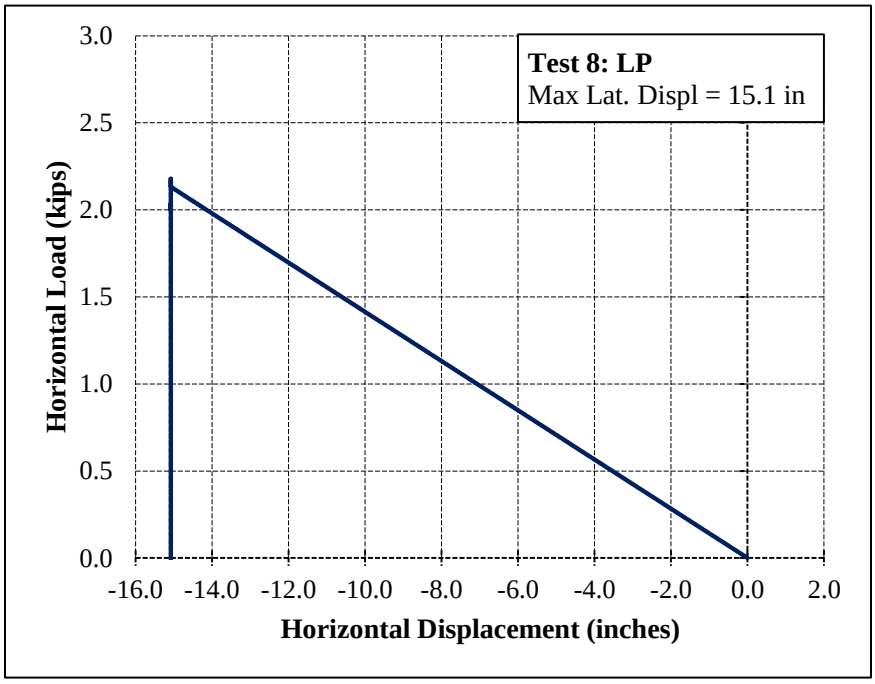

Figure 4.38 Horizontal load-displacement plot for Test 8

A total lateral of force of 2.2 kips was required to displace the top of the shore 15 inches to the right. Afterward, the shore reached its vertical capacity at only 40 kips, revealing the considerable impact wrought on by the lateral shifting of the slab and shore. The back-right post demonstrated the first failure of the shore at 40 kips, followed by the front right-post at roughly 30 kips. Both failures at a knot located along the tension face of the posts. As expected, both of these posts failed in the direction of load eccentricity. Figure 4.39 recounts the progression lateral displacement, and Figure 4.40 presents local failures of the shore.

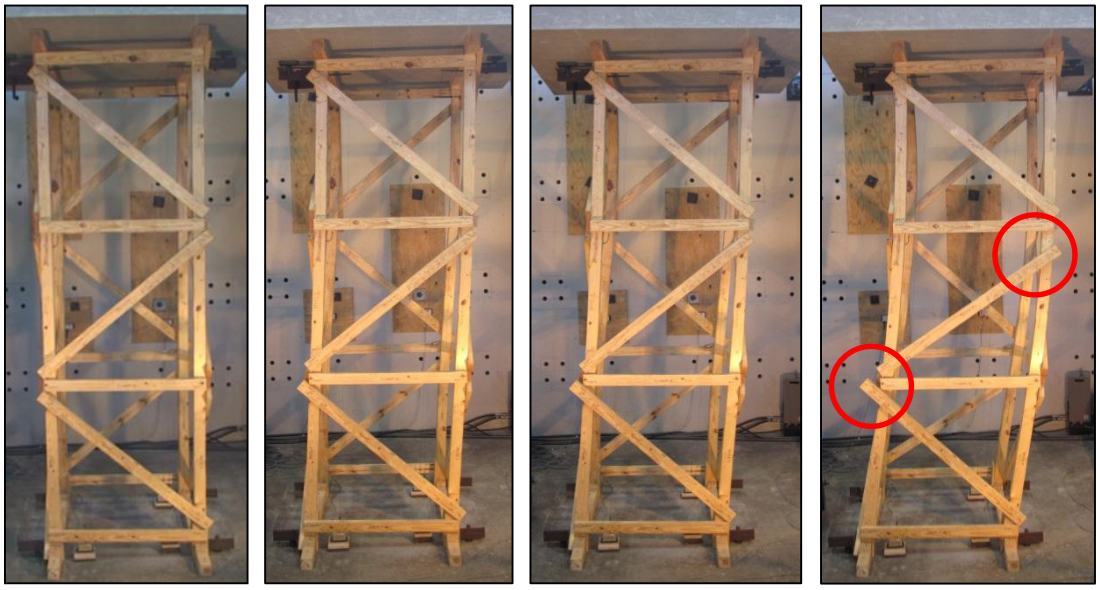

Figure 4.39 Progression of lateral displacement during Test 8

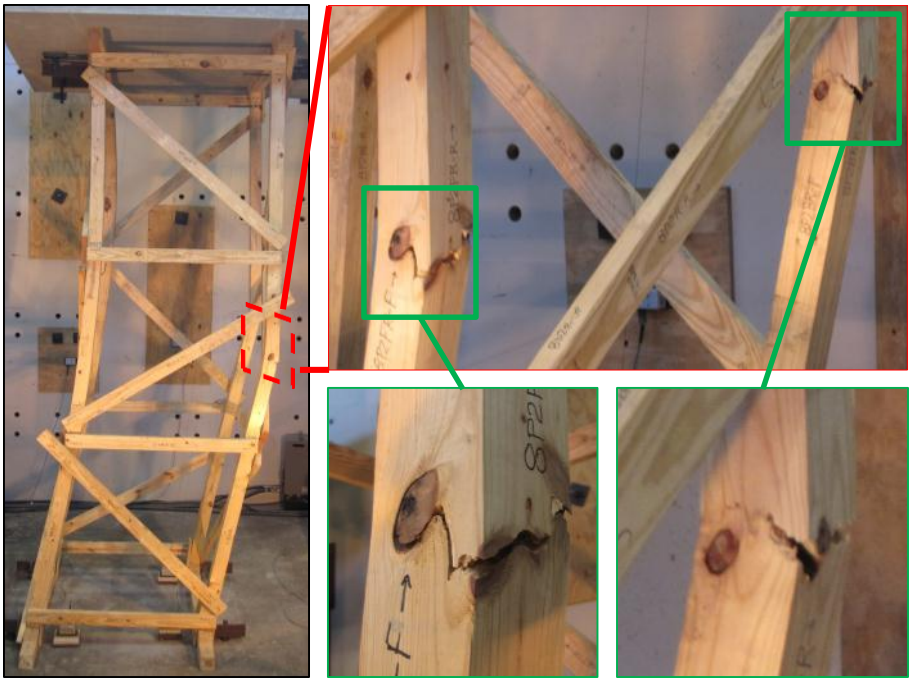

Figure 4.40 Test 8 post failures at knot locations

Throughout the vertical and lateral loading phases of the test, several diagonal braces failed at their connections by means of nail withdrawal. The nails in the first level diagonal braces on both the front and back faces of the structure gradually withdrew as the shore was displaced laterally, completely detaching at a value 10.5 inches of displacement. Somewhere between a lateral displacement of 11 inches and 13 inches, the upper joint nails of the second level diagonal brace began to withdrawal. Included in Figure 4.41 is a diagram of each joint failure location along with some detailed photographs regarding connection failures.

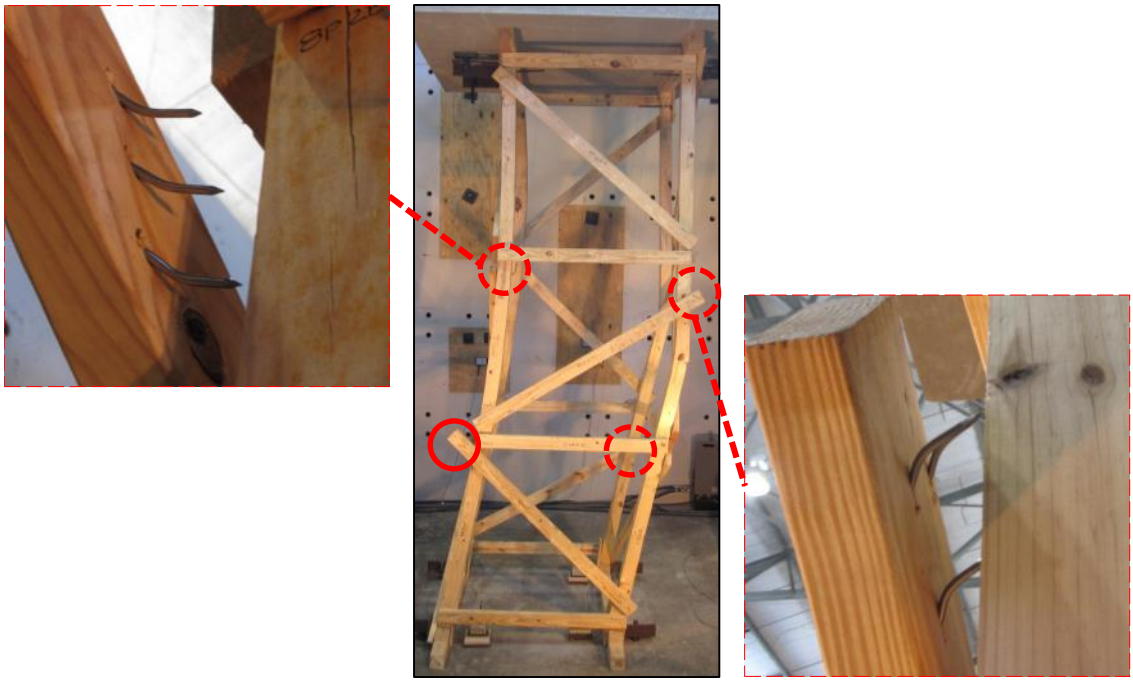

Figure 4.41 Joint failures of horizontal and diagonal braces for Test 8

None of the horizontal braces disconnected from the posts. However, many of their joints experienced significant rotation, hinting at the semi-rigidity offered by nailed joints. Figure 4.42 provides a close up view of a ground level and first level horizontal brace that illustrates rotational resistance of the joint. As seen, the angle between the horizontal braces and the posts they connect to is no longer 90 degrees, but the nails remained intact.

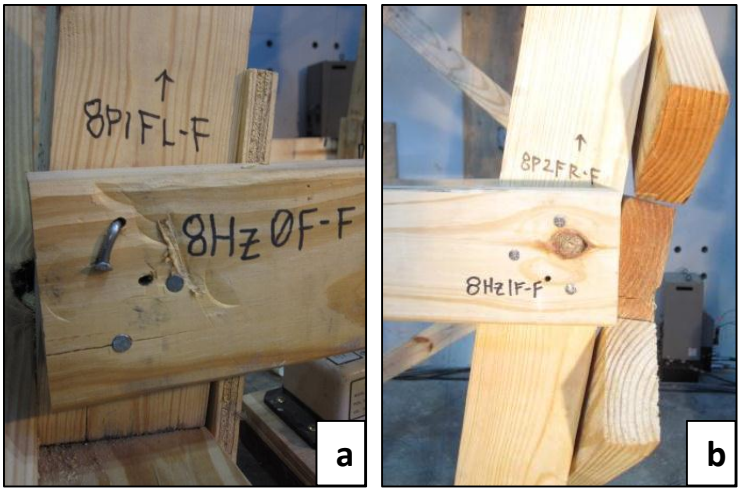

Figure 4.42 Joint rotations (a) Ground level joint (b) First level joint

4.8 TEST SPECIMEN 9

Table 4-8, shown below, contains details pertaining to the test conducted as well as the condition of the specimen shortly before testing commenced.

Table 4-8 Details for Specimen 9

Specimen 9	
Shore Type	PLP, 5ft, Clear Space
Load Scenario	[D] Const Vert Load, Incr Lat Disp
Test Type	Displacement Control
Loading Rate	0.6 in/min
Lateral Braces Used	YES
Avg Initial Out-of-Plumbness (Top rel. to Bottom)	
L-R (North-South)	2.5 in L
F-B (West-East)	FL: 2.25 in B FR: 1.25 in F (Twist)

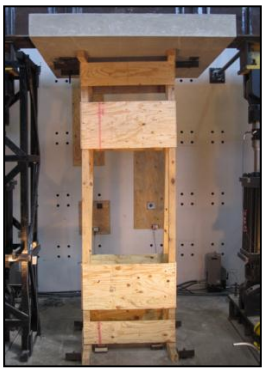

As a direct comparison to the performance of the LP shore in Test 8, Specimen 9 was also loaded to its design capacity (32 kips) and then laterally displaced to the right while maintaining the vertical load. The tower, like the one tested before it, had a clockwise twist of the top relative to the bottom. It also possessed a notable amount of out-of-plumbness to the left. Since lateral displacement was induced to the right, it was necessary to bring the tower to its plumb position in this same plane. Consequently, this initial imperfection, coupled with the stroke limit of 15 inches of the horizontal actuator,

meant that a maximum lateral displacement of 12.5 inches could be achieved for this shore.

As in most of the previous tests, a few moderate cracking noises as the vertical load increased. Additional cracking was observed to occur during lateral loading when the shore had reached a displacement of roughly 7 inches. The first loud cracking noise occurred at a lateral displacement of 11 inches, followed by additional sounds of varying frequency and intensity until 15 inches.

Again, no major cupping was observed during either phase of loading. Only the back right wedge had a minor gap between the two wedges in the pair (Figure 4.43).

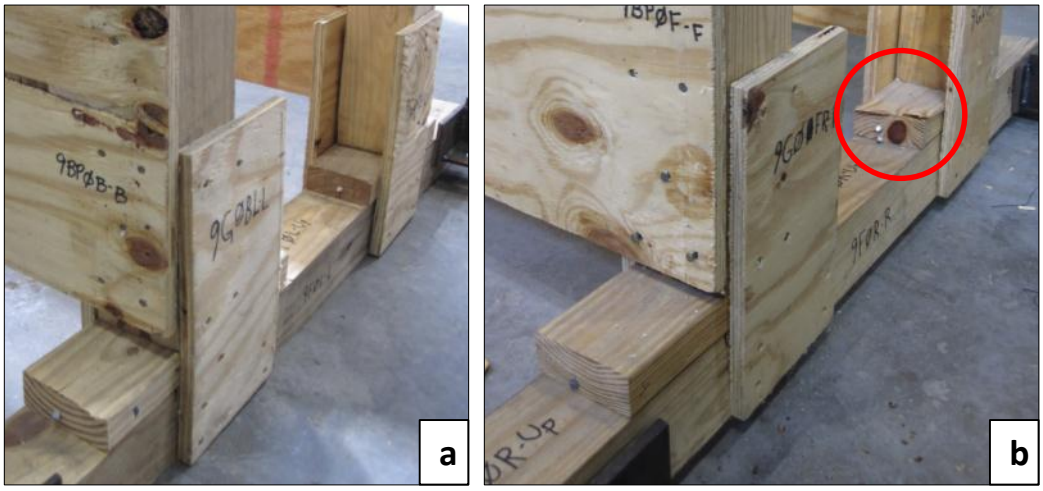

Figure 4.43 Wedge performance for Test 9 (a) Left side of shore (b) Right side of shore

Shortly before the maximum lateral displacement was attained (14.9 inches), the back-left post failed at midlevel by splitting around a knot. In spite of this failure, the vertical load of 32 kips remained unchanged, and the lateral displacement proceeded to the full 15 inches. Next, the shore was loaded vertically to failure while the lateral displacement was held constant. Shown respectively in Figure 4.44 and Figure 4.45 are the vertical load-displacement curve and lateral load-displacement curve for Test 9. The vertical load-displacement curve depicts all stages of the test: initial vertical loading, constant load during lateral displacement, and the increase in vertical load to failure.

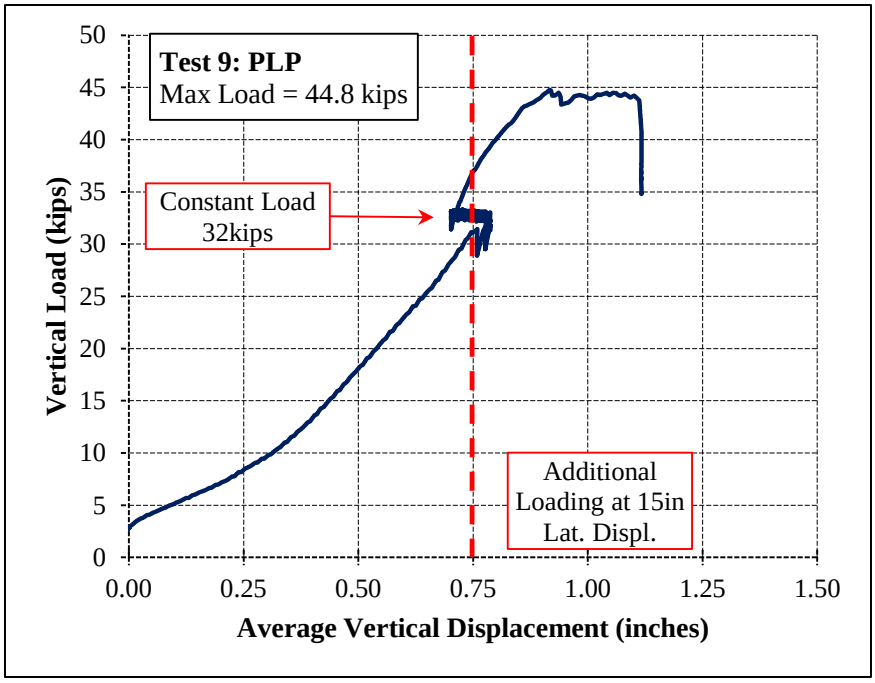

Figure 4.44 Vertical load-displacement plot for Test 9

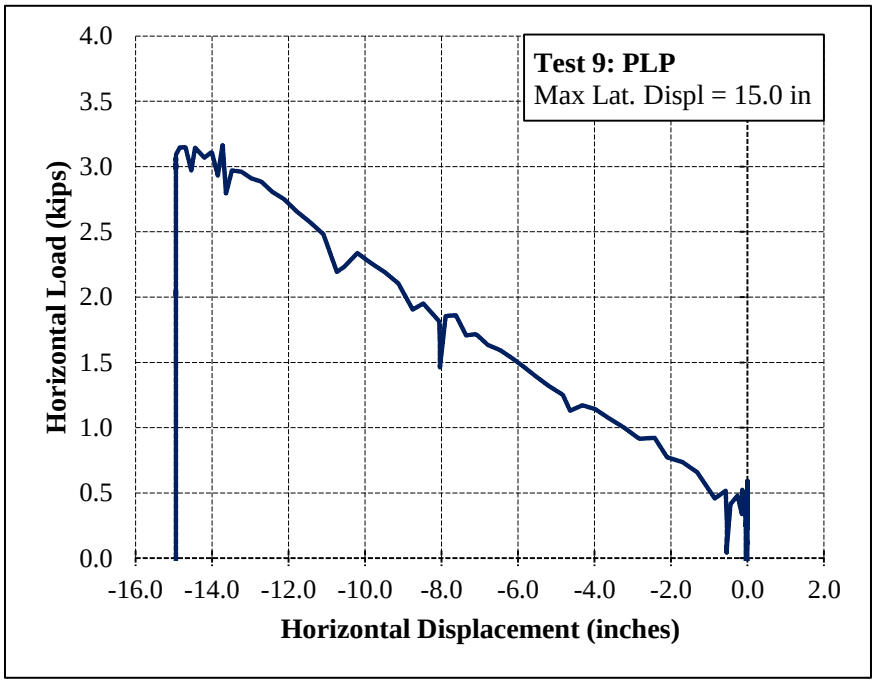

Figure 4.45 Horizontal load-displacement plot for Test 9

A total lateral of force of 3.2 kips was required to displace the top of the shore 15 inches to the right. The plot shown in Figure 4.44 even indicates that the vertical displacement of the shore decreased as it was displaced laterally. Once the vertical load was increased the second time, the shore reached its vertical capacity at only 45 kips, only slightly higher than that of the LP shore from Test 8. Just before this peak load occurred, the back right post experienced a splitting failure at its second level. As the imposed vertical displacement increased, the corresponding vertical load stayed virtually the same, and splits in both the back right and back left post appeared and eventually caused failure in the front left post. At this point, the test ended. Figure 4.46 shows the progressive stages of lateral displacement during the test. Figure 4.47 provides images of the initial failure at 14.9 inches of lateral deflection as well as the final condition of the shore.

Figure 4.46 Test 9 progression of lateral displacement with 32 kip vertical load

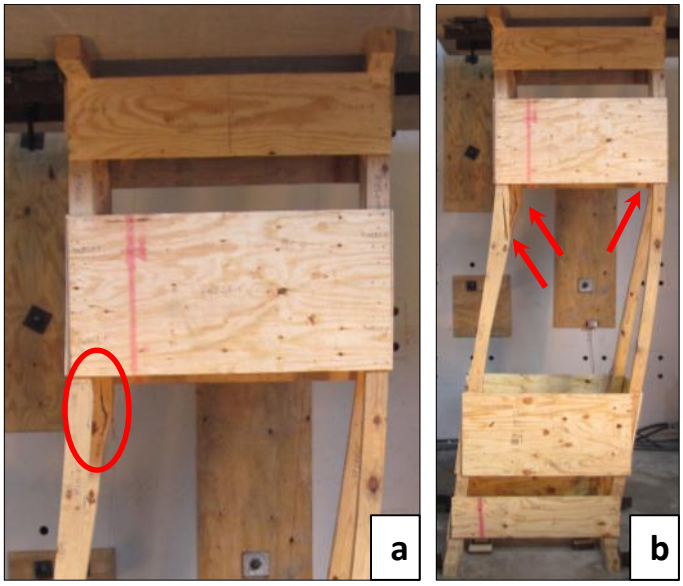

Figure 4.47 Post failures for Test 9 (a) Initial failure during lateral displacement phase (b) Final condition of shore

The three individual post failures are presented in Figure 4.48. Although each failure happened independently, all involved tension-face splitting in the direction of induced lateral displacement.

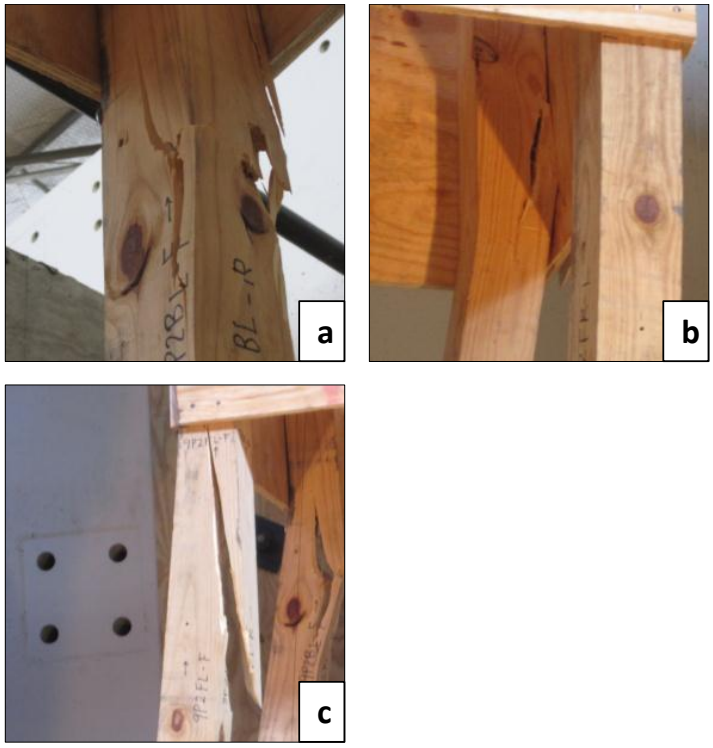

Figure 4.48 Test 9 post failures (a) Back-left (b) Back-right (c) Front-left

Unlike the braces of LP Shore 8, the plywood braces and their respective connections performed quite well in this test. Only minor nail withdrawal was observed on the front and back braces, as shown in Figure 4.49, suggesting that the nailed joints provided sufficient strength to make the material properties of the wood govern the overall capacity of the shore.

Figure 4.49 Images of brace connection failures for Test 9

Comparison of the shore test results discussed in this chapter reveals noticeable differences in the performance of the PLP and LP designs, most notably with respect to vertical capacity and the behavior of the nailed joints.

The aforementioned observations made from the shore test results were taken into careful consideration in developing an appropriate finite element modeling procedure for the shores. The next chapter covers the model setup in detail.

CHAPTER 5

Model Setup

This chapter contains a detailed description of the finite element modeling of the shores. In particular, a model verification study is conducted in order to finalize decisions on modeling solid wood members and connections, followed by a description of the shore modeling process.

As briefly discussed in *Chapter 1*, models serve a variety of beneficial purposes. Among these benefits is the freedom to make any desired design modifications or other parametric studies with the model, often bypassing the need for costly laboratory testing. However, these design modifications and parametric studies must be executed with a model that has been deemed reliable in predicting the desired behavior. For the shores, this includes not only predicting the overall vertical and lateral stiffnesses, but also the loss of stiffness in the connections – which are responsible for maintaining sufficient member alignment that they allow the shores to carry substantial loads before failing.

Abaqus CAE 6.11 (2) is a general-purpose finite element analysis program that can be used to model very complex linear and nonlinear problems faced in structural engineering. As mentioned previously, all the shores were modeled except the ones involving reversed cyclic loading, rapid loading, and sustained loading.

5.1 Model Verification Study

Because of the highly complex nature of the software, it was vital to understand its practical applicability to modeling shores. To accomplish this, it was decided that a simple engineering problem small enough to be solved quickly by hand should be investigated with a model. Thus, a model involving the tension and bending behavior of two wood members (2x4s) joined with three nails in a single shear lap splice connections was analyzed. The objective of this small study was to assess a proposed modeling strategy and its ability to capture stresses in the wood and, most importantly, the overall nailed joint stiffness. Figure 5.1 shows a rendered image of the model selected for this

particular study and Figure 5.2 illustrates the cross-sectional dimensions for a 2x4 wood member.

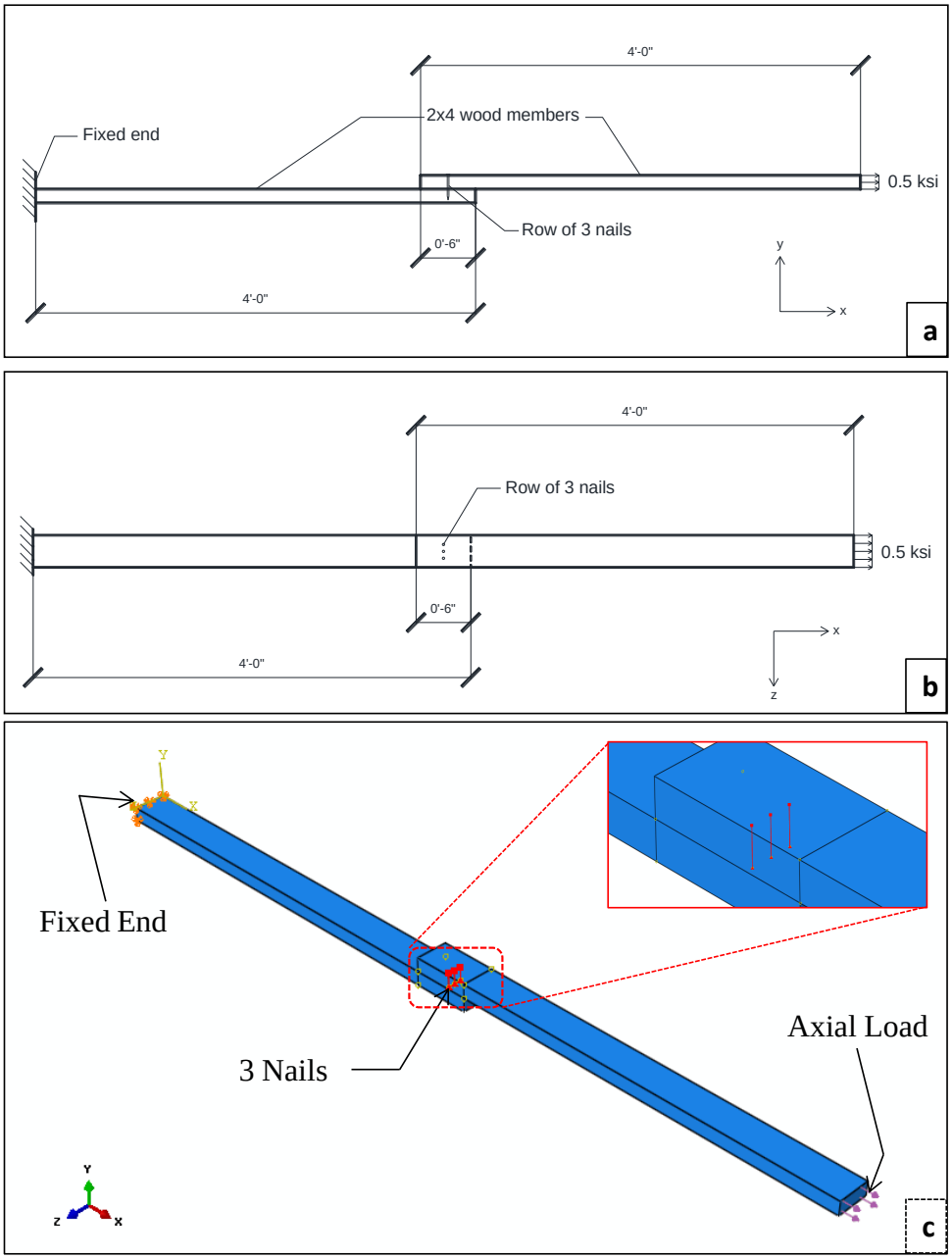

Figure 5.1 Single-shear model (a) Elevation view (b) Plan view (c) Rendered Abaqus model

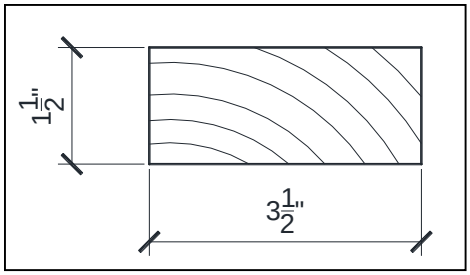

Figure 5.2 Cross section of finished dress size for a 2x4 wood member

The model shown Figure 5.1 aimed to demonstrate the ability of the program to predict the following quantities: joint stiffness, joint slip, axial stress, axial deformations, bending stress, and bending deformations. These responses all depended on data provided to the program by the user, such as material properties and behavior, element types, contact interactions, boundary conditions, loads, mesh, and connector elements. Each of these quantities from the single-shear model described above was computed.

The observed behavior of the shores was dominated by the posts; that is, failure occurred in the posts, and nailed connections underwent large single shear slip – but these connections absorbed sufficient energy to retard the accumulation of failure-inducing curvature in the posts. Thus, it becomes essential to properly account for the single shear slip behavior of the nailed joints. The conclusions reached as a result of the single-shear model apply directly to the shore modeling discussed later.

5.1.1 Material Properties and Behavior

Due to the wide range of unknown variables (particularly the perpendicular-to-grain behavior of the fuses, or wedges, and the top and bottom sole plates) contributing to the observed capacity of each tested shore, the goal of the modeling involved simulating only the linear elastic response given by the vertical load-displacement plot. As such, loading up to the ultimate capacity of the shores was of no concern in the models, and the material properties input in the models did not include any failure theories.

The posts and the wood framing tended to be dominated by axial force and uniaxial bending as observed from the tests, so of all of wood's orthotropic elastic constants, the longitudinal modulus of elasticity was the chief material property characteristic required

for the wood framing. Values for the longitudinal modulus of elasticity of the members in each shore were obtained from material tests at FSEL by Lee (11). After each shore test, the longest surviving elements of the posts, as well as the other framing members, were subjected to 4-point loading to get an estimate of the longitudinal modulus of elasticity and the modulus of rupture. All members were assumed to have remained elastic throughout shore testing – a good, though not ideal, assumption for the surviving sections. These material properties were then used in the modeling of the shores.

5.1.2 Element Type for Framing Members

Each member in a finite element model is generated from an element type, depending on the objective of the model. To capture the local effects surrounding each nail, each member was modeled as a three-dimensional, deformable, homogeneous solid element. This allowed the nodes of each nail to be inserted at any location within the thickness of the members they connected. Had wire elements from Abaqus been used instead, then the location of each nail would have been restricted to the centroidal axis of each member.

5.1.3 Mesh

The accuracy of any finite element model depends upon a judicious meshing scheme of the elements used in the analysis. When all of the desired response measures such as stress, strain, deflection and in this study, connector slip, become independent of the number of elements incorporated in the model, then in most finite element applications, the associated number of elements is considered to be adequate for additional studies. This becomes possible only through multiple trials involving different mesh layouts.

For the both the shore analyses and the single-shear verification analyses, linear hexahedral elements with 8 nodes per element—one at each corner (Figure 5.3a)—were used as the element type for all mesh elements. Although quadratic hexahedral elements with 20 nodes—one at each corner and one mid-side (Figure 5.3b)—showed, after only a

few iterations, faster convergence of the solution for the overall displacement, they consumed considerably more time in terms of computation. The results for the single-shear model include output from both linear and quadratic hexahedral mesh layouts. It was found that although more elements were required to obtain convergence of the solution for linear hexahedral mesh, the results came out very similar.

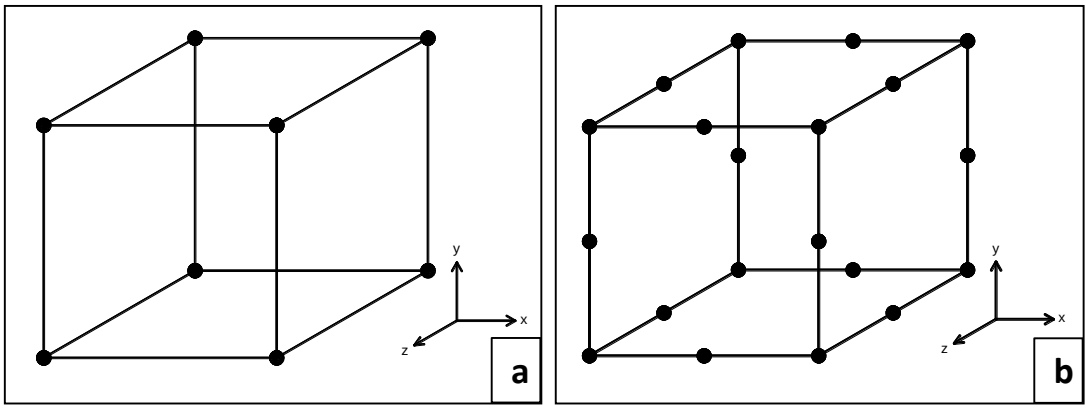

Figure 5.3 (a) Linear hexahedral element (b) Quadratic hexahedral element

Each node in the linear and quadratic hexahedral elements has three translational degrees of freedom: u_x, u_y, and u_z. Consequently, a linear hexahedral element consists of a 24x24 stiffness matrix, while a 60x60 matrix represents a quadratic hexahedral element. The figure below illustrates the orthogonal degrees of freedom for each node.

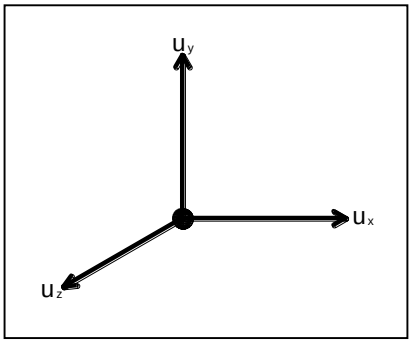

Figure 5.4 Translational degrees of freedom for each node in a hexahedral element

To improve the ability of the model to capture local effects surrounding nailed joints in the single-shear model as well as in the shores, each member was partitioned into smaller cells that encompassed the joint region. This allowed for finer mesh sizes to

be used in these areas without affecting the rest of the member. As shown in Figure 5.5a below, meshing of a member begins by first placing "seeds" along all of its edges, which define the size of the mesh elements. Next, the element is meshed and given the desired mesh element type.

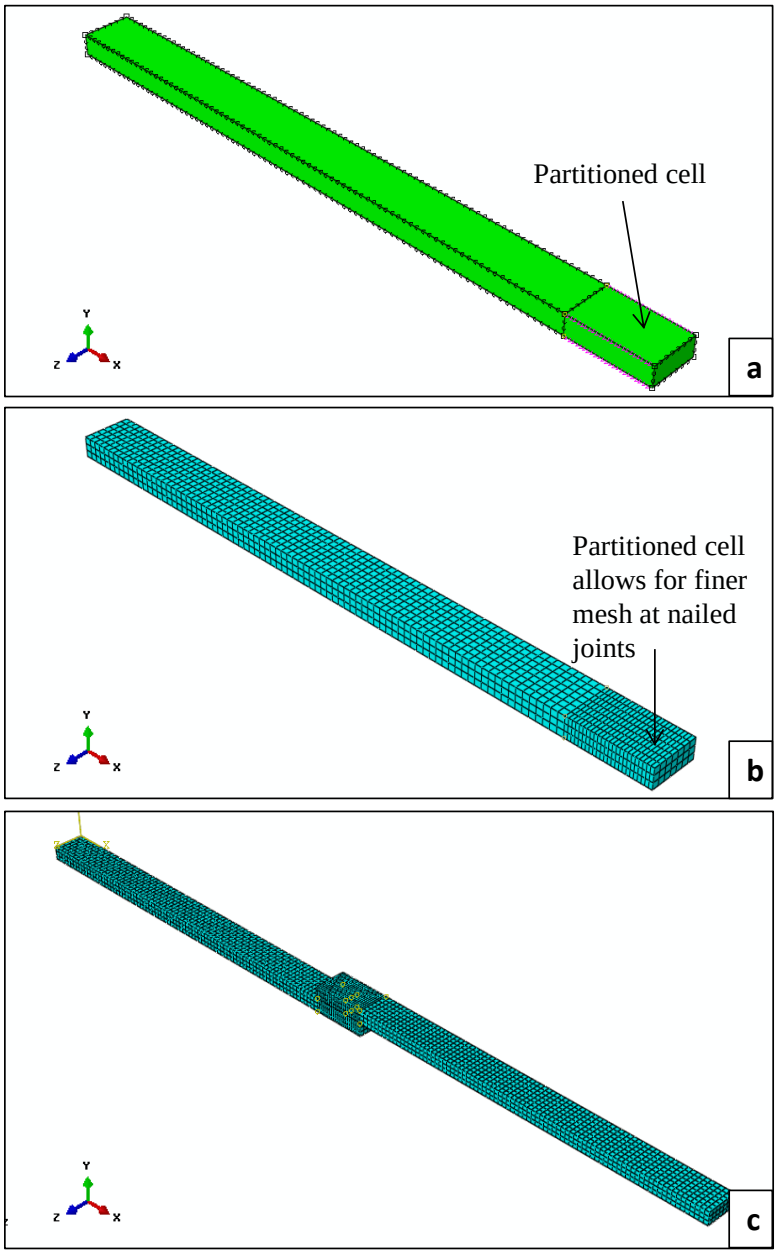

Figure 5.5 (a) Seeded part (b) Meshed part (c) Meshed assembly

5.1.4 Boundary Conditions

As shown in Figure 5.1, the far left end of the model was fixed—all nodes restrained in all directions—resulting in a cantilever system.

For the computations involving joint behavior and axial response, a series of rollers was installed along the length of each member to prevent vertical movement. These rollers served as a vital asset in achieving accurate evaluation of the way in which Abaqus handled axial behavior. For the bending stress and deformation calculations, these rollers were removed so that the induced moment in the nailed joint would force the system to undergo vertical displacement.

5.1.5 Loads

Since each member was represented by a solid element and a uniform response was desired, a uniform pressure load was applied to the surface at the free end (right) of the structure (Figure 5.1). The load had a magnitude of 500 psi, subjecting the top member to axial tension. However, due to the vertical offset between the centroids of the two members, a coupling moment was induced at the joint location. This coupling effect introduced bending stresses in each member, and thus bending deformations, which were accounted for in the hand calculations.

Although Abaqus gives the user the option of specifying follower loads for geometrically nonlinear analyses, the loads in this study and in the shore models were input as non-follower loads. This decision was motivated by the fact that the loading slab used for testing of the shores at FSEL was kept level throughout all tests, regardless of the deformation of the shore below.

Another feature pertaining to applied loads in Abaqus deals with the rate at which they are applied. The default technique is to model the load as a ramp load, meaning the load increases at user-defined increments from zero to the desired magnitude over a user-specified time. A plot of the typical load versus time relationship used for the single-shear model and the shore models is shown in Figure 5.6.

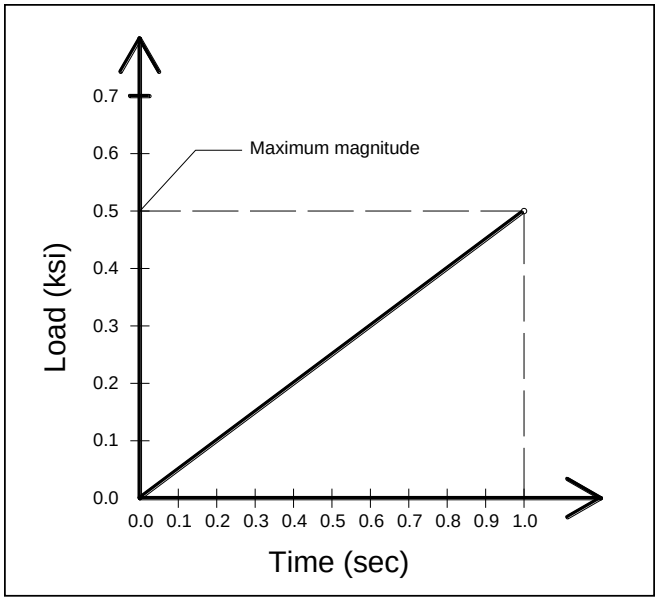

Figure 5.6 Plot of load vs. time used for single-shear model

It should be noted that no dynamic analysis was performed in the shore models – in other words, the specified time over which the load increased from zero to its desired magnitude had no effect on the response of the any of the models. The information discussed above serves only to demonstrate that at multiple times during the application of load, Abaqus can compute the corresponding displacements, stresses, forces, and moments.

5.1.6 Contact Interactions

A contact interaction that consisted of user-defined tangential (parallel to surfaces in contact) and normal (perpendicular to surfaces in contact) behavior was included in the study model. The effects of friction between wood surfaces and wood-to-concrete surfaces were considered to be negligible in all the shore tests. Thus, each contact pair in the model involved a frictionless tangential contact interaction. Moreover, since the effects of nail withdrawal were not included in this study, no separation of surfaces in contact was allowed in the normal direction. The default contact relationship used by Abaqus in the normal direction is termed "hard," which, for any two surfaces in contact, minimizes penetration of one surface into the other. This relationship also prohibits the

transfer of tensile stresses across the interface. The horizontal slip within joints was deemed the most important (as opposed to perpendicular nail withdrawal), which was taken care of by the connector elements selected for the models. The schematic drawing in Figure 5.7 shows the relative movement permitted between members in the Abaqus models. More information on connectors will be presented later.

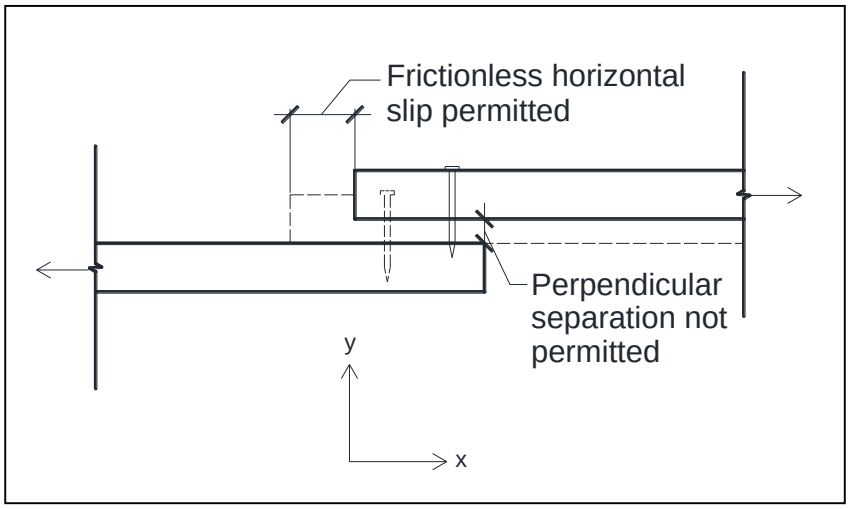

Figure 5.7 Schematic of the normal and tangential contact interactions

5.1.7 Connector Elements

As discussed in *Chapter 4*, the nailed joints played a vital role in the overall behavior of each specimen. Indeed, selection of an appropriate connector element and behavior in Abaqus posed the most critical challenge. The Abaqus connection-type library contains a variety of basic translational and rotational connection components. Based on the success and simplicity of certain methods utilized in the past to model nails as described in *Chapter 2*, spring-like elastic behavior was desired for the nails in the shore models. In turn, two connector elements were selected and investigated in the single-shear study: Cartesian and Projection Cartesian. According to the Abaqus CAE 6.11 User's Manual (2), the Cartesian connector element provides "a connection between two nodes that allows independent behavior in three local Cartesian directions that follow the system at node *a*." On the other hand, Projection Cartesian connector elements boast a slight modification to the Cartesian element in that they provide "a connection between

two nodes that allows independent behavior in three local Cartesian directions that follow the system at both nodes *a* and *b*." Figure 5.8 presents schematic representations of the aforementioned connector elements, followed by a rendering from Abaqus in Figure 5.9.

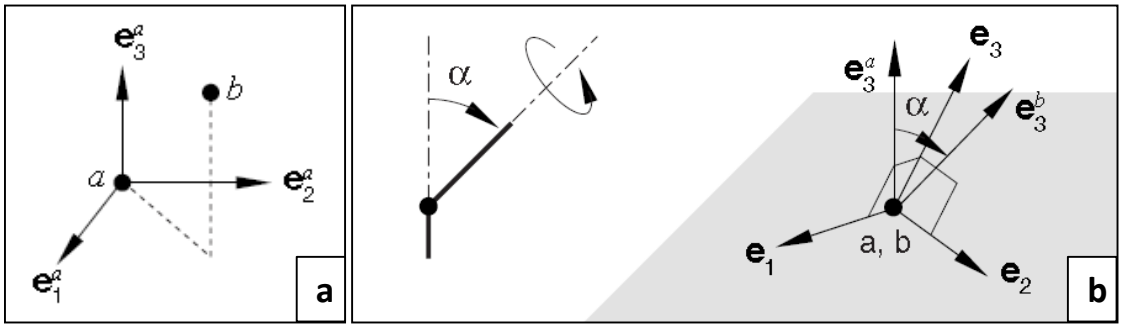

Figure 5.8 Schematic of connector sections (a) Cartesian (b) Projection Cartesian [Source: Dassault Systèmes 2]

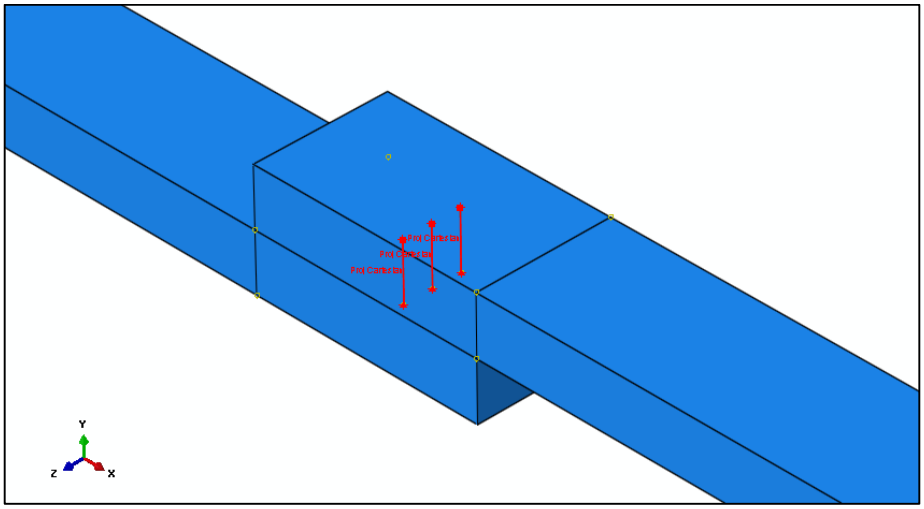

Figure 5.9 Model representation of the three connector elements

For the purposes of this verification study, the connector elasticity was specified as linear and uncoupled, so as to simplify the hand calculations. The following equation can be used for defining linear uncoupled elastic behavior:

$$F_i = D_{ij}u_j \qquad \textbf{Eq. 5-1}$$

The above equation (for the uncoupled case in which the off-diagonal elements are zero) can also be written in matrix form, which yields the following:

$$\begin{bmatrix} F_1 \\ F_2 \\ F_3 \end{bmatrix} = \begin{bmatrix} D_{11} & 0 & 0 \\ 0 & D_{22} & 0 \\ 0 & 0 & D_{33} \end{bmatrix} \begin{bmatrix} u_1 \\ u_2 \\ u_3 \end{bmatrix} \qquad \textbf{\textit{Eq. 5-2}}$$

In regards to the relationship shown above, the user inputs values for D_{11}, D_{22}, and D_{33} which correspond, respectively, to the stiffness in the x, y, and z directions. Each connector has the freedom to exhibit its own orientation, but for simplicity all connectors used in this research were oriented globally. In other words, each connector element in the shore models was positioned so that its local axes aligned with the global axes used to define the overall shore.

The effects of nonlinearity on nail stiffness were not included in the single-shear model study, which was designed to determine if the nail representation would yield anticipated results for nail force and slip. Confining the nail behavior to the linear elastic range helped to simplify the hand calculations and the ensuing comparisons with the model results. However, nonlinearity was incorporated into the nails for all the shores. A discussion of these effects is presented later in this chapter.

5.1.7.1 Constraining the Connector Elements to the Framing Members

In order for Abaqus to properly reflect the effects of the nails, every attachment point for the nails had to be constrained to its associated wood members. Every nail in the model had two constraints, one for each nail end. Abaqus provides the user a number of options within the realm of constraints, so the final decision on the type of constraint came only after intensive studies involving trial and error. A surface-based distributing coupling constraint, which couples the motion of a designated reference node to the average motion of specified coupling nodes, was used in modeling the connections. The name "*surface-based*" means that all of the coupling nodes were on the outer surface of the member to which the constraint was applied. In other words, no internal nodes (within the thickness of a member) could serve as coupling nodes for this type of constraint. The reference node in this case was one node of a connector element, and the coupling nodes represented the surface-based nodes that received the effect of the induced actions on the connector.

Abaqus allows the user to choose from two coupling methods for a surface-based distributing coupling constraint: the continuum coupling method and the structural coupling method. The name "*continuum*" implies that the method used to enforce this constraint couples the translation and rotation of the reference node to the average translation of the coupling nodes (no distribution of moments). The "*structural*" coupling method bears its name because it distributes moments at the coupling nodes as well. The continuum coupling method was selected for the connector constraints in all models discussed in this thesis because it did not require rotational degrees of freedom to be active at the coupling nodes. As described earlier, only translational degrees of freedom are available for the nodes in linear hexahedral elements.

In constraining the attachment points to the wood members, the user must select the node-based surfaces intended to receive the effect of the constraint. It was found that the model results matched the expected theoretical results most closely when only the surfaces in contact with one another were selected for the coupling constraints. Additionally, the effect of the nail was given a spherical radius of influence of 3 inches so that the distribution of the connector elements forces remained near the joint itself. This radius of influence is measured from the reference node to all the surfaces selected for the constraint to provide the user flexibility in controlling the effect of the constraint. Figure 5.10 depicts this radius of influence concept for the single-shear study model.

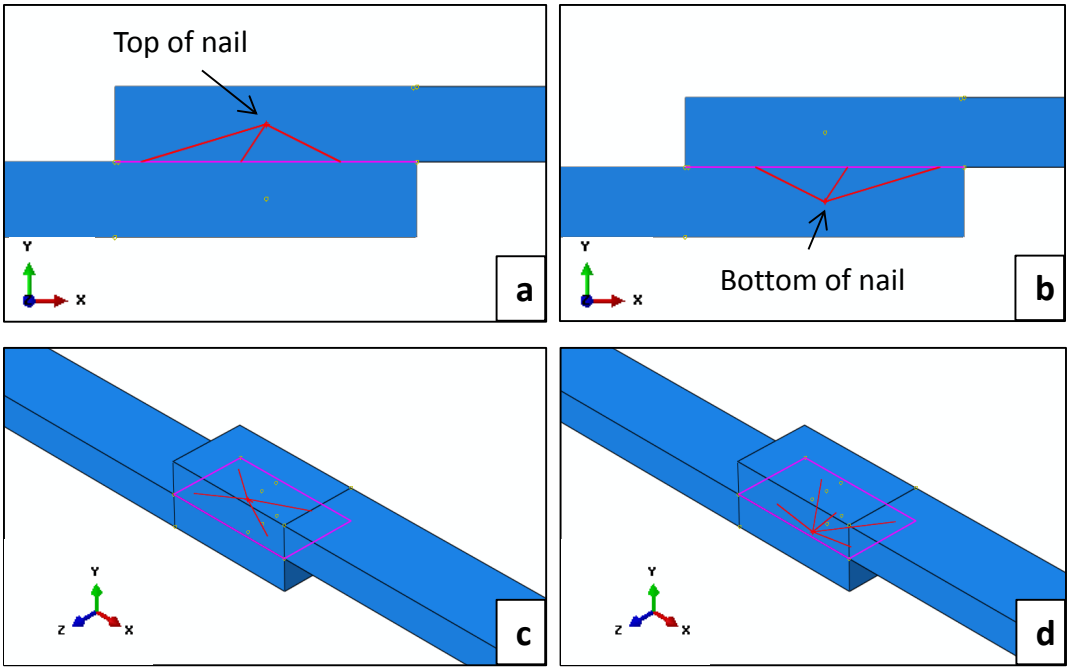

Figure 5.10 Distributing Coupling Constraints (a) Side view of top of nail (b) Side view of bottom of nail (c) Isometric view of top of nail (d) Isometric view of bottom of nail

In the figure above, the "Top of nail" and "Bottom of nail" represent the nodal locations of the connector element (nail) and also the reference nodes for the coupling constraints. The red lines connecting the reference nodes to the surfaces picked for the constraint symbolize the spherical radius of influence—that is, the maximum distance used for inclusion of surface-based nodes as coupling nodes.

5.1.8 Expected Values via Hand Calculations for Single-Shear Model

As mentioned earlier, the following responses were checked by hand in order to assess the validity of the single-shear model: joint stiffness, joint slip, axial deformation, axial stress, bending deformation, and bending stress.

5.1.8.1 Joint Stiffness and Slip

The theoretical horizontal stiffness of the joint was taken simply as the summation of each nail's individual stiffness. An arbitrary elastic stiffness value of 20 kips per inch was designated in all directions for each connector element (D_{11}, D_{22}, and D_{33}). Recall

from Section 5.1.7 that the subscripts 1, 2, and 3 represent the x, y, and z axes, respectively. Since no separation was allowed for members in contact, the D22 term was unnecessary and equal to, in essence, an infinite value.

$$\Sigma D_{joint} = \left(20\frac{kips}{inch}/nail\right)(3\ nails) = \mathbf{60\ k/in}$$

The joint slip, or the relative displacement between the top node and bottom node of each connector element, could be computed easily for the relationship given by Eq. 5-1. A schematic representation of the joint slip is presented in Figure 5.11.

$$u_{joint} = {D_{joint}}^{-1} F_{joint}$$

Where $F_{joint} = \sigma_{applied} A = (0.5\ ksi)(1.5\ in)(3.5\ in) = 2.625\ kips$

$$u_{joint} = \left(60\frac{k}{in}\right)^{-1}(2.625\ kips) = \mathbf{0.04375\ in}$$

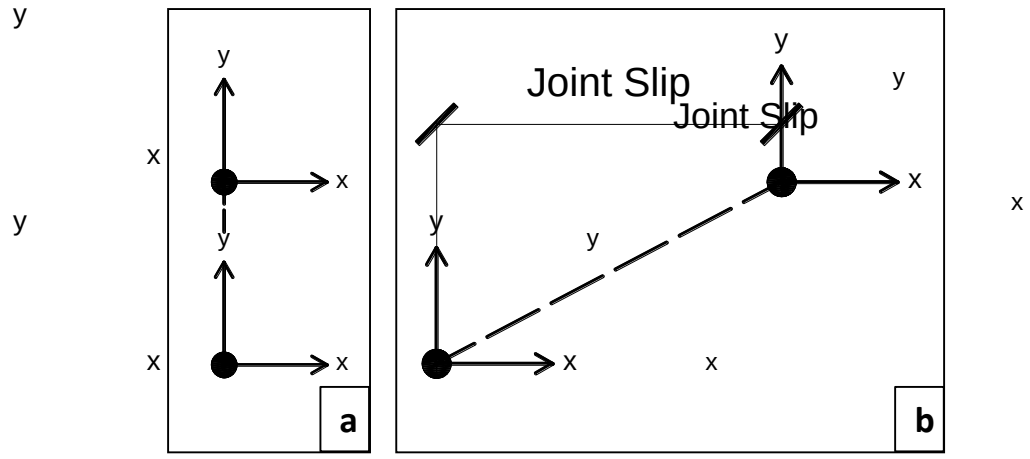

Figure 5.11 Connector movement (a) Before deformation (b) After deformation

5.1.8.2 Axial Deformation and Stress

To obtain strictly axial deformation in the system, rollers were placed along each member to prevent vertical movement. This was only a temporary condition, as the rollers were removed for the bending calculations. A schematic representation of this arrangement is show in Figure 5.12.

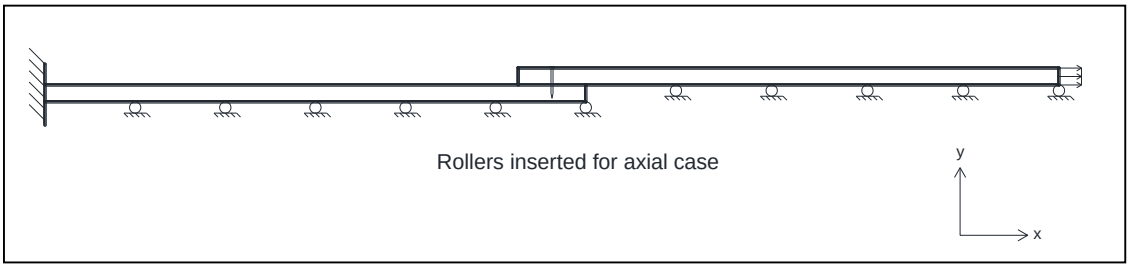

Figure 5.12 Series of rollers added to system for axial calculations

The total axial deformation of the single-shear system involved the elastic deformation of the wood members as well as the horizontal joint slip. The following calculations show the theoretical, or expected, axial deformation:

$$\delta = \frac{PL}{EA} + u_{joint}$$

where P = 2.625 kips

L = 90 inches

E = 1,700 ksi [NDS 2005; Southern Pine No.1]

A = 5.25 in^2

$u_{joint} = 0.04375\ in$

$$\delta = \frac{(2.625\ k)(90\ in)}{(1{,}700\ ksi)(5.25\ in^2)} + 0.04375\ in = \mathbf{0.0702\ in}$$

Throughout both members, the axial stress was simply equal to the applied axial load divided by the cross-sectional area. Near the nailed joint, the axial stress varied in a complicated manner. However, away from the connection it was equal to the end stress, 0.5 ksi.

5.1.8.3 Bending Deformation and Stress

To check deformations due to bending, the rollers were removed from the system to allow for bending moments to develop within the members. Because the centroids of the members are eccentric, a near-concentrated moment forms at the joint location and is transferred through the left member to its fixed end. The member on the right remains unaffected by the induced moment, although it does have a small moment that arises

from slight bearing between the top and bottom members. The concentrated moment was calculated as follows:

$$M = (2.625\ kips)(1.5\ in) = \mathbf{3.938\ k\ in}$$

With the joint moment known, the moment and curvature (M/EI) diagrams could be drawn for the system. Using the curvature diagram, shown in Figure 5.13, the moment-area theorem was used to compute the vertical deflection at the free end of the system.

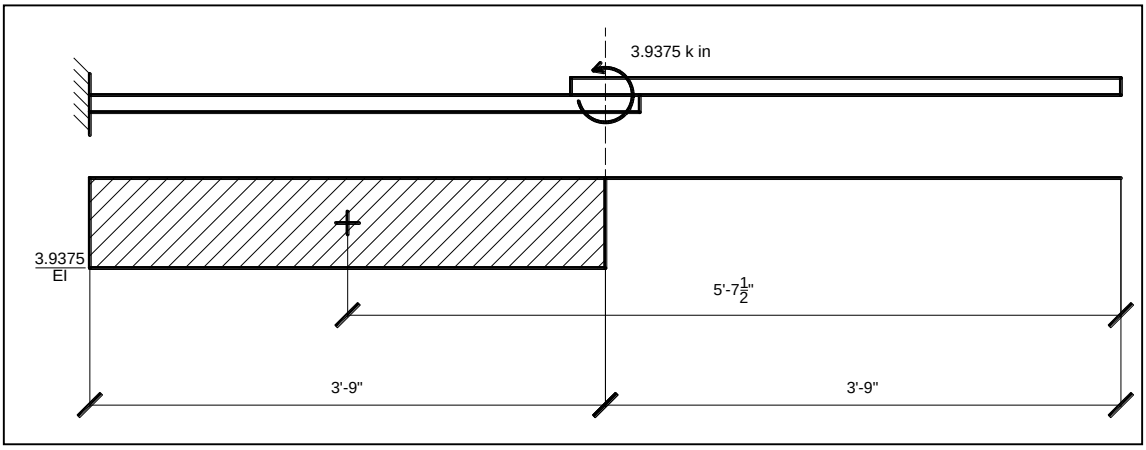

Figure 5.13 Schematic of the concentrated moment and curvature diagram

$$\Delta = \frac{M}{EI} * (45\ in)\left[\frac{1}{2}(45\ in) + 45\ in\right]$$

Where $M = 3.9375\ k\ in$

$E = 1{,}700\ ksi$

$I = \left(\frac{1}{12}\right)(3.5\ in)(1.5\ in)^3 = 0.984\ in^4$

$$\Delta = \frac{(3.938\ k\ in)}{(1{,}700\ ksi)(0.984\ in^4)} * (45\ in)(67.5\ in) = \mathbf{7.147\ in}$$

The bending stress due to the induced moment was then computed using the flexure formula.

$$\sigma_{bending} = \frac{Mc}{I}$$

$c = 0.75\ in$

$$\sigma_{bending} = \frac{(3.938\ k\ in)(0.75\ in)}{(0.984\ in^4)} = \mathbf{3.0\ ksi}$$

Next, the calculated axial and bending stresses were superimposed to obtain the top and bottom fiber stresses for the left member, resulting in the stress diagram shown in Figure 5.14.

$$\sigma_{total} = \sigma_{axial} + \sigma_{bending} = \frac{P}{A} \pm \frac{Mc}{I}$$

$$\sigma_{top} = 0.5\ ksi + 3.0\ ksi = \mathbf{3.5\ ksi}$$

$$\sigma_{bot} = 0.5\ ksi - 3.0\ ksi = \mathbf{-2.5\ ksi}$$

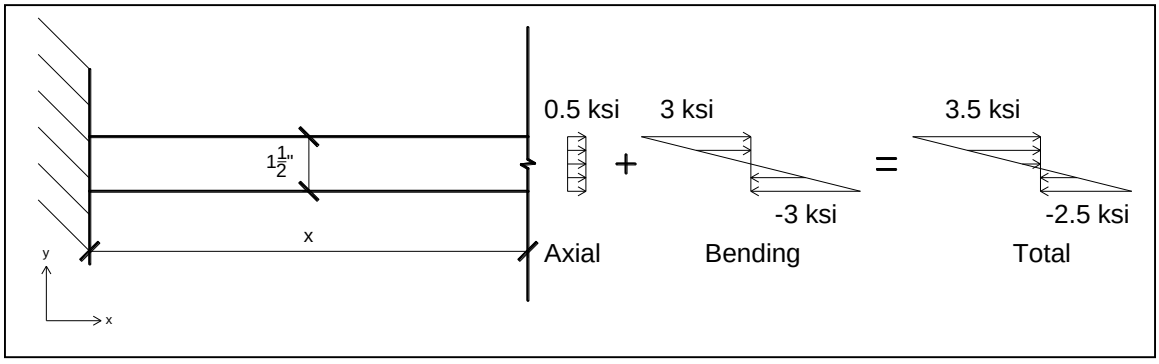

Figure 5.14 Stress diagram for the left member of the single-shear model

5.1.9 Abaqus Results for Single-Shear Model

This section contains a summary of the output given by Abaqus for the single-shear model for comparison with the expected values above. All of the aspects of the system's behavior that were calculated by hand are also presented below as results of the finite element analysis conducted on the model.

5.1.9.1 Joint Stiffness and Slip

As described previously, the expected value for the joint stiffness was the summation of each individual nail stiffness. To determine the joint stiffness from the Abaqus, the joint slip had to first be obtained by the output given by the top and bottom nodes of the connector elements. Figures 5.15 and 5.16 show deformed contour plots of

the single-shear model, with the various colors representing the magnitudes of the normal (x-direction) stress distribution within each member (blue signifies the lowest level of stress whereas red marks the highest level of stress).

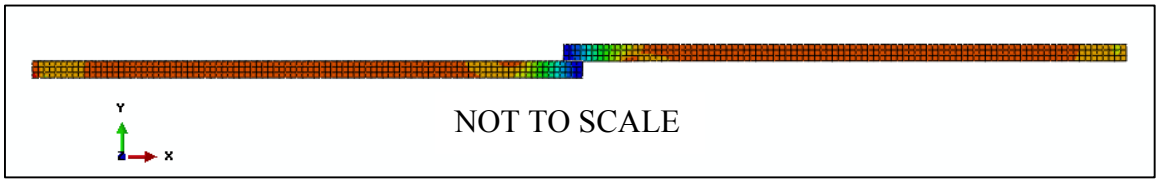

Figure 5.15 Elevation view of deformed plot for axial case

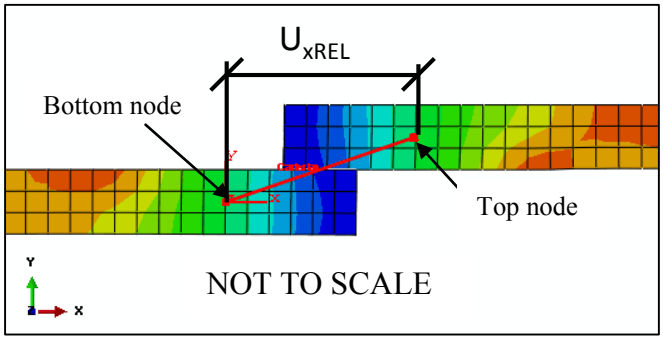

Figure 5.16 Close-up view of connector displacement due to the applied axial load

As indicated in the figures above, the plots are not to scale. The scale has been drastically exaggerated for the purpose of capturing the horizontal joint slip. Table 5-1 gives the computed values from Abaqus for horizontal displacement (along the x-axis) of the top and bottom connector nodes, represented by U_x.

Table 5-1 Abaqus output for the top and bottom nail displacements along with the calculated relative nail displacement

Top of Nail			
Time	U_x (in)	Load (ksi)	Load (k)
0	0	0	0
1	0.0567	0.5	2.625

Bottom of Nail			
Time	U_x (in)	Load (ksi)	Load (k)
0	0	0	0
1	0.01295	0.5	2.625

Relative Nail Displacement			
Time	U_{xREL} (in)	Load (ksi)	Load (k)
0	0	0	0
1	**0.04373**	0.5	2.625

As highlighted in orange, the joint slip was simply the value of the relative nail displacement at t = 1 seconds (after the entire load had been applied). This value was obtained by subtracting the bottom node nail displacement from the top node nail displacement. Therefore, the joint slip according to the model is as follows:

$$u_{joint} = \mathbf{0.04373\ in}$$

The computed joint stiffness was determined from the data by calculating the slope of the load versus relative displacement results. The additional data points selected for this calculation are highlighted in beige in Table 5-1.

$$m = \frac{\Delta y}{\Delta x} = \frac{y_2 - y_1}{x_2 - x_1}$$

$$y_2 = 2.625\ kips$$

$$y_1 = 0.0\ kips$$

$$x_2 = 0.04373\ in$$

$$x_1 = 0.0\ in$$

$$m = \frac{2.625 - 0.0\ kips}{0.04373 - 0.0\ in} = \mathbf{60.02\ k/in}$$

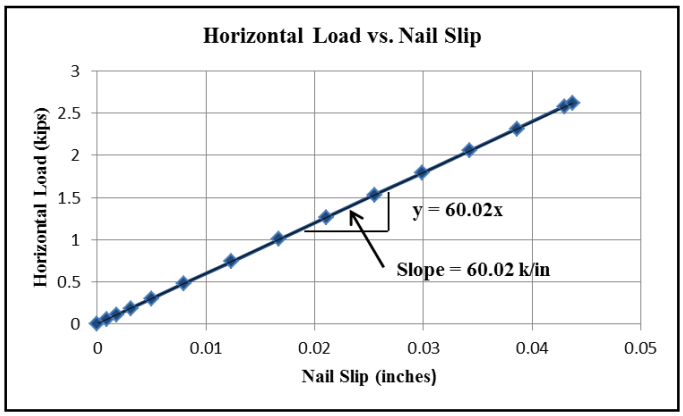

Figure 5.17 Load-Displacement plot for the horizontal nail-slip response

Notice in the graph shown in Figure 5.17 that there are numerous intermediate data points on the plotted line between the origin and the final data point. These points represent the periodic computations that Abaqus performs throughout the analysis, as described earlier in Section 5.1.5. The fact that all of these points are collinear—that is, they all lie on the same straight line—proves that the joint stiffness remained linear elastic throughout the loading process, as desired.

To check the connector response in directions other than the specified x, y, and z components, a second model was examined with a 45 degree angle between the two

members. As before, the axial load was applied to the top member, and the displacements of the top and bottom of one of the nails were computed. The overall purpose of this investigation was to determine whether or not the connector yielded a higher stiffness in the angled direction.

Plots of the deformed structure from the model are shown in Figure 5.18 and plots showing convergence of the solution are provided in Figure 5.19.

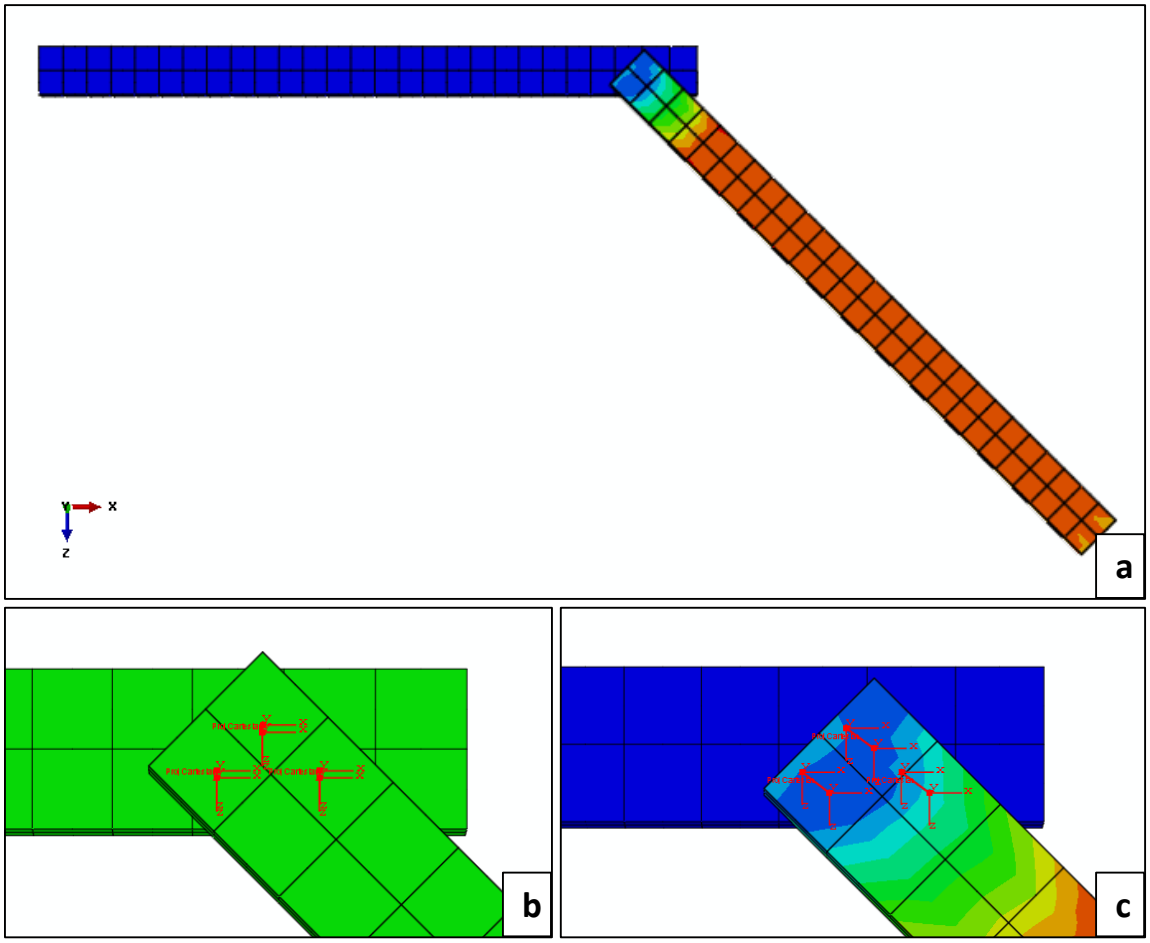

Figure 5.18 (a) Deformed plot (b) Joint before loading (c) Joint after loading

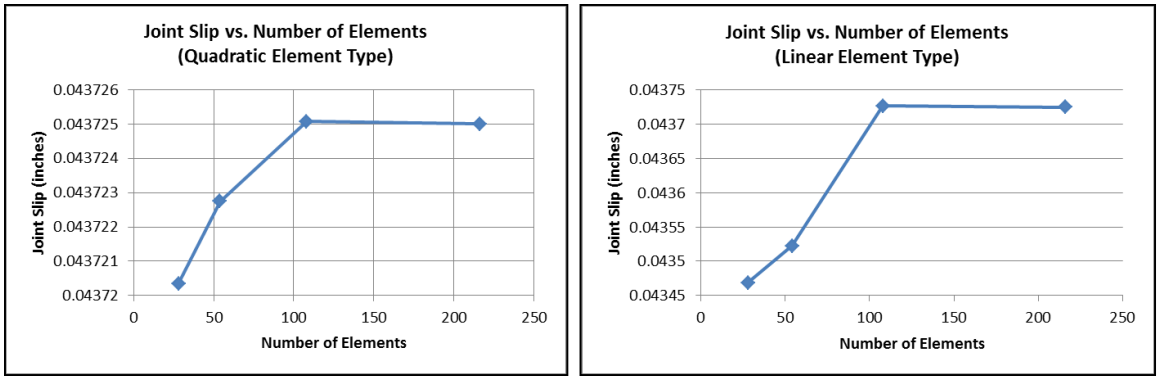

Figure 5.19 Plots showing solution convergence for joint slip

Table 5-2 gives the computed results from Abaqus for the angled joint model. The displacements in three different directions are provided—U_x, along the x-axis—U_z, along the z-axis—and U_{45}, along an axis at 45 degrees measured from the x-axis (halfway between the x-axis and z-axis). Similarly, the magnitude of the applied load is shown in the same three directions.

Table 5-2 Output from Abaqus for relative horizontal nail displacement

RELATIVE NAIL DISPLACEMENT							
Time (s)	**U_x (in)**	**Time (s)**	**U_z (in)**	**U_{45} (in)**	**$Load_{45}$ (ksi)**	**$Load_{45}$ (k)**	**$Load_{x,z}$ (k)**
0	0	0	0	0	0	0	0
1	0.03091	1	0.03093	**0.04373**	0.5	2.625	1.8562

$$m_x = \frac{\Delta y_x}{\Delta x_x} = \frac{y_{x2} - y_{x1}}{x_{x2} - x_{x1}}$$

$$y_{x2} = 1.8562\ kips$$

$$y_{x1} = 0.0\ kips$$

$$x_{x2} = 0.03091\ in$$

$$x_{x1} = 0.0\ in$$

$$m_x = \frac{1.8562 - 0.0\ kips}{0.03091 - 0.0\ in} = \mathbf{60.05\ k/in}$$

$$m_z = \frac{\Delta y_z}{\Delta x_z} = \frac{y_{z2} - y_{z1}}{x_{z2} - x_{z1}}$$

$$y_{z2} = 1.8562\ kips$$
$$y_{z1} = 0.0\ kips$$
$$x_{z2} = 0.03093\ in$$
$$x_{z1} = 0.0\ in$$
$$m_z = \frac{1.8562 - 0.0\ kips}{0.03093 - 0.0\ in} = \mathbf{60.01\ k/in}$$

$$m_{45} = \frac{\Delta y_x}{\Delta x_x} = \frac{y_{45-2} - y_{45-1}}{x_{45-2} - x_{45-1}}$$
$$y_{45-2} = 2.625\ kips$$
$$y_{45-1} = 0.0\ kips$$
$$x_{45-2} = 0.04373\ in$$
$$x_{45-1} = 0.0\ in$$
$$m_{45} = \frac{2.625 - 0.0\ kips}{0.043725 - 0.0\ in} = \mathbf{60.03\ k/in}$$

As demonstrated in the calculations above, the total stiffness for the nailed joint for loading at an angle that does not coincide with any of the local connector directions is the same as the previous case. This study proved that Abaqus does not falsely combine the orthogonal stiffness of the connector in two mutually perpendicular directions.

5.1.9.2 Axial Deformation and Stress

The axial deformation of the free end of the right member was determined by monitoring a degree of freedom on its far end surface. To ascertain convergence of the solution from the model regarding axial displacement, several mesh refinements with linear and quadratic element types were implemented into the model. The plots in Figure 5.20 reveal the results of the output from the different mesh layouts. Figure 5.21 shows a rendered image from Abaqus with the selected node that was monitored throughout the analysis.

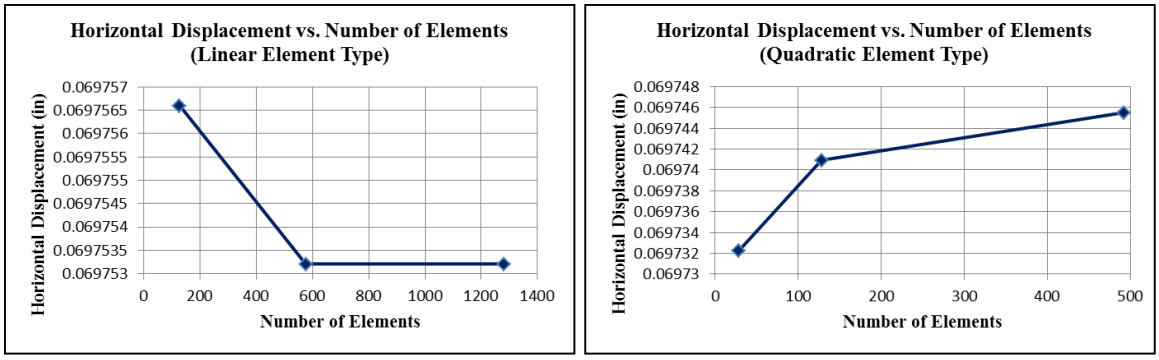

Figure 5.20 Plots showing convergence of solution for horizontal displacement

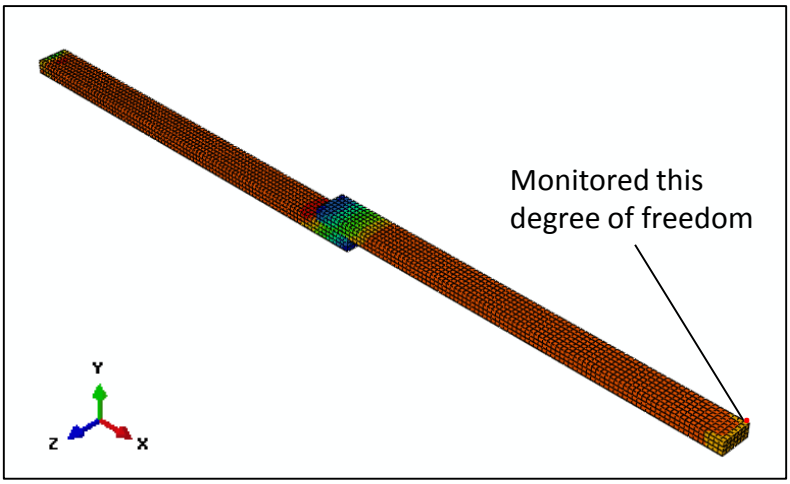

Figure 5.21 Abaqus image showing location of monitored degree of freedom

$$\delta = \mathbf{0.069746}\boldsymbol{in}$$

As for the axial stress, a section cut was made through both members after the analysis completed. The images in Figure 5.22 depict the axial force recorded by these section cuts.

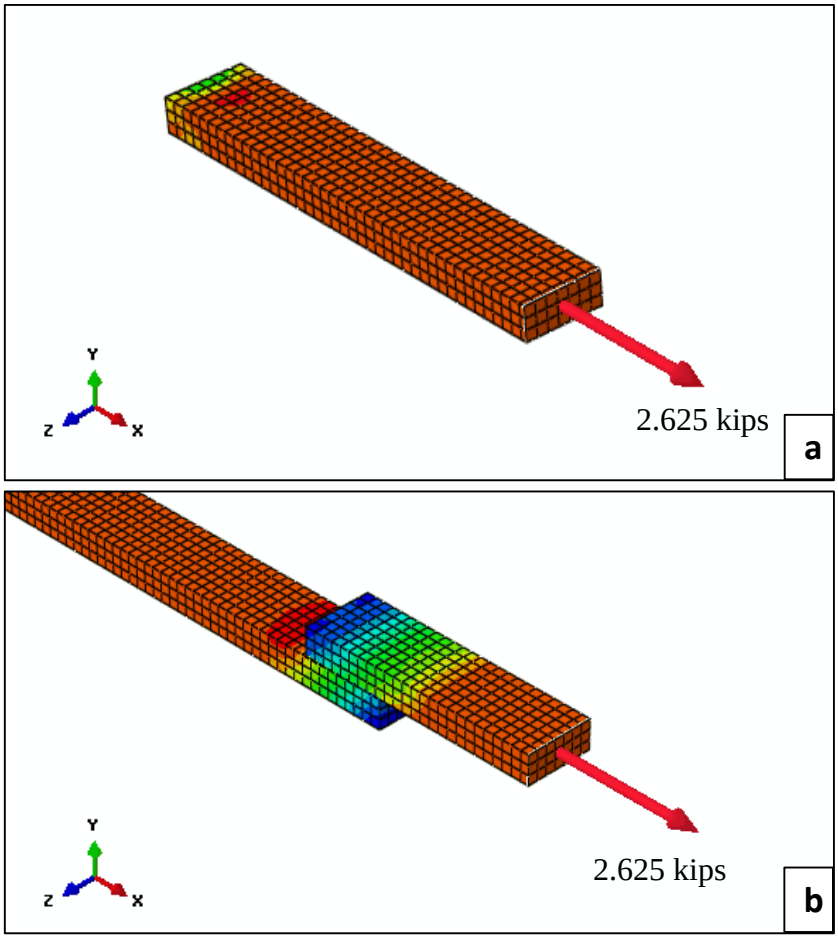

Figure 5.22 Axial force in each member as given by Abaqus output

5.1.9.3 Bending Deformation and Stress

With the rollers removed from the system, the model was re-analyzed to capture the effects of bending deformations and stresses indicated by the deformed position shown in Figure 5.23.

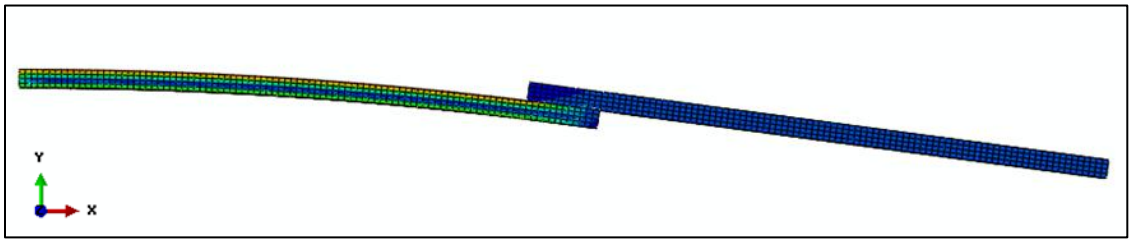

Figure 5.23 Elevation view of deformed plot for bending deformation case

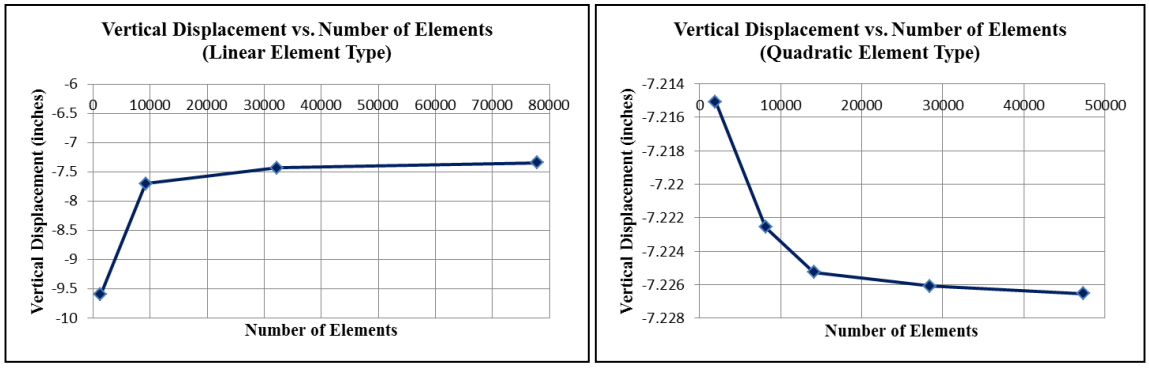

Figure 5.24 Plots showing convergence of solution for vertical displacement

$$\Delta_{end} = -7.227\ in$$

Once it was evident that the solution had converged (Figure 5.24), the top and bottom fiber stresses near the middle of the left member were then obtained from the output.

$$\sigma_{top} = 3.51\ ksi$$

$$\sigma_{bot} = -2.51\ ksi$$

The magnitude of the bending stress at any location within a member depends on the moment at that particular location. Again, numerous mesh layouts were investigated in order to achieve solution convergence (Figure 5.25). It was clear from the plots in the figure below that quadratic elements gave much more accurate results even for a very small number of elements.

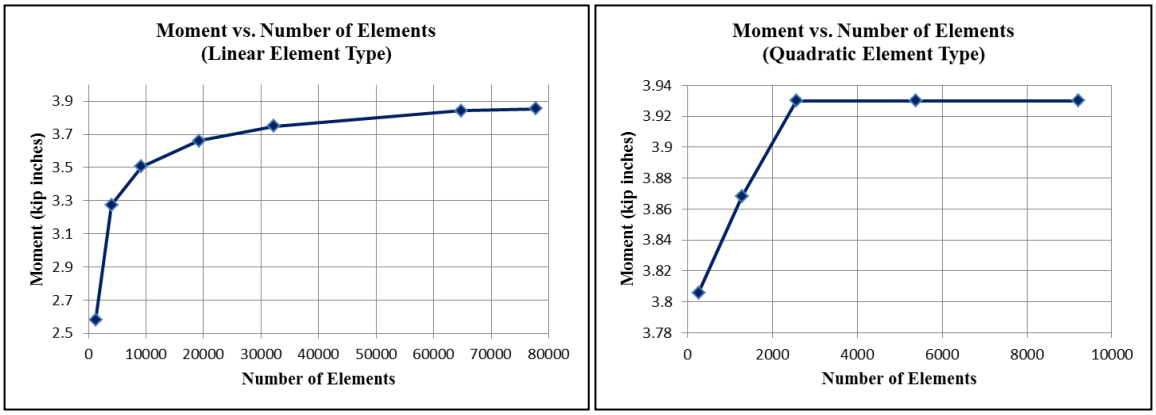

Figure 5.25 Plots for convergence of solution for the induced bending moment

$$M = \mathbf{3.93\ k\ in}$$

5.1.10 Comparing Hand Calculations and Abaqus Output

Table 5-3 provides a comparison for each calculation checked by hand and in the model. The results from the hand calculations exhibited good agreement with the analyses performed in Abaqus.

Table 5-3 Comparison of results from hand calculations and Abaqus output

Behavior	Units	Hand Calculation	Abaqus Result	% Difference
Joint Stiffness	k/in	60	60.02	**0.0333**
Joint Slip	in	0.04375	0.04373	**0.0457**
Axial Deformation	in	0.0702	0.06948	**1.0256**
Axial Stress	ksi	0.5	0.5	**0**
Bending Deformation	in	-7.147	-7.227	**1.1194**
Bending Stress (Top)	ksi	3.5	3.51	**0.2857**
Bending Stress (Bot)	ksi	-2.5	-2.51	**0.4000**

The largest error was shown for the axial and bending deformation calculations. Errors for the axial displacement probably were caused by the complicated behavior near the nailed joint. The difference from the bending deformation likely resulted from a small additional amount of bending moment on the right member in the region of contact.

After studying the output from the single-shear model, it was concluded that quadratic hexahedral elements approached the desired level of accuracy at a much faster rate than linear elements. However, as stated earlier in this chapter, quadratic elements were found to demand significantly higher amounts of computer memory due to the high number of nodes. Since linear elements gave very similar results as the quadratic elements (although at a slower rate), it was decided that these mesh element types should be used exclusively in analyzing the shore models.

5.2 DESCRIPTION OF SHORE MODELING

Using the knowledge gained from the single-shear analyses as foundational tools, the LP and PLP shores were then constructed in Abaqus. The following sections present

a detailed outline of the steps involved in creating the shoring towers, including any notable difficulties encountered during the process.

5.2.1 Material Properties

The data entered for the material properties for each shore was obtained from material tests conducted at FSEL upon the completion of each test (11). Table 5-4 gives the summary of the material data used to define the shore member properties. The data is organized by shore, beginning with PLP Shore 1. The location of each post is designated by the nomenclature system described in *Chapter 4* (FL, FR, BL, and BR). Members are identified by type per the following: "P" for post, "H" for horizontal brace in a LP shore, and "D" for diagonal brace in a LP shore. Lastly, the far right column entitled "MOE (ksi)" gives the calculated value for the longitudinal modulus of elasticity based on the results from the simple bending tests. These values were then adjusted according to the procedures outlined in ASTM 1990D.

Like all the other members, the plywood braces in the PLP shores were also modeled as isotropic. Since no material tests were conducted on any of the plywood members upon completion of testing of each shore, an assumed value of 1,300,000 psi was assumed for the modulus of elasticity. Results from the modeling revealed that the plywood braces experienced very small amounts of stress, whereas the regions near the nails exhibited relatively higher stresses. This behavior proved that due to the tremendous in-plane strength of the plywood members, the nails were responsible for the overall effectiveness of the plywood braces.

Table 5-4 Shore material properties from FSEL tests [Adapted from Lee 11]

Member Identification				MOE (ksi)
Shore #	Member	Level	Location	
1	P	N/A	FL	**682**
1	P	N/A	FR	**N/A**
1	P	N/A	BL	**942**
1	P	N/A	BR	**741**
2	P	N/A	FL	**673**
2	P	N/A	FR	**1725**
2	P	N/A	BL	**767**
2	P	N/A	BR	**876**
3	P	N/A	FL	**1119**
3	P	N/A	FR	**781**
3	P	N/A	BL	**720**
3	P	N/A	BR	**972**
3	H	2	F	**1922**
3	D	1	B	**1409**
3	H	2	R	**1287**
3	D	3	R	**1423**
4	P	N/A	FL	**1040**
4	P	N/A	FR	**1456**
4	P	N/A	BL	**N/A**
4	P	N/A	BR	**558**
4	H	3	F	**3021**
4	D	2	B	**739**
4	H	2	L	**1613**
4	D	3	L	**1929**
6	P	N/A	FL	**1017**
6	P	N/A	FR	**1021**
6	P	N/A	BL	**1226**
6	P	N/A	BR	**1058**
6	H	1	F	**1021**
6	H	1	B	**1805**
6	D	2	L	**1030**
6	D	3	R	**1539**
7	P	N/A	FL	**888**
7	P	N/A	FR	**998**
7	P	N/A	BL	**1335**
7	P	N/A	BR	**2875**
8	P	N/A	FL	**1383**
8	P	N/A	FR	**1452**
8	P	N/A	BL	**884**
8	P	N/A	BR	**892**
8	H	2	B	**846**
8	H	3	B	**1476**
8	D	1	R	**1453**
8	D	2	R	**1535**
9	P	N/A	FL	**792**
9	P	N/A	FR	**1268**
9	P	N/A	BL	**N/A**
9	P	N/A	BR	**891**

5.2.2 Base Springs

Based on the evidence presented in *Chapter 4*, local bearing almost always occurred between the bottom of the posts and the wedges below them. In some cases, the bearing even extended to the sole below the wedges. Since failure stresses were ignored in the model input, the solid elements described previously would not suffice in capturing this behavior. In terms of output, the assumed linear elastic response would yield a model far too stiff to represent the shores from the laboratory tests. Additionally, the tetrahedral elements required to mesh the wedges would become severely distorted when subjected to the high bearing stresses from the posts above them. This would lead to confusing and inaccurate results. Consequently, linear springs were added to serve as replacements for the wedges and soles (Figure 5.26). The stiffness of each spring was based on an assumed value for the tangential modulus of elasticity of the wood members, taken as 1/35th of the published value for the longitudinal modulus of elasticity. The area used in calculating the axial stiffness of the springs was taken as the cross-sectional area of the post, and the length as the distance from the bottom of the posts to the bottom of the soles. Calculations detailing the linear springs are outline below.

$$E_{tangential} = \frac{E_L}{35} = \frac{1{,}700\ ksi}{35} = \mathbf{48.57\ ksi}$$

$$k_{spring} = \frac{E_{tangential} A_{post}}{L}$$

Where

$$A_{post} = (3.5\ in)(3.5\ in) = 12.25\ in^2$$

$$L = t_{wedge} + t_{sole} = 1.5\ in + 3.5\ in = 5\ in$$

$$k_{spring} = \frac{(48.57\ ksi)(12.25\ in^2)}{(5\ in)} = \mathbf{119.0\ k/in}$$

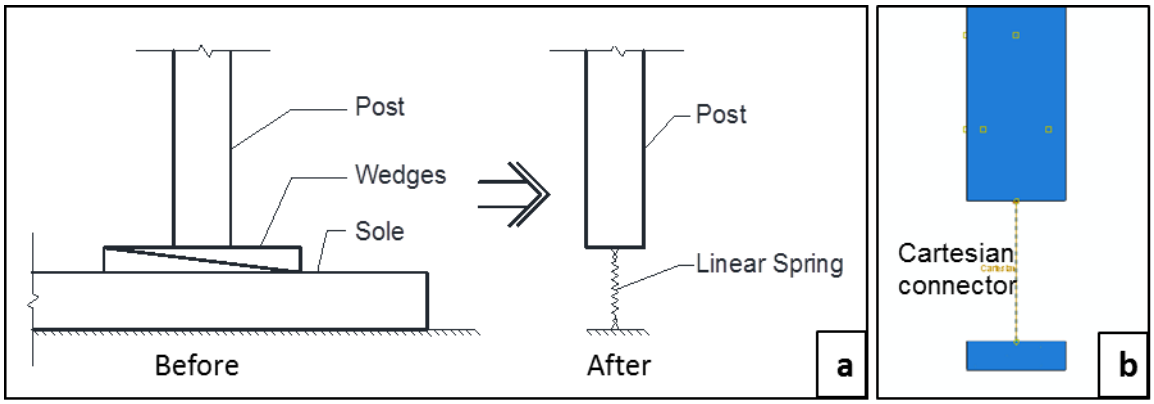

Figure 5.26 (a) Schematic of linear spring replacing wedges and sole (b) Abaqus snapshot of spring element in place

5.2.2.1 Boundary Conditions near the Base Springs

The most critical decision with regards to the springs beneath each post of the shore models involved whether or not the base of each post should be allowed to rotate. Clearly, removing the gusset plates that connected the posts to the footers permits the post bases to rotate more freely, but photographic evidence from the FSEL tests proved that these gussets did little to prevent rotation of the posts. Figure 5.27 and Figure 5.28 show comparisons between the FSEL tests for Shores 8 and 9 and their respective Abaqus model results. Clearly, the laboratory test photos reveal that the top of each post remained fixed while the bottom rotated slightly. This was most likely due to the softness of the wedges beneath each post, which provided a flexible base about which the posts could rotate fairly easily under lateral load.

As a result of this study, the shore models were allowed to rotate at their bases. Hence, the Abaqus snapshots from Figure 5.27(c) and Figure 5.28(c) represent the actual results reported in this thesis from the finite element models. The images shown in these figures capture the instant at which LP Shore 8 and PLP Shore 9 are subjected to 32 kips of vertical load and have just reached 15 inches of lateral displacement at the top.

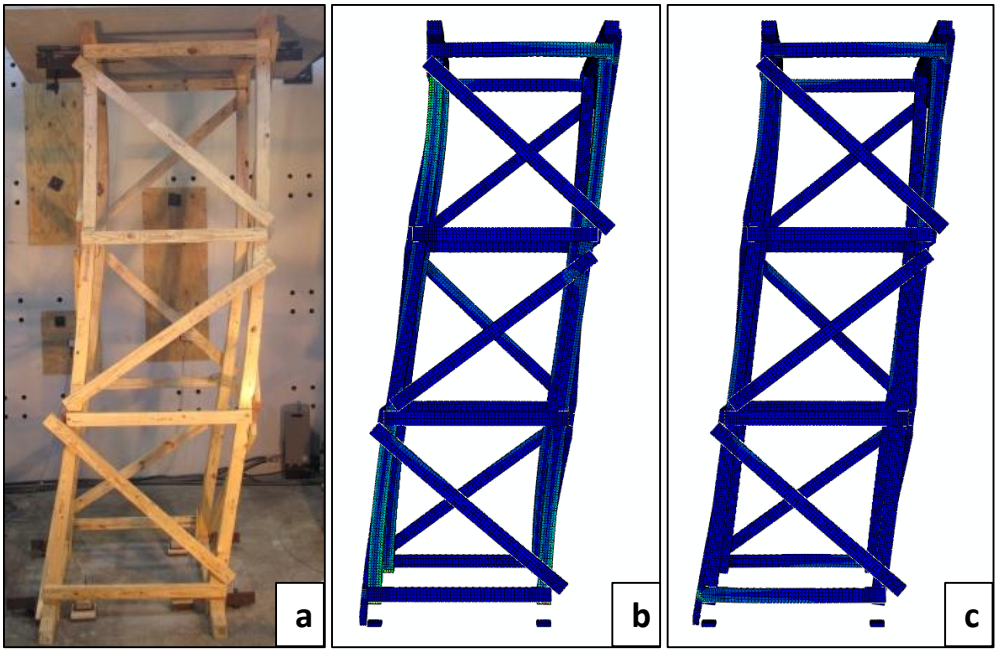

Figure 5.27 Comparison of base fixity for posts in LP Shore 8 (a) FSEL test (b) Posts fixed at base (c) Posts free to rotate at base

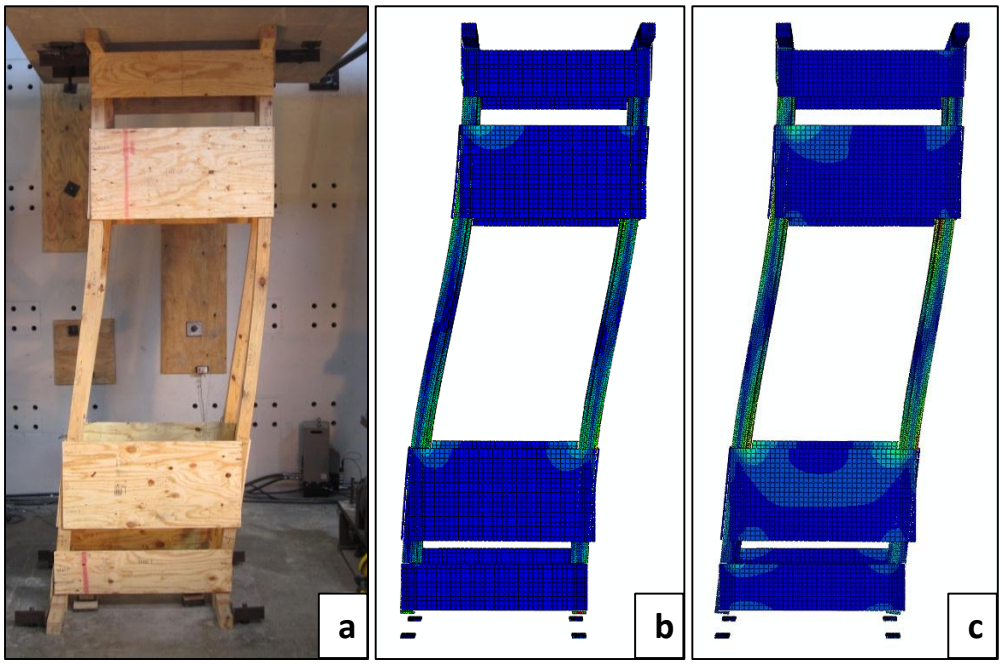

Figure 5.28 Base fixity in PLP Shore 9 (a) FSEL test (b) Posts fixed at base (c) Posts free to rotate at base

5.2.3 Node Locations for Nails

Deciding on the locations of the nodes of each connector element called for a close look at the nail behavior from the FSEL tests. Since complete nail withdrawal was not considered in the Abaqus models, photographs that captured partial nail withdrawal were carefully studied. In the majority of the photographs, the portion of the nails still embedded in the wood members they connected remained unbent. Bending of each nail occurred mostly in the portion of the nail that had been pulled out from the wood members. This was the case for both solid wood-to-wood connections as well as solid wood-to-plywood connections. The photographs in Figure 5.29 illustrate some various degrees of nail withdrawal at the conclusion of Shore Tests 6 and 7.

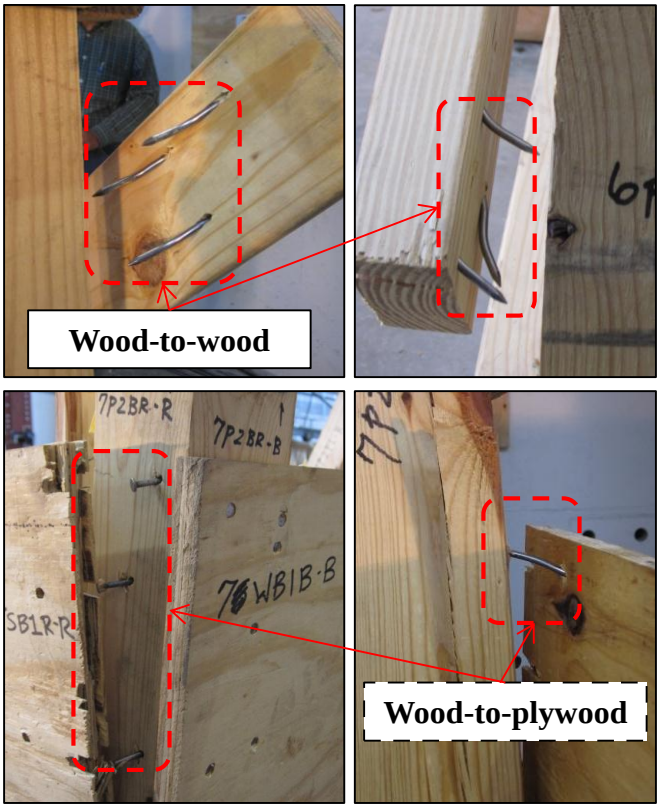

Figure 5.29 Nail withdrawal investigation for LP Shore 6 and PLP Shore 7

By comparing the photographs in Figure 5.29 with the connection yield modes for dowel-type fasteners in the NDS 2005, it became clear that Mode IV most closely resembled the nail withdrawal behavior observed during testing. Figure 5.30 shows a

chart of the connection yield modes with Mode IV encased in a dotted red line for emphasis.

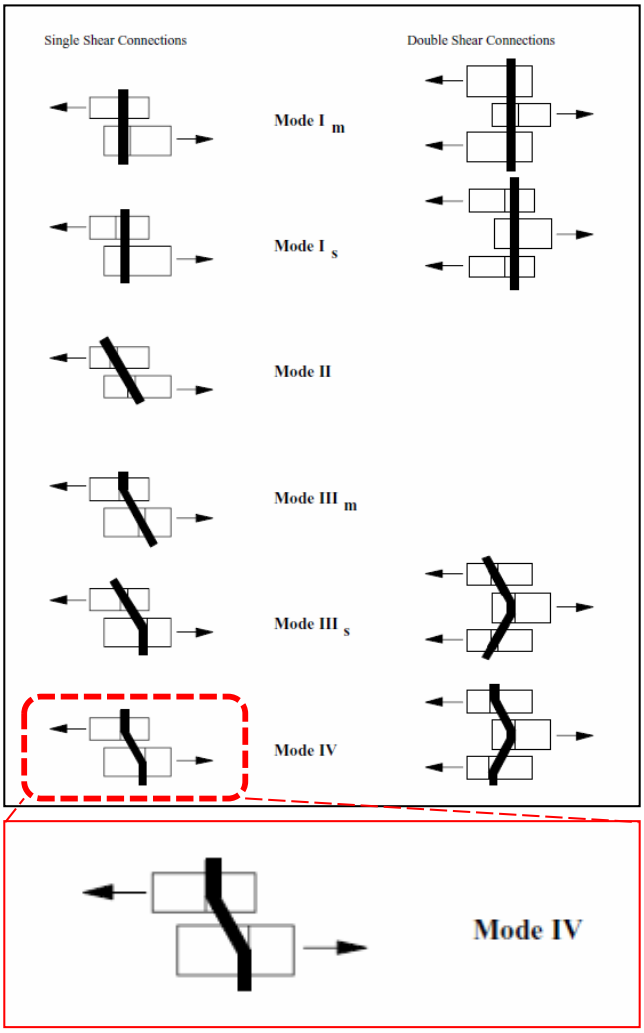

Figure 5.30 Connection Yield Modes [Source: Figure 11 NDS 2005]

Because of the highly variable nature of stress along the length of dowels subjected to single shear, it was impossible to assign an accurate nodal location to each connector element. Thus, a uniform layout for the nodal locations for each nail size was selected, one for the 8d common nails and one for the 12d common nails. It was decided that the nodes for the connector elements be placed at the midpoint of each portion of the nail that was embedded in the main and side members. Schematic representations for each nail are shown in Figure 5.31.

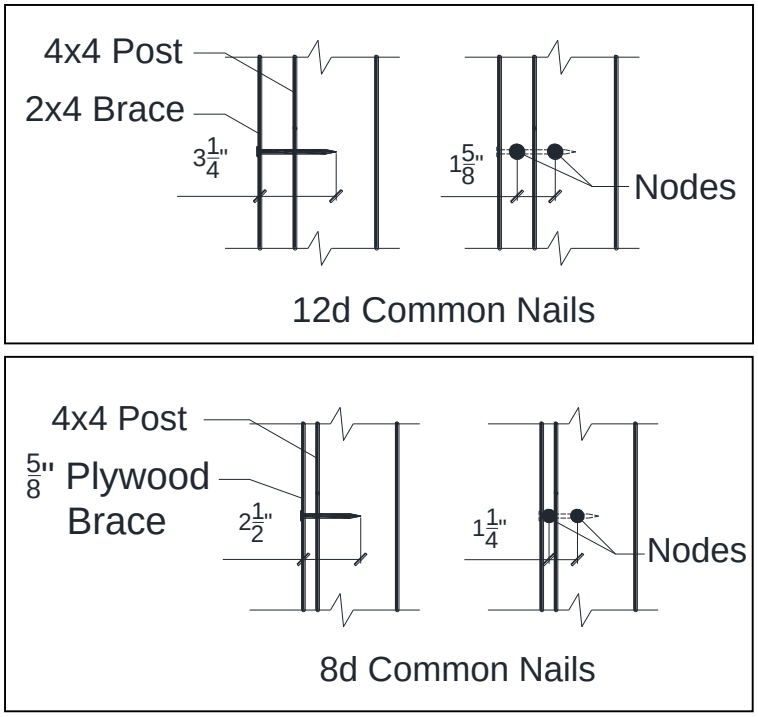

Figure 5.31 Schematic drawings of the nodal locations for the connector elements

The drawings shown above depict the exact locations of the connector element nodes used for every shore model. Notice that the distance between connector element nodes is smaller for an 8d nail (2.5 inches long) than for a 12d common nail (3.25 inches long).

5.2.4 Slab Modeling

The concrete slab was modeled as a solid element capable of only moving vertically during vertical loading. This was accomplished by enforcing boundary conditions on each face of the slab that prevented rigid body movement in the x and z directions. As a result, no deformation of the slab was allowed during loading. Recalling from the information provided in *Chapter 3*, deformation of the slab during the FSEL tests was also not desired, and it was therefore assumed that all vertical displacement read by the MTS actuators occurred in the shore itself. During lateral loading, the z direction was released on all slab faces while the x and y directions were fixed. Rendered images from Abaqus of the slab model are shown in Figure 5.32.

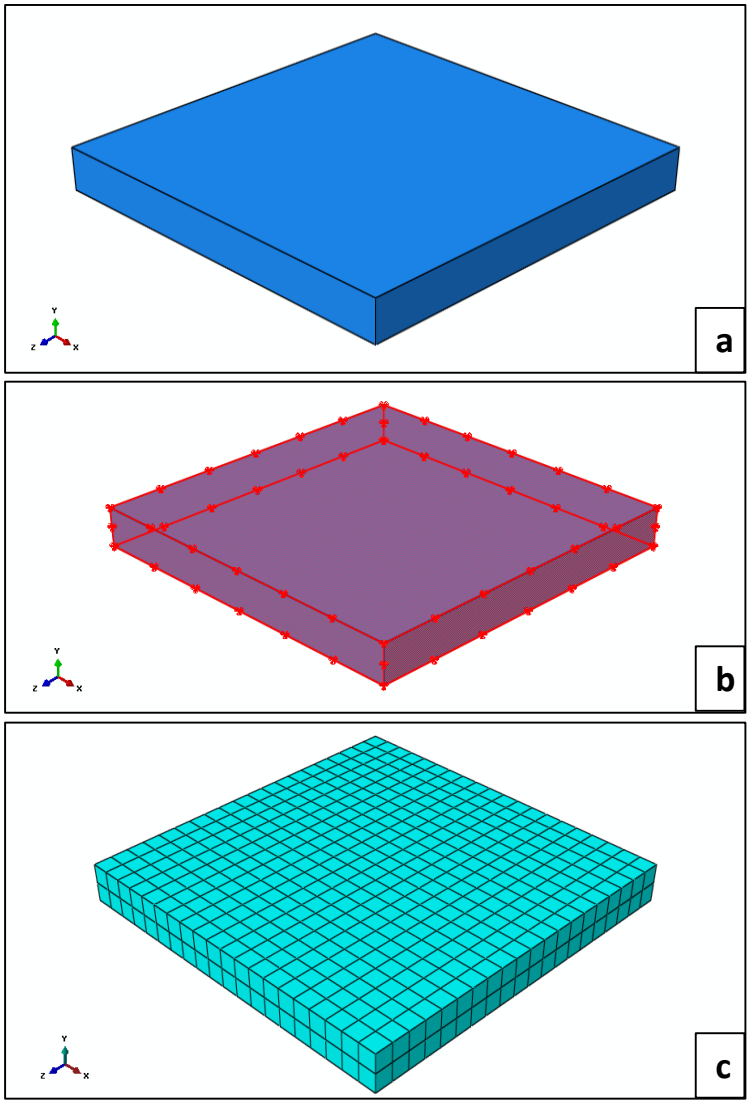

Figure 5.32 Abaqus snapshot of slab (a) Slab element (b) Boundary conditions on all sides (c) Slab mesh layout with linear hexahedral elements

5.2.5 Nail Nonlinearity

Including the effects of nonlinearity in the nail stiffness was of paramount importance in the models, particularly for the shores subjected to lateral displacements during testing. As discussed in *Chapter 2*, a variety of factors contribute to the behavior of a nailed wood joint. Since no experimental test was conducted at FSEL for the nails used in the shoring specimens, trusted data from McLain (14) was utilized. Recalling

from Equation 2-5, the equation supported by McLain contains two curve-fitting parameters:

$$P = A * log_{10}(1 + B\Delta)$$

McLain (14) performed a series of tests on various nailed joint configurations with 8d nails. Although he did not perform a test with Southern Yellow Pine members, he published data for joints comprised of members with specific gravities very close to that of Southern Pine. The results of his analysis showed that specific gravity played the most significant role in determining the parameters A and B. As such, two sets of data consisting of members with similar specific gravities to Southern Yellow Pine (0.55) were taken from his results and averaged to obtain a load-slip curve for the models. The data used is shown below in Table 5-5.

Table 5-5 Results from McLain used for load-slip curve in shore models

Specimen	Fitted Parameters (Static case)		Specific Gravity		Average Specific Gravities	
	A	B				
DFP-L-2/RDO-L-13	**133.7**	**1144.6**	DFP-L-2	0.669	DFP	**0.539**
			RDO-L-13	0.593		
DFP-C-3/RDO-L-14	**146.3**	**639.57**	DFP-C-3	0.408	RDO	**0.594**
			RDO-L-14	0.595		

DFP: Douglas Fir Plywood

RDO: Red Oak

L: Parallel to grain

C: Perpendicular to grain

The following calculations show how the equations for both 8d and 12d nails were obtained from the information provided in the table above.

$$A_{mean} = \frac{1}{2}(133.7 + 146.3) = \mathbf{140}$$

$$B_{mean} = \frac{1}{2}(1144.6 + 639.57) = \mathbf{892.09}$$

To account for the effect of the larger diameter for the 12d nails, the parameter A was increased by a factor equal to the ratio of the slip modulus of a 12d nail to that of an 8d nail. The slip modulus for each nail size was determined from the NDS 2005 equation mentioned in *Chapter 2* (Eq. 2-7).

$$\gamma = 180{,}000 * D^{1.5}$$

$$D_{8d} = 0.131\ in$$

$$D_{12d} = 0.148\ in$$

$$\gamma_{8d} = 180{,}000 * (0.131\ in)^{1.5} = \mathbf{8.53\ k/in}$$

$$\gamma_{12d} = 180{,}000 * (0.148\ in)^{1.5} = \mathbf{10.25\ k/in}$$

$$\frac{\gamma_{12d}}{\gamma_{8d}} = \frac{10.25}{8.53} = \mathbf{1.2016}$$

Therefore, the parameter A for the 12d nails becomes:

$$A_{12d} = 1.2016 * 140 = \mathbf{168.23}$$

Due to the greater amount of variability and uncertainty inherent in the determination of B, only A was increased. These parameters yielded the following load-slip equations:

$$P_{8d} = 140log(1 + 892.09\Delta) \qquad \textbf{Eq. 5-3}$$

$$P_{12d} = 168.23log(1 + 892.09\Delta) \qquad \textbf{Eq. 5-4}$$

Figure 5.33 shows the curves from Eq. 5-3 and Eq. 5-4 and their comparative initial stiffness. The data points used to construct these curves were input into the nonlinear elasticity data for the connector elements in the shore models.

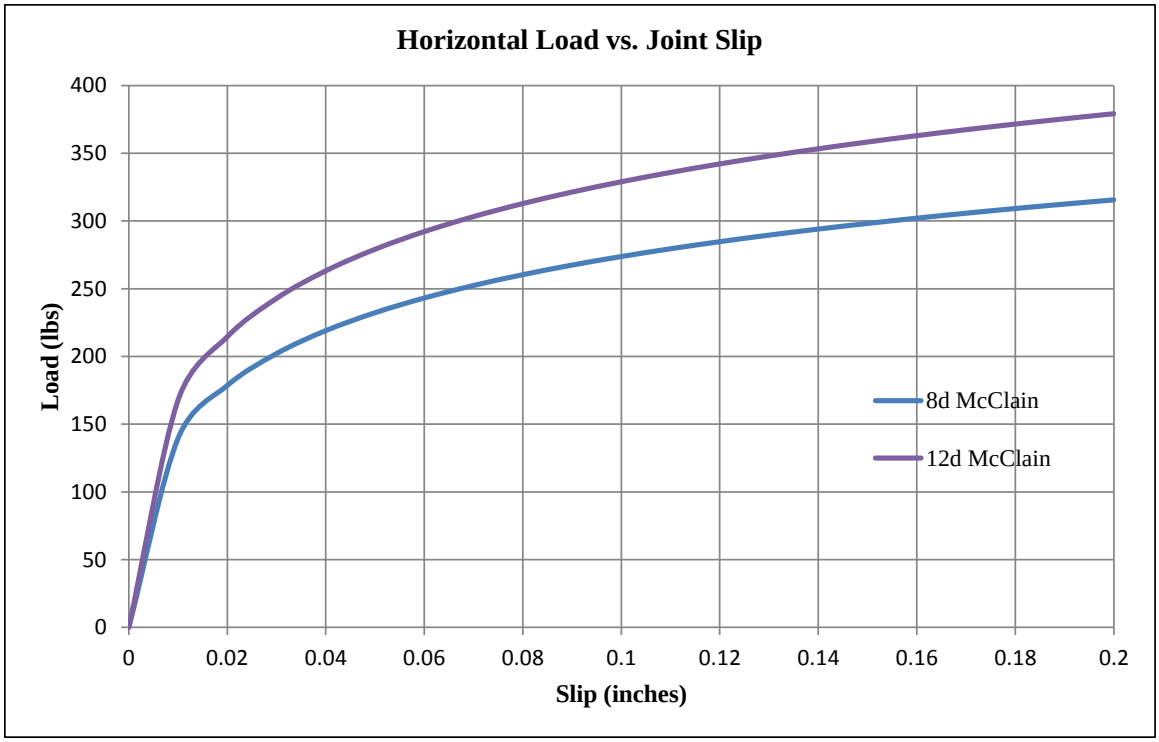

Figure 5.33 Plots of the nail load-slip data used for the shore models in Abaqus

5.2.6 Geometric Nonlinearity

Second-order effects, which capture changes in geometry of a structure during loading, can significantly impact the results in any type of analysis. Due to the large amount of lateral displacement imposed on shores 6 through 9, it was vital to understand the impact of second-order moments in the analyses. Abaqus CAE 6.11 (2) allows the user to specify the inclusion of the effects of geometric nonlinearity by the simple click of a button. However, preliminary trials for running the shore analyses with the incorporation of geometric nonlinearity revealed that convergence was not achievable.

As a result, a study was conducted to investigate the differences between linear and nonlinear analysis on a column with loading and boundary conditions similar to those experienced by a post in a laterally loaded shore. The column studied was from a PLP shore, which possessed a simpler geometry than the LP shores, making the loading and boundary conditions easier to approximate and more trustworthy. The column was assigned a modulus of elasticity of 1,700 ksi, the published value for Southern Yellow

Pine No. 1 from the NDS 2005. Using Eq. 2-3 from the NDS 2005, an approximate nail stiffness was computed based on an imaginary line connecting the origin to the intersection of the McLain and NDS curves for 8d nails (Figure 5.34). The NDS curve was offset from the origin by a value of 0.05 times the diameter of an 8d common nail (0.0066 inches).

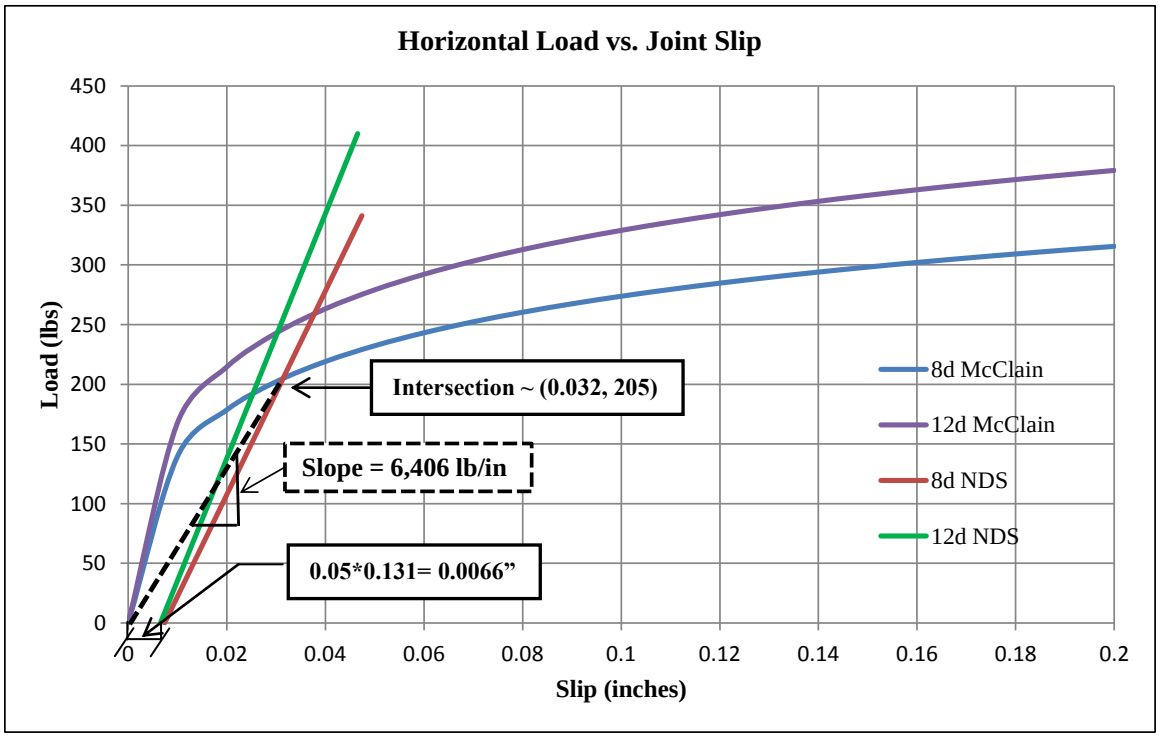

Figure 5.34 Plot showing the approximate slope used for the nail stiffness in the geometric nonlinearity study

Once the nail stiffness for an individual nail was determined, the nail groups in each plywood brace on the post were combined in an equivalent linear spring located at the centroid of each brace (Figure 5.35). The preliminary spring stiffness at each level was calculated by multiplying the number of nails at each level by the individual nail stiffness (6.406 k/in).

To account for the flexibility of the post at the other end of the braces, a new spring stiffness was computed at each level. As shown in Figure 5.35, this was accomplished by inserting a roller support at each level and applying a unit load while

keeping all other supports pinned. The resulting displacement was then divided into the applied force to generate the actual lateral stiffness at that level. As expected, the resulting spring stiffness at each level was much less than the original value.

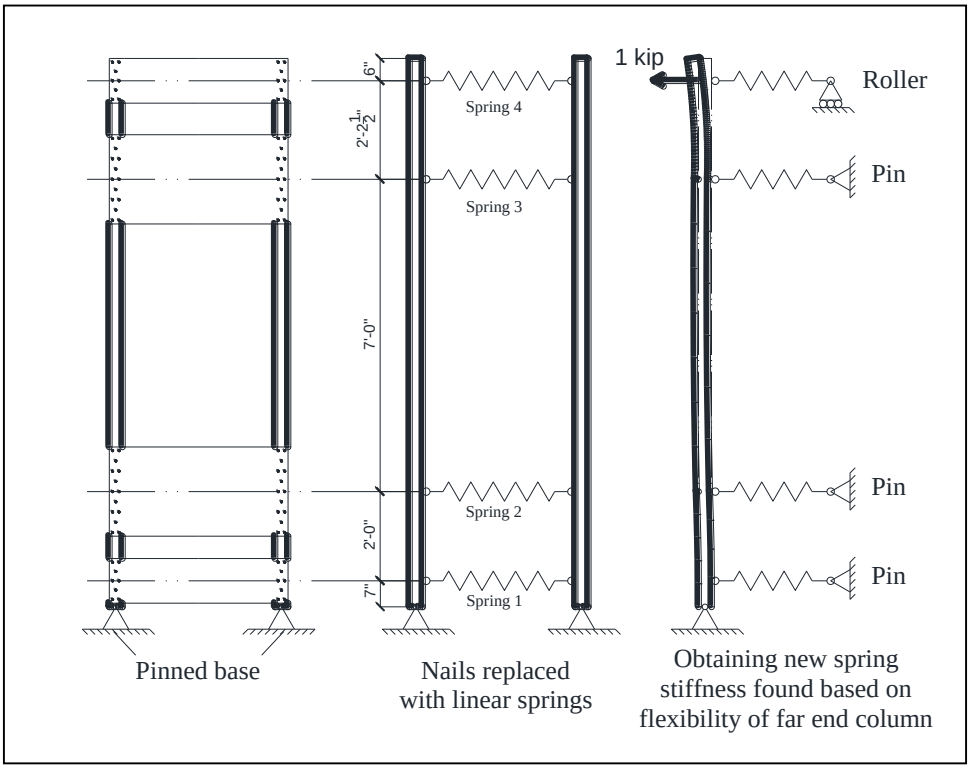

Figure 5.35 Schematic drawings of the process used to obtain nonlinearity in the shores

Table 5-6 Spring stiffness accounting for the flexural stiffness of the restraining column

Spring	Number of Nails	Stiffness	Total Stiffness (including column flexural stiffness)
4 (Top)	8	51.25	4.62
3	14	89.68	5.44
2	14	89.68	8.24
1 (Bot)	8	51.25	37.54

The new spring stiffness at each level shown in Table 5-6 was then input into the model for analysis. In an effort to simulate a loading scenario as close as possible to

those of the FSEL tests, two cases were carefully studied. The first case involved an initial lateral displacement at the top of the post of 6 inches. The second case consisted of an initial lateral displacement of 15 inches. Figure 5.36 shows drawings that represent the initial shape of the post prior to the application of vertical loading in each case.

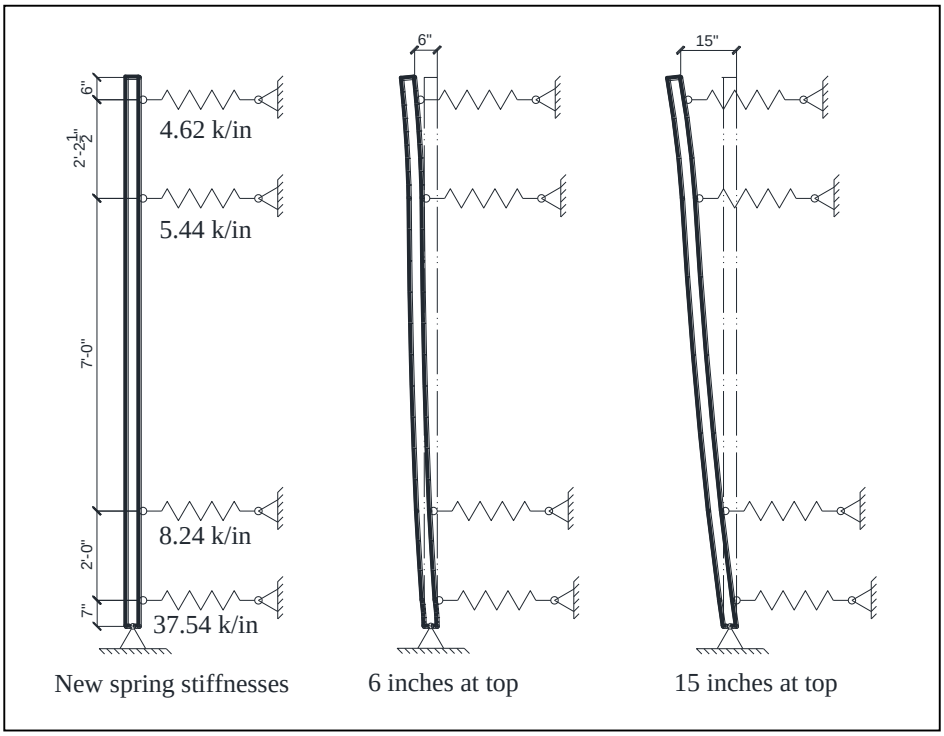

Figure 5.36 Schematic drawings of the column modeled to study the effects of geometric nonlinearity in the shores

In addition to the imposed initial displacement, two different boundary conditions were placed at the top of the post to compare their results. The actual boundary condition at the top of the posts in each shore is difficult to model without the framing members, so one case involved a free end at the top (where the top end of the post could freely move in any direction during loading) while the other involved a fixed end (where the initial position of the post was held fixed throughout the analysis). Figure 5.37 shows the bending moment diagrams about the x-axis for the first case studied.

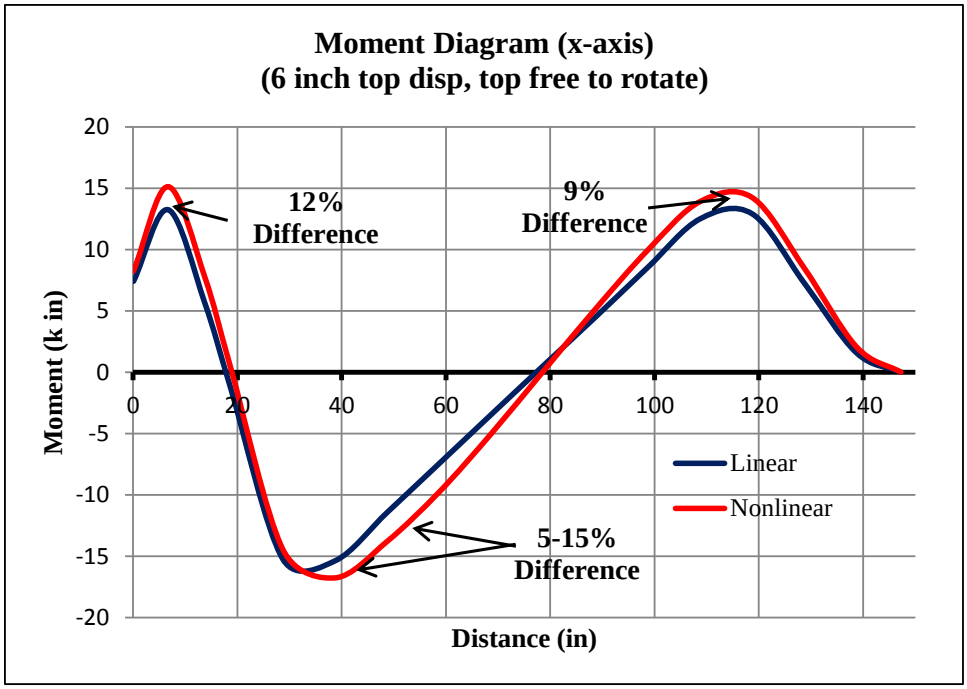

Figure 5.37 Comparison of first and second-order moment diagrams for a PLP post subjected to 6 inches of lateral displacement with the top end free

Comparison of the linear and nonlinear results revealed that the local peak moments were underestimated by the first-order analysis. Additionally, there was substantial difference in the first and second-order moments in the middle portion of the post. Of course, percent differences near a value of zero moment would be extremely high, thus the most critical regions involved the peak regions. Fortunately, however, the profile of the moment diagrams agreed quite well.

It is important to note that this study represents the worst case scenario for second-order moment effects. First of all, as verified by the load-displacement plots from the FSEL tests for each shore, 60 kips was the maximum load reached before the response became nonlinear (upper limit of the linear elastic range). Thus, assuming equal load distribution, 15 kips would be the approximate load experienced by each post. Actually, several of the load-displacement plots indicated the end of the linear elastic range was closer to 50 kips. Secondly, the top end of each post during the tests involving lateral loads was held in a fixed position throughout the loading sequence.

Figure 5.38 shows the results from an analysis conducted in which the top end of the post was held at a constant lateral displacement of 6 inches throughout the application of vertical load.

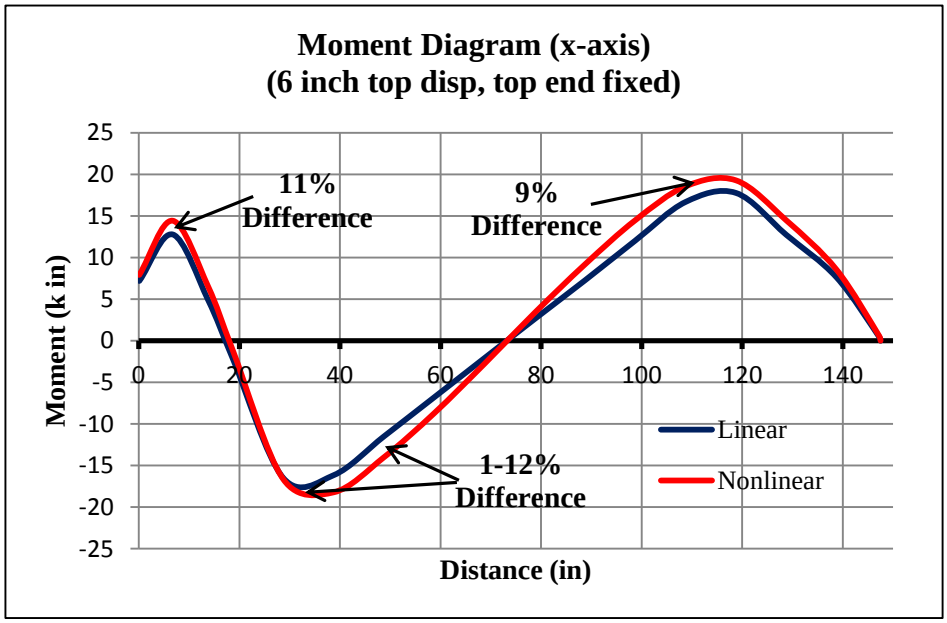

Figure 5.38 Comparison of first and second order moment diagrams for a PLP post subjected to 6 inches of lateral displacement with the top end fixed

From the moment diagrams shown above, it can be seen that the percent difference between the first and second-order curves decreased slightly when the top end of the post remained fixed throughout the loading process. It was believed that this particular loading scenario best represented those of the FSEL tests.

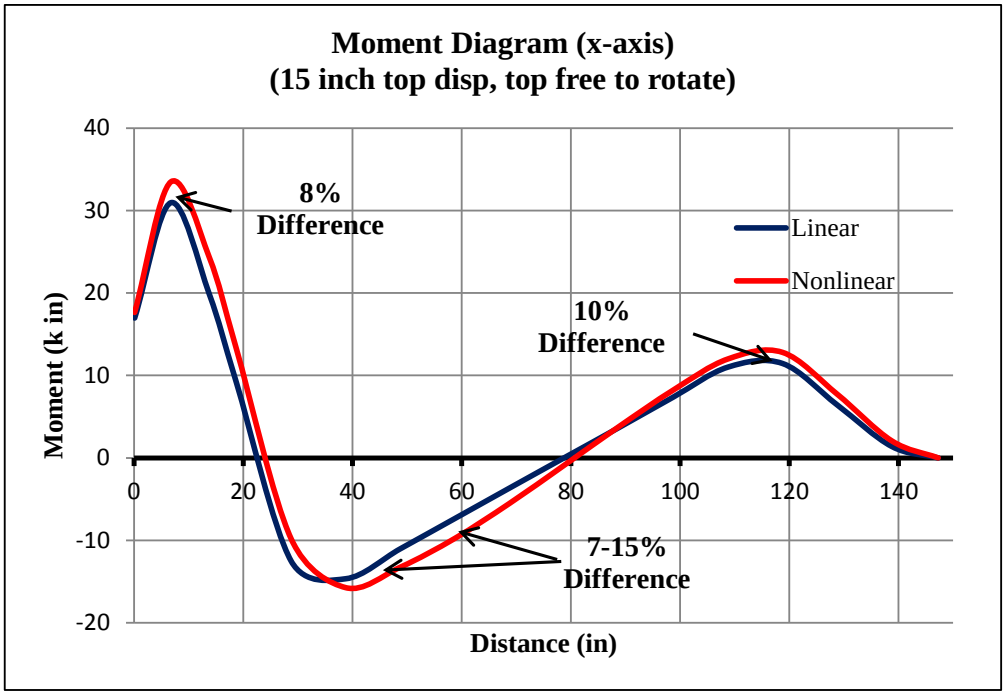

Figure 5.39 Comparison of first and second order moment diagrams for a PLP post subjected to 15 inches of lateral displacement with the top end free

Like the comparison shown for the 6 inch lateral displacement case, the overall shape of the moment diagram is roughly equal for the linear and nonlinear analyses. The maximum differences occur at the peak locations and in the middle of the post. Although the imposed lateral displacement at the top of the post was over twice that of the previous case, the percent differences were similar. Again, these results represent the absolute worst case scenario. In fact, of the two shores subjected to 15 inches of lateral displacement in the FSEL tests, the maximum total vertical load applied after this point was 8 kips. As such, each post experienced roughly 2 kips of additional vertical force.

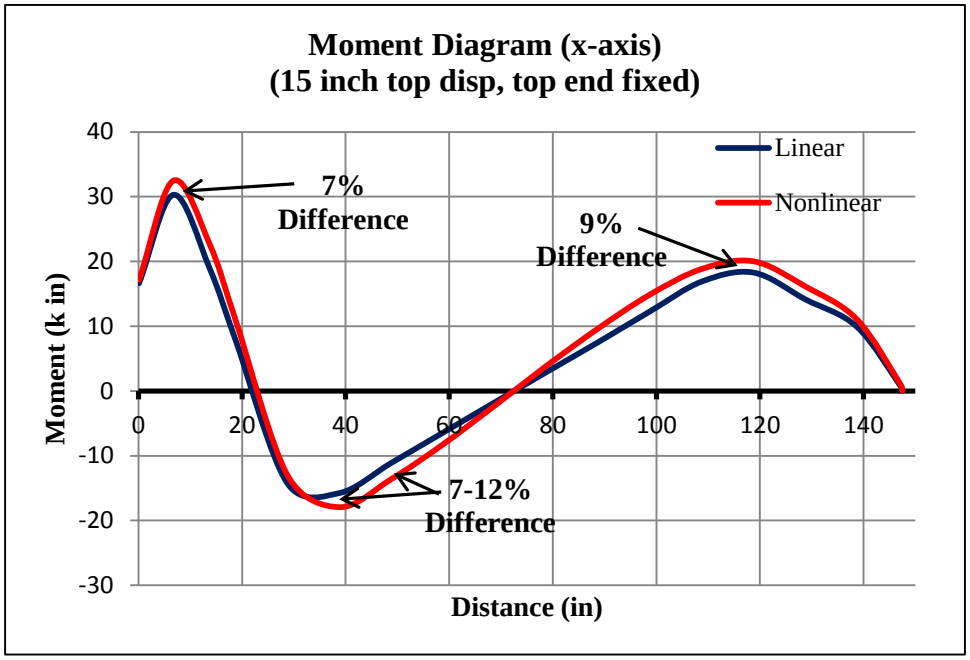

Figure 5.40 Comparison of first and second order moment diagrams for a PLP post subjected to 15 inches of lateral displacement with the top end fixed

The plots shown above confirm that whether for a 6 inch or 15 inch initial lateral displacement, the profile of the moment diagrams for the posts were similar for the linear and nonlinear cases. In conclusion, for loads near the upper end of the linear elastic range, bending moment trends remained the same in the posts for the shores and second-order moments ranged from 1 to 12 percent higher than those computed from first-order analyses.

5.2.7 Assembly of Shore Models

Assembly of the shore models was accomplished by taking all of the aspects discussed in this chapter into account. All shore models were assembled according to the as-built schematic drawings provided in McCord (13). Elevations are shown next to the model assemblies in Figures 5.41 and 5.42.

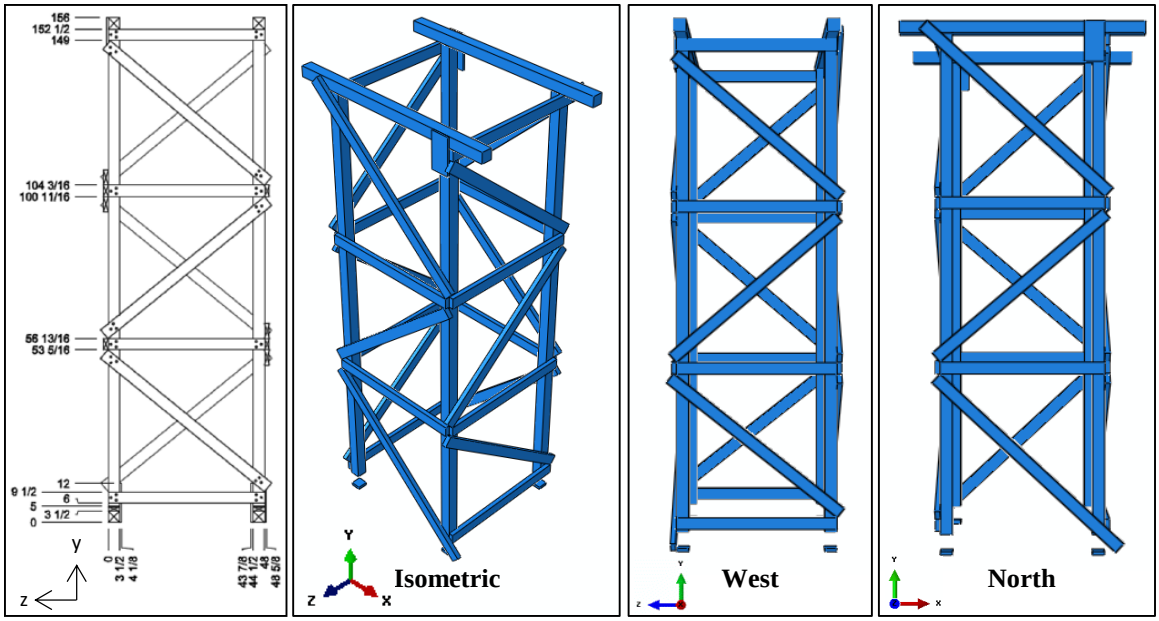

Figure 5.41 LP shore as-built drawing along with Abaqus snapshots

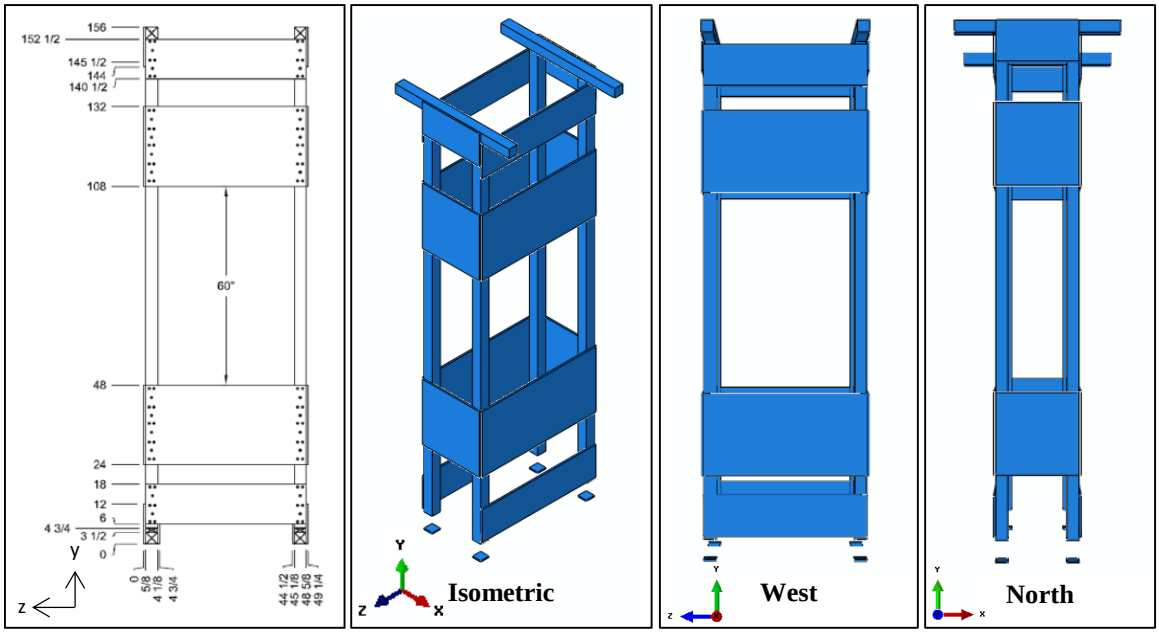

Figure 5.42 PLP shore as-built drawing along with Abaqus snapshots

All the shores modeled in Abaqus contained Projection Cartesian connector elements with nonlinear elasticity defined per the curves shown in Figure 5.33. Joints

involving plywood to 4x4 members contained 8d nails while all other joints used 12d nails.

Each investigation described in this chapter—the model verification study, the determination of an appropriate nail-slip curve, and the effects of second-order moments—contributed to the success of modeling the shores. The results from the finite element analyses performed on the shore models are presented in the next chapter.

CHAPTER 6

Model Results

This chapter presents a detailed summary of the results for each shore model in Abaqus CAE 6.11. The results from each finite element analysis served to provide valuable insight into the design modifications to be recommended in *Chapter 7*. These recommendations will be made based on the best estimate of the behavior of the shores in their respective linear elastic ranges. These analyses then forecast the pre-failure interactions among the vertical posts, the diagonal framing (for the LP shores) and the plywood braces (for the PLP shores), and the nailed connections, including their single shear behavior. For each shore, a comparison between the model results and those obtained from the FSEL tests is shown. Furthermore, several images of the deformed structure are provided for each shore model along with tables showing moments, displacements, forces, and stresses throughout each structure. The bending moment diagrams for the individual posts in each shore are also shown. These diagrams show only the moments about the axis which the first post failure occurred (the z-axis for the first 3 shores and x-axis for the rest). Each set of data is followed by a discussion of relevant observations. Additional output from Abaqus (including curvatures in the posts as well as stresses in the plywood braces) regarding the shores discussed in this chapter can be found in Appendix A.

As mentioned previously, only linear elastic response was considered in this thesis when comparing the model results to the FSEL results. For this reason, it was necessary to identify and justify the loading range that exhibited apparent linear elastic behavior for each test. The range varied for each shore, so some shore models were subjected to greater loads than others. All of the data shown in this chapter represents conditions within this specific range of linear elastic response. Figure 6.1 illustrates the procedure for obtaining the linear elastic portion of the load-displacement curve from PLP Shore 1; a similar process was used for the other shores. Moreover, in each curve was adjusted so

that the linear extension of the elastic slope would intersect the origin. This permitted better visual comparison between the FSEL and Abaqus curves.

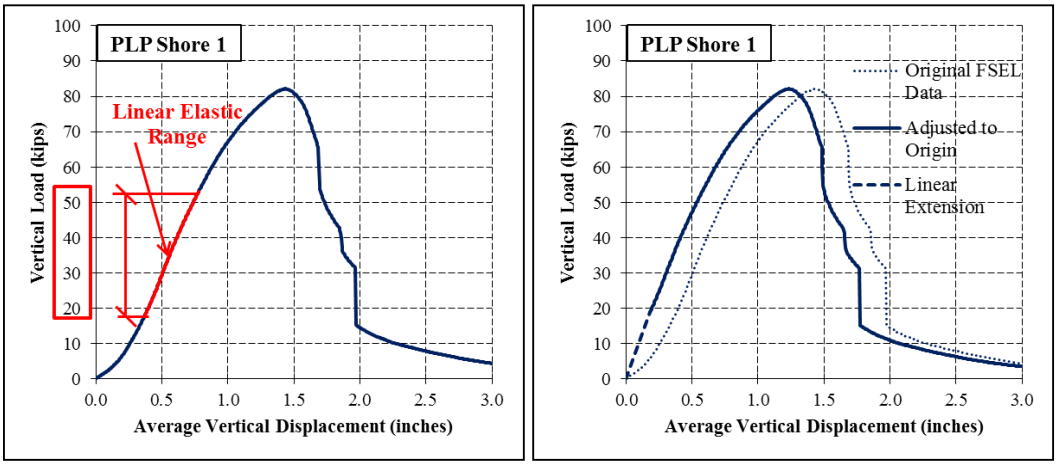

Figure 6.1 Example of the region of linear elasticity considered exclusively for the purpose of modeling and analyzing each shore

In Figure 6.1, the lower limit of the linear elastic range (around 18 kips) represents the end of the transition zone as the structure settles. At the upper limit (around 52 kips), inelastic behavior begins in the wood as well as nonlinearity in the connections.

Data computed in Abaqus and reported in this chapter was taken at specific locations in each shore model. Figure 6.2 contains schematic elevations of each shore type investigated and shows the locations where axial stresses, axial forces, and moments were computed. A plan view of the PLP and LP shores is provided in Figure 6.3 which shows the nodal locations where axial stresses and vertical displacements were computed.

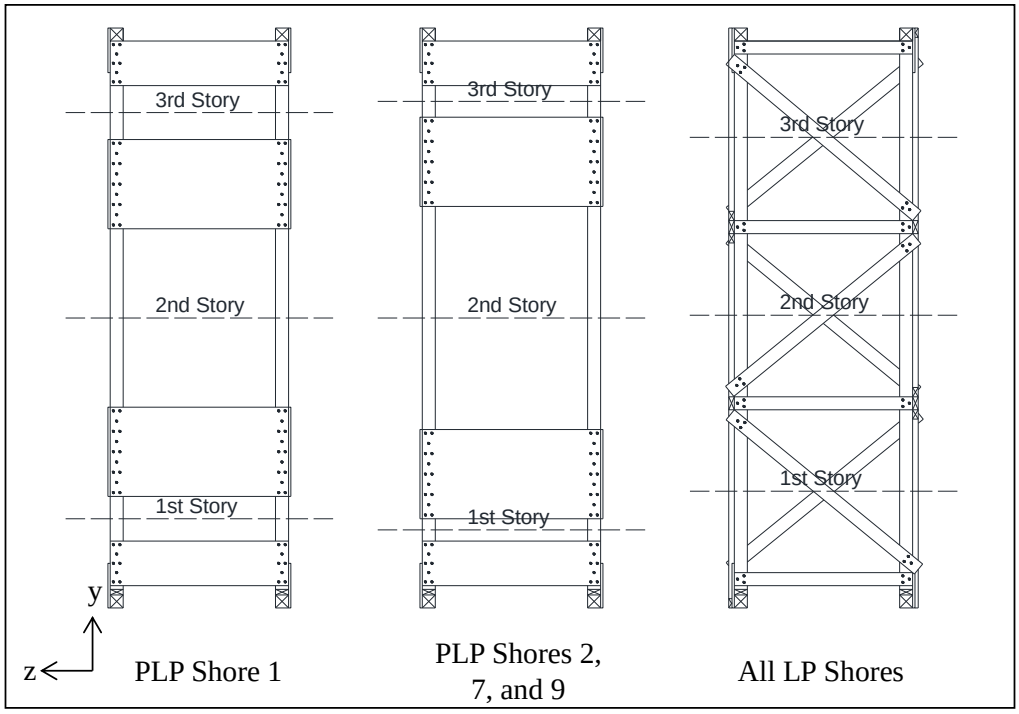

Figure 6.2 Elevation views of PLP and LP shores showing the locations where axial forces and moments were extracted from Abaqus

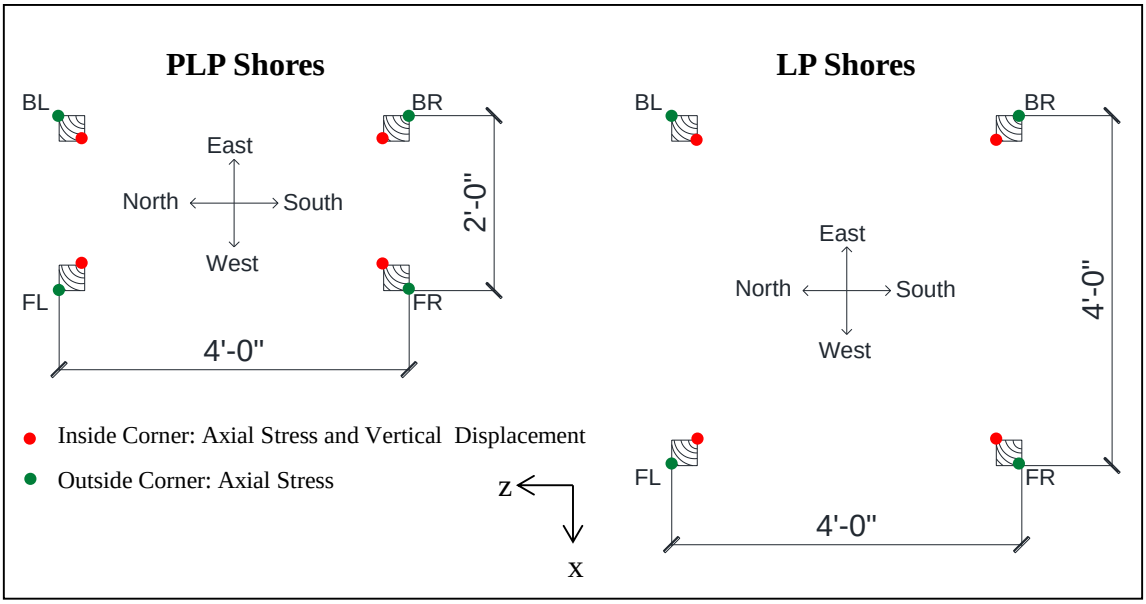

Figure 6.3 Plan view of PLP and LP shores showing location of nodes where axial stress and vertical displacement were extracted from Abaqus

As shown in the schematic drawings in Figure 6.3, the axial stresses reported in the tables in this chapter were computed at the inside and outside corners of each post (red dots). The vertical displacement of each post was computed at the inside corner of each post, as denoted by the green dots.

A key difference between the FSEL test data and the Abaqus data worth mentioning is the location at which the displacements were taken. While the vertical displacements in the finite element models were computed and reported at the inside corner node of each post, the data from the string potentiometers in the FSEL tests recorded the vertical displacement at a distance offset several inches from this same corner point. The string potentiometers were attached to 12-inch long metal rods that were fastened to the posts. In light of the high levels of lateral displacement imposed on the shores in certain tests, it was speculated that the tops of each post could undergo significant rotation, thereby creating a potentially inaccurate reading for the actual vertical displacement of the post (Figure 6.4). However, after inspecting all of the deformed positions of the shores in the FSEL tests, it became quite clear that the posts only experienced rotation at their base (the string potentiometers were attached to the floor at this level, not to the posts). The top end of each post remained fixed against rotation.

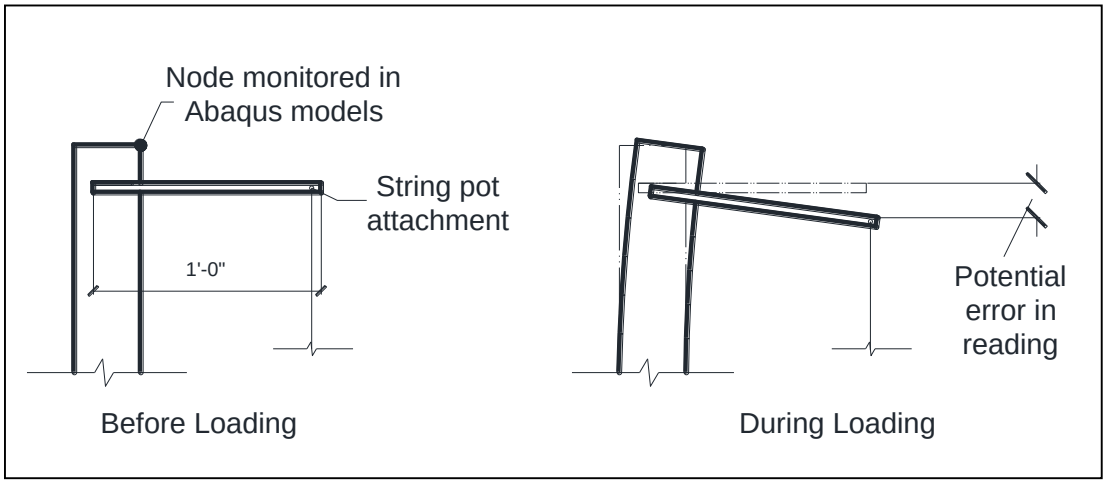

Figure 6.4 Schematic of the potential error in measuring post vertical displacement due to rotation of the top of the post

6.1 SHORE 1 MODEL RESULTS

Table 6-1 below presents the details pertaining to the loading scenario investigated as well as the material and connector data input in the model for Shore 1.

Table 6-1 Details for the modeling of Shore 1

PLP Shore 1				
Load Scenario	[A] Vertical Only			
Connector Elements	Projection Cartesian, 8d nails			
Constraints	Distributing Coupling, R = 3			
Model Input	**FL Post**	**FR Post**	**BL Post**	**BR Post**
Modulus of Elasticity (ksi)	682	788*	942	741

*Material data not available. The average MOE of the other 3 posts was used instead.

For the constraints, "R=3" signifies that a radius of influence of 3 inches was used for all connector elements. This same value was used for every shore model presented in this thesis.

To ascertain convergence of the solution for PLP Shore 1, several mesh layouts were examined. Several variables were monitored, such as vertical displacement, moment about the x-axis, axial force, and axial stress (Figure 6.5).

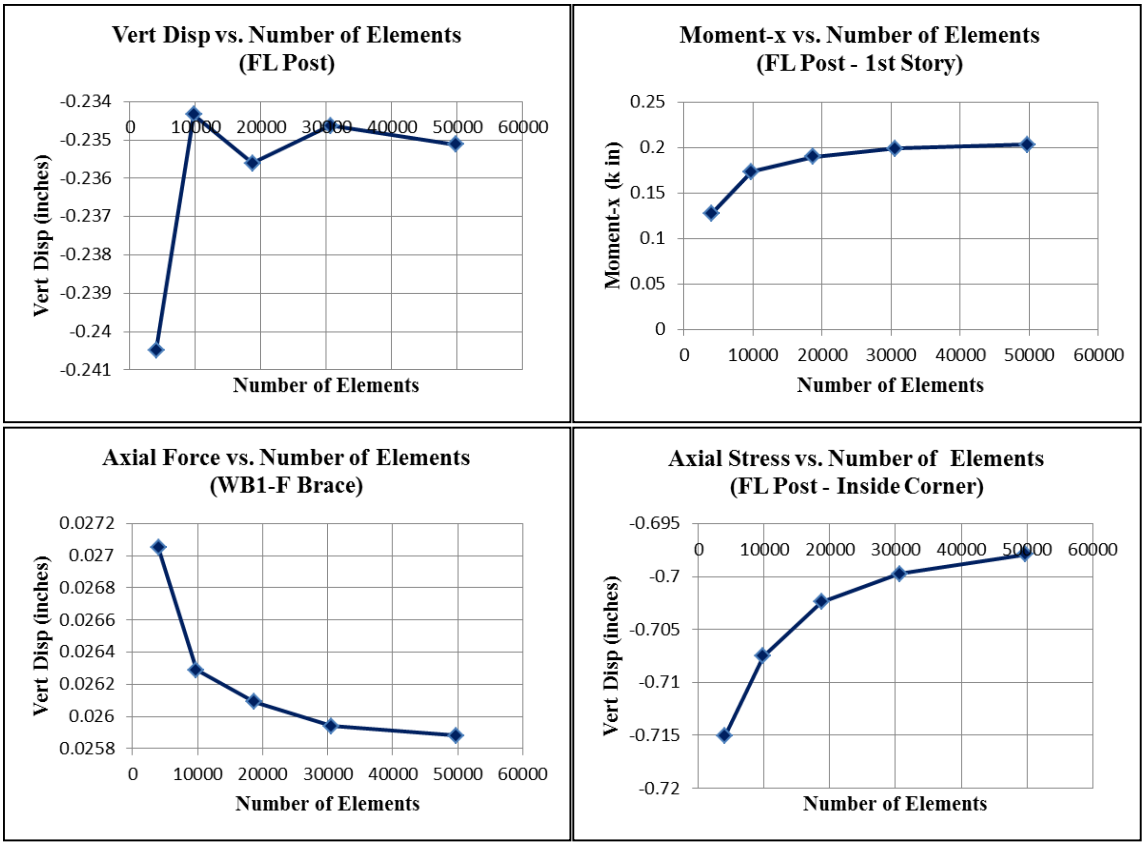

Figure 6.5 Plots from the results of PLP Shore 1 showing the convergence of the solution with a varying amount of elements

From the plots shown above in Figure 6.5, it was concluded that 50,000 linear hexahedral elements sufficed for a reliable solution. Therefore, this same mesh layout was used for all subsequent PLP shores. This same convergence study was performed on the LP shores; it is discussed later.

Figure 6.6 gives the bending moment diagrams along the length of each post in PLP Shore 1. The computed moments shown are about the z-axis since the first failure occurred about this axis in the FSEL test for this shore. The light blue shaded rectangles in each plot represent the locations of the plywood braces, and the red circle identifies the approximate location of bending failures.

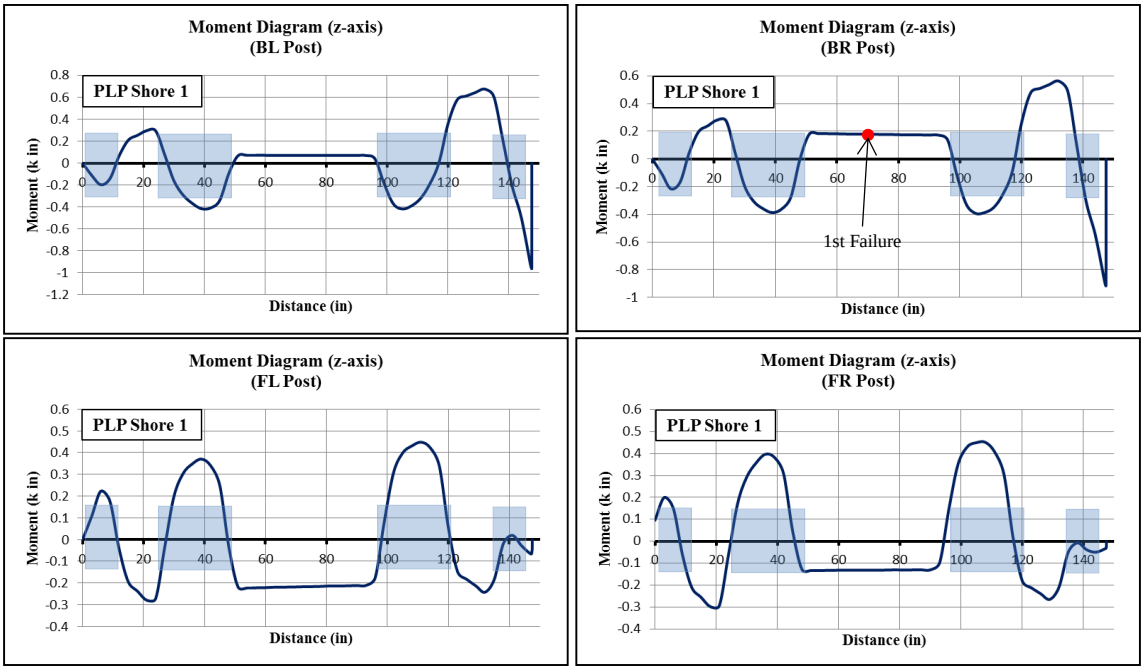

Figure 6.6 Bending moment diagrams obtained from Abaqus for PLP Shore 1

The bending moment diagrams shown above in Figure 6.6 reveal that each post experienced a similar magnitude and distribution of moments. The regions near the middle plywood braces reveal local maximum values for each post, with two posts failing near the first story joint. For the back-left (BL) and back-right (BR) posts, the absolute maximum moment occurred near the top, indicative of the high amount of rotational restraint provided at these ends. Interestingly, these same two posts failed at locations where the moment was relatively small.

Table 6-2 gives a summary of computational results from Abaqus for PLP Shore 1. In this table and in all subsequent tables for the remaining shores, the following notes apply. First, the reported axial stresses were taken at the inside and outside corners of each post, respectively. In other words, the first value of axial stress given for each post represents the inside corner, and the value below it represents the outside corner. Secondly, positive axial force and axial stress values denote tension, whereas negative values denote compression. Lastly, the resultant moments shown in each table were computed about the geometric centroid of each shore.

Table 6-2 Model results generated by Abaqus for Shore 1 posts

PLP Shore 1 (40 kips)							
Location	**Computed Quantity**	**FL Post**	**FR Post**	**BL Post**	**BR Post**	**Total Axial Force**	**Resultant Moment**
Top of Post	Displacement (in)	0.2351	0.2323	0.2294	0.2345	----	----
1st Story	Axial Stress (ksi)	-0.6948	-0.7557	-0.8442	-0.7371	----	----
		-0.8117	-0.8735	-0.9575	-0.8563	----	----
	Axial Force (k)	-9.227	-9.979	-11.04	-9.759	-40.005	----
	Moment-x (k in)	0.2032	-0.1878	0.1719	-0.2097	----	11.64
	Twisting Moment-y (k in)	-0.08678	0.1195	0.1118	-0.07319	----	0.0001364
	Moment-z (k in)	-0.2573	-0.2755	0.2727	0.2593	----	16.28
2nd Story	Axial Stress (ksi)	-0.7031	-0.7818	-0.8785	-0.7503	----	----
		-0.8006	-0.8492	-0.9259	-0.8413	----	----
	Axial Force (k)	-9.21	-9.99	-11.05	-9.747	-39.997	----
	Moment-x (k in)	0.167	-0.1351	0.1173	-0.1796	----	11.64
	Twisting Moment-y (k in)	-0.1102	0.1411	0.13	-0.09261	----	0.001057
	Moment-z (k in)	-0.2161	-0.1315	0.07037	0.1778	----	16.29
3rd Story	Axial Stress (ksi)	-0.6633	-0.7195	-0.7505	-0.6628	----	----
		-0.8448	-0.9143	-1.049	-0.9263	----	----
	Axial Force (k)	-9.236	-10.01	-11.02	-9.732	-39.998	----
	Moment-x (k in)	0.544	-0.5707	0.5826	-0.5442	----	11.63
	Twisting Moment-y (k in)	-0.05895	0.08804	0.06942	-0.02854	----	0.001283
	Moment-z (k in)	-0.2083	-0.2365	0.6407	0.5342	----	16.25

Per Table 6-2, the difference in values of axial stress at opposite corners in each post indicates the presence of bending at each story. All computed axial stresses were compressive, as expected in the case of a specimen subjected to vertical load only. The back-left (BL) post, which had the highest measured modulus of elasticity, had the highest axial stress at each story. It also carried the most amount of axial force at each story and exhibited the least amount of overall vertical displacement. On the contrary, the post with the lowest recorded modulus of elasticity, the front-left (FL) post, had the lowest axial stress and axial load at each story while yielding the highest vertical displacement.

None of the computed moments were significant in magnitude. Moreover, the resultant moments about each orthogonal axis remained relatively low and hardly

changed from story to story. The fact that none of the resultant moments was large may have had to do with the small amount of spread in the moduli of elasticity for the posts.

Table 6-3 presents additional results from Abaqus concerning nail slip as well as axial and shear forces in the plywood braces. It should be noted that in-plane forces in the plywood braces were computed at a vertical cross-section midway through the member. For example, for a plywood brace that was 48 inches wide, the section cut was made at 24 inches.

Table 6-3 Additional model results generated by Abaqus for Shore 1

PLP Shore 1 (40 kips)			
Location	**Computed Quantity**	**Abaqus Results**	
1st Story Joint	**Nail slip (in)**	**y-direction**	**z-direction**
	WB1-F (Top Left)	0.0101	0.0029
	WB1-F (Bot Left)	0.00911	0.00152
1st Story Braces	**In-Plane Force**	**WB1-F**	**WB1-B**
	Axial (kips)	0.0259	0.02433
	Shear (kips)	0.00605	-0.00608
2nd Story Braces	**In-Plane Force**	**WB2-F**	**WB2-B**
	Axial (kips)	-0.0387	-0.0427
	Shear (kips)	0.00257	-0.00139

Examination of Table 6-3 shows that at the first story joint the nails experienced hardly any slip. Both the horizontal and vertical components of nail slip were quite small, suggesting that nail slip was trivial for this test. This says nothing about the importance of the nails in maintaining overall stability of the structure, however.

As for the plywood braces, no significant axial or shear forces were observed from the model output. It would appear as if the braces in this test simply moved downward with the posts without any significant resistance to overall shore deformation. On the other hand, the plywood braces may have contributed a notable amount to the overall stability of the shore.

Figure 6.7 gives the comparison for each post between the vertical load-displacement plots obtained from the laboratory test and computed from Abaqus.

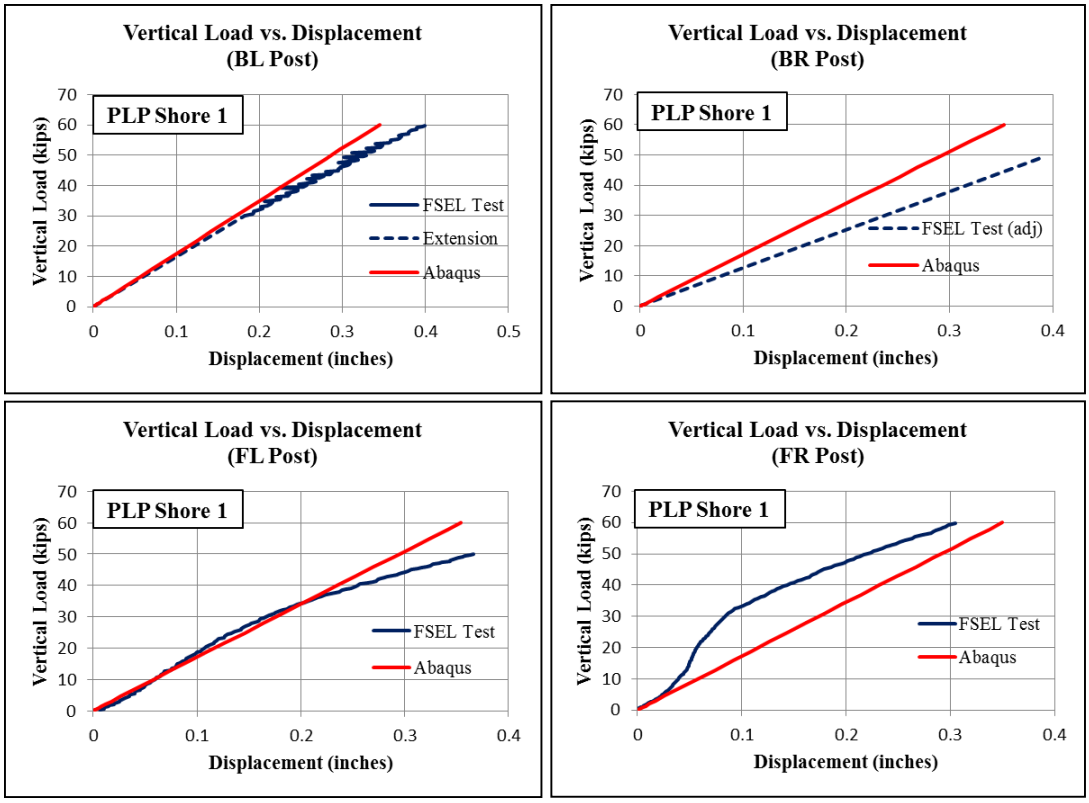

Figure 6.7 Plot comparisons between model results and laboratory tests for Shore 1

According to the plots in Figure 6.7, the Abaqus model tended to over-predict the axial response for each post. From the plot for the front-right (FR) post from the FSEL test, it appears that the string potentiometer became stuck during the early stages of loading and then was released. This is most likely the reason for the high initial slope shown by the curve between 0 and 0.1 inches of vertical displacement. Once the curve transitioned into the linear elastic range for the post, it can be easily seen that the slope of the Abaqus model curve slightly exceeded that of the FSEL test, just like the other three plots.

Figure 6.8 shows contour plots of the computed magnitudes of vertical (global y-direction) stresses present in PLP Shore 1 at the end of loading. The legend to the left of the plots indicates the ranges of stress (ksi) that correspond to each color. Additional data concerning the stresses in some of the plywood braces can be found in Appendix A.

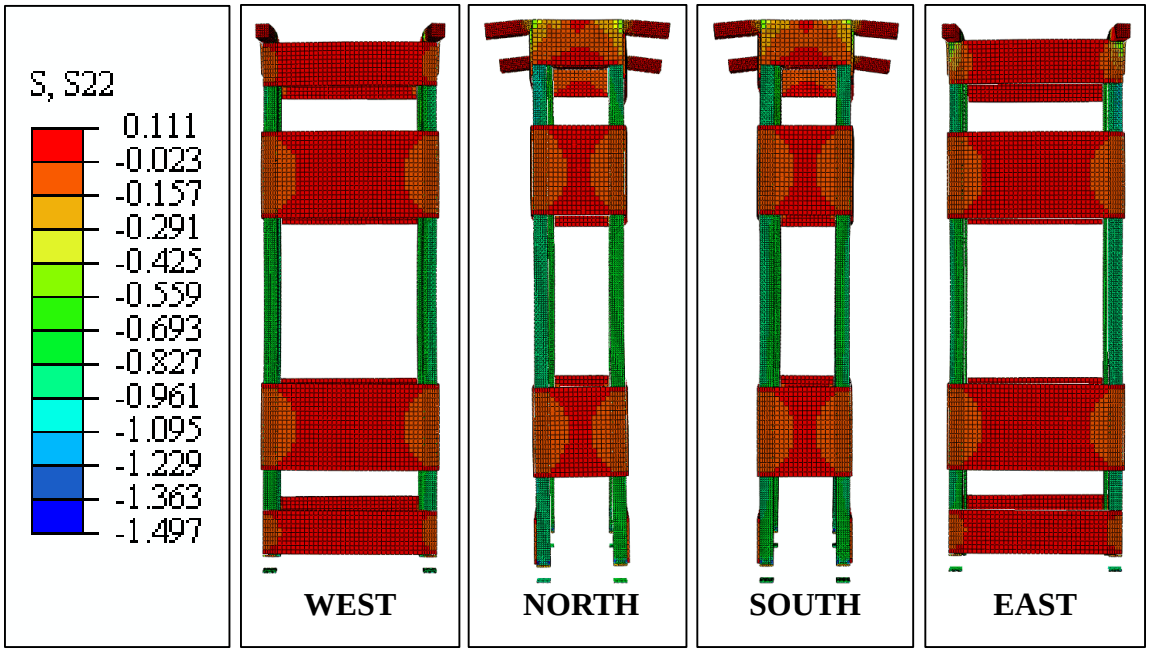

Figure 6.8 Contour plots showing the deformed shape and vertical stress distribution for Shore 1

The contour plots shown in Figure 6.8 predict that the posts were subjected to the highest values of axial stress, as revealed by the shades of green and blue in these members. These plots also confirm that the plywood braces experienced very small amounts of stress, although the orange regions near the nailed joints indicate that the nails underwent higher stress (and hence, did more work) than the plywood members.

6.2 SHORE 2 MODEL RESULTS

Table 6-4 below presents the details pertaining to the loading scenario investigated as well as the material and connector data input in the model for Shore 2.

Table 6-4 Details for the modeling of Shore 2

PLP Shore 2				
Load Scenario	[A] Vertical Only			
Connector Elements	Projection Cartesian, 8d nails			
Constraints	Distributing Coupling, R = 3			
Model Input	**FL Post**	**FR Post**	**BL Post**	**BR Post**
Modulus of Elasticity (ksi)	673	1725	767	876

The bending moment diagrams for each post from PLP Shore 2 are shown in Figure 6.9. Like PLP Shore 1, these moments were computed about the z-axis of the shore since the first post failure occurred about this axis in the laboratory test.

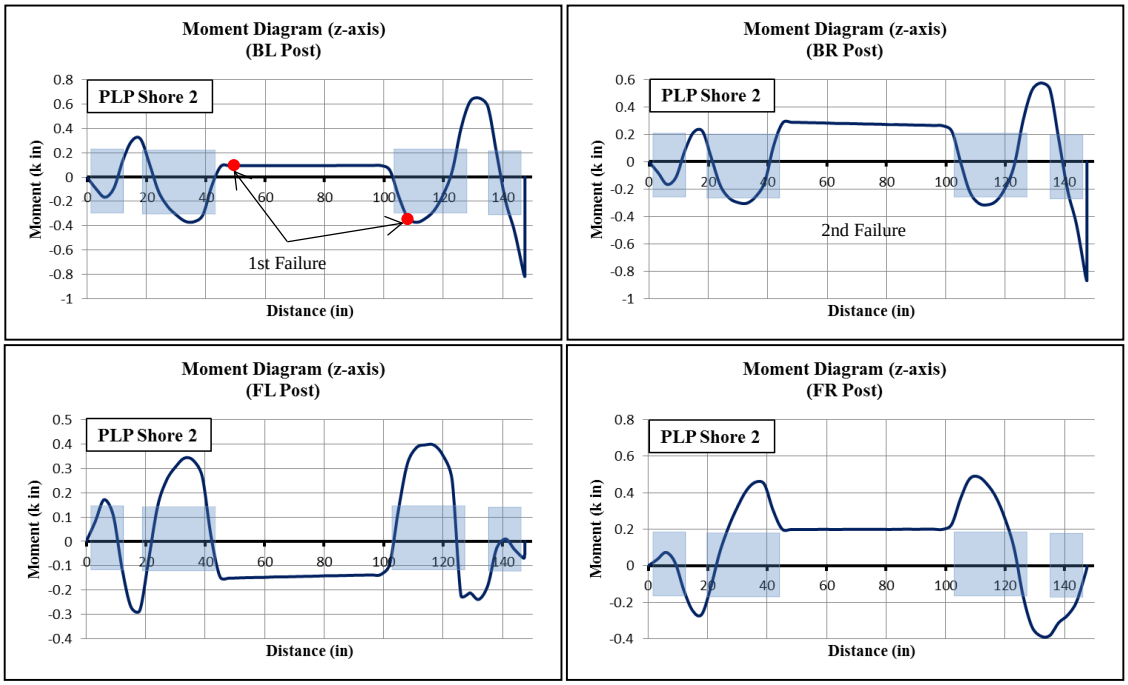

Figure 6.9 Bending moment diagrams obtained from Abaqus for PLP Shore 2

Like the moment diagrams for PLP Shore 1, those given by the figure above for PLP Shore 2 exhibit fairly similar behavior for each post. Notice how the intermediate regions of protrusion (like "hills" or "valleys") in these diagrams are a bit further spread apart than those of PLP Shore 1, due to the increased separation between the plywood braces for this shore (60 inches compared to 48 inches for Shore 1). Again, the absolute maximum moments occurred near the top end of the two posts on the back-side of the shore (BL and BR). As will be become clear when compared to the shores involving lateral load, bending moments for PLP shores subjected to purely vertical load are not significant in the linear elastic region.

Table 6-5 Model results generated by Abaqus for Shore 2 posts

PLP Shore 2 (40 kips)							
Location	**Computed Quantity**	**FL Post**	**FR Post**	**BL Post**	**BR Post**	**Total Axial Force**	**Resultant Moment**
Top of Post	Displacement (in)	0.2148	-0.1968	-0.2136	-0.2105	----	----
1st Story	Axial Stress (ksi)	-0.6118	-1.006	-0.6677	-0.7395	----	----
		-0.7571	-1.092	-0.8148	-0.851	----	----
	Axial Force (k)	-8.367	-12.84	-9.064	-9.726	-39.997	----
	Moment-x (k in)	0.2763	-0.06818	0.2527	-0.1992	----	-114
	Twisting Moment-y (k in)	-0.09892	0.2635	0.07512	-0.09329	----	0.0001964
	Moment-z (k in)	-0.2975	-0.2708	0.3257	0.2402	----	-24.78
2nd Story	Axial Stress (ksi)	-0.6383	-1.09	-0.714	-0.7421	----	----
		-0.7244	-1.014	-0.7695	-0.8388	----	----
	Axial Force (k)	-8.347	-12.88	-9.086	-9.683	-39.996	----
	Moment-x (k in)	0.1944	0.0979	0.1269	-0.103	----	-113.9
	Twisting Moment-y (k in)	-0.1041	0.2731	0.08981	-0.1193	----	0.001083
	Moment-z (k in)	-0.1431	0.1995	0.09399	0.276	----	-24.81
3rd Story	Axial Stress (ksi)	-0.5781	-0.8975	-0.5877	-0.6414	----	----
		-0.79	-1.204	-0.8944	-0.9405	----	----
	Axial Force (k)	-8.374	-12.87	-9.074	-9.686	-40.004	----
	Moment-x (k in)	0.6632	-0.9082	0.6244	-0.675	----	-113.9
	Twisting Moment-y (k in)	-0.06482	0.1796	0.05938	-0.05167	----	0.001649
	Moment-z (k in)	-0.232	-0.3708	0.6427	0.562	----	-24.83

Like the axial stresses from Shore 1, the results for Shore 2 revealed strictly compressive stresses that varied somewhat across each post cross-section (Table 6-5). The front-right (FR) post for Shore 2 had a measured modulus of elasticity that was significantly higher than the other 3 posts. Consequently, this post carried a substantially greater amount of axial stress and axial load than the others, and also underwent the smallest amount of vertical displacement.

Interestingly, the results predict that Shore 2 had a significantly larger resultant moment about the x-axis than Shore 1. This is most likely due to the stark difference in values of the moduli of elasticity.

Table 6-6 Additional model results generated by Abaqus for Shore 2

PLP Shore 2 (40 kips)			
Location	**Computed Quantity**	**Abaqus Results**	
1st Story Joint	**Nail slip (in)**	**y-direction**	**z-direction**
	WB1-F (Top Left)	0.00909	0.0023
	WB1-F (Bot Left)	0.00864	0.00133
1st Story Braces	**In-Plane Force**	**WB1-F**	**WB1-B**
	Axial (kips)	0.0222	0.0289
	Shear (kips)	0.0136	-0.0131
2nd Story Braces	**In-Plane Force**	**WB2-F**	**WB2-B**
	Axial (kips)	-0.0677	-0.0563
	Shear (kips)	-0.0051	-0.0102

Per the computed data in Table 6-6, nail slip near the first story joint again remained insignificant for this test. In general, the nail slip values were similar to those given in PLP Shore 1, indicating that the differences in the spread of the moduli of elasticity for each test has no pertinent effect on the nail slip for a shore loaded exclusively with vertical load.

Although the second story plywood braces were subjected to compressive forces that were more than twice the tensile forces in the first story braces, the magnitude of each remained extremely low.

Figure 6.10 gives the comparison for each post between the vertical load-displacement plots obtained from the laboratory test and computed from Abaqus.

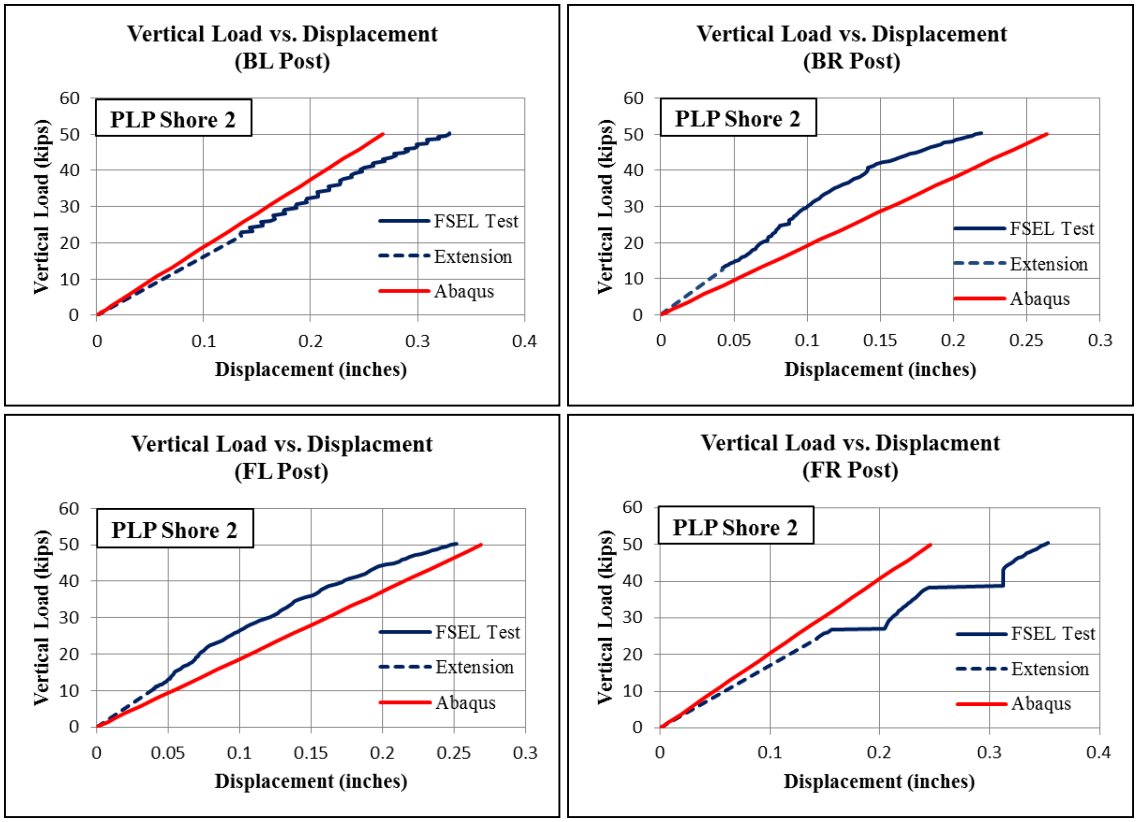

Figure 6.10 Plot comparisons between model results and laboratory tests for Shore 2

In general, the model exhibited good agreement with the laboratory results as shown in Figure 6.10. It appears that in this case, the string potentiometers attached to the back-right (BR) and front-left (FL) posts were stuck at the onset of loading. The gradual decrease in stiffness in these two plots results in a curve that fits rather well with the plots obtained from the computer output.

Figure 6.11 shows contour plots of the computed magnitudes of vertical (global y-direction) stresses present in PLP Shore 2 at the end of loading. The legend to the left of the plots indicates the ranges of stress (ksi) that correspond to each color. Additional data concerning the stresses in some of the plywood braces can be found in Appendix A.

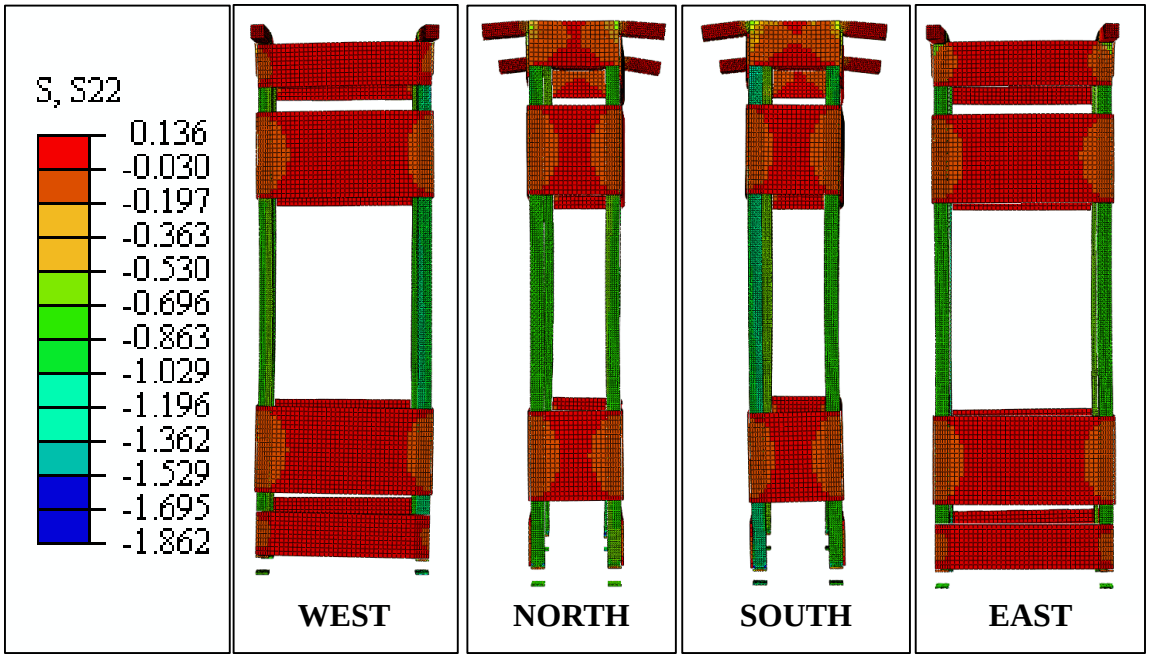

Figure 6.11 Contour plots showing the deformed shape and vertical stress distribution for Shore 2

6.3 SHORE 3 MODEL RESULTS

Table 6-7 below presents the details pertaining to the loading scenario investigated as well as the material and connector data input in the model for Shore 3.

Table 6-7 Details for the modeling of Shore 3

LP Shore 3				
Load Scenario	[A] Vertical Only			
Connector Elements	Projection Cartesian, 8d and 12d nails			
Constraints	Distributing Coupling, R = 3			
Model Input	**FL Post**	**FR Post**	**BL Post**	**BR Post**
Modulus of Elasticity (ksi)	1119	781	720	972

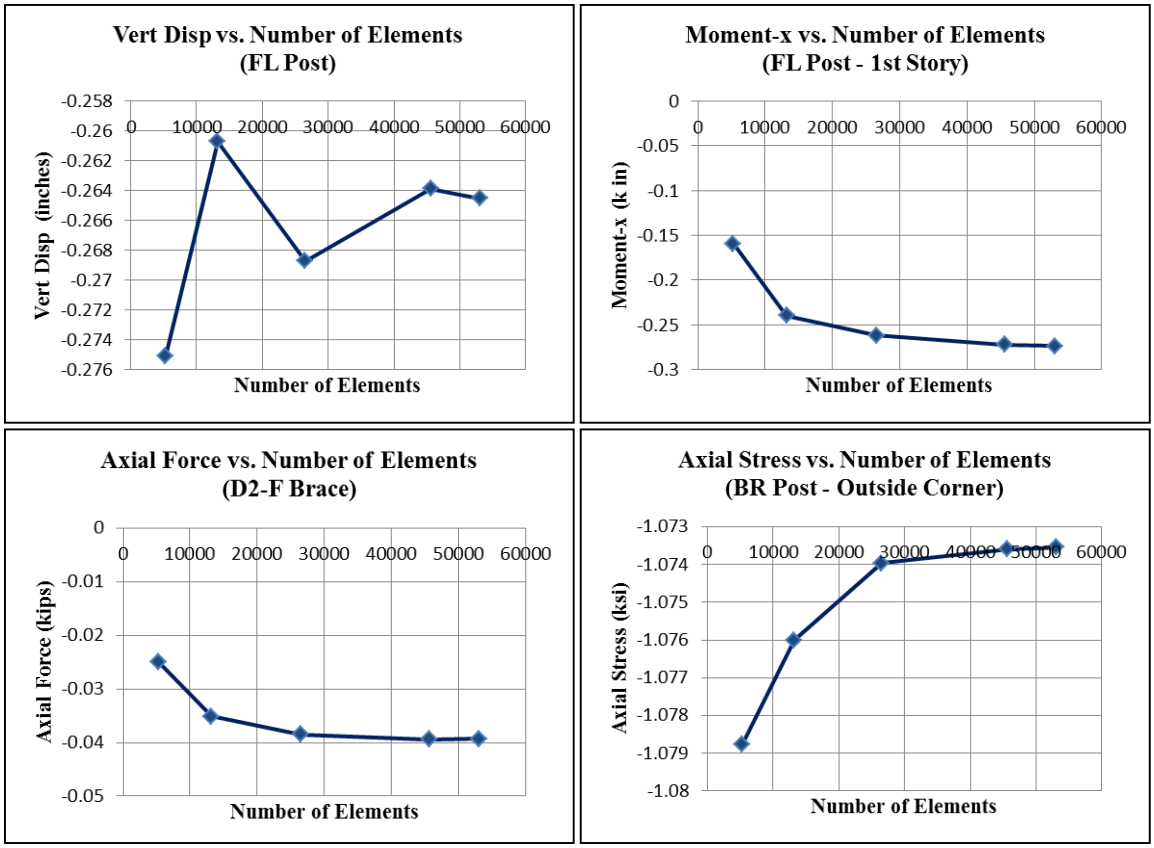

Figure 6.12 Plots from the results of LP Shore 3 showing the convergence of the solution with a varying amount of elements

Since LP Shore 3 was the first LP Shore modeled and analyzed, it set the precedent for the remaining 3 LP shore models as far as mesh layouts. Figure 6.12 confirms that roughly 53,000 linear hexahedral elements were needed to obtain a comfortable solution. Henceforth, this same mesh layout was utilized for the rest of the LP shore models.

The bending moment diagrams for each post from LP Shore 3 are shown in Figure 6.13. As in the case of PLP Shores 1 and 2, these moments were computed about the z-axis of the shore since the first post failure occurred about this axis in the laboratory test. The approximate locations of the horizontal 2x4 braces are indicated by the four lightly shaded rectangles in each plot.

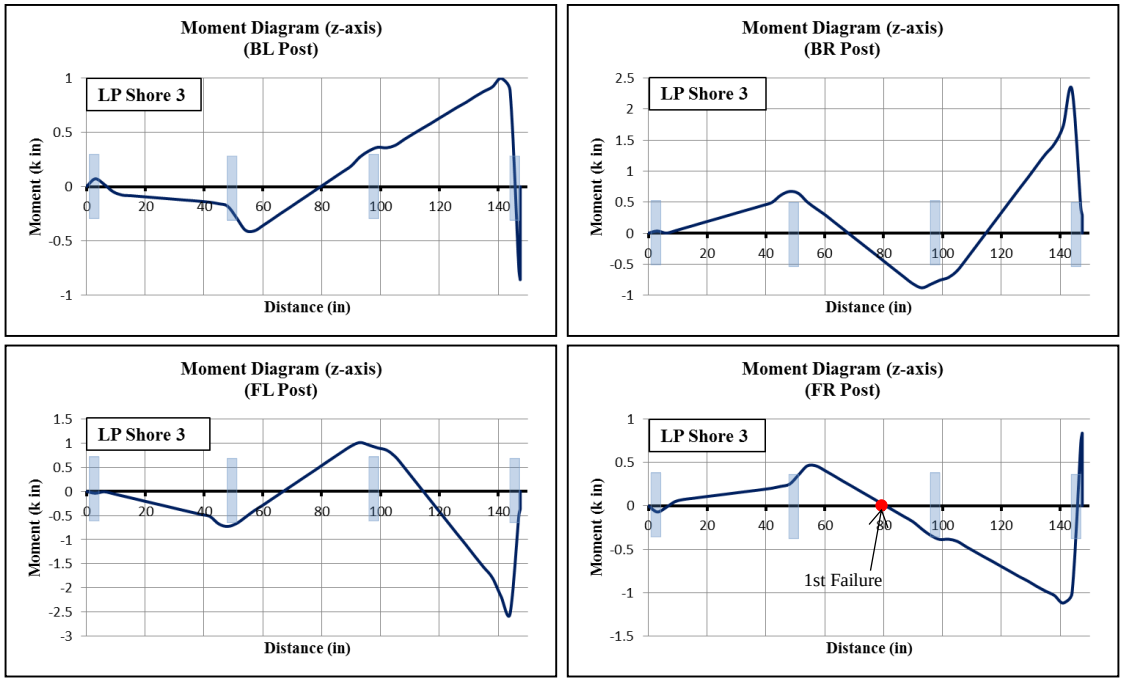

Figure 6.13 Bending moment diagrams obtained from Abaqus for LP Shore 3

Unlike PLP Shores 1 and 2, the profiles for the bending moments in each post of LP Shore 3 reveal a certain degree of variability. The local peak moments in the middle of the posts were about equal in magnitude to those that occurred at the top end of each post. It was speculated that due to the fewer amount of nails per joint in the posts for LP shores, the posts were allowed to bend more freely. The high number of points of inflection (points of zero moment) in each post indicates the presence of triple and quadruple curvature—that is, the posts switched bending directions several times. Notice also that each post has a point of inflection near mid-height of the shore (approx. 74 inches). It is also important to point out that this shore was subjected to 50 kips of total vertical load (10 kips greater than the previous two PLP shores), and yet the maximum moments in each post were less than those in the PLP posts.

As for failure locations, it is quite interesting that the first failure occurred near a point of zero moment (FR post). Looking back to the laboratory test results presented in *Chapter 4*, it is evident that knots were present at this failure location.

Table 6-8 Model results generated by Abaqus for Shore 3 posts

LP Shore 3 (50 kips)							
Location	**Computed Quantity**	**FL Post**	**FR Post**	**BL Post**	**BR Post**	**Total Axial Force**	**Resultant Moment**
Top of Post	Displacement (in)	0.2645	0.2731	0.2753	0.2681	----	----
1st Story	Axial Stress (ksi)	-1.148	-0.9529	-0.9076	-1.07	----	----
		-1.15	-0.9408	-0.9007	-1.073	----	----
	Axial Force (k)	-14.07	-11.6	-11.08	-13.13	-49.88	----
	Moment-x (k in)	-0.2736	-0.09239	0.08972	0.2457	----	9.334
	Twisting Moment-y (k in)	-0.2052	-0.1719	-0.1631	-0.1707	----	-3.7
	Moment-z (k in)	-0.277	0.1299	-0.1052	0.2574	----	-32.65
2nd Story	Axial Stress (ksi)	-1.198	-0.9703	-0.9235	-1.112	----	----
		-1.106	-0.9123	-0.8732	-1.038	----	----
	Axial Force (k)	-14.11	-11.53	-11	-13.17	-49.81	----
	Moment-x (k in)	-0.09412	0.09589	-0.09399	0.08498	----	9.284
	Twisting Moment-y (k in)	0.126	0.09467	0.08342	0.1087	----	5.272
	Moment-z (k in)	0.2775	0.1352	-0.1066	-0.2138	----	-32.63
3rd Story	Axial Stress (ksi)	-0.9936	-0.8392	-0.8023	-0.936	----	----
		-1.319	-1.042	-0.9927	-1.225	----	----
	Axial Force (k)	-14.16	-11.52	-10.99	-13.24	-49.91	----
	Moment-x (k in)	0.7629	-0.1115	0.095	-0.7257	----	8.884
	Twisting Moment-y (k in)	-0.1711	-0.2051	-0.1991	-0.1442	----	-4.403
	Moment-z (k in)	-0.6108	-0.7458	0.6724	0.4895	----	-32.64

As in the case for the PLP shores, all axial stresses computed for LP Shore 3 were compressive (Table 6-8). Interestingly, the stresses in the first story posts were nearly identical at opposite corners of each post. The differences between opposing corner stresses in each posts varied by increasing amounts in the second and third stories. Like the first 2 shore results presented (both PLP), the post with the largest measured modulus of elasticity in Shore 3, the front-left (FL) post, claimed the highest proportion of axial load and least amount of vertical displacement. Also, the post with the smallest measured modulus of elasticity, the back-left (BL) post, carried the smallest proportion of the total axial load and experienced the largest vertical displacement.

The summation of axial force in each post does not quite equal the applied axial load on the shore of 50 kips. Upon investigation, it was found that the axial forces in the

diagonal braces took care of the rest of the load, even though it was a relatively small amount.

The resultant twisting moments shown in the table are much higher than those given in the results for the first 2 PLP shores. One reason for this could be that the greater surface area afforded by the plywood joints helped to restrain twist much more effectively than the 2x4 braces in the LP shores. Overall, the resultant moments were rather low, which was likely a result of the small amount of spread among the various values of the modulus of elasticity for each post for LP Shore 3.

Table 6-9 Additional model results generated by Abaqus for Shore 3

LP Shore 3 (50 kips)					
Location	**Computed Quantity**	**Abaqus Results**			
1st Story Joint	**Nail slip (in)**	**y-direction**		**z-direction**	
	D1-F (Upper End)	0.00164		0.00434	
	D1-F (Lower End)	0.00353		0.00174	
1st Story Braces	**In-Plane Force**	**Front**	**Left**	**Back**	**Right**
	Axial (kips)	-0.103	0	-0.101	0
2nd Story Braces	**In-Plane Force**	**Front**	**Left**	**Back**	**Right**
	Axial (kips)	-0.0393	-0.106	-0.0357	-0.103
3rd Story Braces	**In-Plane Force**	**Front**	**Left**	**Back**	**Right**
	Axial (kips)	-0.0525	-0.0657	-0.0536	-0.0462

Per Table 6-9, the nail slip values were not substantial for this shore. In fact, the horizontal and vertical components of nail slip computed for LP Shore 3 were even smaller than those from PLP Shores 1 and 2.

All the diagonal braces in this shore were, as one would expect, in compression. In general, the axial forces in the braces for this LP shore were over three times greater than those in the plywood braces for the previous two PLP shores.

Figure 6.14 gives the comparison for each post between the vertical load-displacement plots obtained from the laboratory test and computed from Abaqus.

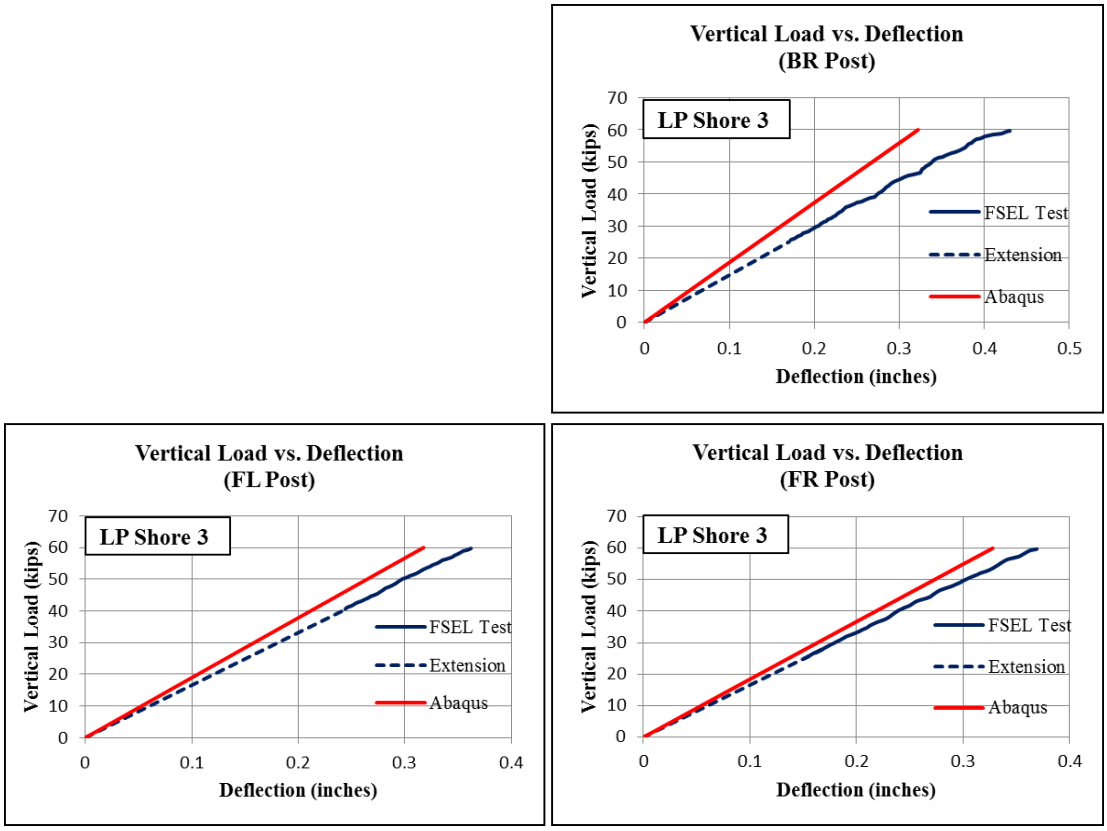

Figure 6.14 Plot comparisons between model results and laboratory tests for Shore 3

Since the string potentiometer attached to the back-left (BL) post for Specimen 3 gave bad readings throughout the test, it was not included as part of the results. However, the other 3 posts for Shore 3 demonstrated closer agreement with the laboratory results than those from the previous 2 shores.

Figure 6.15 shows contour plots of the computed magnitudes of vertical (global y-direction) stresses present in LP Shore 3 at the end of loading. The legend to the left of the plots indicates the ranges of stress (ksi) that correspond to each color.

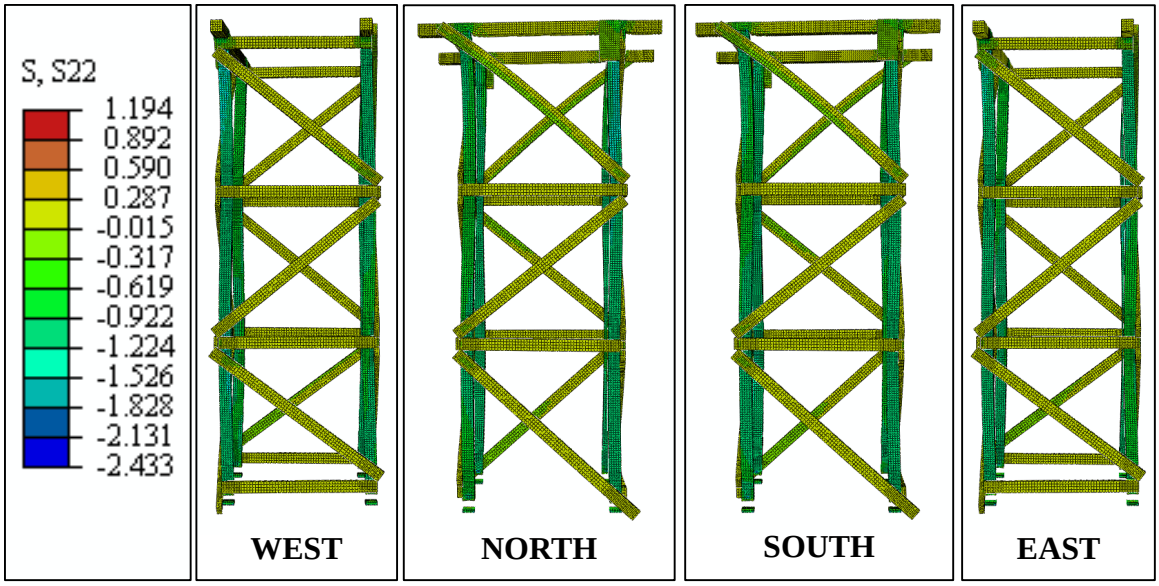

Figure 6.15 Contour plots showing the deformed shape and vertical stress distribution for Shore 3

6.4 SHORE 4 MODEL RESULTS

Table 6-10 below presents the details pertaining to the loading scenario investigated as well as the material and connector data input in the model for Shore 4.

Table 6-10 Details for the modeling of Shore 4

LP Shore 4				
Load Scenario	[A] Vertical Only			
Connector Elements	Projection Cartesian, 8d and 12d nails			
Constraints	Distributing Coupling, R = 3			
Model Input	**FL Post**	**FR Post**	**BL Post**	**BR Post**
Modulus of Elasticity (ksi)	1040	1456	1018*	558

*Material data not available. The average MOE of the other 3 posts was used instead.

The bending moment diagrams for each post from LP Shore 4 are shown in Figure 6.16. These moments were computed about the x-axis of the shore since the first post failure occurred about this axis in the laboratory test.

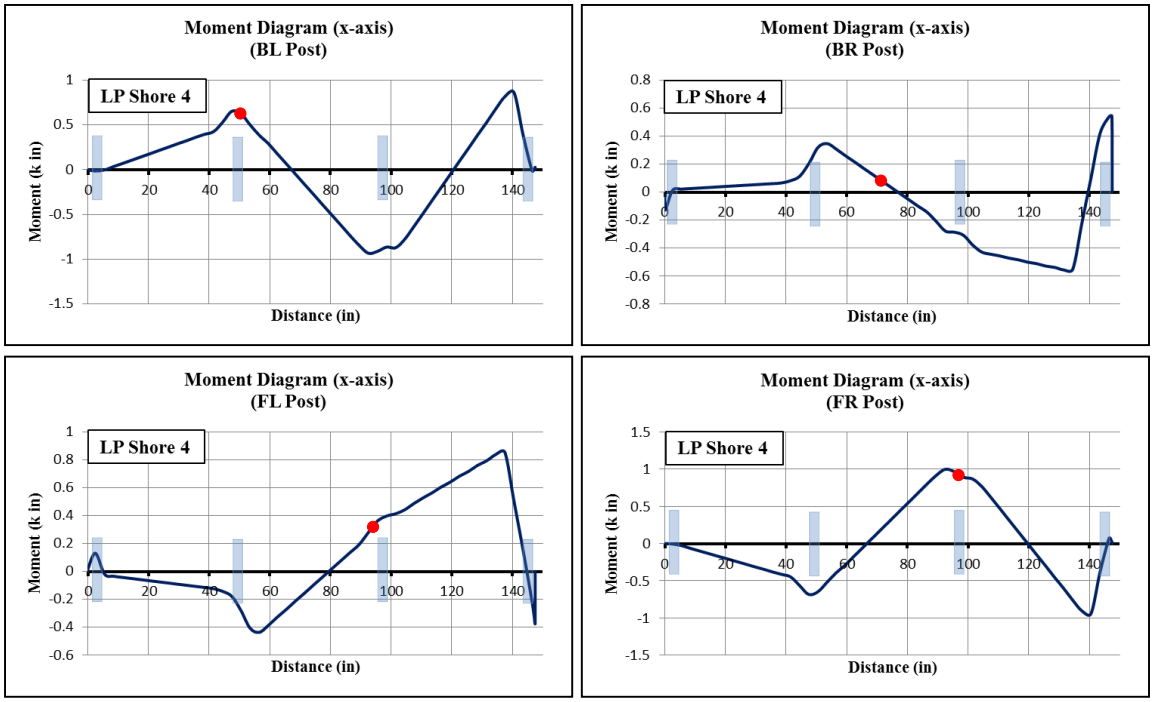

Figure 6.16 Bending moment diagrams obtained from Abaqus for LP Shore 4

Like the results from LP Shore 3, the bending moment diagrams for LP Shore 4 exhibited some obvious variability among each post. Regardless of the profile of the bending moments along the length of the posts, each post had a point of inflection near the mid-height of the shore. The post that experienced the largest bending moments (FR post) was the one that had the highest measured modulus of elasticity.

Because this test was load-controlled, all failures occurred at almost exactly the same time. Three of these four failures were located at a nailed joint. The other failure occurred near a knot in the middle of the back-right (BR) post. As discussed in *Chapter 3*, the load-controlled scenario represents what a shore might actually experience more closely than one that is displacement-controlled. Judging from these results, posts in vertically loaded shores in the field will likely experience high bending moments and failures at the locations where horizontal and diagonal braces frame into them.

Table 6-11 Model results generated by Abaqus for Shore 4 posts

LP Shore 4 (50 kips)							
Location	**Computed Quantity**	**FL Post**	**FR Post**	**BL Post**	**BR Post**	**Total Axial Force**	**Resultant Moment**
Top of Post	Displacement (in)	0.2548	0.2459	0.2548	0.2689	----	----
1st Story	Axial Stress (ksi)	-1.044	-1.249	-1.038	-0.7336	----	----
		-1.083	-1.195	-1.038	-0.7587	----	----
	Axial Force (k)	-13.03	-14.97	-12.72	-9.14	-49.86	----
	Moment-x (k in)	-0.0788	-0.2579	0.2346	0.04336	----	36.46
	Twisting Moment-y (k in)	-0.2034	-0.2489	-0.1796	-0.1208	----	-3.46
	Moment-z (k in)	-0.2436	0.485	-0.237	0.1526	----	-136.3
2nd Story	Axial Stress (ksi)	-1.095	-1.302	-1.086	-0.7589	----	----
		-1.019	-1.152	-0.9999	-0.7213	----	----
	Axial Force (k)	-12.95	-15.03	-12.77	-9.148	-49.898	----
	Moment-x (k in)	-0.1094	0.2861	-0.2491	0.09141	----	36.29
	Twisting Moment-y (k in)	0.1323	0.04994	0.04084	0.1013	----	5.1
	Moment-z (k in)	0.1927	0.3123	-0.09863	-0.05861	----	-136.2
3rd Story	Axial Stress (ksi)	-0.9164	-1.039	-0.9094	-0.6571	----	----
		-1.202	-1.42	-1.18	-0.8365	----	----
	Axial Force (k)	-12.97	-15.06	-12.8	-9.148	-49.978	----
	Moment-x (k in)	0.683	-0.146	0.09467	-0.4999	----	34.84
	Twisting Moment-y (k in)	-0.2567	-0.2118	-0.2179	-0.1539	----	-3.266
	Moment-z (k in)	-0.5237	-1.457	0.9961	0.2451	----	-136.2

The results shown in Table 6-11 above reveal that the front-right (FR) post, which had the highest measured modulus of elasticity, carried the highest amount of axial stress and the highest proportion of axial load. It also experienced the smallest amount of vertical displacement. Moreover, the back-right post (BR), which had the smallest measured value for the modulus of elasticity, carried the least amount of axial stress, axial load, and yielded the greatest vertical displacement.

As for the moment components, the highest values were shown in the third story for each post, with the highest and smallest given by the FR and BR post, respectively. Again, the resultant moments did not change much from story to story, but the z-axis resultant moments were significantly higher than those about the x and y axes. By inspection of the modulus of elasticity values in Table 6-10, it can be seen that the spread in these values among the posts was quite large. Thus, it was speculated that this caused the high resultant z-axis moments in each story of LP Shore 4.

Based on the results obtained for the shores subjected to vertical load only, it appears that a smaller amount of spread between the measured values for the modulus of elasticity for each post results in smaller resultant moments. Also, from story to story, the proportion of total axial force carried by each post changes by a very negligible amount. Nail slip apparently posed no major threat in any of the aforementioned tests.

Table 6-12 Additional model results generated by Abaqus for Shore 4

LP Shore 4 (50 kips)					
Location	**Computed Quantity**	**Abaqus Results**			
1st Story Joint	**Nail slip (in)**	**y-direction**		**z-direction**	
	D1-F (Upper End)	0.00076		0.00182	
	D1-F (Lower End)	0.00363		0.00123	
1st Story Braces	**In-Plane Force**	**Front**	**Left**	**Back**	**Right**
	Axial (kips)	0.0127	-0.111	0.0146	-0.121
2nd Story Braces	**In-Plane Force**	**Front**	**Left**	**Back**	**Right**
	Axial (kips)	-0.106	-0.0356	-0.0972	-0.0347
3rd Story Braces	**In-Plane Force**	**Front**	**Left**	**Back**	**Right**
	Axial (kips)	-0.0583	-0.0545	-0.0663	0.0567

Per Table 6-12, Shore 4 demonstrated the smallest amount of nail slip of the first four shores. However, because each shore discussed so far has yielded miniscule values for nail slip, this observation does not provide any conclusive information.

Three of the diagonal braces revealed tensile axial forces, indicating that these members served to prevent lateral movement of the posts to which they were nailed. None of the braces had a computed axial force high enough in magnitude to merit concern.

Figure 6.24 gives the comparison for each post between the vertical load-displacement plots obtained from the laboratory test and computed from Abaqus.

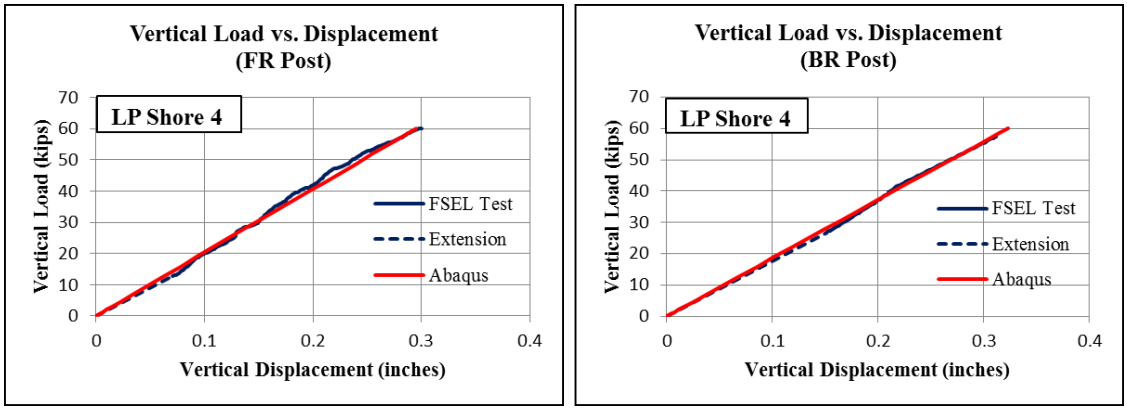

Figure 6.17 Plot comparisons between model results and laboratory tests for Shore 4

The plots in Figure 6.17 show that of all the shores discussed in this chapter, Shore 4 produced the closest agreement between the model and laboratory results. The fact that this test was the only load-controlled test conducted was not believed to have had any effect on the success of the plot comparisons.

Figure 6.18 shows contour plots of the computed magnitudes of vertical (global y-direction) stresses present in LP Shore 4 at the end of loading. The legend to the left of the plots indicates the ranges of stress (ksi) that correspond to each color.

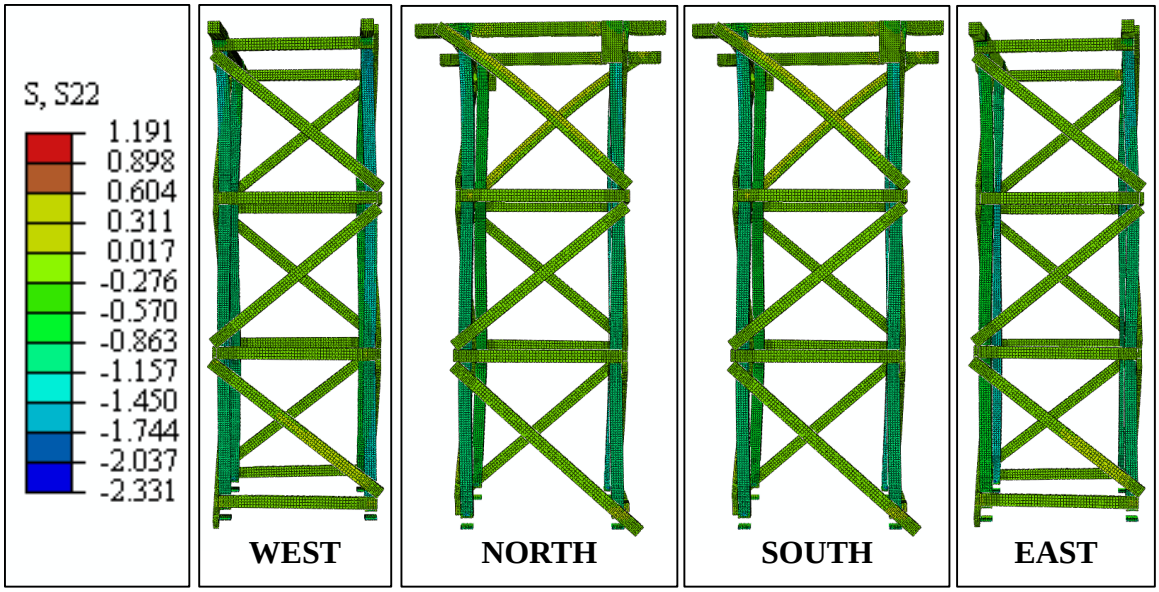

Figure 6.18 Contour plots showing the deformed shape and vertical stress distribution for Shore 4

6.5 SHORE 6 MODEL RESULTS

Table 6-13 below presents the details pertaining to the loading scenario investigated as well as the material and connector data input in the model for Shore 6.

Table 6-13 Details for the modeling of Shore 6

LP Shore 6				
Load Scenario	[C] Const Lat Disp, Inc Vert Load			
Connector Elements	Projection Cartesian, 8d and 12d nails			
Constraints	Distributing Coupling, R = 3			
Model Input	**FL Post**	**FR Post**	**BL Post**	**BR Post**
Modulus of Elasticity (ksi)	1017	1021	1226	1058

The bending moment diagrams for each post from LP Shore 6 are shown in Figure 6.19. These moments were computed about the x-axis of the shore since the first post failure occurred about this axis in the laboratory test.

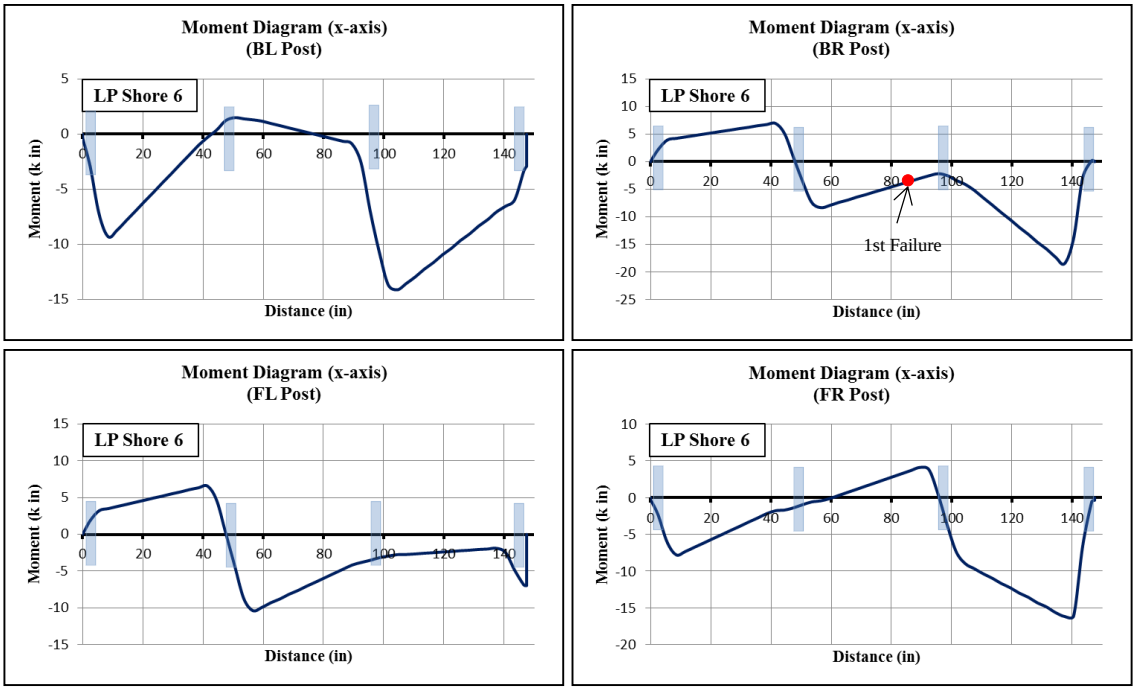

Figure 6.19 Bending moment diagrams obtained from Abaqus for LP Shore 6

As one would expect, the bending moments induced in the posts for LP Shore 6 were significantly higher than those from the tests involving vertical load only. The majority of moments along the length of each post are negative, with the maximum value occurring near the top for three of the members. Local peak moments appear to have occurred within the unbraced length of each post.

Similar to LP Shore 3, the first bending failure of a post (BR) occurred away from horizontal brace locations and at a point of relatively small moment. Again, investigation of the failure photographs for this shore from *Chapter 4* reveals the presence of knots at this location.

Table 6-14 Model results generated by Abaqus for Shore 6 posts

LP Shore 6 (50 kips)							
Location	**Computed Quantity**	**FL Post**	**FR Post**	**BL Post**	**BR Post**	**Total Axial Force**	**Resultant Moment**
Top of Post	Displacement (in)	-0.2135	-0.2267	-0.2353	-0.2408	----	----
1st Story	Axial Stress (ksi)	-0.2636	-0.1746	-2.051	-1.741	----	----
		-2.008	-1.71	-0.1382	-0.00237	----	----
	Axial Force (k)	-13.91	-11.54	-13.41	-10.68	-49.54	----
	Moment-x (k in)	5.089	-4.777	-4.852	5.654	----	114.6
	Twisting Moment-y (k in)	0.2846	0.2793	-0.5994	0.07785	----	-3.131
	Moment-z (k in)	-1.978	-1.18	-2.563	-1.361	----	-37.55
2nd Story	Axial Stress (ksi)	-1.942	-1.379	-0.8818	-0.2509	----	----
		0.2425	-0.5591	-1.325	-2.08	----	----
	Axial Force (k)	-10.41	-11.87	-13.51	-14.28	-50.07	----
	Moment-x (k in)	-7.136	1.879	0.2199	-5.532	----	-59.96
	Twisting Moment-y (k in)	0.5131	0.8144	0.08103	-0.7042	----	7.434
	Moment-z (k in)	1.407	1.433	1.524	1.594	----	128.6
3rd Story	Axial Stress (ksi)	-0.9508	0.689218	-2.1758	0.189108	----	----
		-0.7389	-3.137	0.4889	-2.466	----	----
	Axial Force (k)	-10.35	-14.99	-10.33	-13.95	-49.62	----
	Moment-x (k in)	-2.322	-13	-10.34	-11.91	----	-221.2
	Twisting Moment-y (k in)	-0.2387	0.1288	-0.3113	-0.1943	----	-2.863
	Moment-z (k in)	-1.555	-2.376	-0.2325	-0.8364	----	-28.58

Unlike the shores subjected to purely vertical load, the axial stresses and forces in each post for Shore 6 changed significantly from story to story. The drastic changes in axial stress for each post corner from story to story imply that there was a significant amount of curvature throughout the height of each post. Intuitively, the initial lateral displacement induced at the top of the shore caused tensile stresses to develop along certain faces of each post. The relatively low tensile stresses in the FL and BR posts compared to their compressive counterparts were most likely the result of the applied vertical load.

The fact that the back-left (BL) post had the highest measured modulus of elasticity did not ensure that it carried the greatest amount of total axial load. Interestingly, the front-left (FL) post underwent the least amount of vertical displacement and had the smallest measured modulus of elasticity. Of course, the 6 inches of lateral

displacement imposed on the shore prior to the application of vertical load surely had an effect on the final displacements of each post.

Since the Shore was displaced laterally in the yz-plane, it was expected that the x-axis moments would be the highest. The results in Table 6-14 confirm this hypothesis in each story. Note the differences in direction and magnitude revealed by the resultant moments.

Table 6-15 Additional model results generated by Abaqus for Shore 6

LP Shore 6 (50 kips)					
Location	**Computed Quantity**	**Abaqus Result**			
1st Story Joint	**Nail slip (in)**	**y-direction**		**z-direction**	
	D1-F (Upper End)	0.64		1.029	
	D1-F (Lower End)	0.0095		0.0929	
1st Story Braces	**In-Plane Force**	**Front**	**Left**	**Back**	**Right**
	Axial (kips)	2.6	-0.0939	-2.91	-0.284
2nd Story Braces	**In-Plane Force**	**Front**	**Left**	**Back**	**Right**
	Axial (kips)	-2.37	0.133	2.59	0.123
3rd Story Braces	**In-Plane Force**	**Front**	**Left**	**Back**	**Right**
	Axial (kips)	1.95	0.0774	-2.18	-0.48

As one might expect in the case of a laterally loaded shore, the computed nail slip values (Table 6-15) were much higher for LP Shore 6 than those of any of the first 4 shores. One end of the first story front diagonal brace (D1-F) experienced a very high nail slip while the other end did not. This logic makes sense when one considers that in order for nail withdrawal to occur for a given member, one end of the member must provide sufficient restraint so as to induce a high force at the other end.

For a given side of the shore, the axial forces in the diagonal braces tended to alternate from tension to compression from story to story. Also, the front and back diagonals carried significantly higher axial loads than the left and right diagonals. This find makes sense when one considers that the shore was displaced laterally, which would cause more strain on the front and back faces of the shore.

Figure 6.20 gives the comparison for the back-right (BR) post between the vertical load-displacement plots obtained from the laboratory test and computed from Abaqus.

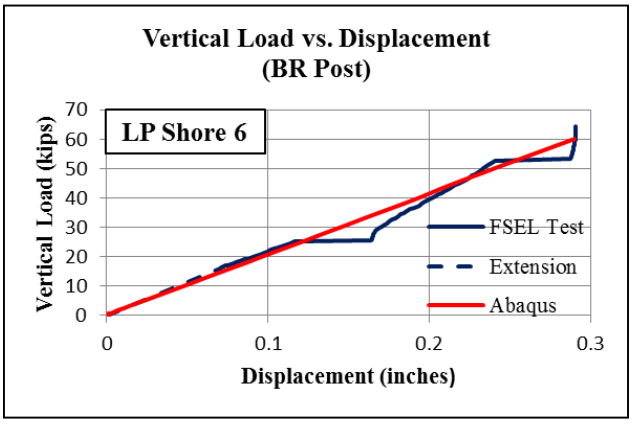

Figure 6.20 Plot comparison between model results and laboratory test for Shore 6

Only the string potentiometer attached to the back-right (BR) post for Shore 6 gave reliable results from the FSEL test. Nevertheless, the plot obtained from the model output demonstrated excellent agreement with the plot obtained from the laboratory.

Figure 6.21 shows contour plots of the computed magnitudes of vertical (global y-direction) stresses present in LP Shore 6 at the end of loading. The legend to the left of the plots indicates the ranges of stress (ksi) that correspond to each color.

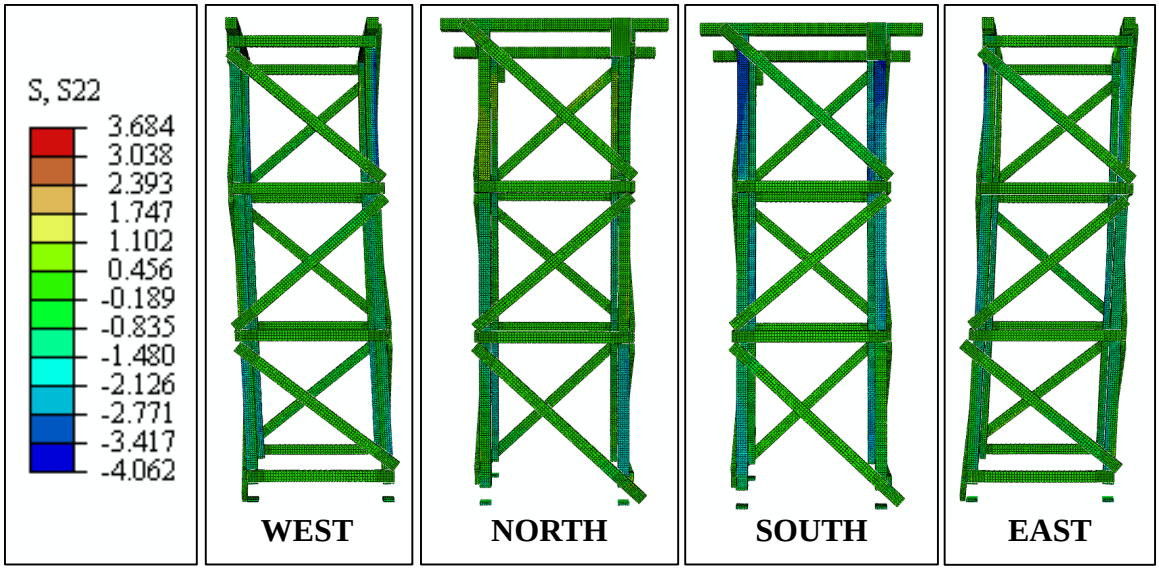

Figure 6.21 Contour plots showing the deformed shape and vertical stress distribution for Shore 6

A stark difference between the contour plots from LP Shore 6 and those subjected to vertical load only is the computed axial stress in the braces. The plots shown in Figure 6.21 suggest that for a vertically loaded LP shore that is subjected to a 6 inch lateral displacement, the braces play a significant role in maintaining equilibrium of forces on the structure.

Figure 6.22 presents an image to scale of the first story joint slip experienced by the upper end of the front diagonal member. Since the shore was displaced laterally to the left, the directional slip displayed by the close-up image appears valid. In the actual laboratory test, the nails on the lower end of this diagonal member withdrew from the front-right (FR) post before failure occurred (Figure 6.23).

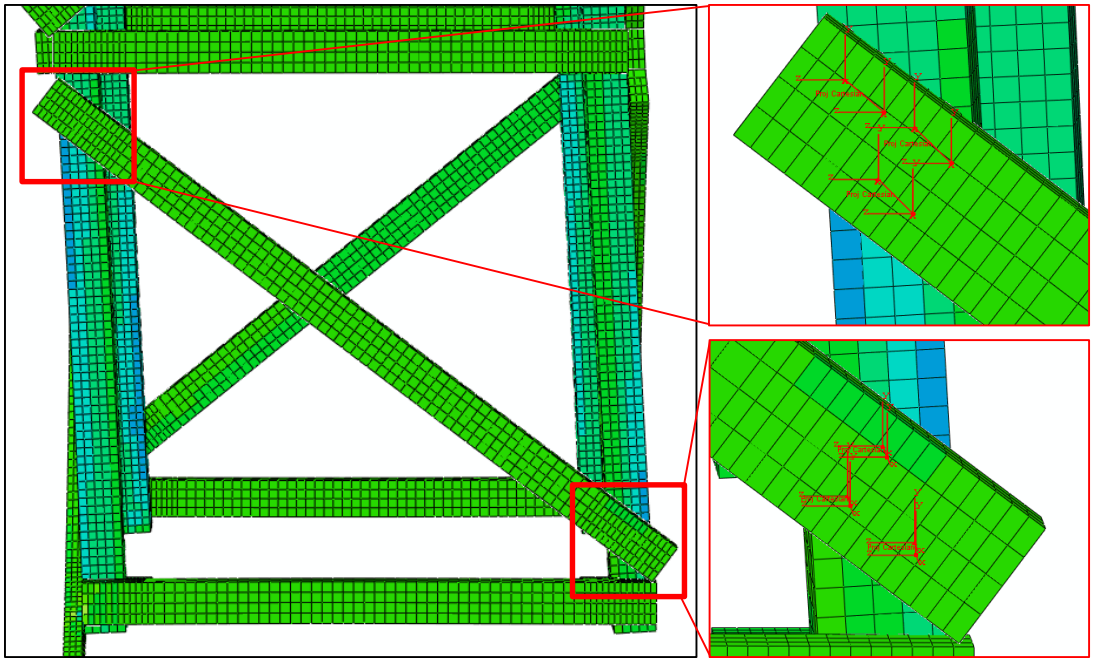

Figure 6.22 Deformed image of computed nail slip at ground level and first story joint of Shore 6

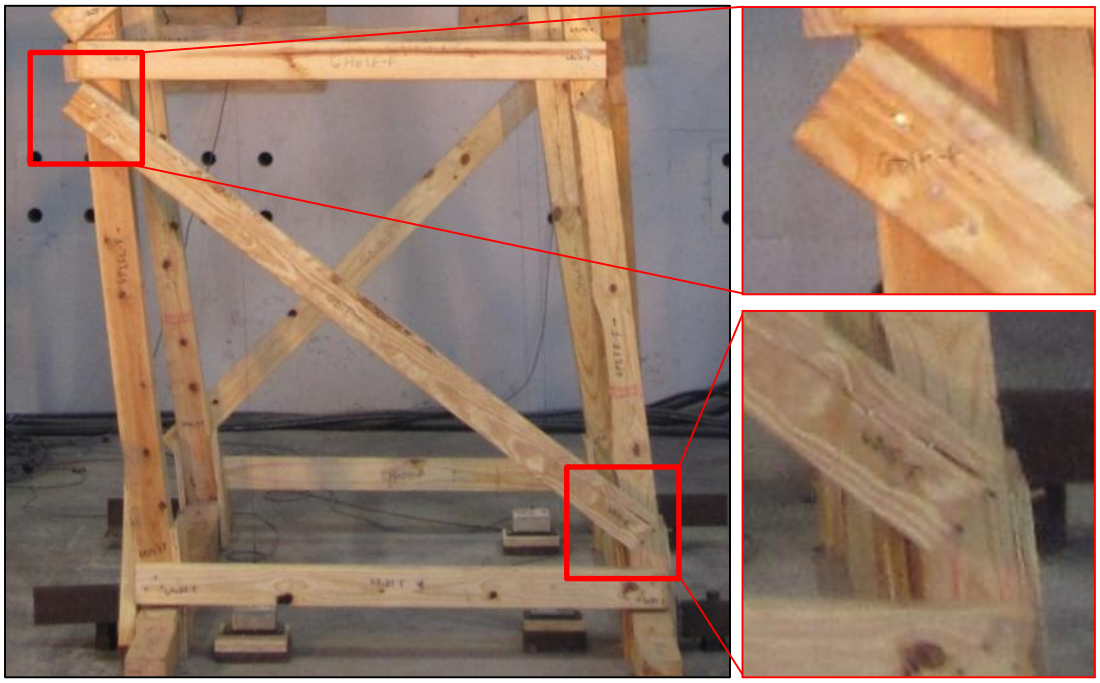

Figure 6.23 Deformed image of actual nail slip at ground level and first story joint of Shore 6

The images shown in Figures 6.22 and 6.23 exhibit good agreement with respect to the displaced position of the shore. However, there is one anomaly in comparing the computed nail slips with the observed nail slips: The computed slip values are very large at the upper left end of the front diagonal brace (D1-F) in Figure 6.22 and they are small at the bottom right. The observed slip pattern from the physical test is the opposite, with the large slip values occurring at the upper left end of the brace and small values at the bottom right. Nonetheless, with regards to the direction in which slip occurred, the computed nail slip values appear to closely reflect the actual behavior of the specimen.

6.6 SHORE 7 MODEL RESULTS

Table 6-16 presents the details pertaining to the loading scenario investigated as well as the material and connector data input in the model for Shore 7.

Table 6-16 Details for the modeling of Shore 7

PLP Shore 7				
Load Scenario	[C] Const Lat Disp, Inc Vert Load			
Connector Elements	Projection Cartesian, 8d nails			
Constraints	Distributing Coupling, R = 3			
Model Input	**FL Post**	**FR Post**	**BL Post**	**BR Post**
Modulus of Elasticity (ksi)	888	998	1335	2875

The bending moment diagrams for each post from PLP Shore 7 are shown in Figure 6.24. These moments were computed about the x-axis of the shore since the first post failure occurred about this axis in the laboratory test.

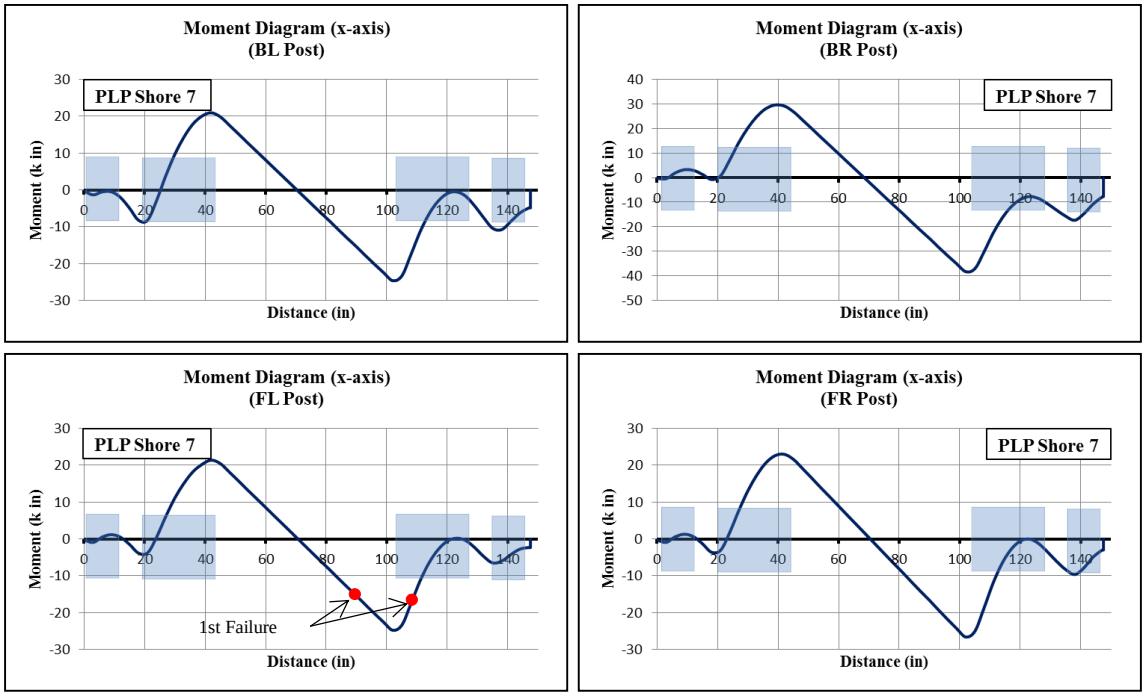

Figure 6.24 Bending moment diagrams obtained from Abaqus for PLP Shore 7

The bending moment diagrams from PLP Shore 7 exhibited a stark contrast to those from LP Shore 6 in that they all look almost exactly the same. Upon closer inspection, it is clear that although the profiles are extremely similar for each post, the magnitude of the peak moments corresponds directly the post's modulus of elasticity. For instance, the plot with highest range of moments was that of the back-right (BR) post, which had an E value over twice that of the other three posts. Another interesting trend in these plots is that the absolute maximum moment in each post occurs near the plywood brace joints instead of near the top of the member. Furthermore, even under the same vertical load and lateral displacement, PLP Shore 7 revealed much higher bending moment values within each post.

As indicated by the red dots on the diagram for the front-left (FL) post, simultaneous failures occurred near the second story plywood brace, where the computed bending moment was almost at its absolute maximum value (approximately 25 kip inches).

Table 6-17 Model results generated by Abaqus for Shore 7 posts

PLP Shore 7 (50 kips)							
Location	**Computed Quantity**	**FL Post**	**FR Post**	**BL Post**	**BR Post**	**Total Axial Force**	**Resultant Moment**
Top of Post	Displacement (in)	-0.2209	-0.2261	-0.2049	-0.2212	----	----
1st Story	Axial Stress (ksi)	-1.333	-0.4041	-2.039	-1.167	----	----
		-0.6497	-1.082	-0.3184	-1.188	----	----
	Axial Force (k)	-12	-9.198	-14.26	-14.54	-49.998	----
	Moment-x (k in)	-2.611	-2.457	-6.53	0.2778	----	45
	Twisting Moment-y (k in)	-1.793	-0.9655	2.689	0.707	----	3.544
	Moment-z (k in)	-0.03958	-0.0874	-0.09256	0.2195	----	77.88
2nd Story	Axial Stress (ksi)	-1.044	-0.5844	-1.245	-0.7729	----	----
		-0.5544	-1.27	-0.6597	-2.033	----	----
	Axial Force (k)	-9.791	-11.36	-11.66	-17.19	-50.001	----
	Moment-x (k in)	-2.465	-2.831	-2.865	-6.097	----	-171.8
	Twisting Moment-y (k in)	-1.506	-0.8485	1.575	1.223	----	3.531
	Moment-z (k in)	-0.7452	-0.36	-0.07254	-0.4764	----	77.95
3rd Story	Axial Stress (ksi)	-1.043	-0.54	-1.476	0.1364	----	----
		-0.2087	-1.69	-0.03373	-3.313	----	----
	Axial Force (k)	-7.656	-13.64	-9.258	-19.44	-49.994	----
	Moment-x (k in)	-4.025	-5.339	-6.569	-12.46	----	-388.2
	Twisting Moment-y (k in)	-1.601	-0.8228	2.309	0.7266	----	3.552
	Moment-z (k in)	-0.1573	0.8948	0.0941	0.9067	----	77.78

Like the results from Shore 6, the axial force in each post in Shore 7 changed by a significant amount from story to story (Table 6-17). Even with the back-right (BR) post boasting a modulus of elasticity over twice that of every other post, it did not experience the least amount of vertical displacement. However, it did carry the highest proportion of total axial force in each story, although this amount varied considerably. Unlike the posts in Shore 6, none of the posts in Shore 7 exhibited compressive axial stresses on each post corner. In fact, every single post in this case demonstrated a combination of tensile and compressive axial stresses. For each post, the magnitude of the compressive stress was much greater than that of the tensile stress. Again, this was to be expected since the applied vertical load was compressive.

The x-component moments again yielded the largest magnitudes, with the highest of these consistently in the third story for each post. Moreover, the resultant moment

about the x-axis increased dramatically from the first to the third stories. Twisting moments did not reach substantial values for this shore.

Clearly, when a lateral displacement is involved in the loading sequence, the assumptions made for the vertically loaded shores (1-4) cannot be directly applied.

Table 6-18 Additional model results generated by Abaqus for Shore 7

PLP Shore 7 (50 kips)			
Location	**Computed Quantity**	**Abaqus Result**	
1st Story Joint	**Nail slip (in)**	**y-direction**	**z-direction**
	WB1-F (Top Left)	0.0158	0.495
	WB1-F (Bot Left)	0.0234	0.0953
1st Story Braces	**In-Plane Force**	**WB1-F**	**WB1-B**
	Axial (kips)	-0.0248	-0.4021
	Shear (kips)	2.241	2.571
2nd Story Braces	**In-Plane Force**	**WB2-F**	**WB2-B**
	Axial (kips)	0.008254	0.3026
	Shear (kips)	2.161	2.381

Per Table 6-18, the vertical and horizontal components of joint slip for Shore 7 were less than half those recorded in Shore 6. Most likely, the fact that the plywood brace had 14 nails on each attached face compared to the 3 nails for the diagonal braces contributed to the reduced amount of slip in the PLP shore.

While the in-plane axial forces remained low for Shore 7 as in the case of the previous two PLP shores investigated, the shear forces were relatively high. This suggests that the plywood braces serve to resist the lateral displacement of the shore to a fairly reasonable extent.

Figure 6.25 gives the comparison for each post between the vertical load-displacement plots obtained from the laboratory test and computed from Abaqus.

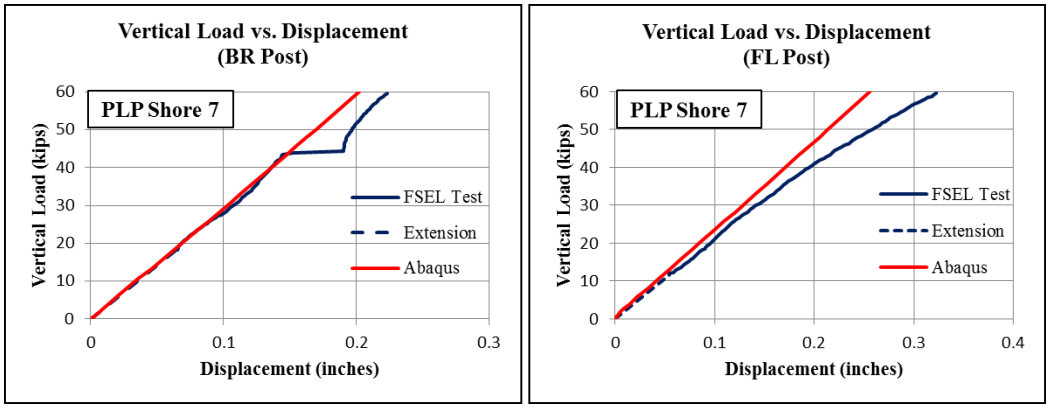

Figure 6.25 Plot comparisons between model results and laboratory tests for Shore 7

The plots shown in Figure 6.25 reveal good agreement between the FSEL test results and the model results. For the front-left (FL) post results, the model tends to slightly overestimate the stiffness of the response.

Figure 6.26 shows contour plots of the computed magnitudes of vertical (global y-direction) stresses present in PLP Shore 7 at the end of loading. The legend to the left of the plots indicates the ranges of stress (ksi) that correspond to each color. Additional data concerning the stresses in some of the plywood braces can be found in Appendix A.

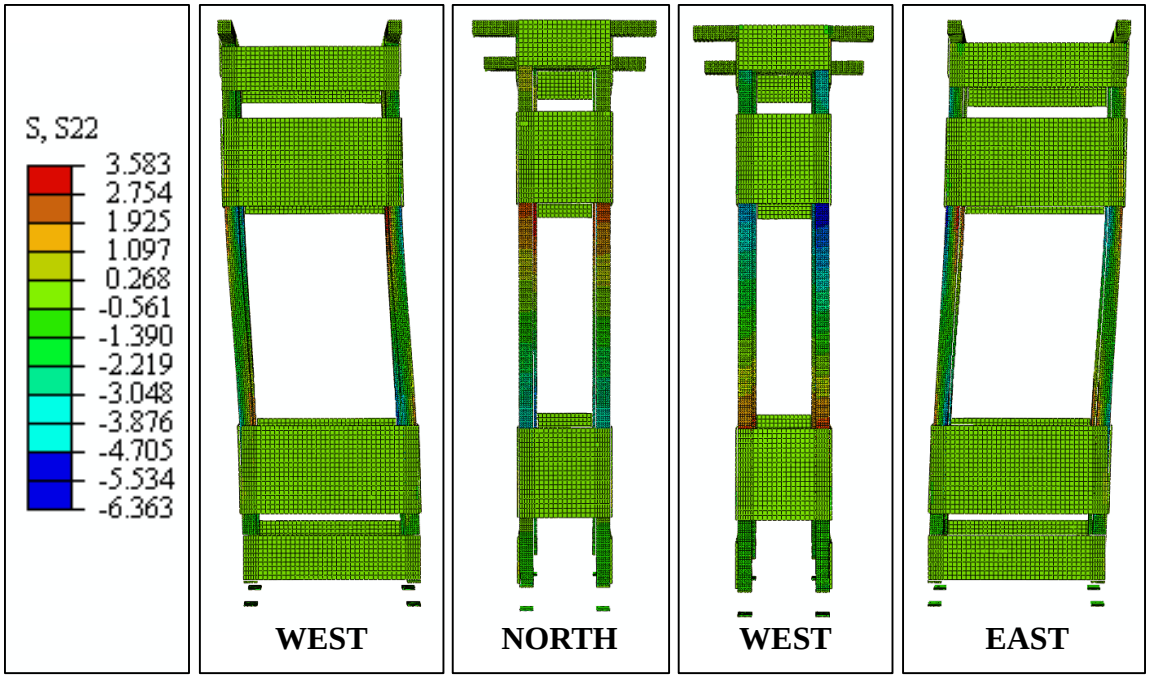

Figure 6.26 Contour plots showing the deformed shape and vertical stress distribution for Shore 7

Figure 6.27 shows an image to scale obtained from the output database in Abaqus of the joint slip experienced by the first story wide front brace (WB1-F). The directional slip shown in the close-up image makes sense, as this shore was displaced laterally to the left. The relative moment between the plywood brace and the front two posts closely resembled the behavior observed in the FSEL test for Shore 7. Photographs of these corresponding areas of PLP Shore 7 from the laboratory test are shown in Figure 6.28.

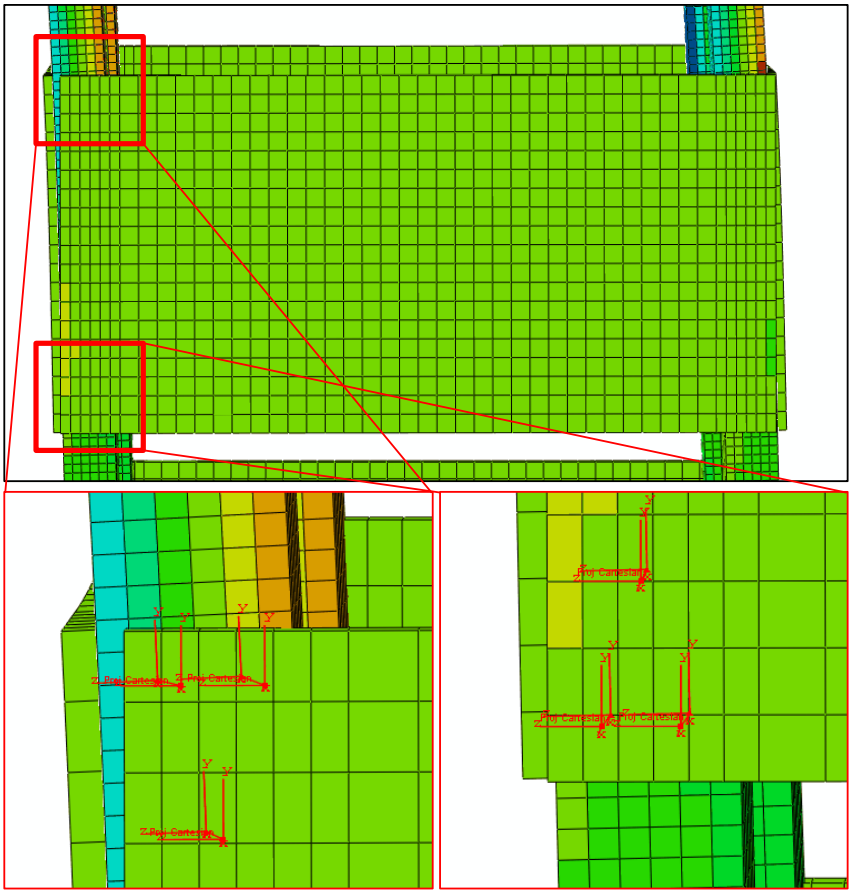

Figure 6.27 Deformed image of the computed first story nail slip of Shore 7

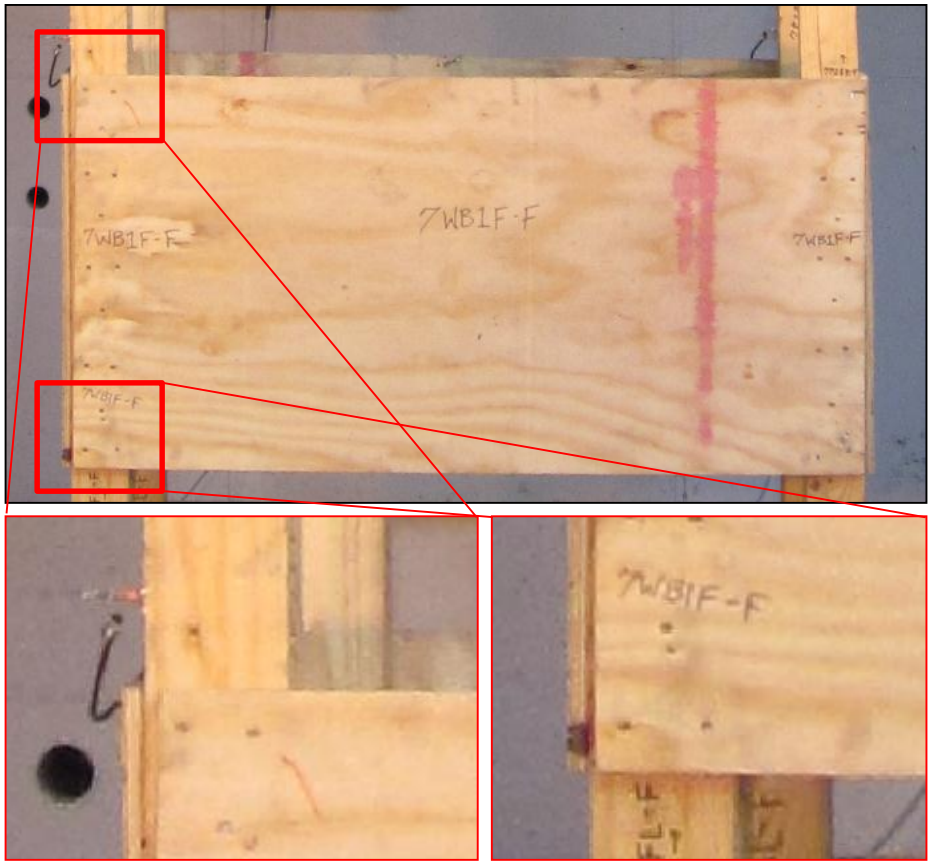

Figure 6.28 Deformed image of the actual first story nail slip of Shore 7

Comparison of the images in Figures 6.27 and 6.28 indicates good agreement between the predicted joint deformations and the actual joint deformations for the first story plywood brace in the linear elastic range. Both the model and the laboratory images show the top left corner of the brace experiencing larger joint slip than the bottom left corner.

6.7 SHORE 8 MODEL RESULTS

Table 6-19 presents the details pertaining to the loading scenario investigated as well as the material and connector data input in the model for Shore 8.

Table 6-19 Details for the modeling of Shore 8

LP Shore 8				
Load Scenario	[D] Const Vert Load, Inc Lat Disp			
Connector Elements	Projection Cartesian, 8d and 12d nails			
Constraints	Distributing Coupling, R = 3			
Model Input	**FL Post**	**FR Post**	**BL Post**	**BR Post**
Modulus of Elasticity (ksi)	1383	1452	884	892

The bending moment diagrams for each post from LP Shore 8 are shown in Figure 6.29. These moments were computed about the x-axis of the shore since the first post failure occurred about this axis in the laboratory test.

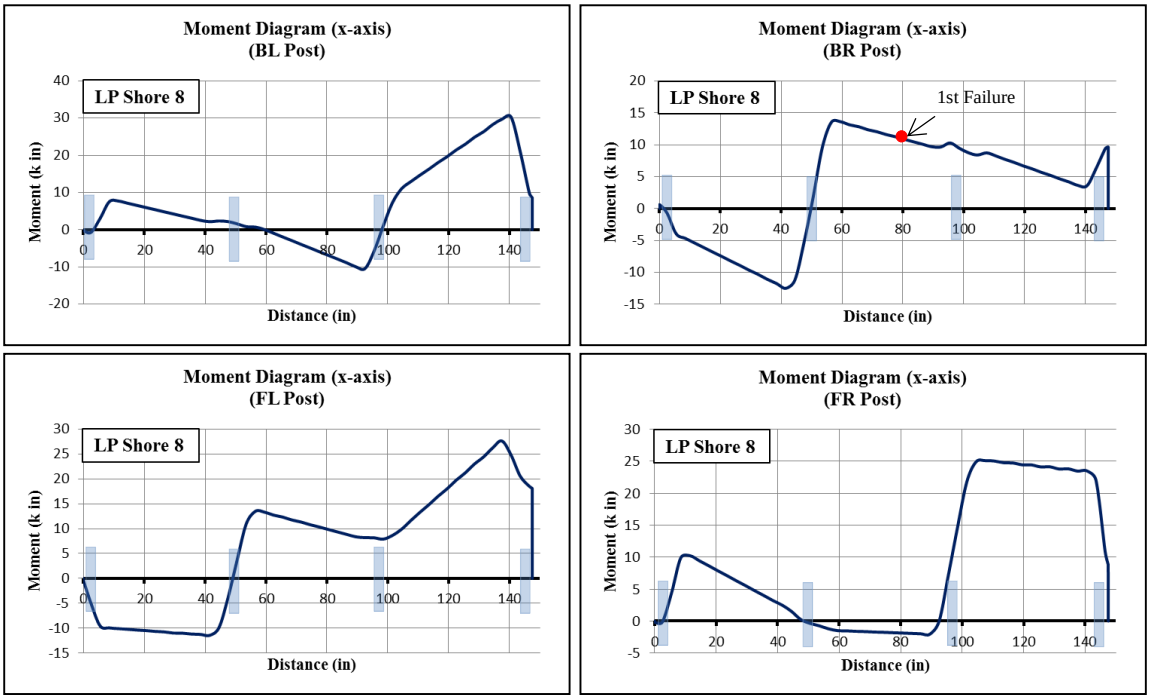

Figure 6.29 Bending moment diagrams obtained from Abaqus for LP Shore 8

The diagrams in Figure 6.29 show that like the results from all of LP shores, the posts from LP Shore 8 exhibited unique bending moment behavior. For all except one of the posts, the absolute maximum bending moment occurred near the top end of the member. Although some posts had more points of inflection than others, each post in this shore had one at approximately the location of the first story horizontal brace. Like the

computed results from LP Shore 3 and LP Shore 6, the first post failure (BR) occurred away from nailed joint locations. However, the region in which this failure occurred was still in a region of high computed bending moment.

Table 6-20 Model results generated by Abaqus for Shore 8 posts

LP Shore 8 (36 kips)							
Location	**Computed Quantity**	**FL Post**	**FR Post**	**BL Post**	**BR Post**	**Total Axial Force**	**Resultant Moment**
Top of Post	Displacement (in)	-0.2318	-0.1176	-0.1840	-0.1157	----	----
1st Story	Axial Stress (ksi)	-2.204	-2.228	0.4271	0.4091	----	----
		1.166	0.4939	-1.491	-2.293	----	----
	Axial Force (k)	6.357	10.62	6.514	11.54	35.031	----
	Shear Force (k)	0.04818	0.2798	0.2063	0.2558	0.79008	----
	Moment-x (k in)	-10.71	6.726	5.141	-8.614	----	-214.1
	Twisting Moment-y (k in)	-1.192	0.2478	0.9024	0.9093	----	1.306
	Moment-z (k in)	2.841	3.935	2.31	2.375	----	35.49
2nd Story	Axial Stress (ksi)	0.5775	-0.2691	-1.346	-2.18	----	----
		-2.607	-1.57	0.1919	1.239	----	----
	Axial Force (k)	12.43	11.26	7.071	5.764	36.525	----
	Shear Force (k)	0.1772	0.01961	0.3558	0.1399	0.69251	----
	Moment-x (k in)	10.87	-1.736	-4.62	11.65	----	71.2
	Twisting Moment-y (k in)	-0.6891	-0.2149	1.63	0.5388	----	8.707
	Moment-z (k in)	-1.589	-3.43	-1.607	-1.76	----	-250
3rd Story	Axial Stress (ksi)	1.209	-3.763	1.994	-1.068	----	----
		-3.174	2.831	-3.958	0.1867	----	----
	Axial Force (k)	12.03	5.71	12.03	5.4	35.17	----
	Shear Force (k)	-0.582	0.05485	-0.6101	0.1832	-0.95405	----
	Moment-x (k in)	19.76	24.42	21.47	6.223	----	360.1
	Twisting Moment-y (k in)	-1.829	1.56	2.364	-0.2577	----	-0.7606
	Moment-z (k in)	1.647	1.657	2.336	1.387	----	-0.03835

Because such a large lateral displacement was imposed on the shore, the shear force at each story was also computed and included in Table 6-20 above. Similar to the results for LP Shore 6, the computed axial forces in LP Shore 8 varies substantially from story to story. A significant difference was observed between the predicted displacements of the top end of the posts—the front-left (FL) and back-left (BL) posts experienced roughly twice the displacement as the front-right (FR) and back-right (BR) posts. With the exception of the FR post at the second story, each post revealed the presence of bending at almost every location reported in the table, as indicated by the

opposing signs at each corner. Moreover, as would be expected for a shore subjected to a larger lateral displacement, the computed resultant moments were much larger for LP Shore 8 and for LP Shore 6.

Table 6-21 Additional model results generated by Abaqus for Shore 8

LP Shore 8 (36 kips)					
Location	**Computed Quantity**	**Abaqus Result**			
1st Story Joint	**Nail slip (in)**	**y-direction**		**z-direction**	
	D1-F (Upper End)	0.007924		0.1683	
	D1-F (Lower End)	1.788		2.476	
1st Story Braces	**In-Plane Force**	**Front**	**Left**	**Back**	**Right**
	Axial (kips)	-4.605	-0.5886	4.388	-0.6059
2nd Story Braces	**In-Plane Force**	**Front**	**Left**	**Back**	**Right**
	Axial (kips)	4.623	0.1302	-4.369	0.4559
3rd Story Braces	**In-Plane Force**	**Front**	**Left**	**Back**	**Right**
	Axial (kips)	-3.731	-0.6674	3.041	0.06768

Per Table 6-21, the vertical and horizontal nail slip near the ground level joint was much higher than all previously analyzed shores. At the top end of the first story front diagonal brace (D1-F), the slip was much smaller.

For three of the four sides of the shore, the axial forces in the diagonal braces changes from compression to tension in each story.

Figure 6.30 gives the comparison for each post between the vertical load-displacement plots obtained from the laboratory test and computed from Abaqus.

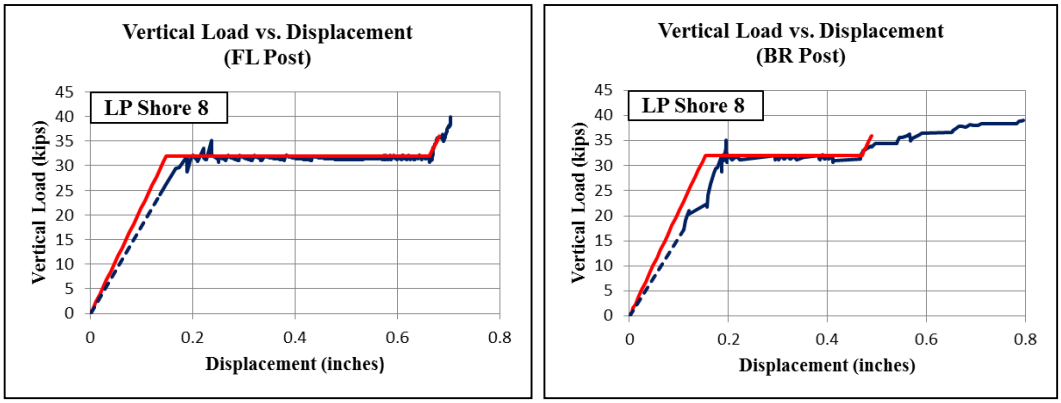

Figure 6.30 Plot comparisons between model results and laboratory tests for Shore 8

Figure 6.31 shows contour plots of the computed magnitudes of vertical (global y-direction) stresses present in LP Shore 8 at the end of loading. The legend to the left of the plots indicates the ranges of stress (ksi) that correspond to each color.

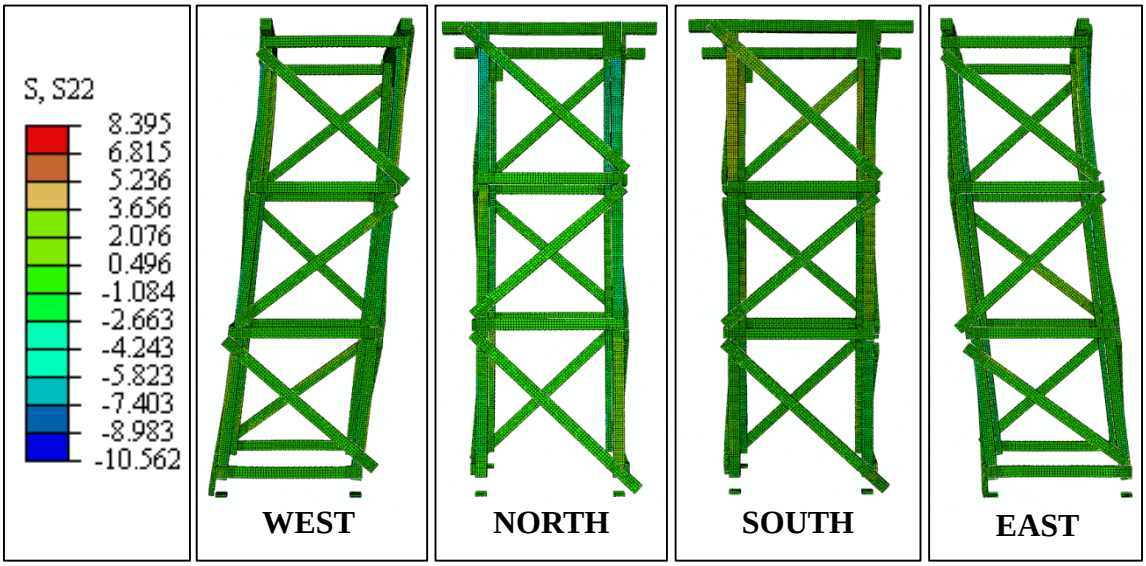

Figure 6.31 Contour plots showing the deformed shape and vertical stress distribution for Shore 8

Figure 6.32 shows a deformed plot to scale obtained from Abaqus of the first story diagonal brace (WB1-F) on the front of Shore 8, followed by images of the same member during laboratory testing in Figure 6.33. By examining the displaced positions of the posts and the diagonal brace in both figures, it can be easily seen that the nails in this member underwent substantially higher joint slip than those from the diagonal brace in LP Shore 6 (Figures 6.22 and 6.23). These higher nail slip values were expected since LP Shore 8 was subjected to over twice the amount of lateral displacement than LP Shore 6.

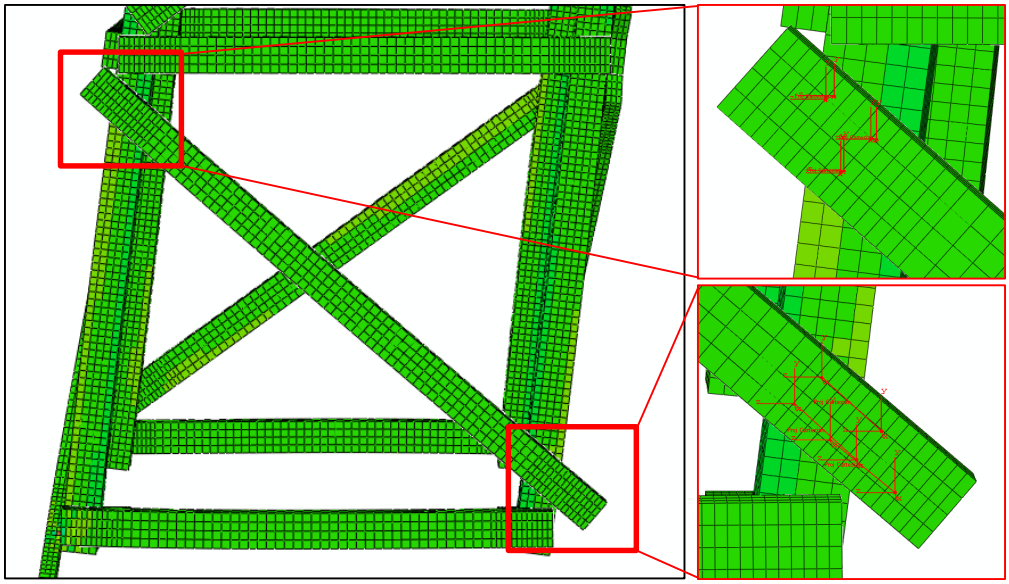

Figure 6.32 Deformed image of computed ground level and first story nail slip of Shore 8

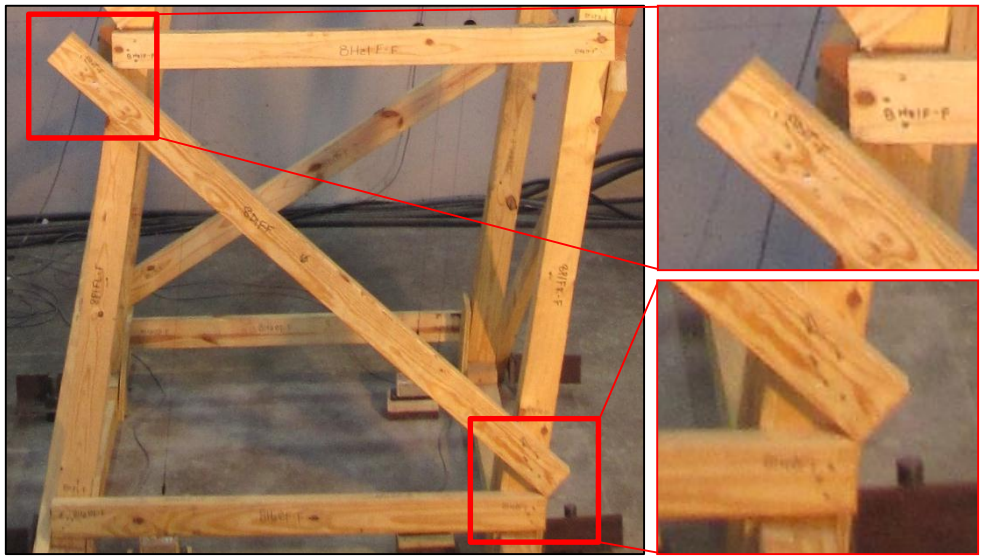

Figure 6.33 Deformed image of actual ground level and first story nail slip of Shore 8

In terms of the overall displaced shape of the shore, the images shown in Figures 6.32 and 6.33 demonstrate good agreement between the predicted and actual behavior of the structure. However, like the comparison done for the first-story brace nail slip in LP Shore 6, there is an exception. The model results for LP Shore 8 predict the bottom right

end of the diagonal brace to experience the large nail slip, while the nails in the top left end of the member undergo almost zero slip. It was suspected that many factors beyond those considered in the modeling process contributed to which end of the member experienced nail greater nail slip. Nevertheless, good agreement was consistently obtained when comparing the computed nail slips with those observed from the laboratory tests.

6.8 SHORE 9 MODEL RESULTS

Table 6-22 presents the details pertaining to the loading scenario investigated as well as the material and connector data input in the model for Shore 9.

Table 6-22 Details for the modeling of Shore 9

PLP Shore 9				
Load Scenario	[D] Const Vert Load, Inc Lat Disp			
Connector Elements	Projection Cartesian, 8d nails			
Constraints	Distributing Coupling, R = 3			
Model Input	**FL Post**	**FR Post**	**BL Post**	**BR Post**
Modulus of Elasticity (ksi)	792	1268	984*	891

*Material data not available. The average MOE of the other 3 posts was used instead.

The bending moment diagrams for each post from PLP Shore 9 are shown in Figure 6.34. These moments were computed about the x-axis of the shore since the first post failure occurred about this axis in the laboratory test.

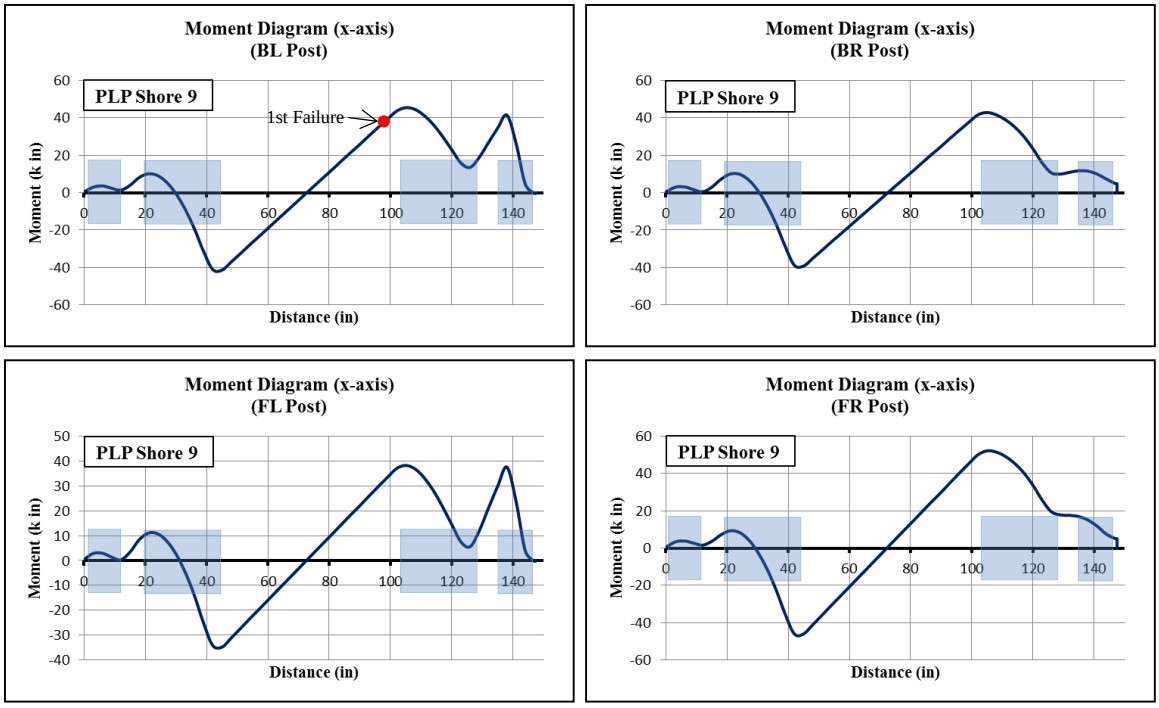

Figure 6.34 Bending moment diagrams obtained from Abaqus for PLP Shore 9

Much like the results from PLP Shore 7, the bending moment diagram for each post in PLP Shore 9 had a very similar profile with differing magnitudes. Again, all posts revealed a strong point of inflection near mid-height of the shore, with peak moments tending to occur near the plywood brace locations. Each post in PLP Shore 9 exhibited higher peak moments than those from LP Shore 8. Clearly, a wider spread of nails in a given joint along a post will result in increased rotational resistance at that location and, thus, higher moments.

Another similar characteristic of this shore model with regards to computed moments for PLP Shore 7 is that the first bending failure occurred near the second story plywood brace in a region of very large moment. It would appear as if the posts in PLP shores tend to fail first near a nailed joint whereas the posts in LP shores tend to be governed by knots within the second story unbraced length of the members. Judging from the results presented in this chapter, the presence of knots within this region (away from nailed joints) seems to have less effect on the location of the first bending failure in the PLP shores (for combined vertical and lateral loading).

Table 6-23 Model results generated by Abaqus for Shore 9 posts

PLP Shore 9 (40 kips)							
Location	**Computed Quantity**	**FL Post**	**FR Post**	**BL Post**	**BR Post**	**Total Axial Force**	**Resultant Moment**
Top of Post	Displacement (in)	-0.1978	-0.1850	-0.1944	-0.2032	----	----
1st Story	Axial Stress (ksi)	0.2783	-1.835	0.1773	-1.669	----	----
		-1.284	-0.4603	-1.404	-0.3668	----	----
	Axial Force (k)	-6.08	-14.02	-7.461	-12.44	-40.001	----
	Shear Force (k)	-1.849	-1.266	-1.565	-1.517	-6.197	----
	Moment-x (k in)	5.826	5.284	5.968	4.928	----	-265.3
	Twisting Moment-y (k in)	1.779	1.469	-0.9677	-1.652	----	0.9515
	Moment-z (k in)	-0.07945	-0.01776	0.0587	-0.00868	----	-2.041
2nd Story	Axial Stress (ksi)	-0.742	-1.009	-0.8813	-0.7674	----	----
		-0.9359	-0.5965	-1.015	-0.5837	----	----
	Axial Force (k)	-10.28	-9.835	-11.61	-8.276	-40.001	----
	Shear Force (k)	-1.336	-1.786	-1.58	-1.505	-6.207	----
	Moment-x (k in)	1.513	2.574	1.561	1.675	----	91.4
	Twisting Moment-y (k in)	1.592	3.11	-2.018	-2.377	----	0.64031
	Moment-z (k in)	0.0181	0.03009	-0.1731	0.1273	----	-2.299
3rd Story	Axial Stress (ksi)	0.9015	-2.791	1.705	-1.721	----	----
		-3.155	1.739	-4.147	0.9175	----	----
	Axial Force (k)	-13.6	-6.568	-14.77	-5.058	-39.996	----
	Shear Force (k)	-3.205	0.085	-2.756	-0.3314	-6.2074	----
	Moment-x (k in)	18.54	17.66	24.56	10.65	----	444.1
	Twisting Moment-y (k in)	5.526	0.6095	-4.801	-1.061	----	0.5456
	Moment-z (k in)	0.1148	0.173	0.6497	0.01348	----	-2.557

The values presented in Table 6-23 confirm that the axial forces in each post varied from story to story. In the first story, the post with the highest measured modulus of elasticity, the front-right (FR), carried the largest proportion of total axial load on the shore. However, this was not the case for the second or third stories. The recorded shore force in each post changed slightly from the first to second story and changed drastically from the second the third story. The highest recorded shear force occurred in the front-left (FL) post at in the third story. As for the displacements, the FR post did indeed experience the least amount of vertical displacement.

As anticipated, the x-components for the moments yielded the largest magnitudes, with the highest occurring in the third story. The individual moments in each post about the x-axis were relatively small in the second story, likely due to the presence of points of

inflection. PLP Shore 9 exhibited the highest resultant moments under 40 kips of total axial load even though many of the other shores modeled were subjected to a total vertical load 50 kips.

Table 6-24 Additional model results generated by Abaqus for Shore 9

PLP Shore 9 (40 kips)			
Location	**Computed Quantity**	**Abaqus Result**	
1st Story Joint	**Nail slip (in)**	**y-direction**	**z-direction**
	WB1-F (Top Right)	0.0847	0.2581
	WB1-F (Bot Right)	0.1033	1.638
1st Story Braces	**In-Plane Force**	**WB1-F**	**WB1-B**
	Axial (kips)	-0.02481	-0.4021
	Shear (kips)	2.241	2.571
2nd Story Braces	**In-Plane Force**	**WB2-F**	**WB2-B**
	Axial (kips)	0.008254	0.3026
	Shear (kips)	2.161	2.381

Per Table 6-24, nail slip in the front plywood brace (WB1-F) was rather large at the bottom right corner of the member. Recall from *Chapter 4* that the back-left (BL) post split near the second story joint as the slab reached a lateral displacement of 15 inches. This failure enabled the nails to perform sufficiently well to cause the capacity of the shore to be governed by the failure properties of the posts. Consequently, the nails in PLP Shore 9 did not slip or withdraw from the posts much. However, since no failure stresses were considered in the finite-element modeling of the wood members, a high nail slip was expected.

The plywood braces did not experience significant axial forces in this shore. The second story braces ended up in tension whereas the first story braces were in compression. Like the braces from PLP Shore 7, shear forces within the members were relatively high and remained between 2 and 3 kips.

Figure 6.35 gives the comparison for each post between the vertical load-displacement plots obtained from the laboratory test and computed from Abaqus.

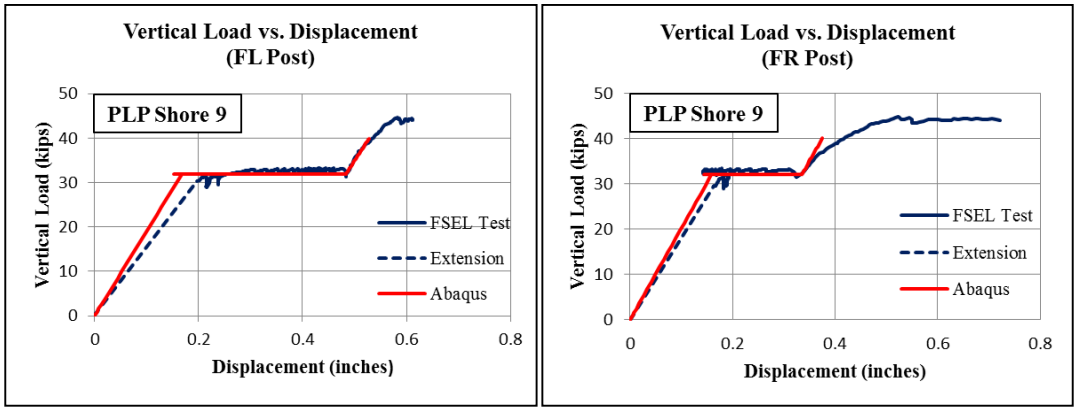

Figure 6.35 Plot comparisons between model results and laboratory tests for Shore 9

Obtaining a reasonable linear elastic approximation from the FSEL tests proved to be quite difficult for this shore. It was speculated that the initial region of system engagement (as discussed in *Chapter 4*) affected the load-displacement plots up to around 32 kips of vertical load. Therefore, the first loading curve in each plot shown in Figure 6.35 has been adjusted to best reflect the slope of the load-displacement curve shortly before the commencement of lateral displacement. Nonetheless, the plots agreed quite well, with the exception of the reloading curve for the front-right (FR) post. Since the vertical capacity of the shore was only 44 kips, a loss of stiffness near this peak region was expected.

Figure 6.36 shows contour plots of the computed magnitudes of vertical (global y-direction) stresses present in PLP Shore 9 at the end of loading. The legend to the left of the plots indicates the ranges of stress (ksi) that correspond to each color. Additional data concerning the stresses in some of the plywood braces can be found in Appendix A.

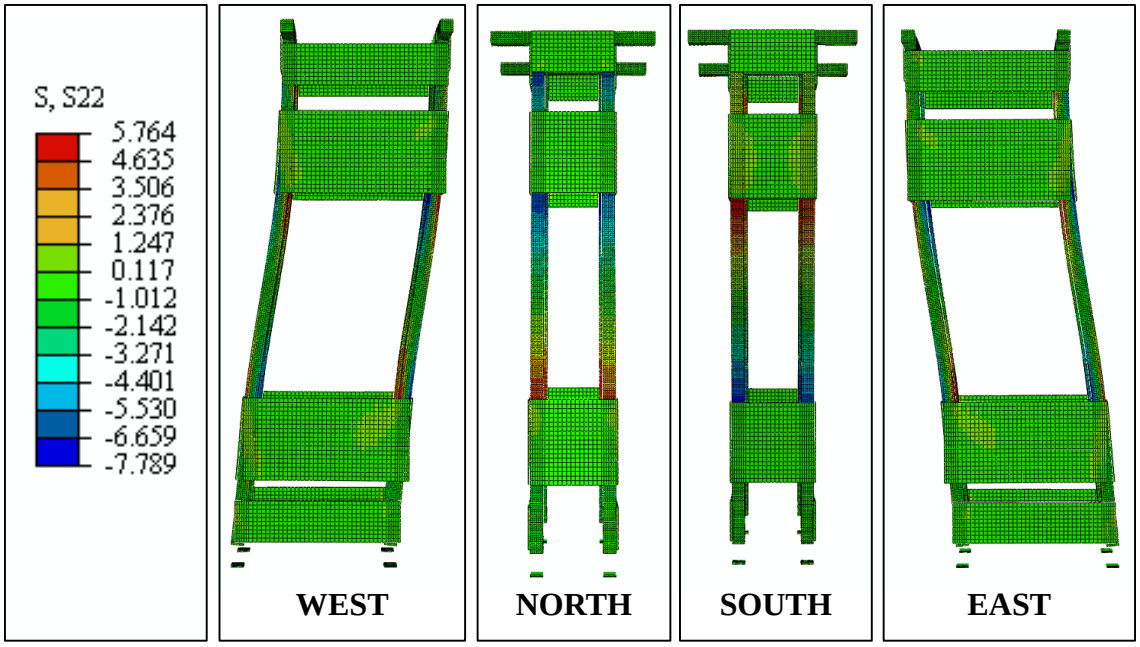

Figure 6.36 Contour plots showing the deformed shape and vertical stress distribution for Shore 9

As in the case for LP Shore 8, the contour plots shown in Figure 6.36 indicate the presence of heavy bending in each post (noted by the red and blue color changes). The values in the legend suggest that the axial stresses in the posts were highest near the plywood brace joints, with certain regions in tension and others in compression. The green color on the plywood braces suggests that these members, relative the posts, experienced small amounts of vertical stress.

Figure 6.37 shows a deformed plot to scale obtained from Abaqus of the first story wide brace (WB1-F) on the front of Shore 9, followed by images of the same member during laboratory testing in Figure 6.38. By examining the displaced positions of the posts and the plywood brace, it can be easily ascertained that the nails near the top-right corner of the brace shifted in the opposite direction to the ones near the bottom-right corner of the brace.

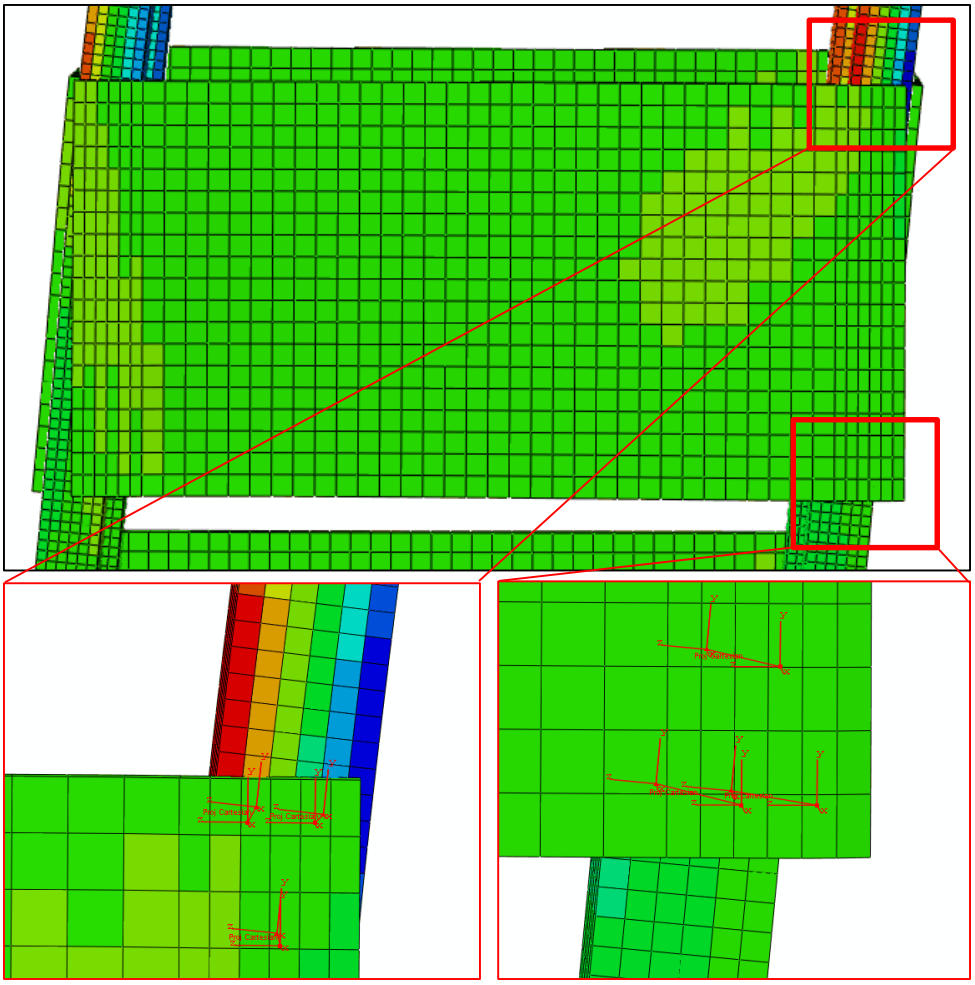

Figure 6.37 Deformed image of the computed first story nail slip of Shore 9

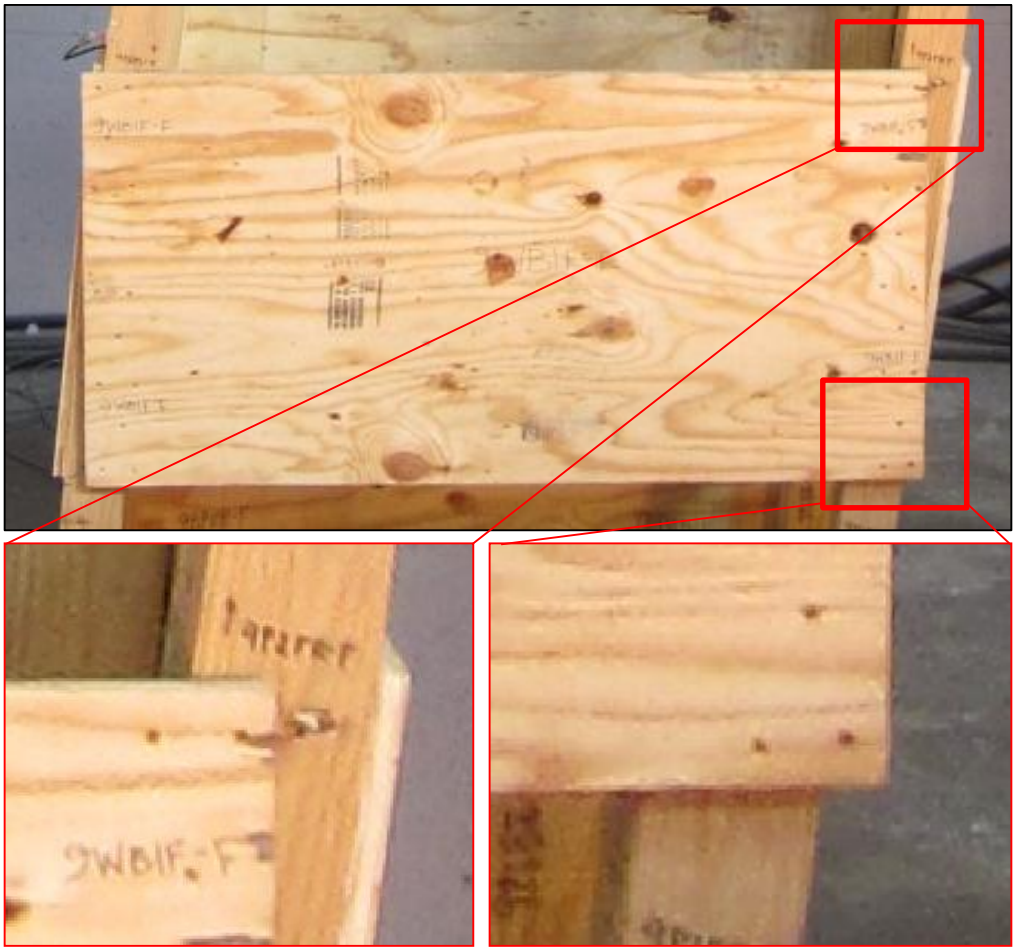

Figure 6.38 Deformed image of the actual first story nail slip of Shore 9

Similar to the case for PLP Shore 7, good agreement is shown for PLP Shore 9 between the predicted joint deformations and the actual joint deformations for the first story plywood brace in the linear elastic range. Interestingly, the model results predict that the lower right corner of the plywood brace experienced larger nail slip than the top right corner. The high computed slip shown for the bottom right corner suggests complete withdrawal of these nails. On the contrary, the images from the laboratory test illustrate that the nails at the top right end of the plywood brace had completely withdrawn. Again, numerous factors could have been responsible for the differences in the locations of high nail slip between the models and the physical tests.

In light of the results discussed in this chapter, the modeling scheme selected for the objectives outlined in this thesis proved, in general, to be successful in predicting the linear elastic response of the both the PLP and LP shores. All of the information presented above was used in determining appropriate design modifications to the LP and PLP shores that could improve the overall response of each structure. A summary of these design changes and analyses is presented in *Chapter 7*.

CHAPTER 7

Synthesis

This chapter is a discussion and analysis of the results from six different design modifications investigated for the purpose of improving overall shore behavior. Five design changes were studied for the plywood laced post (PLP) shore design while one was studied for the laced post (LP) shore design. It had been discussed during testing at FSEL that FEMA US&R was interested in possible improvements in the PLP design, so more emphasis is placed herein on obtaining new design and behavior performances for this particular shore. It should be noted that each design modification model incorporated the same values for the modulus of elasticity as the corresponding original shore.

Since apparent bending failures in the posts controlled the behavior of each specimen, it was decided that bending moments along the length of each post should be computed and compared with other designs. For each design change studied, the bending moment diagram for each post is presented. Additional output for the vertical stress distribution for each design modification model is available in Appendix B.

7.1 INVESTIGATIVE STUDIES FOR DESIGN IMPROVEMENTS

Prior to constructing new design models in Abaqus, a few studies were conducted based on the laboratory results as well as the results discussed in *Chapter 6*. The primary goal of these investigations was to determine any potential strengths and weaknesses of the PLP and LP shores that could inspire design improvements.

7.1.1 Average Axial Stiffness of Shores from Laboratory Tests

First, using the data obtained from the FSEL tests for each shore, an average axial shore stiffness was computed based on the average value of the modulus of elasticity for each post and the linear elastic portion of each shore's vertical load versus vertical displacement curve. Two plots are presented in Figure 7.1; they compare the average axial stiffness of the PLP and LP shores. The first plot includes the four shores subjected

to vertical load alone while the second plot reports the data from the shores subjected to both vertical and lateral loading.

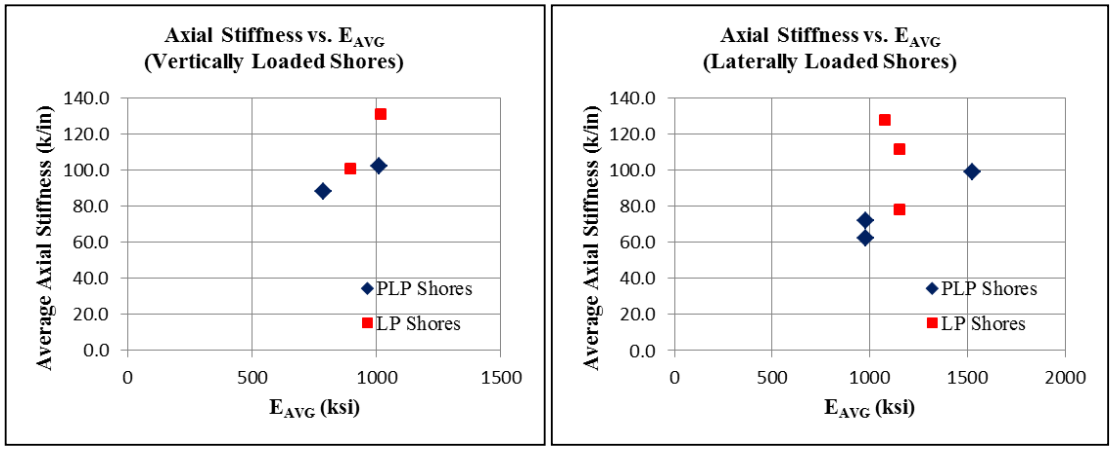

Figure 7.1 Average axial stiffness between PLP and LP shores from FSEL tests

The plots shown in Figure 7.1 show that for a given value for E_{AVG}, the LP shores yielded a higher overall axial stiffness than the PLP shores. This means that, in general, under a given vertical load, the LP shores would experience a smaller amount of vertical displacement than would the PLP shores. It was believed that the LP shore design owed its higher average axial stiffness to the layout of its braces. Along the length of each post in the LP shores, the horizontal and diagonal braces are spaced at roughly equal distances apart from one another. On the contrary, each post in the PLP shores has a large unbraced length between plywood braces. Because of this observation, a variety of unbraced lengths were incorporated into the design changes.

7.1.2 Bending Moment Diagram Comparisons

Next, a comparison of the computed bending moments for the posts in each shore from the finite element models was conducted. Figures 7.2 and 7.3 show the x-axis bending moment diagrams from *Chapter 6*. These plots, grouped by post location and loading scenario, served to reveal the magnitude and distribution of bending in each post based on its design type, PLP or LP. Recall from *Chapter 4* and *Chapter 6* the nomenclature for each post: FL for front-left, FR for front-right, BL for back-left, and BR for back-right.

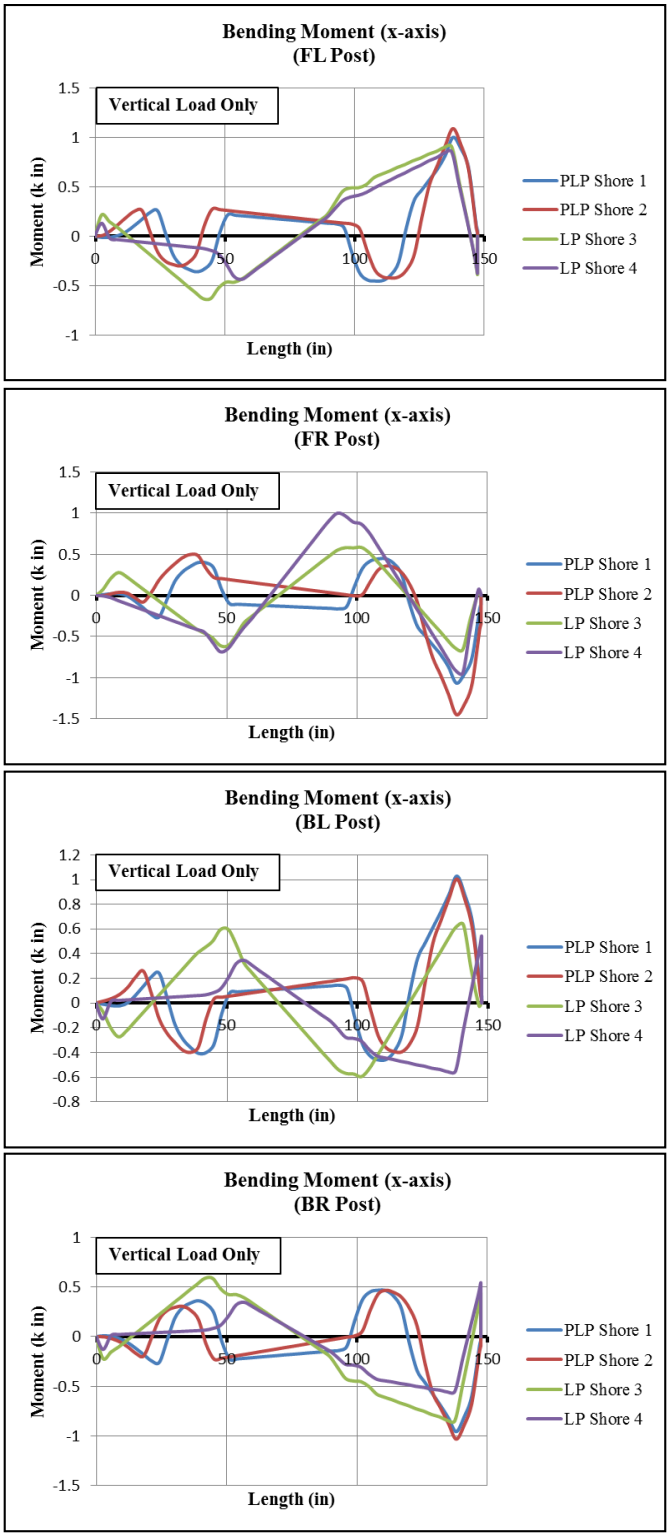

Figure 7.2 Bending moment diagrams for the shores subjected to vertical load only

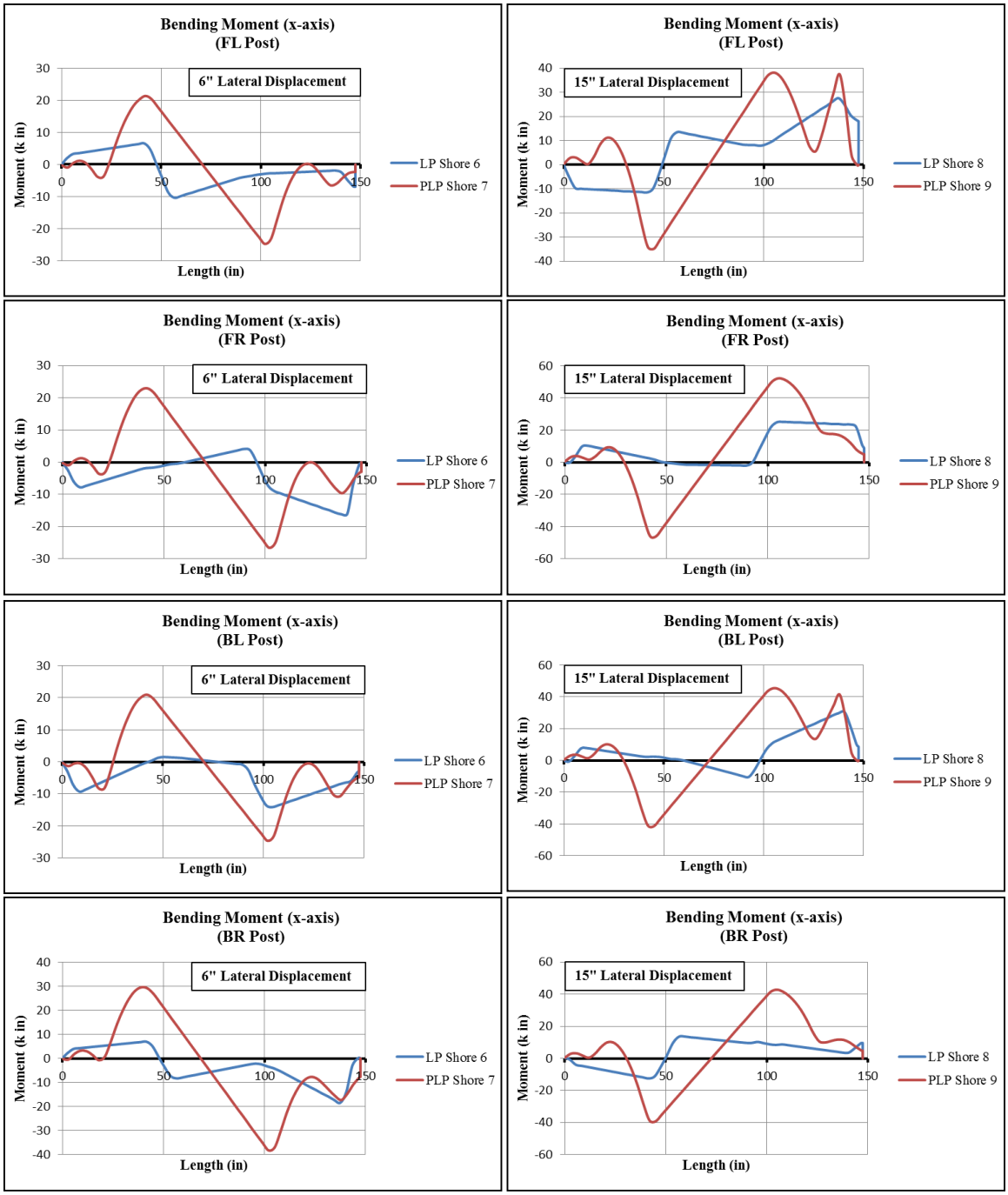

Figure 7.3 Bending moment diagrams for the shores subjected to both vertical and lateral load

The bending moment diagrams shown in Figure 7.2 reveal that the LP shores tended to have higher computed moment values along the length of the posts than did the

PLP shores. This trend was expected, however, since LP shores 3 and 4 in the finite element models were subjected to a total vertical load of 50 kips (10 kips higher than PLP Shores 1 and 2). Still, the PLP shores experienced higher maximum moment values at the top of the posts. Perhaps this difference was due to the higher number of nails fastened into the top region of the posts in the PLP shores.

Figure 7.3 has clear evidence of the dramatic difference in computed moments between the LP and PLP shores when subjected to both vertical and lateral load. As mentioned in the previous chapter, the PLP shores exhibited a very consistent profile in each post while the LP shore posts seemed to have no overarching pattern. Interestingly, for the shores subjected to an initial lateral displacement of 6 inches, the PLP shore posts revealed bending moments over twice those of the LP shores. By comparison of the LP and PLP plots in Figures 7.2 and 7.3, it was learned that the plywood braces have a much more significant impact on the bending response of the posts when lateral loading is involved. The difference in bending moment magnitudes between the LP and PLP shores in Figure 7.3 (for combined vertical and lateral loading) is substantial, whereas the plots in Figure 7.2 (for vertical load only) indicate that both shore designs produced similar ranges of bending moments.

7.1.3 Nail-Slip Comparisons

Lastly, the maximum computed first-story nail-slips in each shore were compared. The bar charts in Figure 7.4 present the maximum horizontal and vertical nail-slip values obtained from Abaqus.

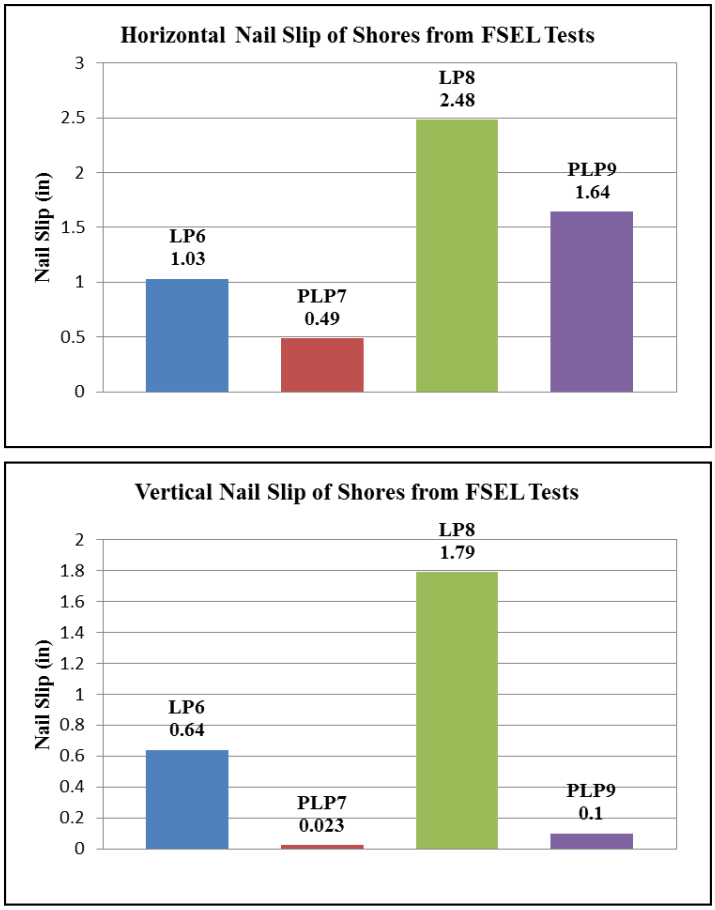

Figure 7.4 Horizontal and vertical nail-slip values obtained from Abaqus

The high computed nail slip values given for the LP shores in Figure 7.4 indicate that the nails have completely pulled out of the posts, as confirmed by the photographic evidence in *Chapter 4* and the comparisons between the computed and observed nail slips in *Chapter 6*. These plots also show that even though the PLP shores allowed high bending moments to develop in their posts, their joints tended to experience much less nail withdrawal under the presence of lateral load than those in the LP shores. As a result, the plywood braces in the PLP shores remained attached to the posts longer and thus became more effective throughout the loading sequence. Indeed, the FSEL data confirmed that the PLP shores boasted higher ultimate capacities than the LP shores (*Chapter 4*).

7.2 DISCUSSION OF DESIGN MODIFICATIONS

All of the studies described and summarized in the previous sections provided valuable insight and inspiration for the design modifications discussed hereafter. Some of the design changes simply consisted of rearranging members while others involved the addition of members to the original design. Recall the original designs used for the shores in the laboratory tests, as currently published in the USACE FOG (24). Sketches of these shores are presented in Figure 7.5.

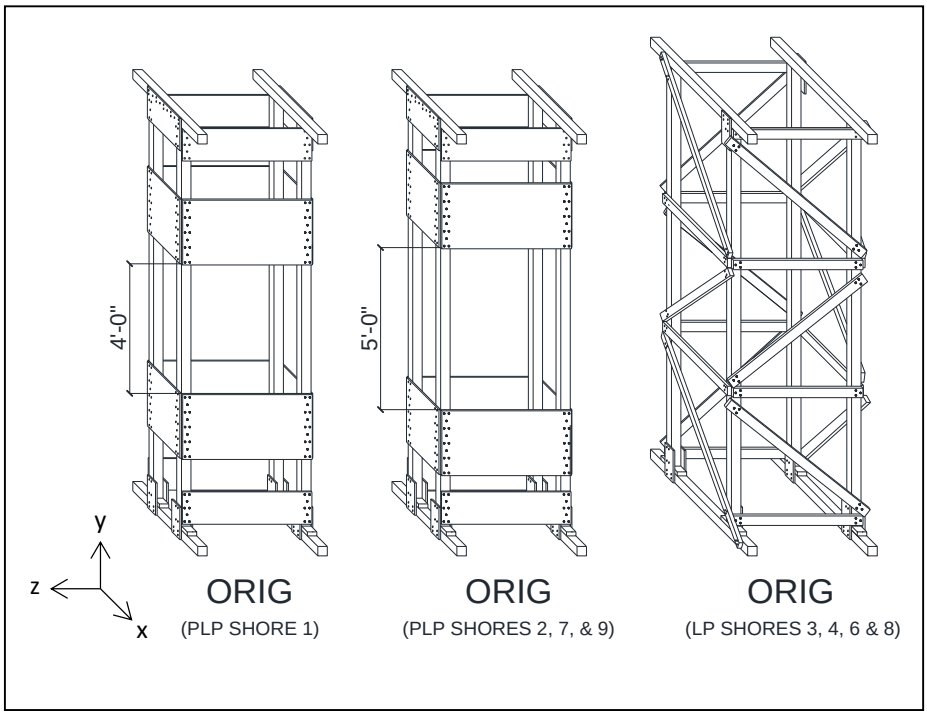

Figure 7.5 Schematic drawings of the original shores tested in the laboratory

Sketches of the five design modifications investigated for PLP shore design are shown in Figure 7.6 while Figure 7.7 presents the design change analyzed for the LP shore design.

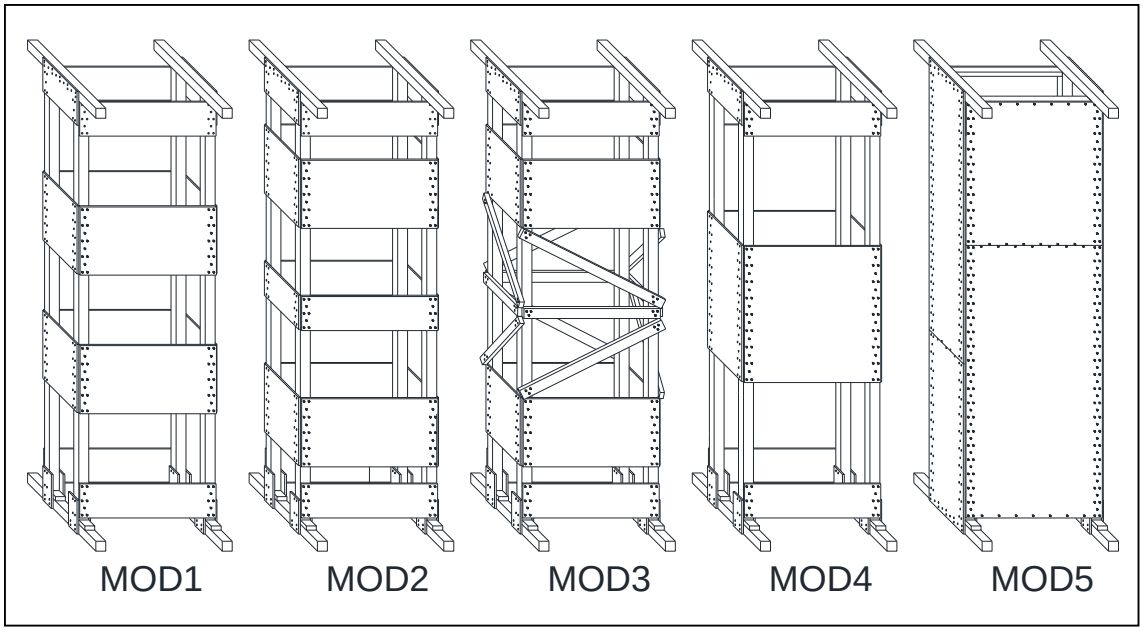

Figure 7.6 Design modifications made for the PLP shore design

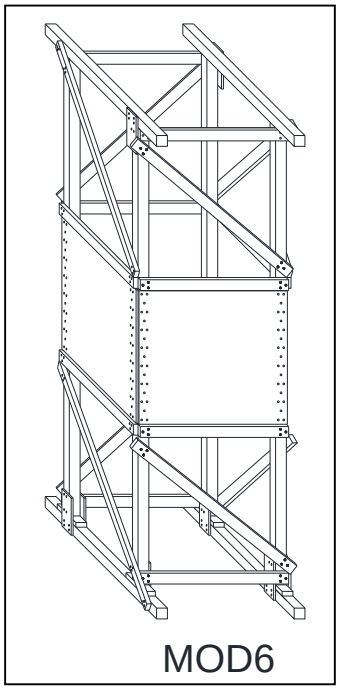

Figure 7.7 Design modification made for the LP shore design

7.2.1 Design Modification 1

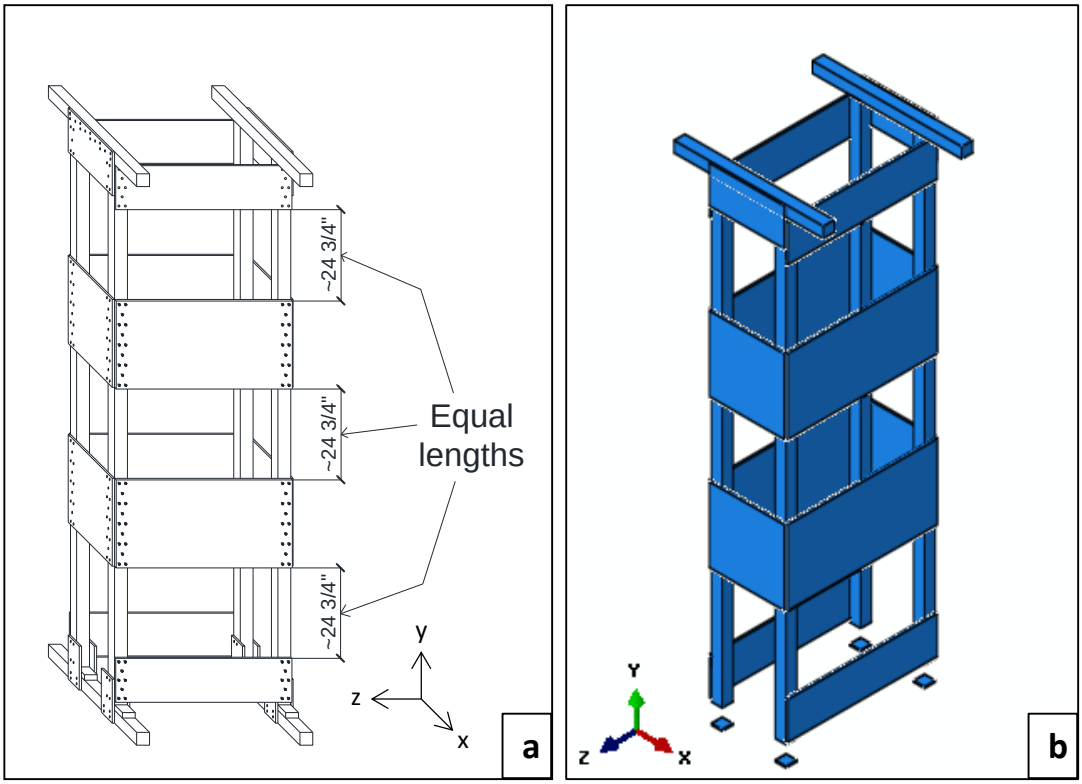

Figure 7.8 Design modification 1 (a) Sketch (b) Rendered Abaqus model

The purpose of the first design change was to observe differences in behavior of the shore by simply moving the two levels of plywood braces toward the center of the tower, resulting in three equidistant unbraced lengths for the posts. As discovered by the plots in Figure 7.1, the average axial stiffness of the LP shores exceeded those of the PLP shores. Since it was hypothesized that this trend was due to the relatively equal unbraced lengths in the posts of the LP shore design, this philosophy was applied to the PLP shore.

7.2.2 Design Modification 2

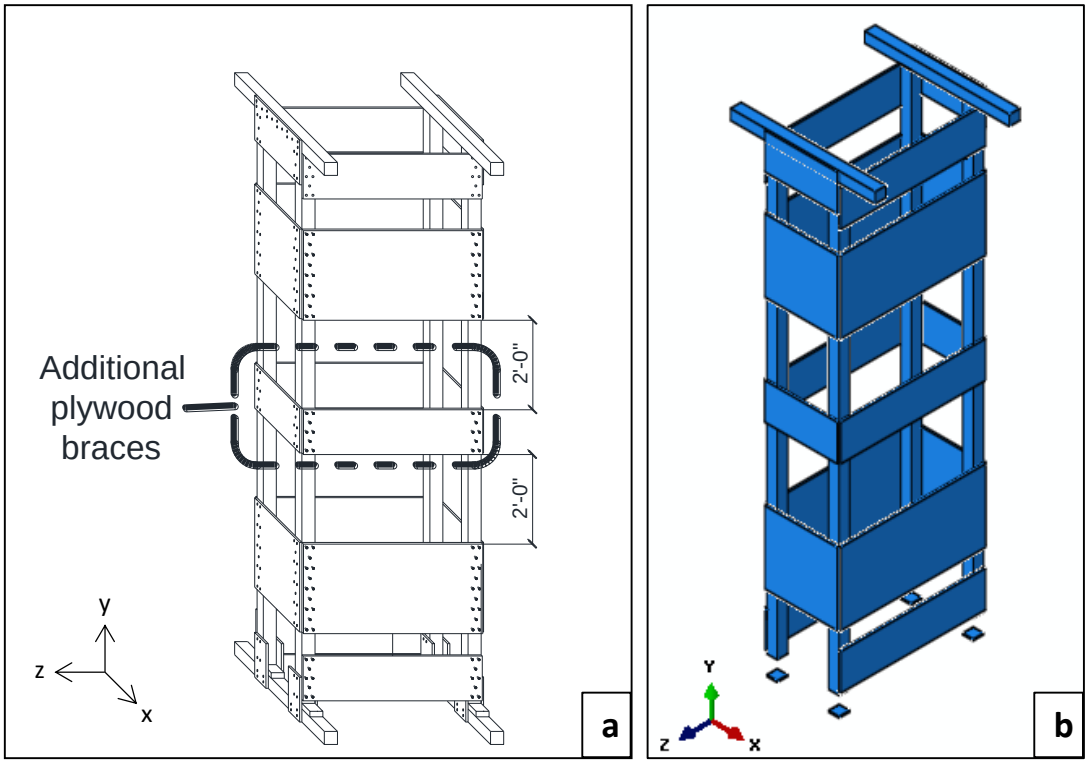

Figure 7.9 Design modification 2 (a) Sketch (b) Rendered Abaqus model

The second design change involved the addition of 12-inch wide plywood braces at mid-height of the shore while keeping all other members in their original positions. The idea behind this modification was that these braces would help to increase the average axial stiffness of the shore and mitigate the bending effect in the center of the posts. Another way of thinking about this particular design is like a PLP shore within a PLP shore.

7.2.3 Design Modification 3

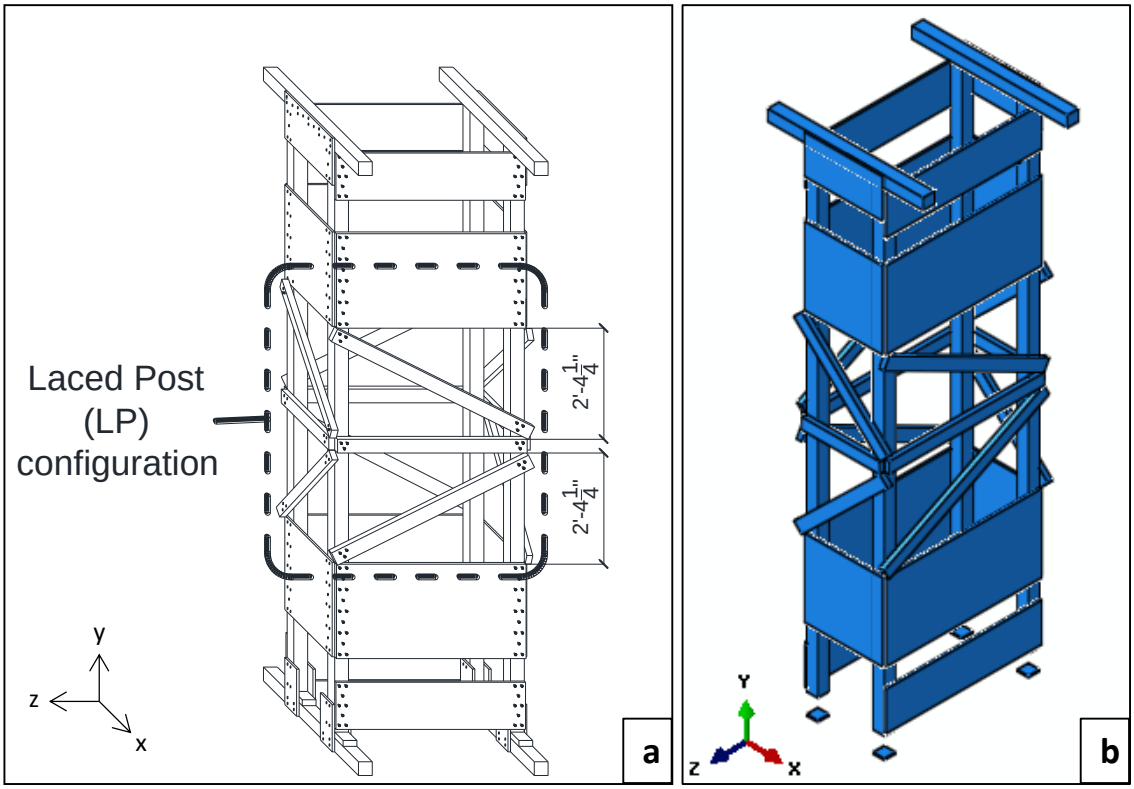

Figure 7.10 Design modification 3 (a) Sketch (b) Rendered Abaqus model

To compare the effectiveness of adding different bracing systems to the posts of the PLP shores, a LP configuration was added for the third design change. Based on the bending moment diagram comparisons from Figure 7.3, the LP bracing system seemed to provide the best alternative for minimizing bending moments. Thus, the major goal in this design change was to decrease the bending moments developed in the posts during lateral loading.

Whereas the second design change was thought of as a PLP shore within a PLP shore, this design change resembled a LP shore within a PLP shore. It was anticipated that this particular design would yield the most favorable results, since it combined the geometry of both shoring systems.

7.2.4 Design Modification 4

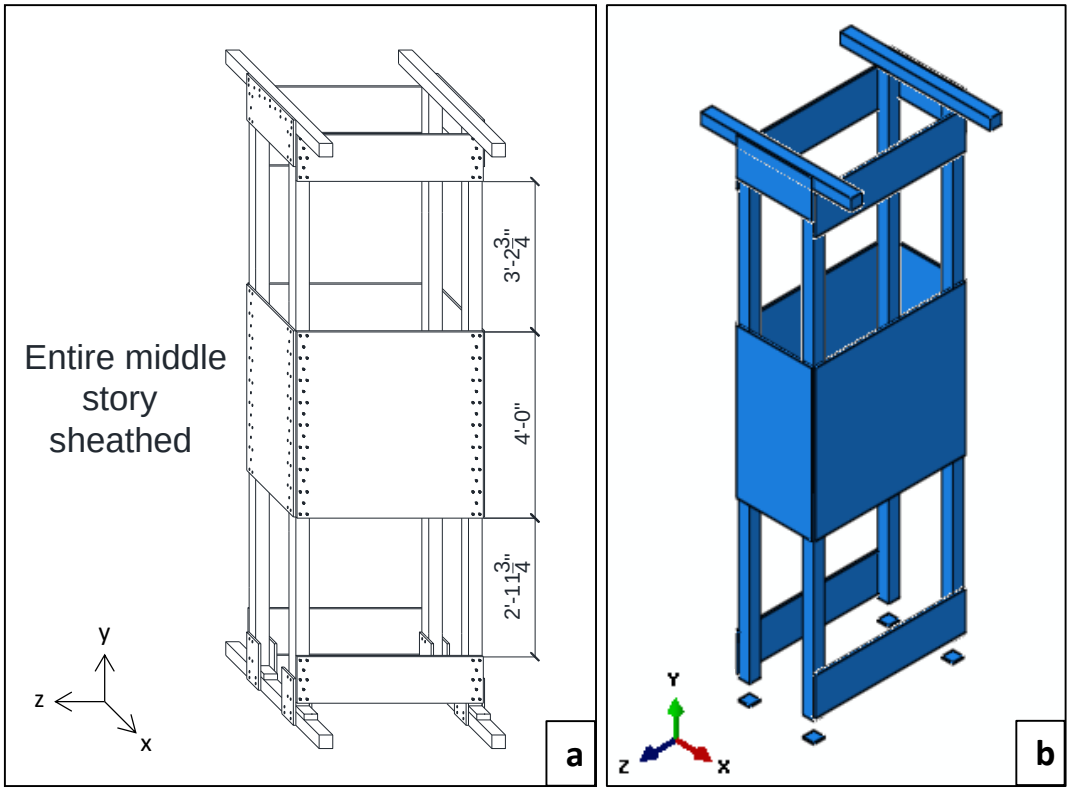

Figure 7.11 Design modification 4 (a) Sketch (b) Rendered Abaqus model

The fourth design change aimed to demonstrate what happens when the plywood braces from the original PLP design are combined at mid-height of the shore to form a single level of bracing. Upon initial inspection of the design, it seemed that nail slips could be reduced and outward bowing of the posts in the middle of the shore would be minimized. At the same time, however, as determined in *Chapter 6*, the bending moments in each post tended to be highest at plywood joint locations.

7.2.5 Design Modification 5

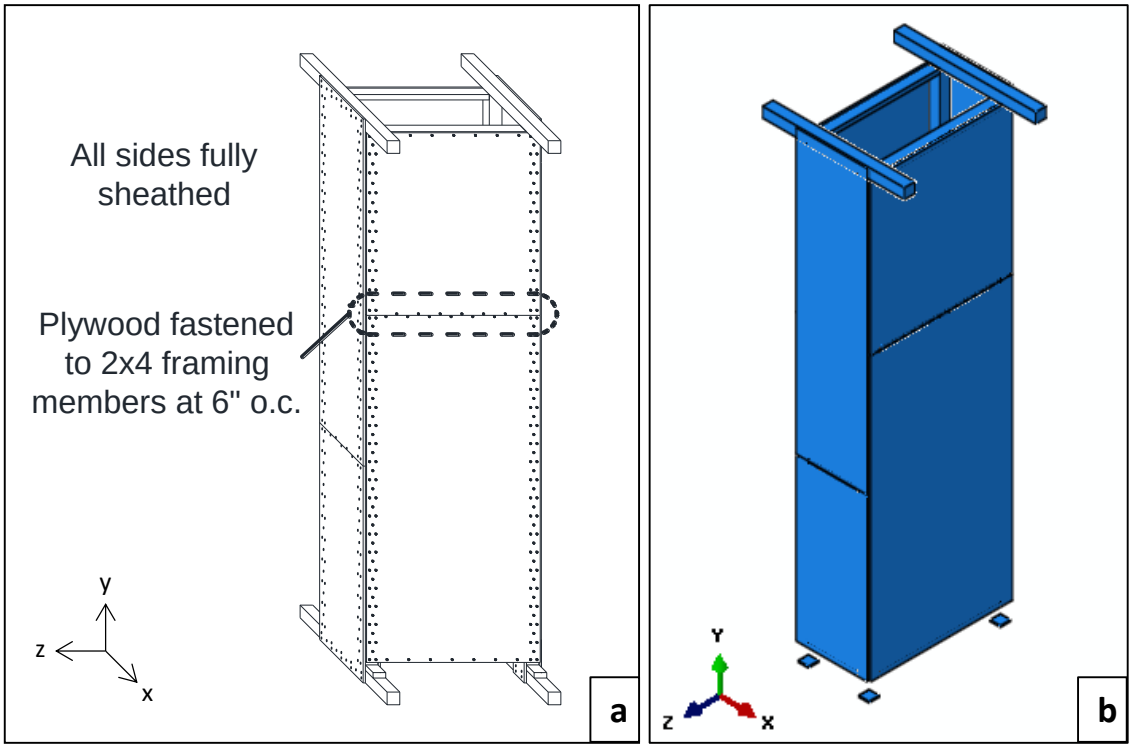

Figure 7.12 Design modification 5 (a) Sketch (b) Rendered Abaqus model

The fifth and final design change made to the PLP shores consisted of full-sheathing on all four sides of the shore. To maximize the effect of the plywood braces, each member was fastened to intermediate framing members. Consequently, the system mimicked that of a shear wall, providing enormous lateral stiffness to the shore. It had been discussed during testing at FSEL that this design had interested the FEMA US&R teams for quite some time. Of particular concern was the response of this shore to lateral loading at the top. Without any region of unbraced length along the posts, it seemed difficult to imagine the resulting deformed shape if the shore were subjected to 15 inches of lateral displacement.

7.2.6 Design Modification 6

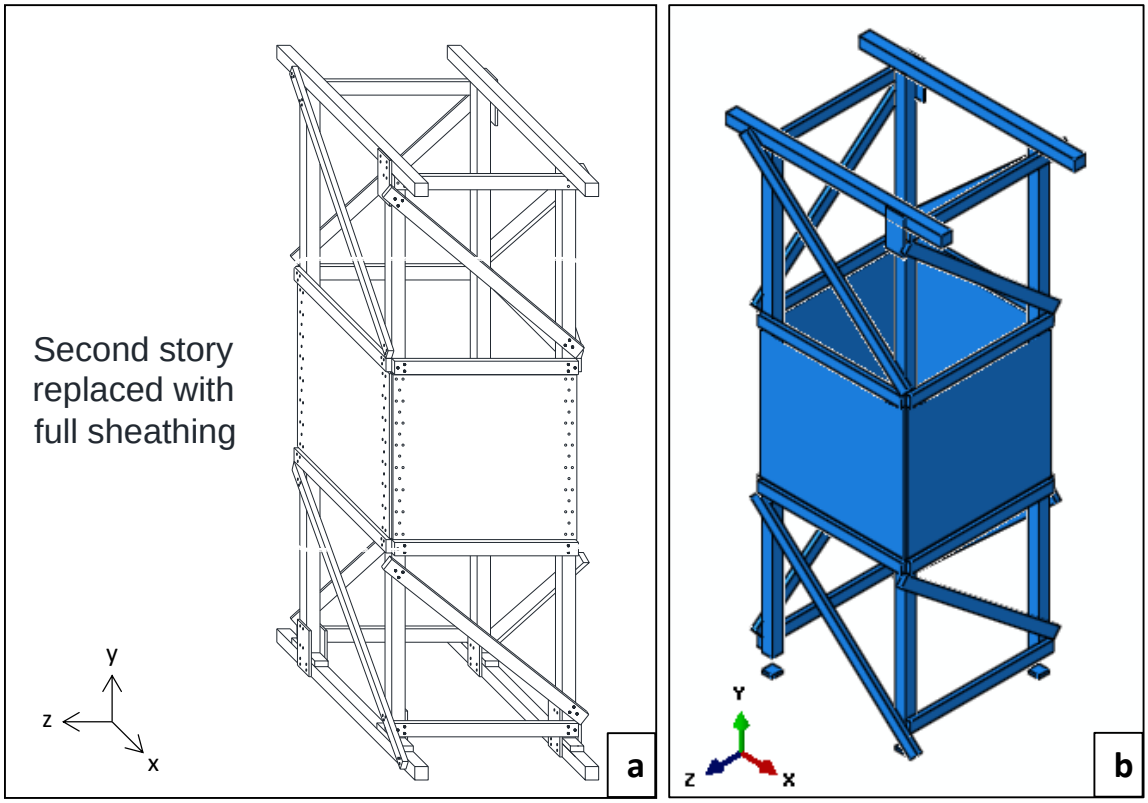

Figure 7.13 Design modification 6 (a) Sketch (b) Rendered Abaqus model

The only design modification investigated for the LP shores consisted of replacing the diagonal braces in the second story with sheathing. Each plywood brace in this design is fastened to the neighboring posts using the same layout as the PLP shores. Also, a small gap separated the top and bottom edges of each plywood brace from the horizontal braces that framed into them. Of particular interest was the nail-slip behavior under lateral loading.

7.3 COMPARISON OF RESULTS

The following sections contain comparisons of the results acquired from the design changes analyzed in Abaqus. Bending moments along each post as well as nail-slip responses were compared to evaluate the effectiveness of each design.

7.3.4 Bending Moment Comparisons for Posts in PLP Shores

Bending moment diagrams for each post in a shore were computed and plotted for each design modification. The results from each analysis are presented in a group of plots that encompass all four of the PLP shores tested in the laboratory, as shown in Figure 7.14 through 7.17.

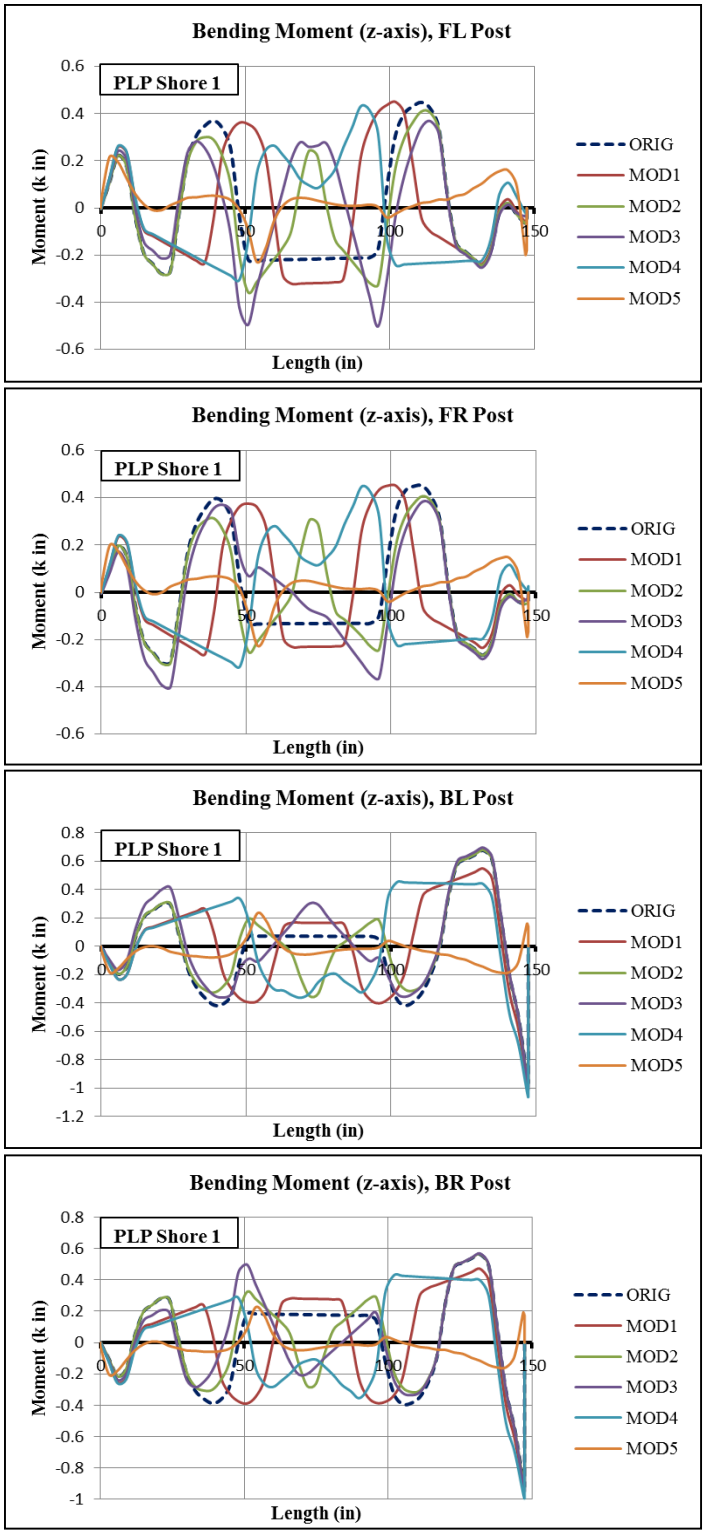

Figure 7.14 Bending moment diagram comparisons for PLP Shore 1

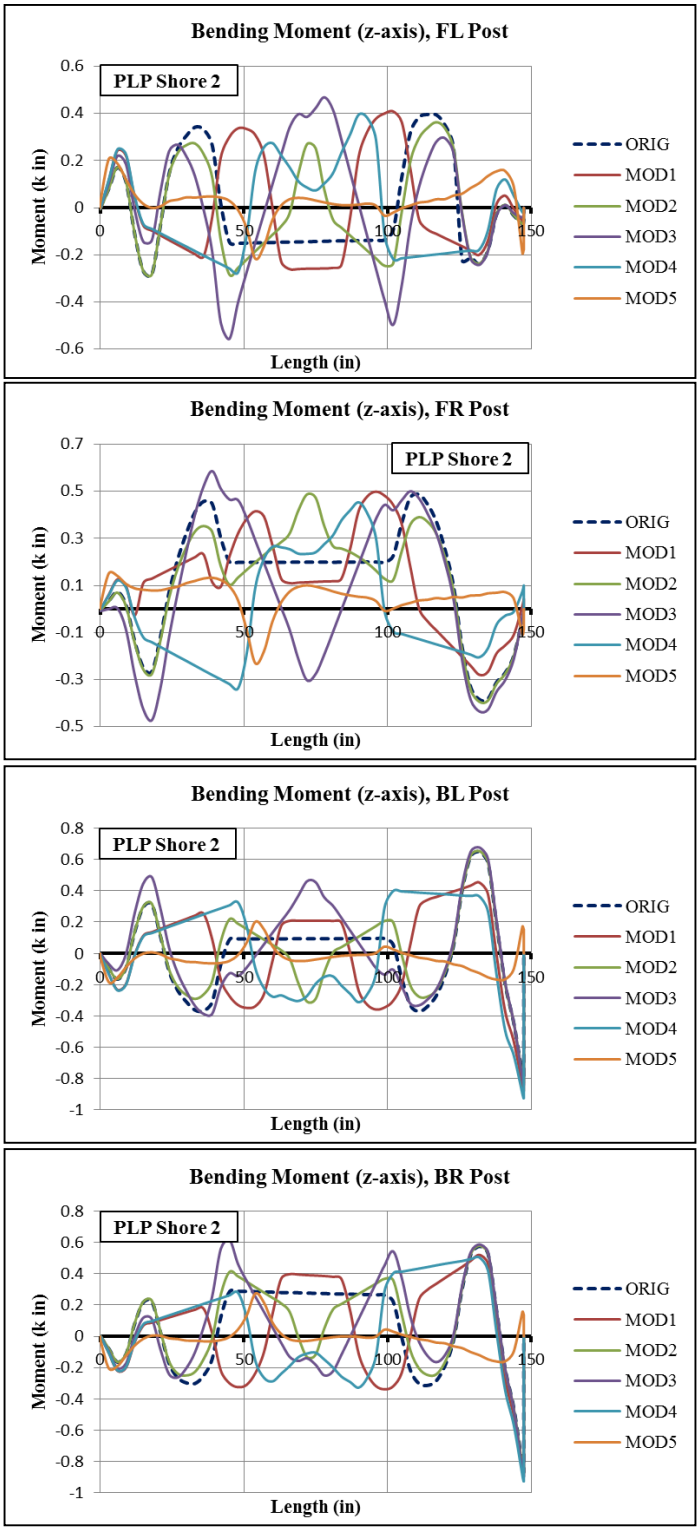

Figure 7.15 Bending moment diagram comparisons for PLP Shore 2

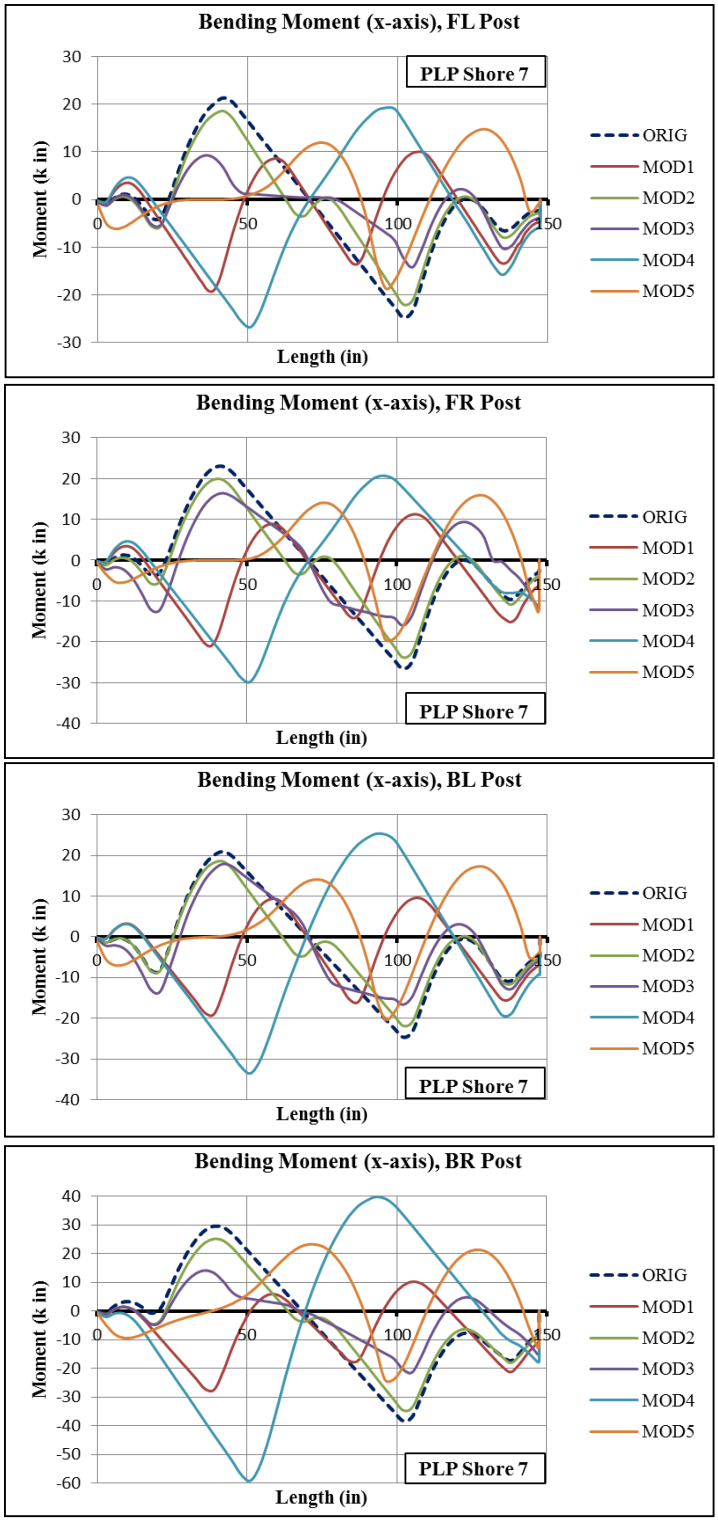

Figure 7.16 Bending moment diagram comparisons for PLP Shore 7

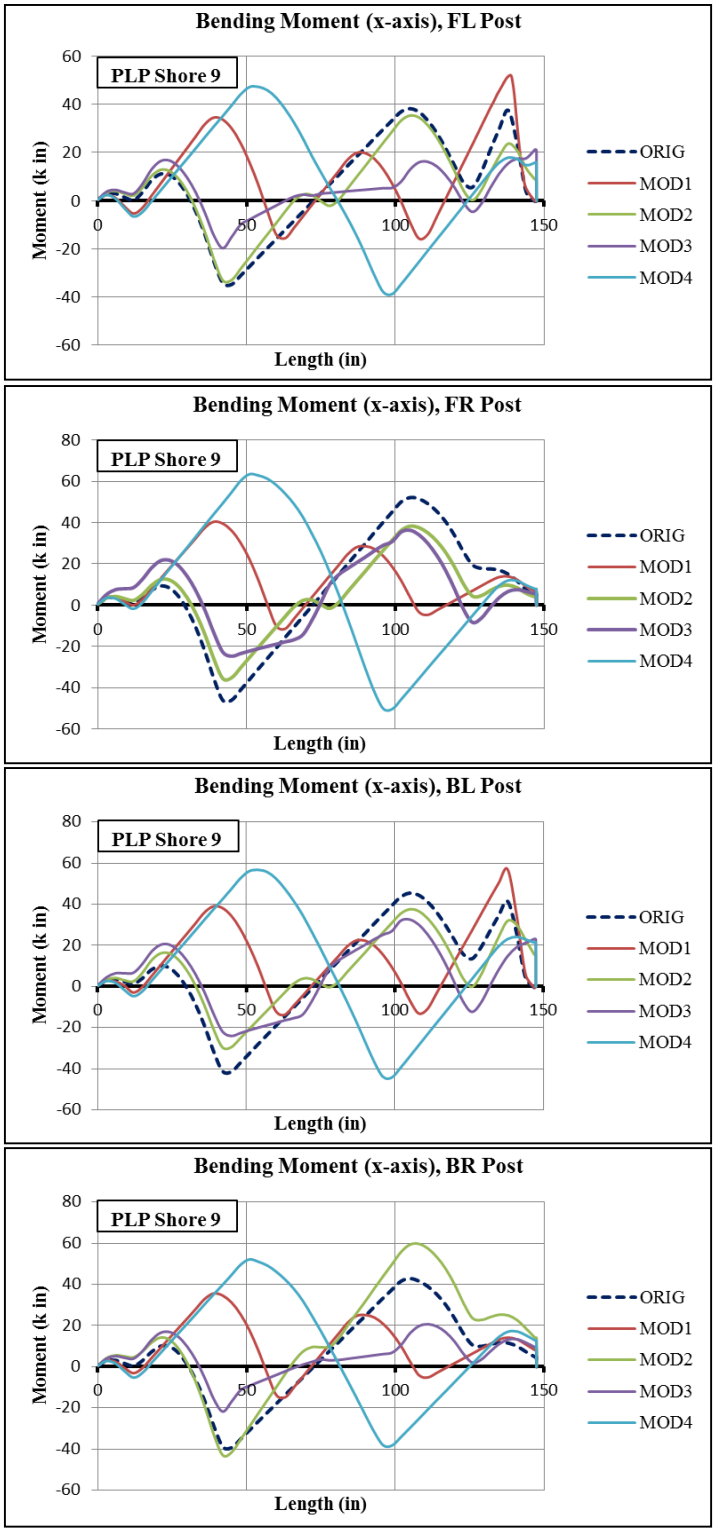

Figure 7.17 Bending moment diagram comparisons for PLP Shore 9

Figures 7.14 and 7.15 indicate that MOD1 makes little difference in bending moment values for shores subjected to purely vertical load. The humps (local regions of higher moment values) occurred closer to mid-height of posts as would be expected with the new plywood brace locations. The curves from MOD2 in these same figures reveal that the addition of small plywood braces at mid-height of the shore resulted in a slight decrease in moments at the other two brace locations. However, this decrease was accompanied by two curvature changes—that is, regions where the bending moment changed from a positive value to a negative value or vice versa—as well as an increase in moment at the center of each post. In general, MOD3 showed a consistent and noticeable decrease in the bending moments near the plywood braces. Occasionally, there would also be a local peak moment at mid-height of some of the posts. In terms of magnitude and profile, the moment diagrams from MOD4 yielded the most inconsistent results. However, MOD4 was the only design modification to show a substantial decrease in the maximum bending moment at the top of the posts. The design change with the most desirable impact on the bending behavior of each post was MOD5. Throughout the height of each post, the bending moments were much smaller than those from the other designs. In nearly every post, MOD5 avoided the high moment experienced at the top of the member by every other design modification, including the original design.

As expected, the moment diagrams for the shores involving vertical and lateral loads produced much more varied results. Upon first glance of Figures 7.16 and 7.17, a designer can almost immediately rule out MOD4 as a desirable option. In many of the plots, MOD4 revealed an increase in peak moments from the original design. The curves given by MOD1 indicate that the bending moments were distributed more evenly along the height of each post. Moreover, MOD1 yielded smaller peak bending moments than the original shore. The modification that produced the greatest improvements in terms of bending moment was MOD3. This design change displayed consistent decreases in peak bending moments in each post. In all plots except for one, MOD2 showed a slight decrease in bending moments along the height of each post.

A successful analysis from MOD5 for PLP Shore 9 was not able to be obtained. It was speculated that the difficulty in running the analysis was due to high nail slip values at the line of contact between the two plywood sheets on the front and back sides of the shore. The lack of any portion of unbraced length on the posts for MOD5 forces the adjacent plywood braces to work against one another. This tight arrangement of plywood braces is thought to rapidly accelerate the rate of nail slip. In other words, for shores expected to undergo a combination of vertical and lateral loads, it is desirable to keep the plywood sheets separated by a small gap (1 to 2 inches) in order to eliminate their interaction.

7.3.4 Maximum Nail-Slip Values for PLP shores

The column charts shown in Figure 7.18 show the maximum horizontal and vertical nail-slip experienced by the plywood braces in the PLP shore modifications. The values from the original shore tested at FSEL are also included.

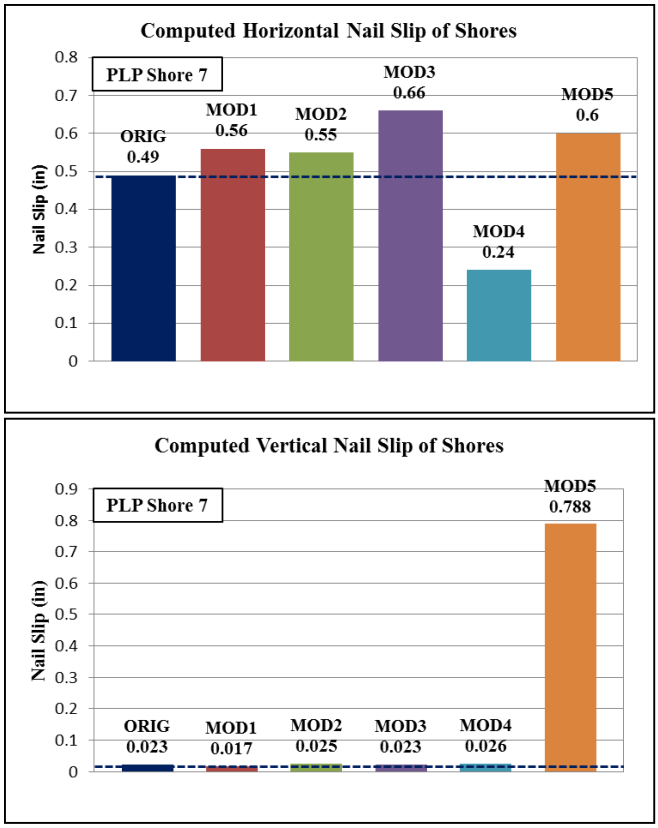

Figure 7.18 Comparison of maximum plywood brace nail-slips for PLP Shore 7

Clearly, the horizontal component of nail-slip proved to be the highest in magnitude for all shores except MOD5. The only design to actually achieve a decrease in horizontal nail-slip was MOD4, which was likely due to the brace's location at mid-height of the shore. Surprisingly, MOD5 yielded an extreme outlier for the vertical component of nail-slip. Apparently, not including a separation between plywood members forces the nails to undergo more deformation under the action of lateral load.

Figure 7.19 presents the maximum nail-slip values obtained for PLP shore 9. Data for MOD5 is not included since a successful analysis for this design could not be achieved.

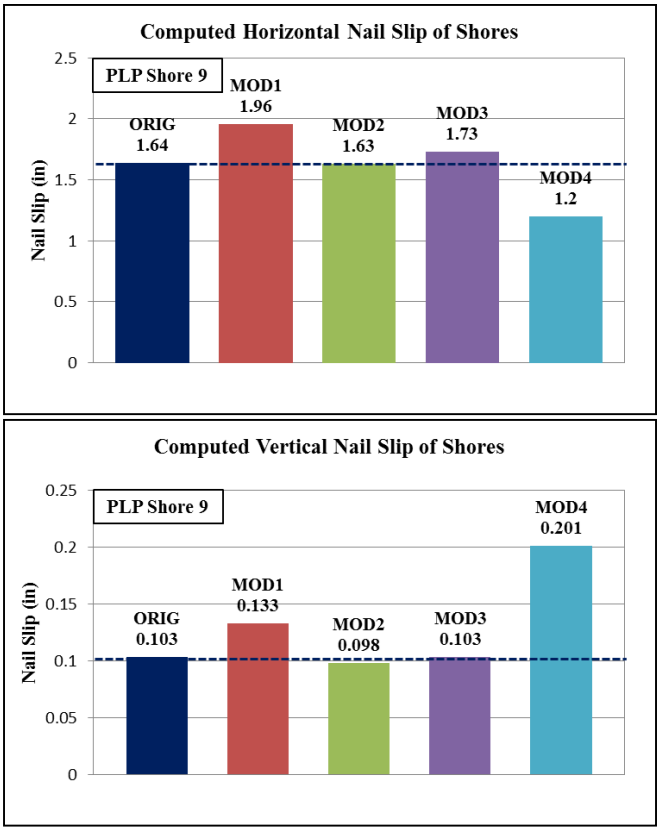

Figure 7.19 Comparison of maximum plywood brace nail-slips for PLP Shore 9

Again, MOD4 produced the greatest decrease in maximum horizontal nail-slip. However, this same design yielded the highest increase for the vertical component. All other designs tended to remain relatively similar to the original values, with MOD1 revealing consistent increases for both the horizontal and vertical components.

7.3.4 Bending Moment Comparisons for Posts in LP Shores

The next few figures (7.20 through 7.22) illustrate the moment diagrams obtained for the LP shores.

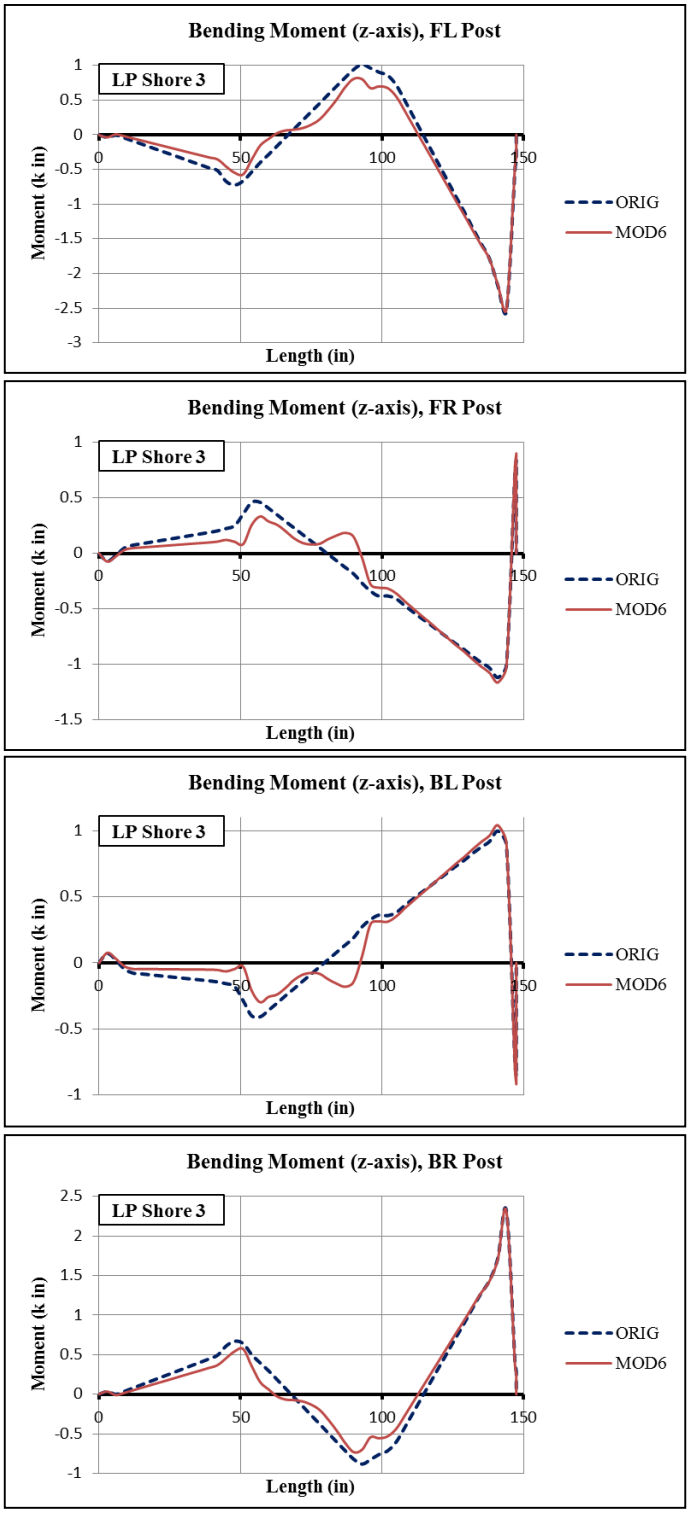

Figure 7.20 Bending moment diagram comparisons for LP Shore 3

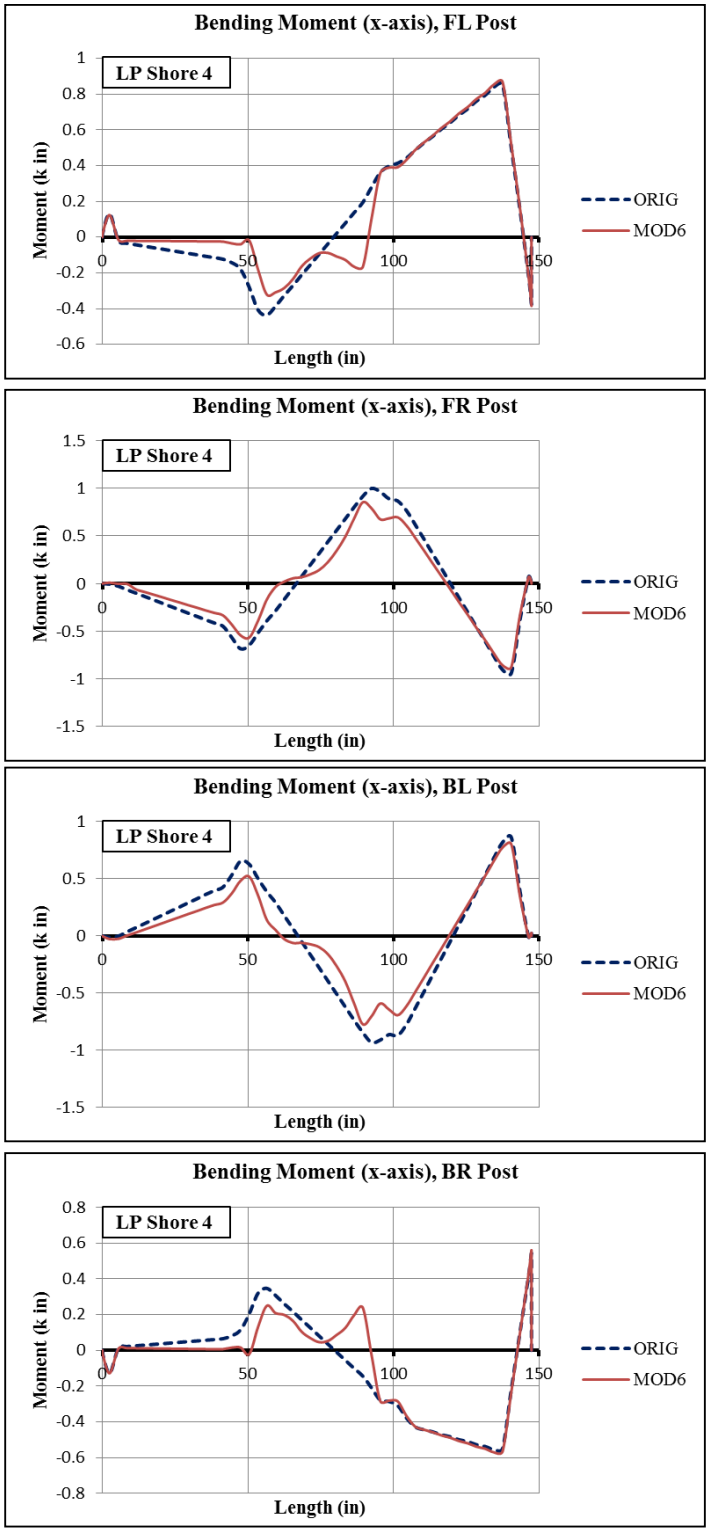

Figure 7.21 Bending moment diagram comparisons for LP Shore 4

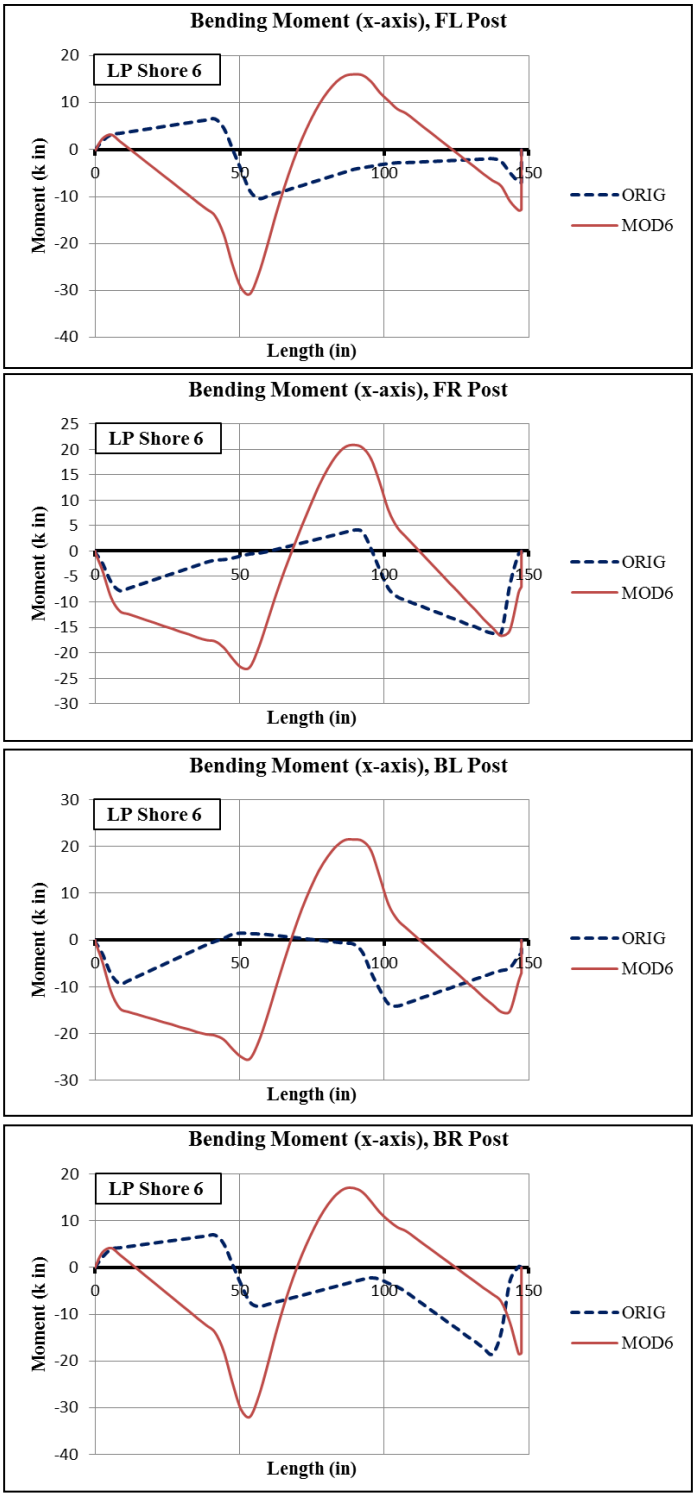

Figure 7.22 Bending moment diagram comparisons for LP Shore 6

Figures 7.20 and 7.21 demonstrate that MOD6 yielded bending moments in the posts that were slightly smaller than those of the original shore. At the same time, the middle region of the post exhibited some unpredictable bending behavior due to the presence of the large plywood braces.

As for the laterally loaded Shore 6, Figure 7.22 confirms the analysis run for MOD6 resulted in enormous increases in bending moments along the entire length of the posts. In essence, even without conducting a nail-slip comparison, it appears that no worthwhile benefit is afforded by constructing a shore using the MOD6 design.

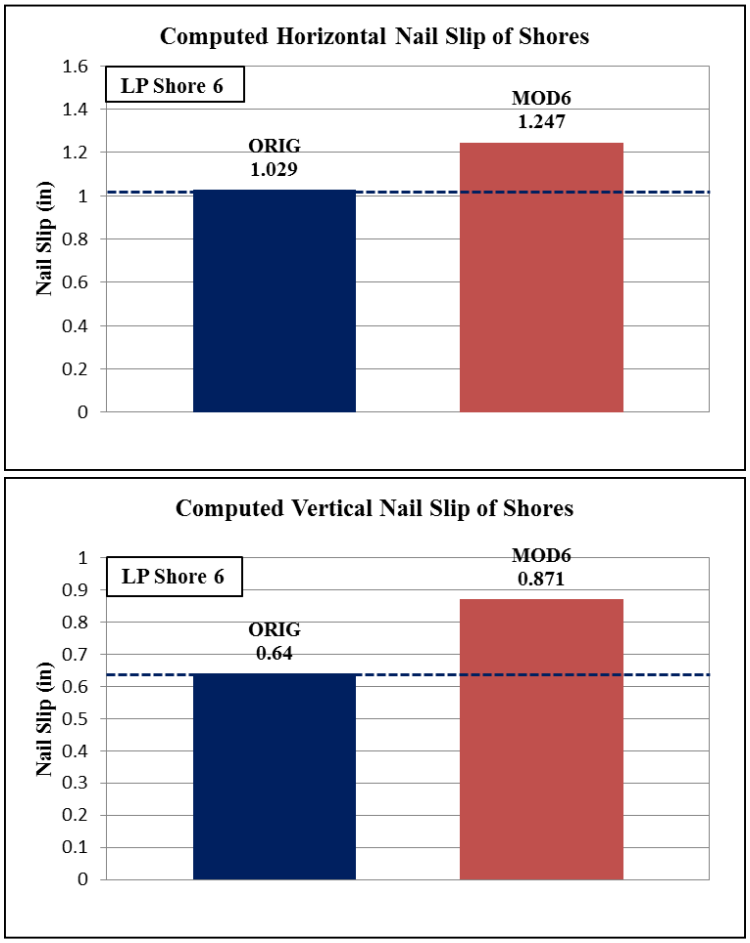

Figure 7.23 Comparison of maximum plywood brace nail-slips for LP Shore 6

Indeed, as shown in Figure 7.23, the addition of plywood braces to the second story of the LP shore not only increased the post bending moments but also the maximum nail slip in the first story diagonal brace.

7.3.4 Design Recommendations Based on Model Results

The following sections contain recommendations based on the observations discussed in this chapter with respect to the model results.

7.3.4.1 PLP Design Recommendations for Vertical Load Only

In regards to shores subjected to purely vertical load, MOD5 offers, in the most straightforward sense, the most desirable improvements in terms of post bending. The posts in this particular design consistently produced the smallest bending moments. At the same time, the designs given by MOD2 and MOD3 appear to produce reliable and consistent results with regards to decreasing the peak bending moments in the shore posts. However, these decreases amounted to nowhere near those provided by MOD5. As discussed above, MOD1 only served to shift the locations of the local peak bending moments in the posts with hardly any effect on the magnitudes. Although MOD4 showed some improvements in nail-slip values and maximum bending moments, the results were extremely inconsistent.

7.3.4.2 PLP Design Recommendations for Combined Vertical and Lateral Load

For a situation in which the probability for lateral loading on a shore is high, it seems best to opt for MOD3 or MOD1. Each of these designs revealed substantial decreases in post bending moments with respect to the original shore. Although the nail slips in the first story joint might be higher than the original shore design, MOD3 has additional members that could help to redistribute stresses if a nail withdrawals. MOD1 is an especially desirable alternative to the original shore because it consists of the exact same members, just slightly rearranged. The large computed bending moments for MOD4 make it clear that this design would not serve as an appropriate alternative for use in the context of combining vertical and lateral loads. Even with all of the additional

nails used in the design for MOD5, bending moments in the posts did not decrease much from those of the original shore.

7.3.4.3 LP Design Recommendations for Vertical Load Only

As discussed in this chapter, MOD6 showed little to no changes in the post bending moments for LP Shore 3 and LP Shore 4. Because the same apparent behavior can be achieved with the original LP shore design (which uses fewer nails than MOD6), it is not recommended to use MOD6 for purely vertical load applications.

7.3.4.4 LP Design Recommendations for Combined Vertical and Lateral Load

The results clearly indicate that MOD6 negatively affects the bending and nail slip behavior when lateral load is involved. In the field, there is never certainty that a given shore will experience strictly vertical load. Therefore, in no situation is it recommended to use MOD4 as an alternative for the LP shore design.

In light of the output obtained for all the PLP shore models, MOD3 proved to be an overall desirable design alternative. Even though other shores yielded favorable results as well (such as MOD5 for vertical load only and MOD1 for vertical and lateral load combined), MOD3 yielded improved behavior for both of these cases. It is recommended, therefore, that this shore design or a shore of a similar geometry be constructed and tested experimentally to verify the predicted improvement in behavior.

Chapter 8 provides an all-encompassing summary of the observations and conclusions reached with the respect to the shore tests, shore models, and design modifications.

CHAPTER 8

Summary and Conclusions

This thesis has presented a structural finite element analysis of wood shoring used by Urban Search and Rescue (US&R). As part of a previous study (14), several tests were conducted on Laced Post (LP) and Plywood Laced Post (PLP) shores at the Ferguson Structural Engineering Laboratory in Austin, Texas. A selected set of these laboratory results then was used to construct finite element models—using Abaqus—of the shores for the purpose of suggesting improved designs for future use by US&R.

Although a total of thirteen shores were constructed and tested at FSEL, computer models were built for eight of them. The five shores that were excluded from the modeling involved reversed cyclic loading and load rate effects. The following sections summarize the findings in this research as a response to the objectives of this thesis.

8.1 Agreement Between Laboratory Results and Finite Element Models

Typical vertical load-displacement responses of the eight shores modeled had the following regions: system engagement (stiffening), fully-engaged loading (linear and nonlinear up to the peak load), and a failure region. The finite element models only included the linear response portion of the fully-engaged loading region; however, nonlinear nail-slip behavior was included for all nails in the models.

Some key observations from the comparisons between the predicted and actual shore behavior for the test specimens:

- In general, the computed results from Abaqus for the vertical load-displacement response in the linear elastic region exhibited close agreement with the results from the laboratory tests. The discrepancies encountered when making these comparisons for the shores subjected to large lateral displacements (LP Shore 8 and PLP Shore 9) are believed to be the result of members becoming inelastic and nails at or near complete withdrawal from the posts.

- For the majority of the shore posts, the computed bending moment diagrams showed that the first failure of posts occurred near a local maximum value, as expected. However, the presence of knots throughout each post sometimes caused this failure to occur at a location where the computed bending moment was rather small.
- The deformed positions of the shore predicted by Abaqus, when compared with the deformed position of the laboratory specimen at a similar value of load, yielded good agreement with regards to overall displaced position of the structure as well as joint behavior. Even though the Abaqus models predicted the first-story diagonal braces in LP Shore 6 and LP Shore 8 to displace in opposite directions to the actual members, the apparent magnitude and direction of the nail slips closely resembled those of the test specimens.
- Based on the good agreement observed between the computed results and the laboratory results, the modeling scheme utilized in this research has proven adequate for further use in obtaining model results for shore design modifications.

8.2 RESULTS FOR PLYWOOD LACED POST DESIGN MODIFICATIONS

Some key observations from the model results for the five PLP design modifications:

- For shores subjected to vertical load only, MOD1 did not provide any decreases in bending moments in the posts. In fact, bending moments at mid-height of the posts actually increased. The local peak moments only shifted locations to reflect the new positions of the plywood braces. However, when a combination of vertical and lateral load is involved, then MOD1 predicts significant reductions in peak bending moments in all posts.

- Like MOD1, the design for MOD2 reveals a consistent increase in bending moment in all posts at mid-height for shores subjected to only vertical load. On the other hand, MOD2 also displays slight, but consistent, decreases in local peak bending moments. In general, MOD2 shows modest decreases in bending moments throughout the height of each post for shores experiencing combined vertical and lateral loads.
- Based on the model results, the design for MOD3 appears to be a universally trustworthy shore. When compared to the original shores tested in the laboratory, this particular design produced consistent decreases in bending moment values in all posts for all loading scenarios investigated. Furthermore, the maximum computed nail slip values for MOD3 remained close to those of the original PLP shores.
- In all analyses run for the shore design of MOD4, whether for vertical load only or a combination of vertical and lateral loads, peak bending moments increased substantially in every post. Therefore, it is unlikely that this would be an effective design for a shore.
- For shores subjected to vertical load only, providing full sheathing on all four sides of the shore (MOD5) significantly decreases the bending moments experienced in all posts. The tremendous in-plane strength and stiffness of the plywood braces serves to mitigate bending throughout the height of each post.
- Providing sheathing on all four sides of the shore (MOD5) is not recommended for shores that may experience combined vertical and lateral loading. In this case, it appears that the high strength and stiffness of the plywood braces prevents the shore from displacing laterally while remaining intact. With no region of unbraced length for the posts to sway freely, many of the nails likely experience withdrawal prior to the shore reaching a large lateral displacement. Some of these connection issues may be mitigated by providing a physical gap between sheets of sheathing

at various levels. It is speculated that along nailed sheathing edges that may be in contact, the nails therein are required to carry high loads, which may force them toward a withdrawal state.

- Nail-slip values for all PLP shores subjected to vertical load only were extremely small in magnitude. Also, normal and shear forces in the plywood braces were negligible, indicating these members did little more than serve as connections between posts. Therefore, it is believed that thinner plywood members could be used on PLP shores subjected to vertical only.

8.3 RESULTS FOR LACED POST DESIGN MODIFICATIONS

Some key observations from the model results for the LP design modification:

- The addition of plywood bracing to an entire story of an LP shore provides no benefit in terms of induced bending moments in posts or nail slip values. In fact, bending moments in all posts increased (for combined vertical and lateral loading) when the second story diagonal braces were replaced with plywood sheathing. Moreover, maximum computed nail-slip values increased in both the horizontal and vertical directions for MOD6. Consequently, in light of the model results, the design for MOD6 is not encouraged for use in future shores.

8.4 RECOMMENDATIONS FOR FURTHER RESEARCH

The modeling presented in this thesis is intended to serve as a foundation to be extended upon through future modeling of wood shoring towers. Choices of element types for sheathing, wood framing, and connections herein appear to give rational results that are generally consistent with observations from physical tests, and they provide a staging ground for future modeling.

Extensions of the research points described in this thesis will require the following:

- A review and possible expansion of design modifications based on continued modeling.
- Laboratory tests of shores constructed with the suggested design modifications.
- Extension of the modeling to include means of predicting member failure—that is, investigation of shore behavior up to ultimate loads. Given the inherent variability of wood, this may require the use of a simulation process, such as the Monte Carlo method.
- Incorporation into the modeling of the hysteretic behavior of nailed joints in shores subjected to load reversals.

APPENDIX A

Additional Results for FSEL Shore Models

The first set of figures in this appendix (A.1 to A.8) presents the predicted deformed shape from Abaqus of each post in the shore models representative of the laboratory test specimens. For convenience, the approximate locations of the brace members (plywood for PLP and 2x4 horizontal braces for LP) are shown by dashed red lines. The view shown in each image corresponds to the front side of the shore (west).

The next set of figures (A.9 to A.40) shows contour plots of the computed normal and shear stresses in the plywood braces for Shores 1, 2, 7, and 9. To produce a more continuous effect across element boundaries, values at nodes common to two or more elements were averaged if their computed percent difference did not exceed 75 percent.

A.1 POST CURVATURES AS VIEWED FROM WEST

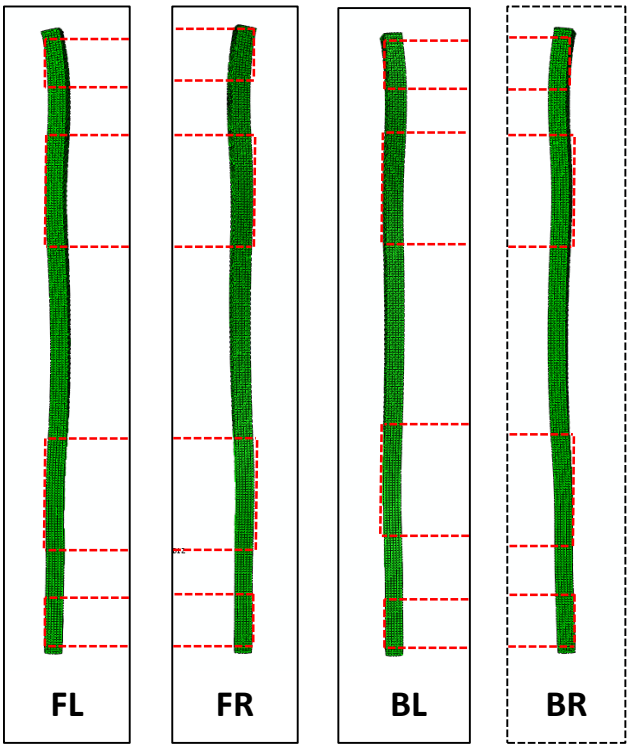

Figure A.1 Deformed plots from Abaqus of posts for PLP Shore 1

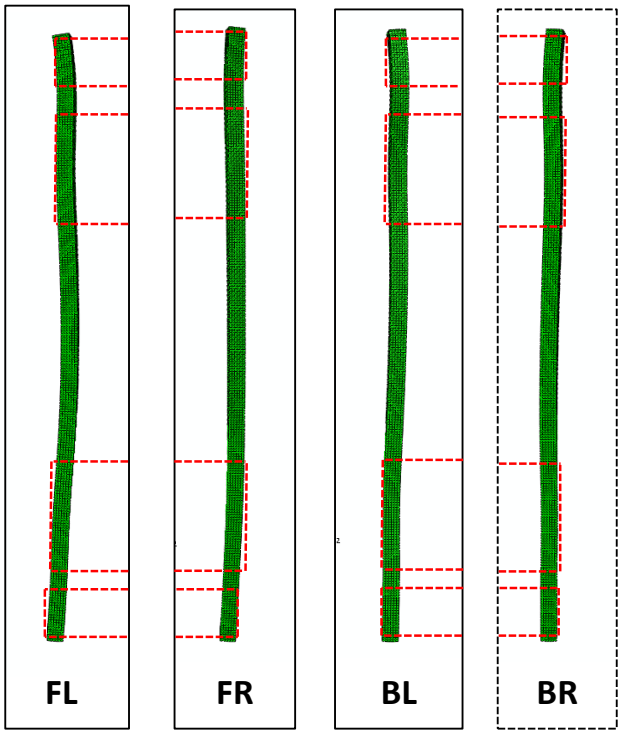

Figure A.2 Deformed plots from Abaqus of posts for PLP Shore 2

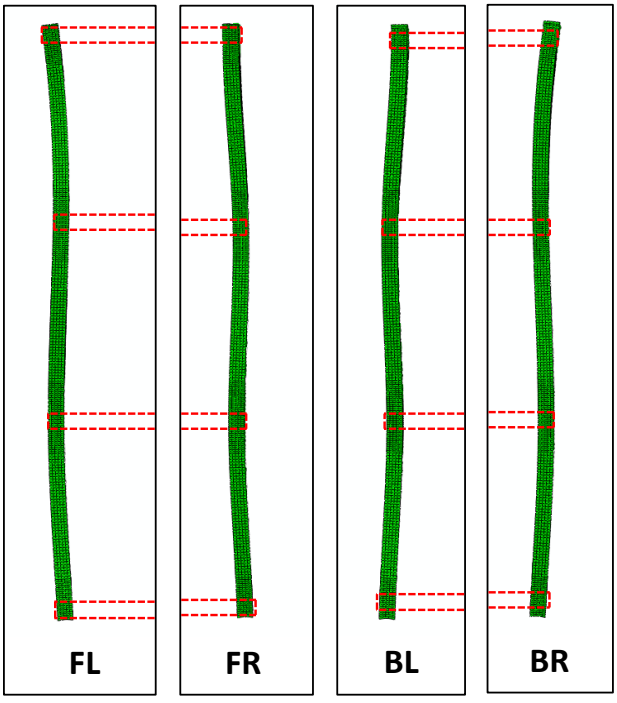

Figure A.3 Deformed plots from Abaqus of posts for LP Shore 3

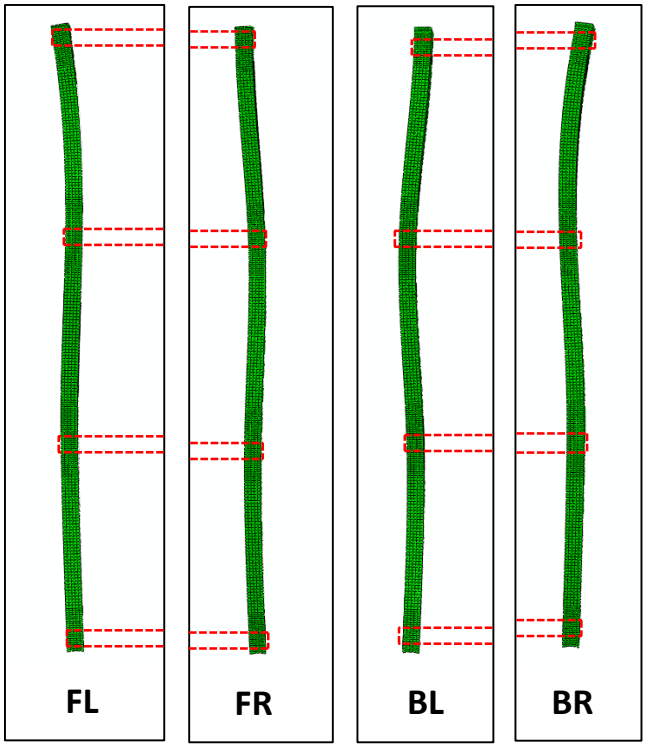

Figure A.4 Deformed plots from Abaqus of posts for LP Shore 4

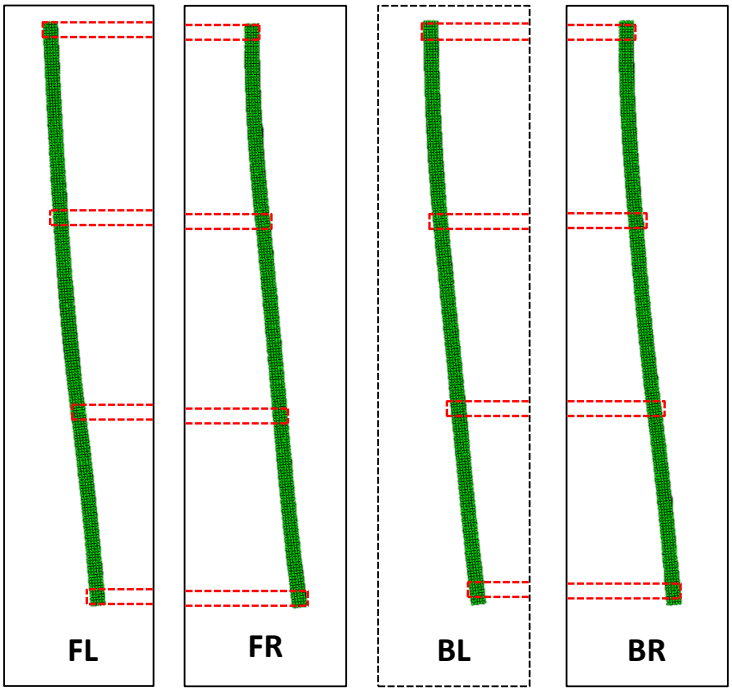

Figure A.5 Deformed plots from Abaqus of posts for LP Shore 6

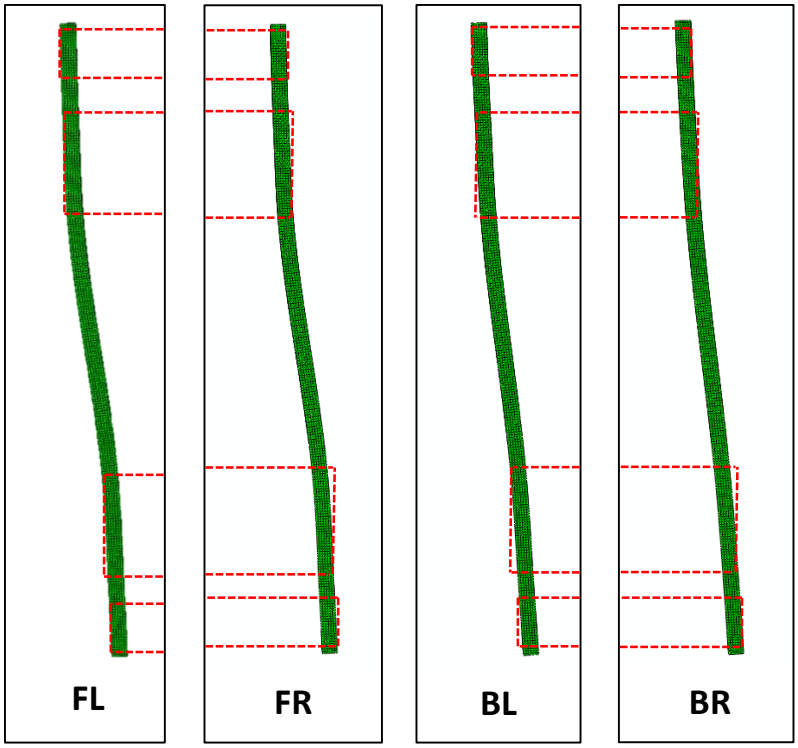

Figure A.6 Deformed plots from Abaqus of posts for PLP Shore 7

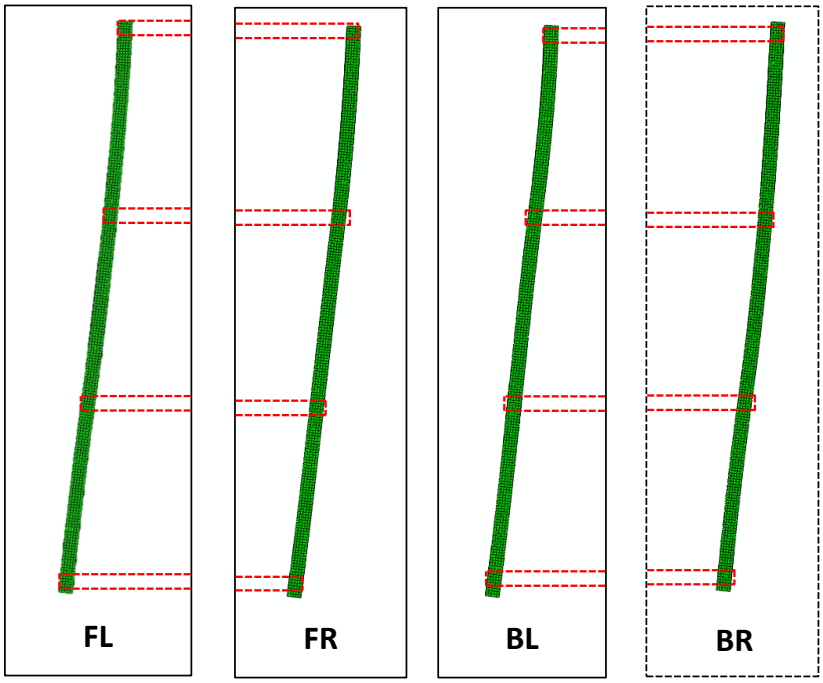

Figure A.7 Deformed plots from Abaqus of posts for LP Shore 8

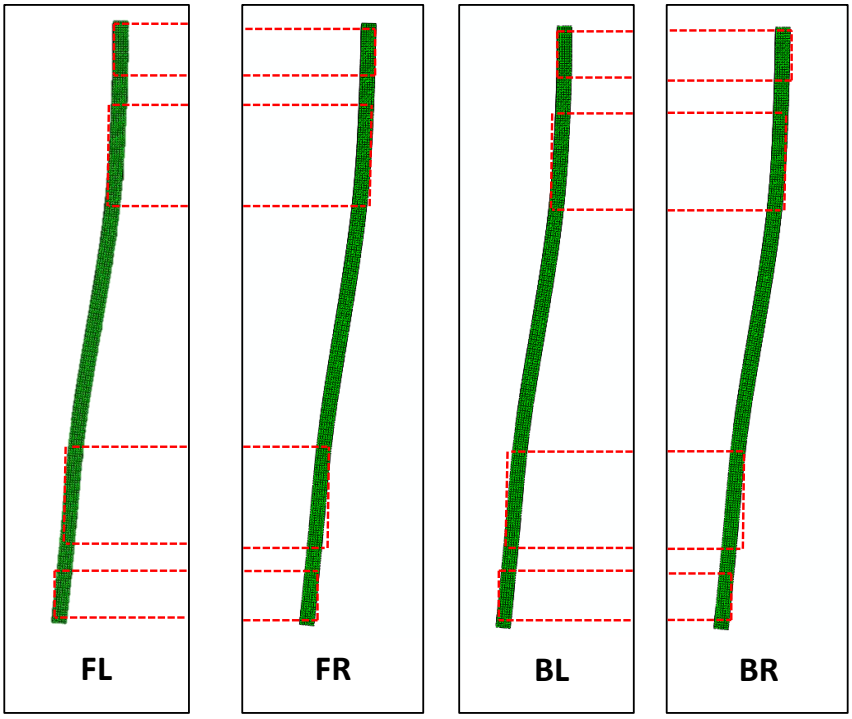

Figure A.8 Deformed plots from Abaqus of posts for PLP Shore 9

A.2 NORMAL AND SHEAR STRESSES IN PLYWOOD BRACES

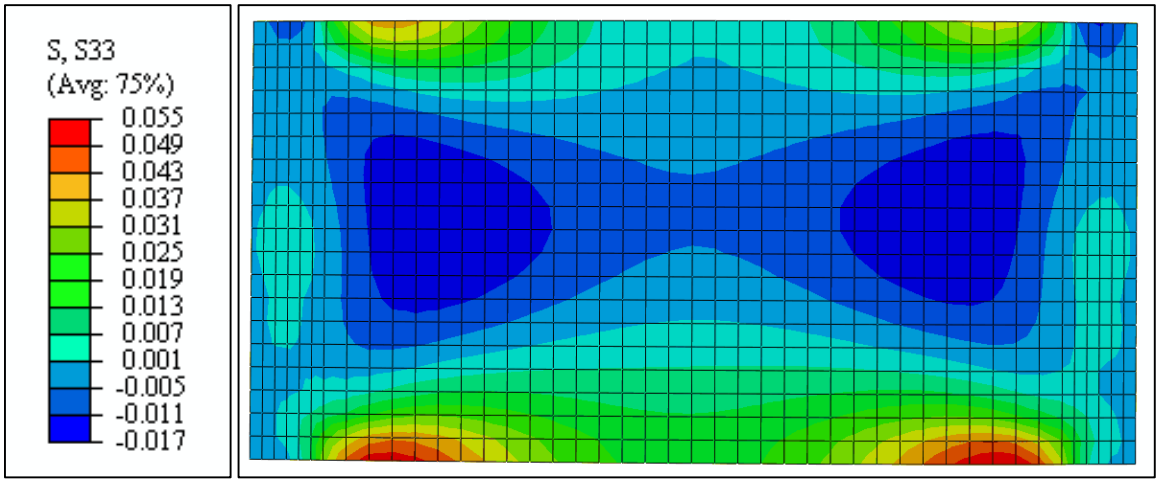

Figure A.9 Contour plot of normal stress in WB1-F of PLP Shore 1

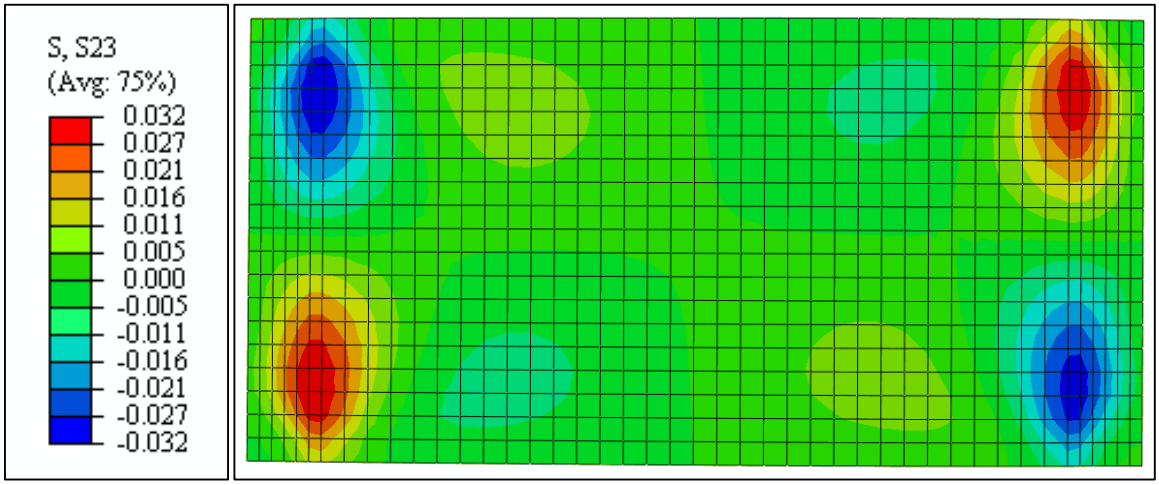

Figure A.10 Contour plot of shear stress in WB1-F of PLP Shore 1

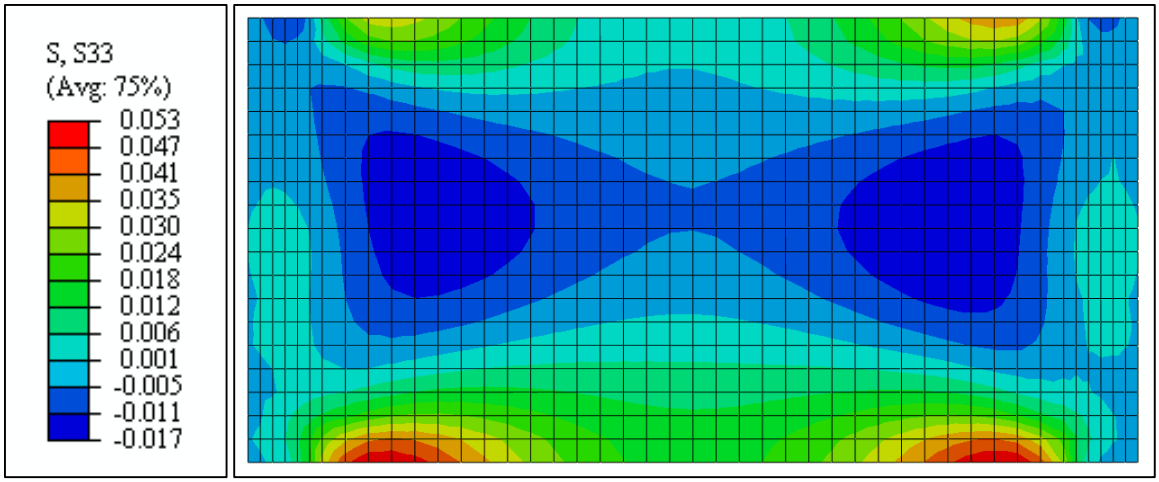

Figure A.11 Contour plot of normal stress in WB1-B of PLP Shore 1

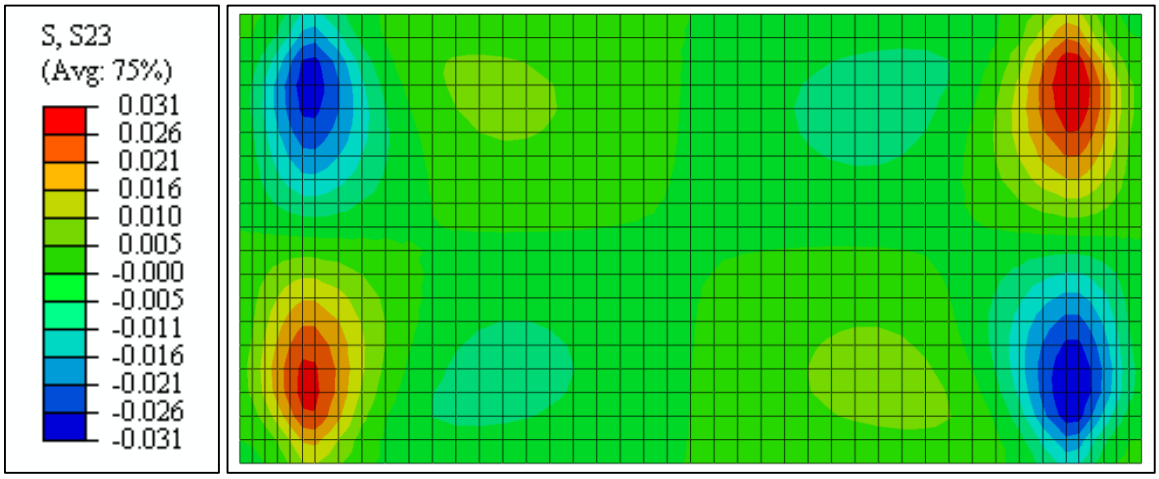

Figure A.12 Contour plot of shear stress in WB1-B of PLP Shore 1

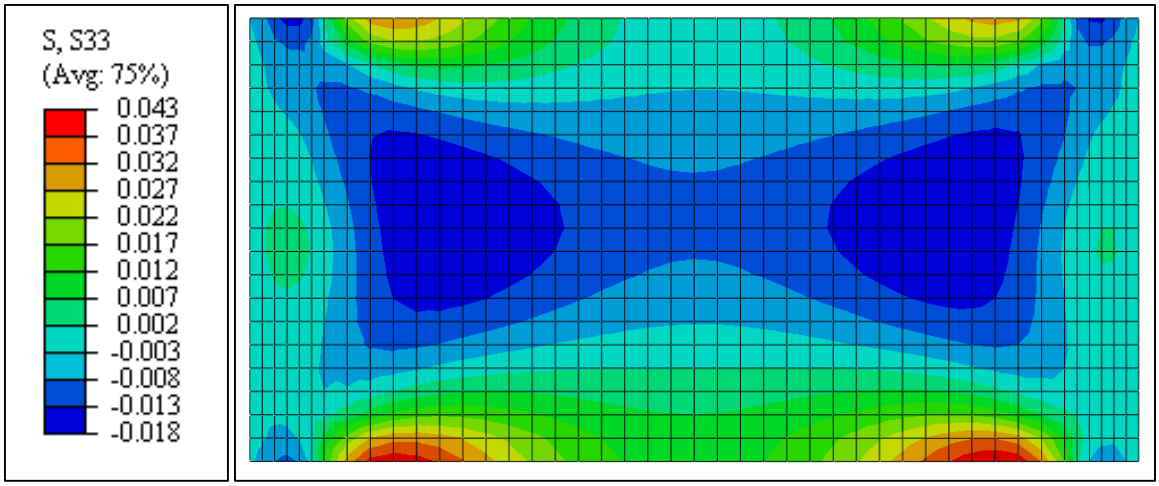

Figure A.13 Contour plot of normal stress in WB2-F of PLP Shore 1

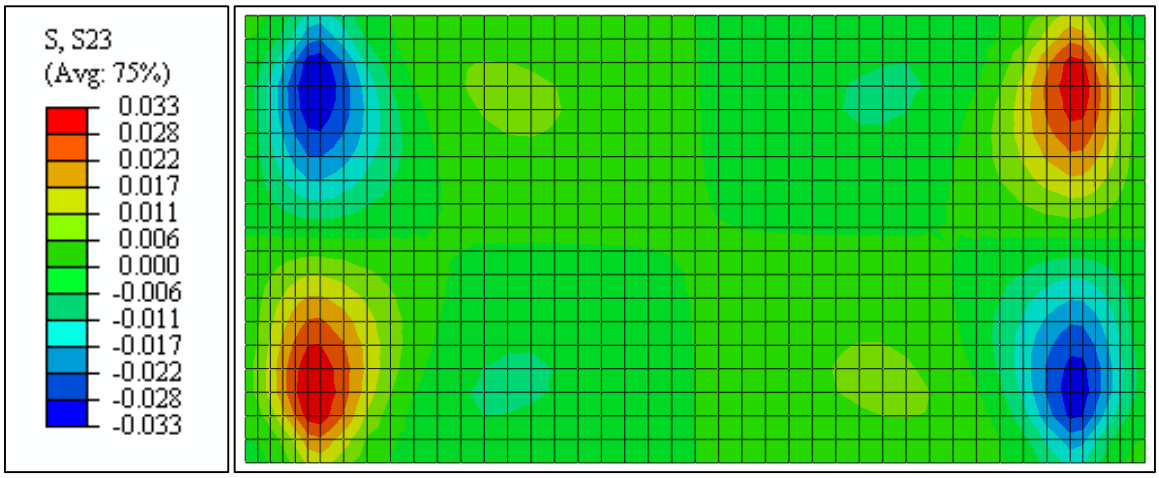

Figure A.14 Contour plot of shear stress in WB2-F of PLP Shore 1

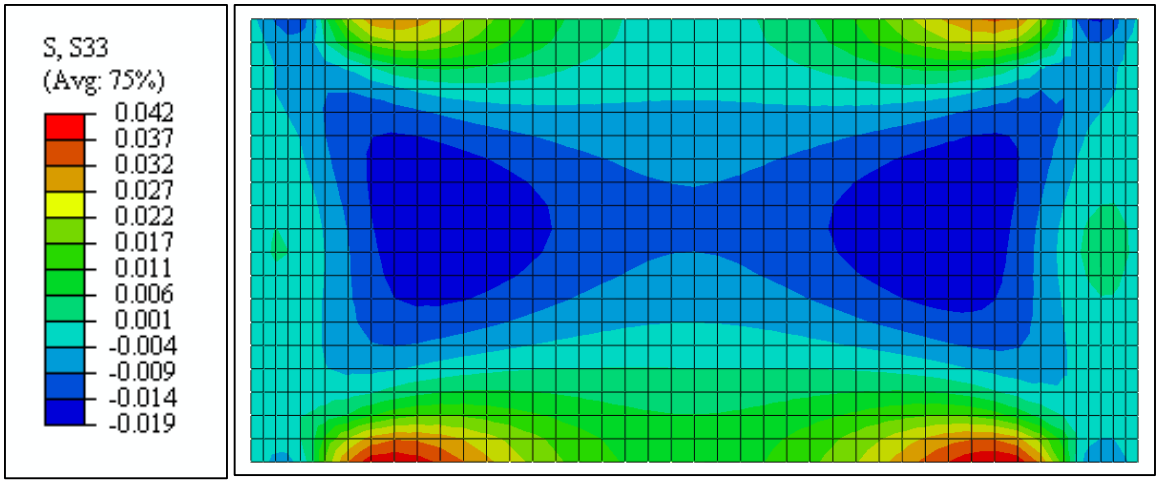

Figure A.15 Contour plot of normal stress in WB2-B of PLP Shore 1

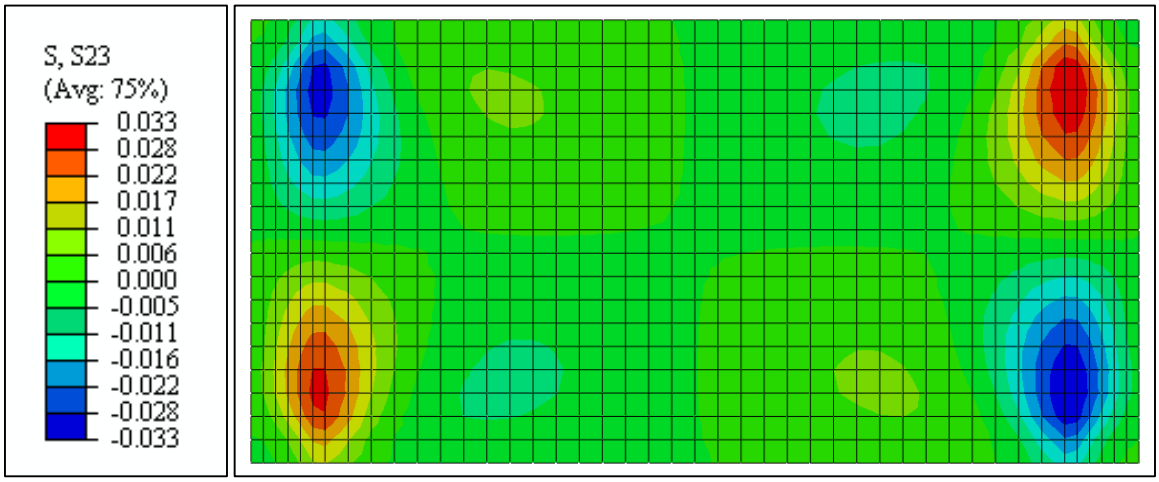

Figure A.16 Contour plot of shear stress in WB2-B of PLP Shore 1

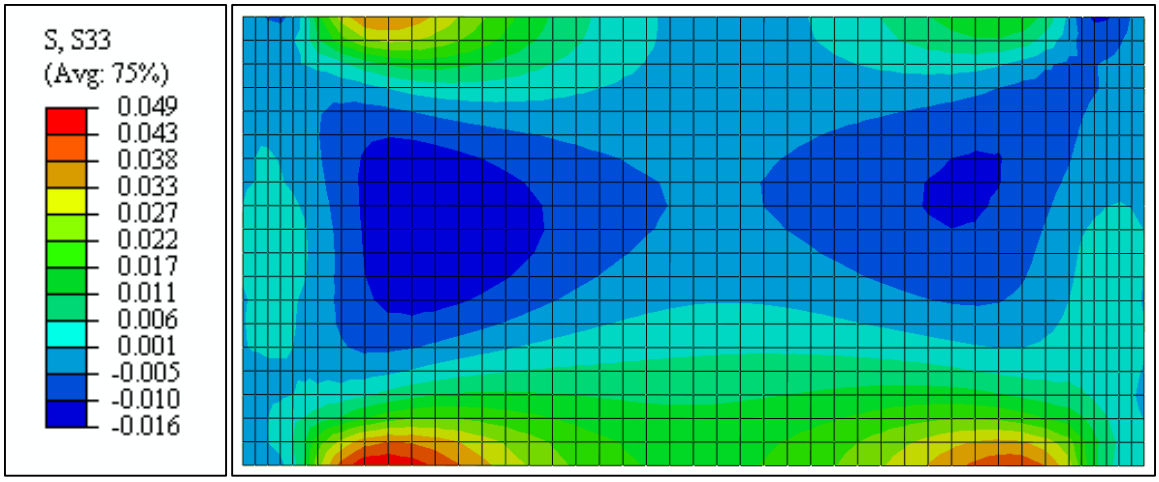

Figure A.17 Contour plot of normal stress in WB1-F of PLP Shore 2

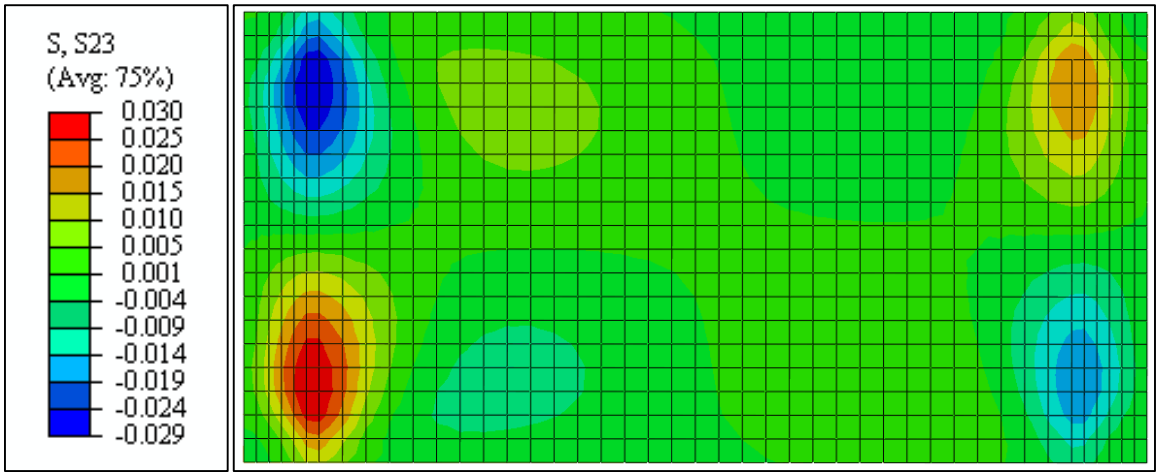

Figure A.18 Contour plot of shear stress in WB1-F of PLP Shore 2

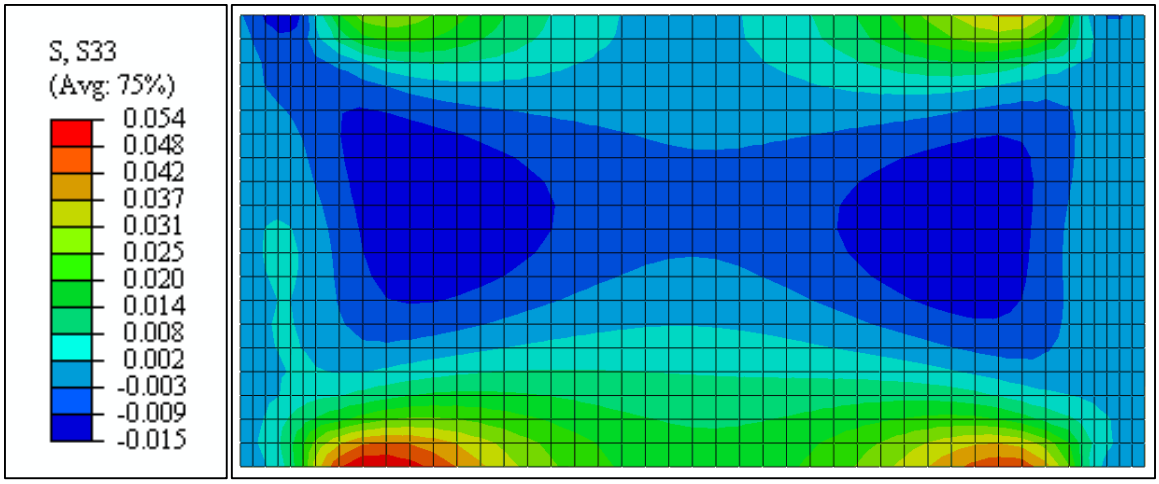

Figure A.19 Contour plot of normal stress in WB1-B of PLP Shore 2

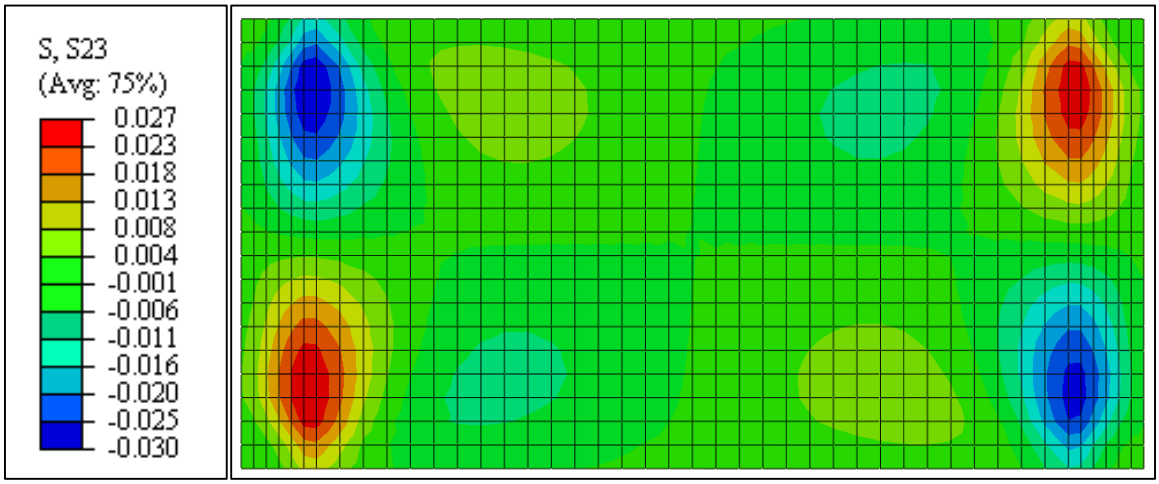

Figure A.20 Contour plot of shear stress in WB1-B of PLP Shore 2

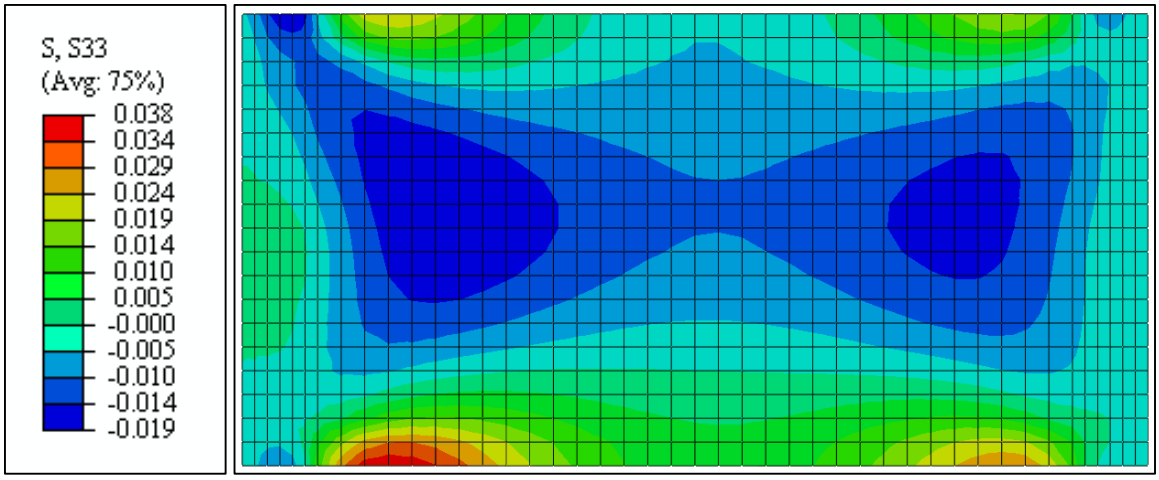

Figure A.21 Contour plot of normal stress in WB2-F of PLP Shore 2

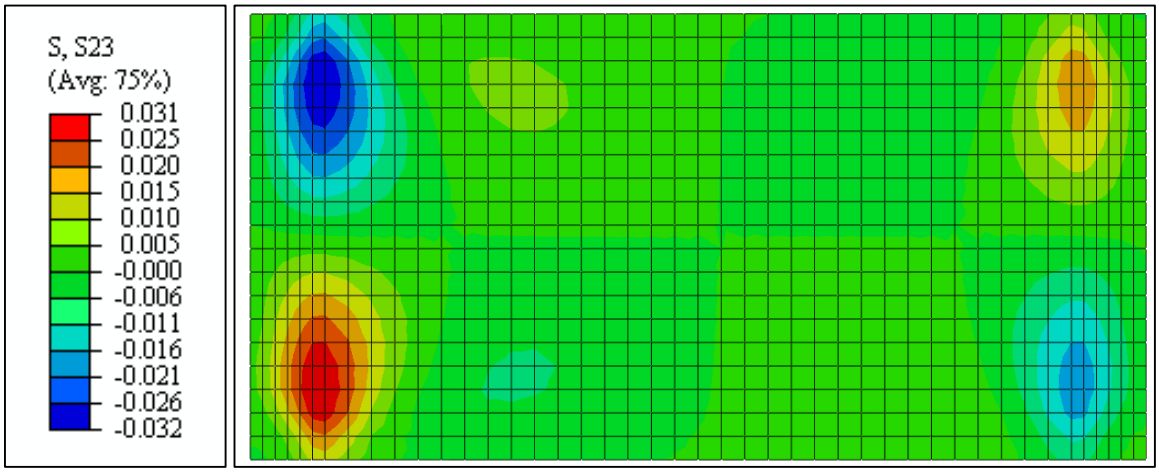

Figure A.22 Contour plot of shear stress in WB2-F of PLP Shore 2

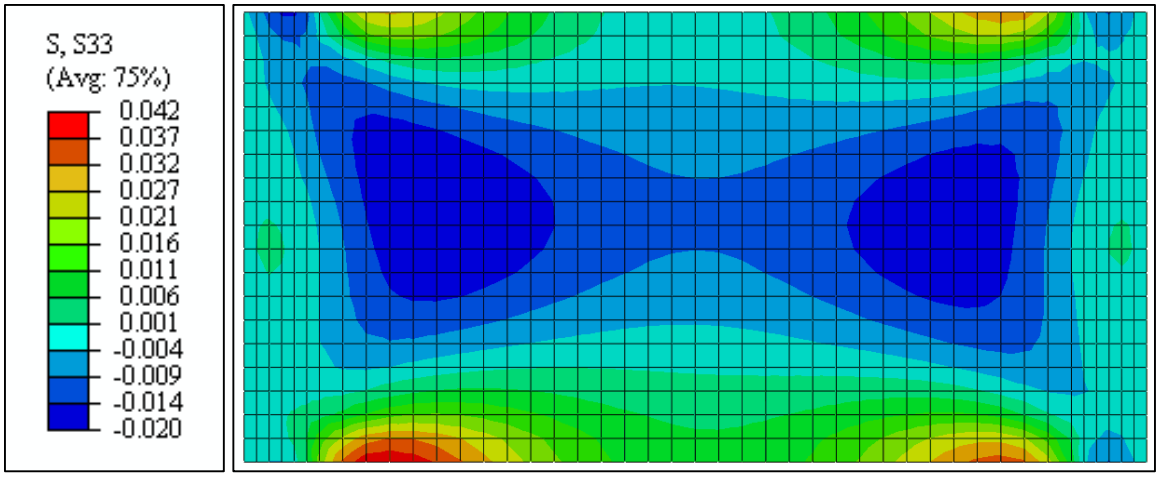

Figure A.23 Contour plot of normal stress in WB2-B of PLP Shore 2

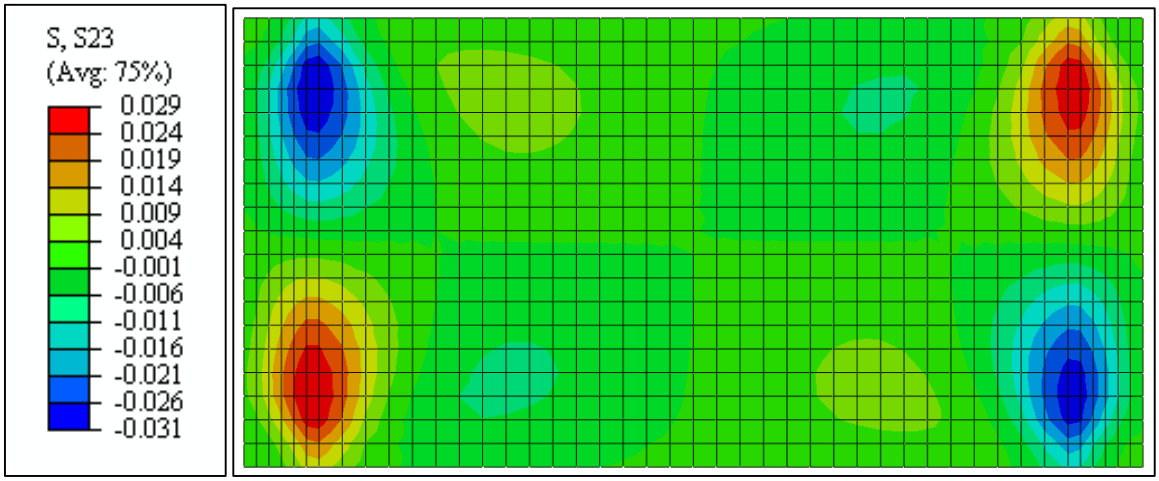

Figure A.24 Contour plot of shear stress in WB2-B of PLP Shore 2

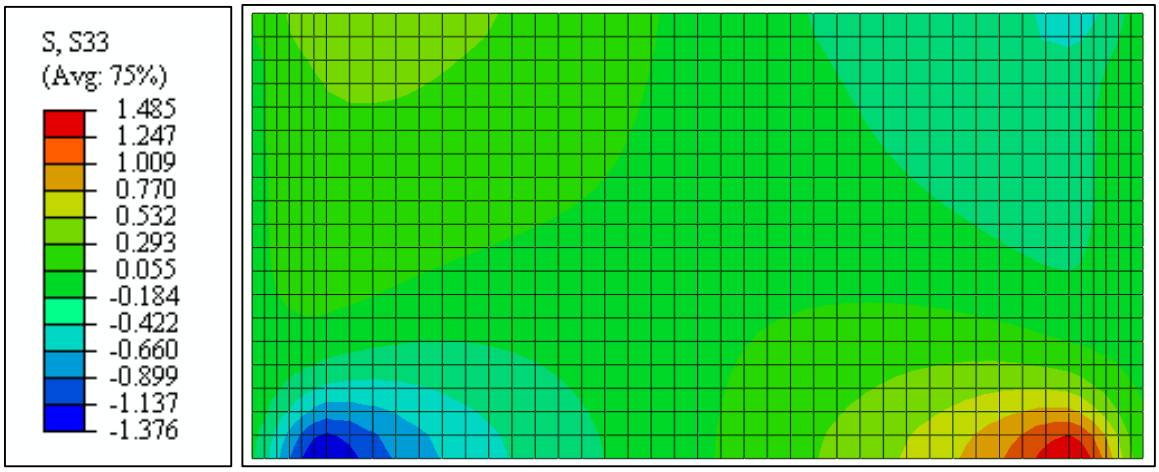

Figure A.25 Contour plot of normal stress in WB1-F of PLP Shore 7

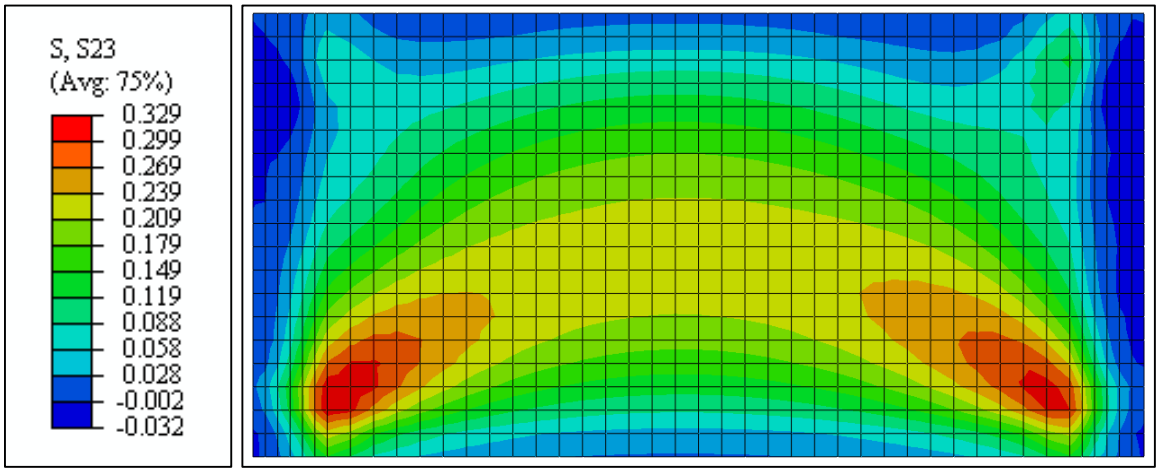

Figure A.26 Contour plot of shear stress in WB1-F of PLP Shore 7

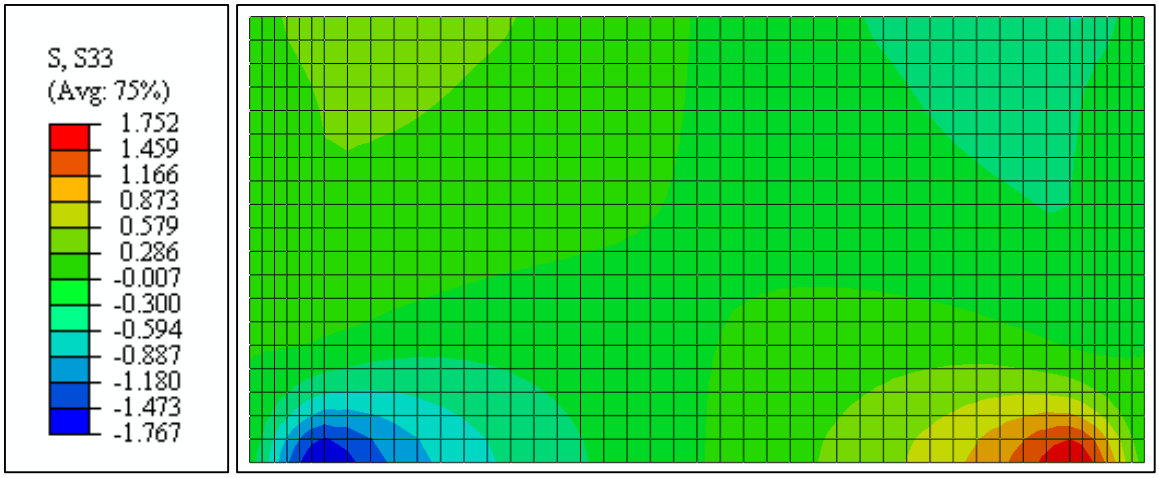

Figure A.27 Contour plot of normal stress in WB1-B of PLP Shore 7

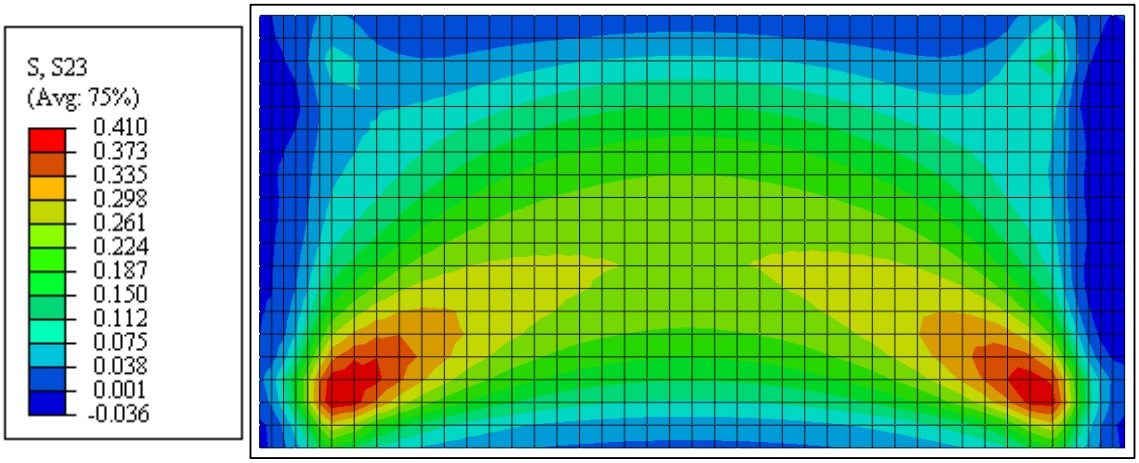

Figure A.28 Contour plot of shear stress in WB1-B of PLP Shore 7

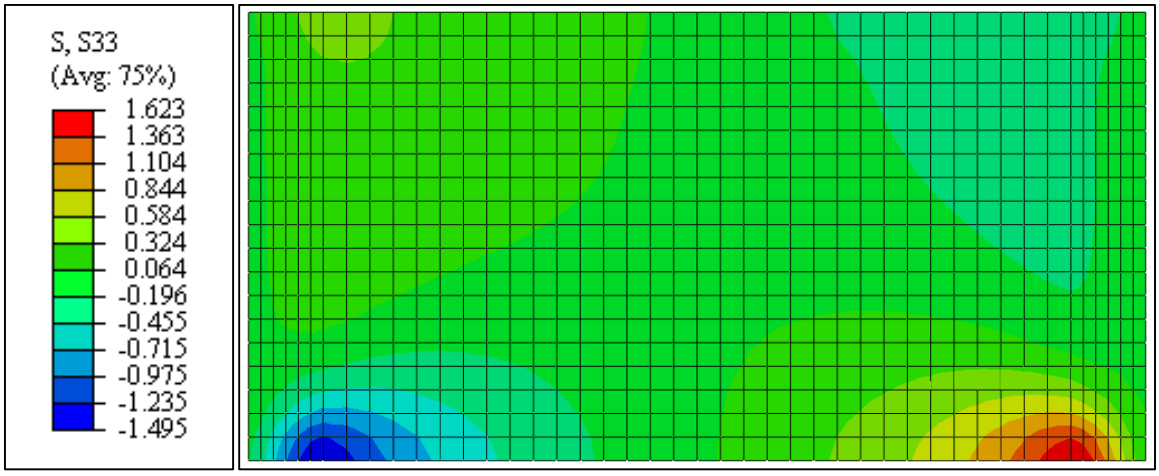

Figure A.29 Contour plot of normal stress in WB2-F of PLP Shore 7

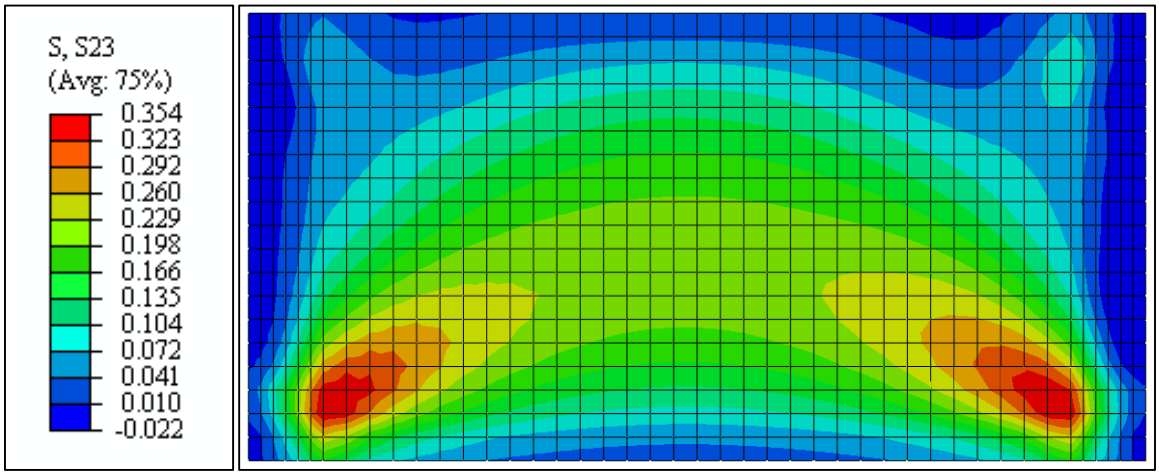

Figure A.30 Contour plot of shear stress in WB2-F of PLP Shore 7

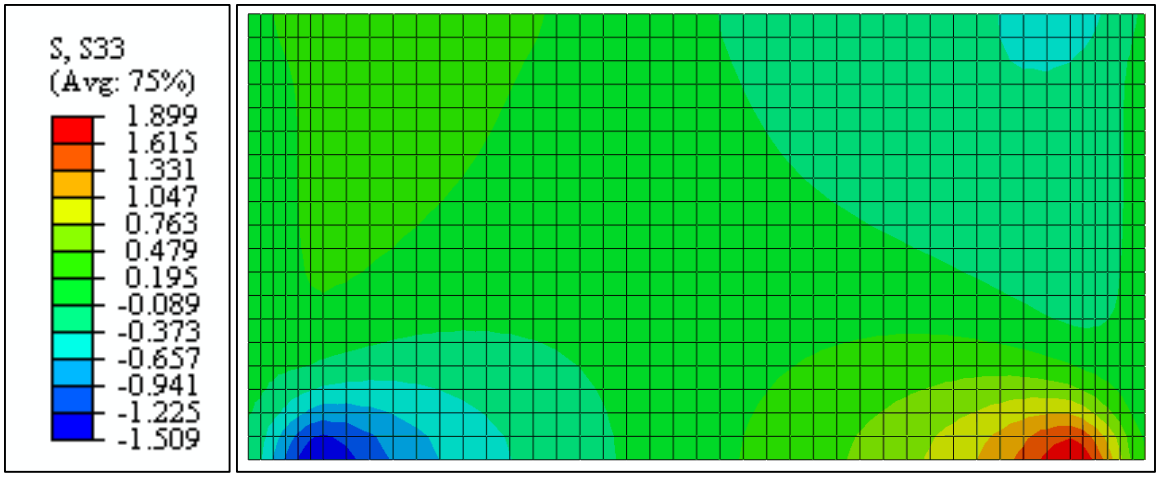

Figure A.31 Contour plot of normal stress in WB2-B of PLP Shore 7

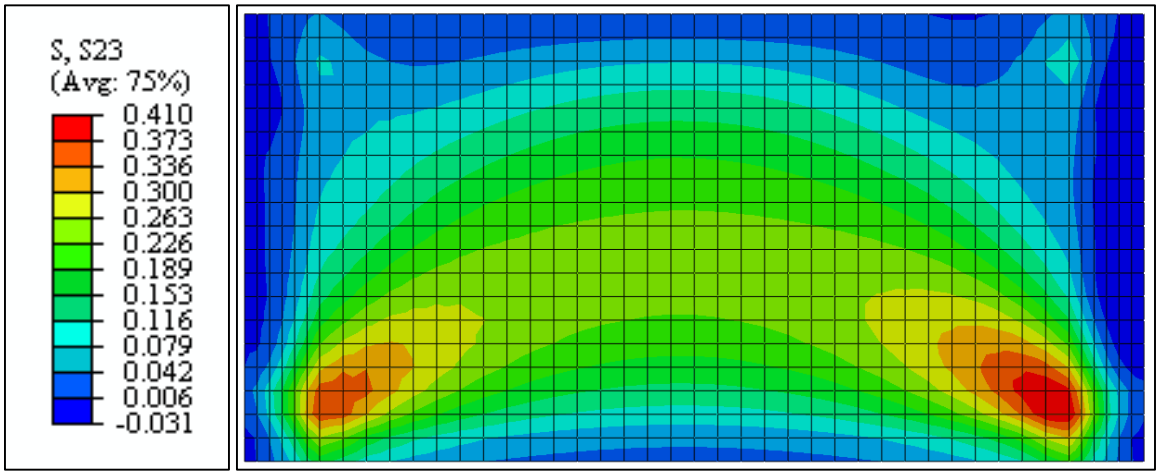

Figure A.32 Contour plot of shear stress in WB2-B of PLP Shore 7

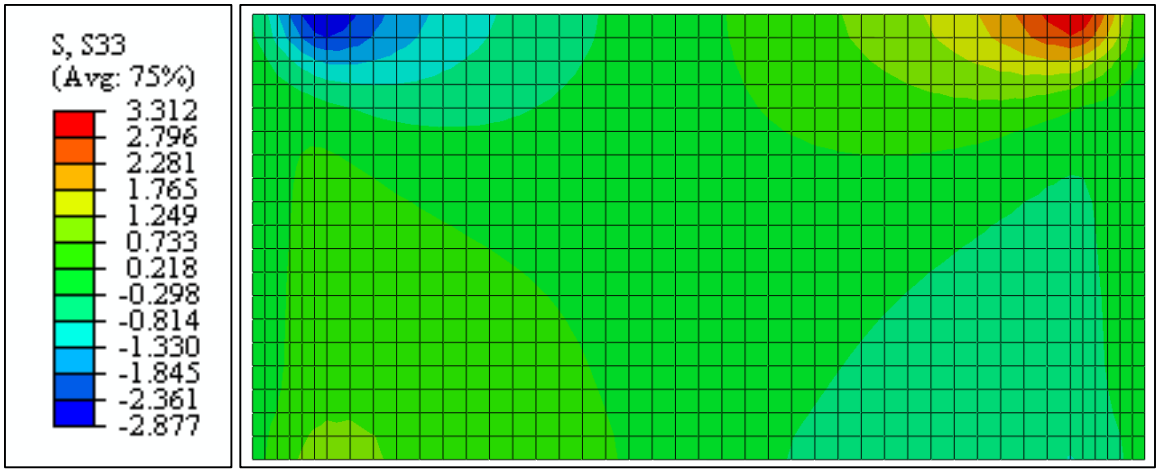

Figure A.33 Contour plot of normal stress in WB1-F of PLP Shore 9

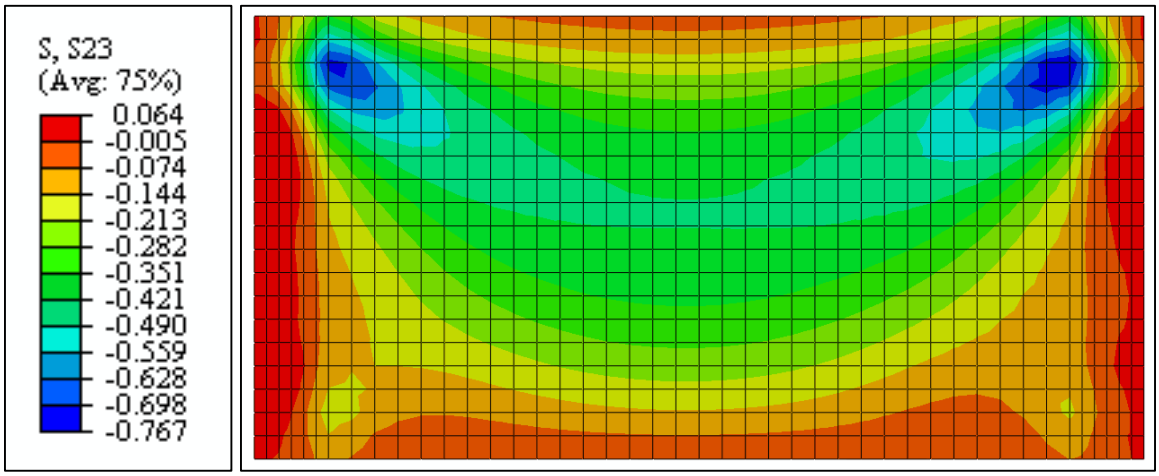

Figure A.34 Contour plot of shear stress in WB1-F of PLP Shore 9

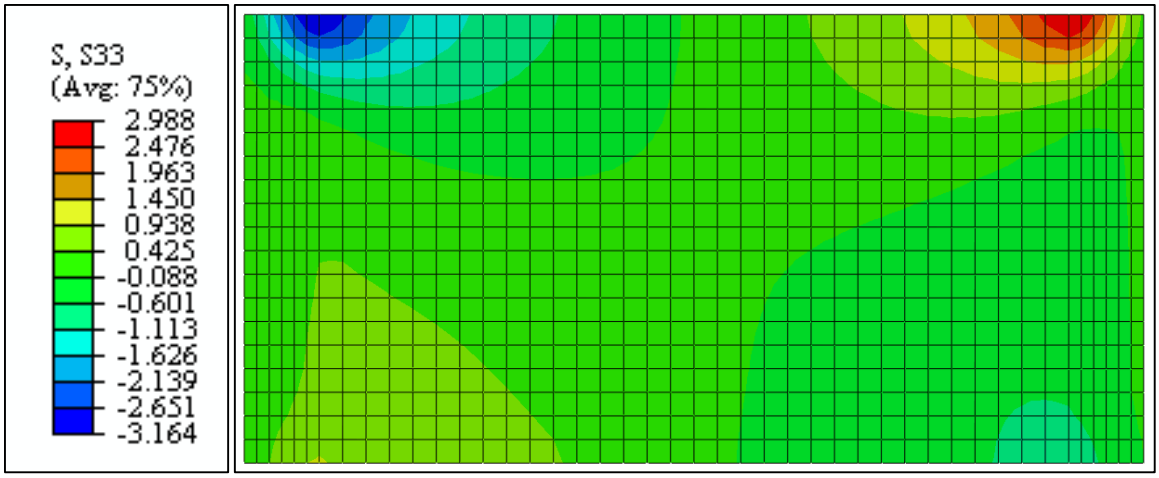

Figure A.35 Contour plot of normal stress in WB1-B of PLP Shore 9

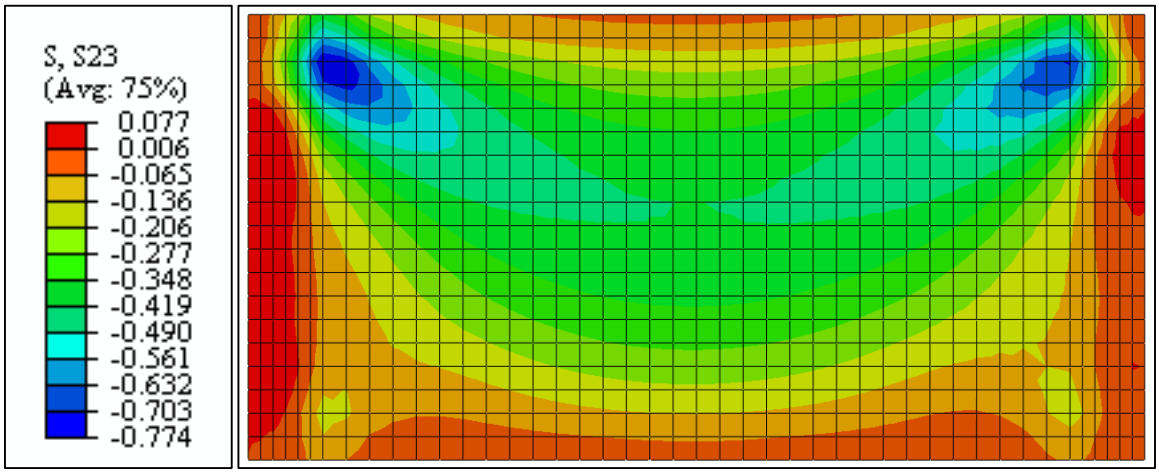

Figure A.36 Contour plot of shear stress in WB1-B of PLP Shore 9

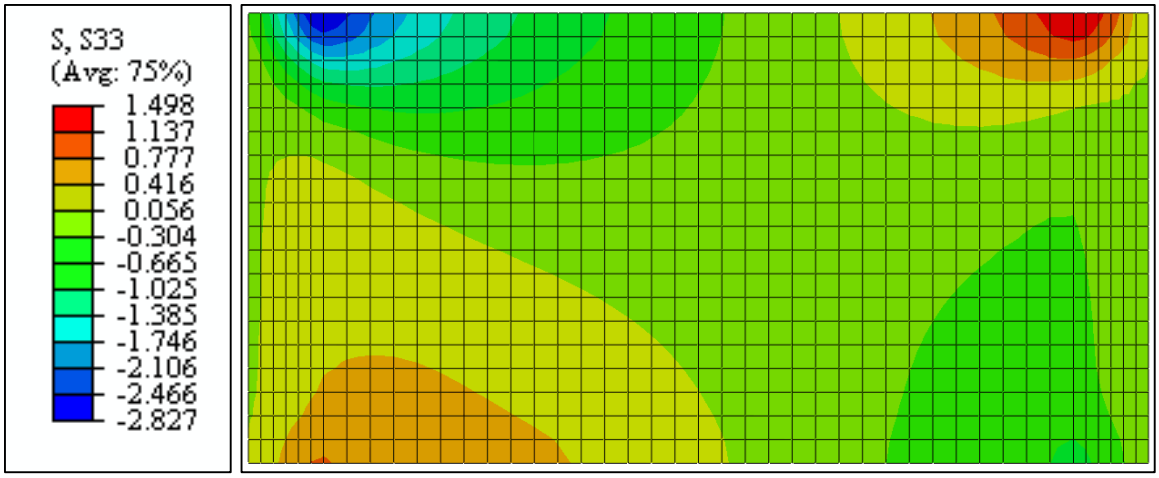

Figure A.37 Contour plot of normal stress in WB2-F of PLP Shore 9

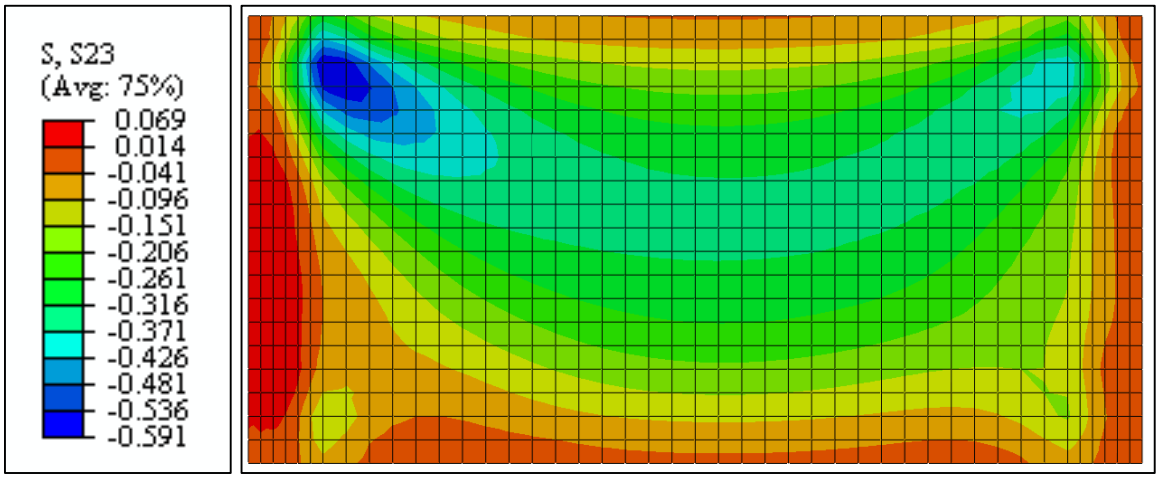

Figure A.38 Contour plot of shear stress in WB2-F of PLP Shore 9

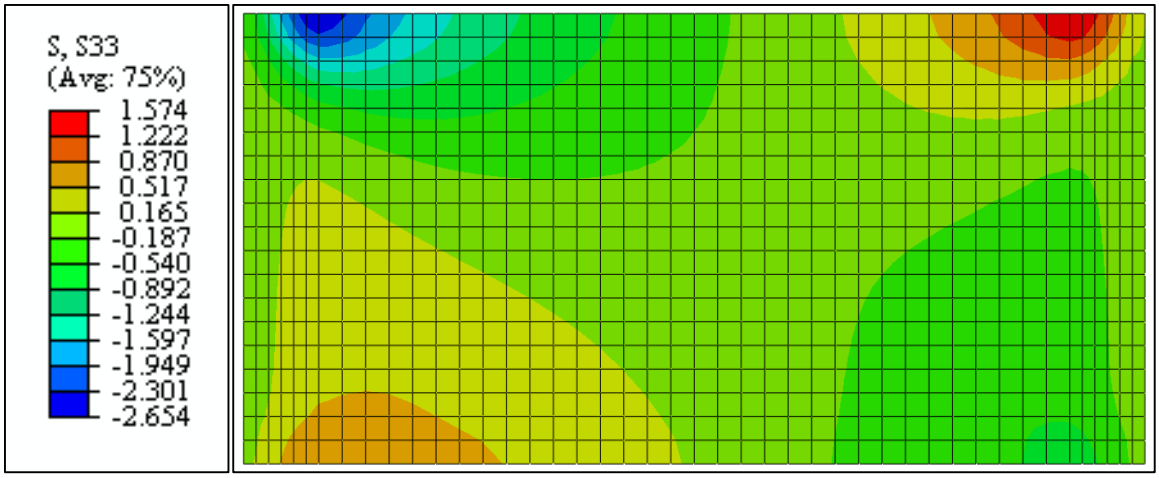

Figure A.39 Contour plot of normal stress in WB2-B of PLP Shore 9

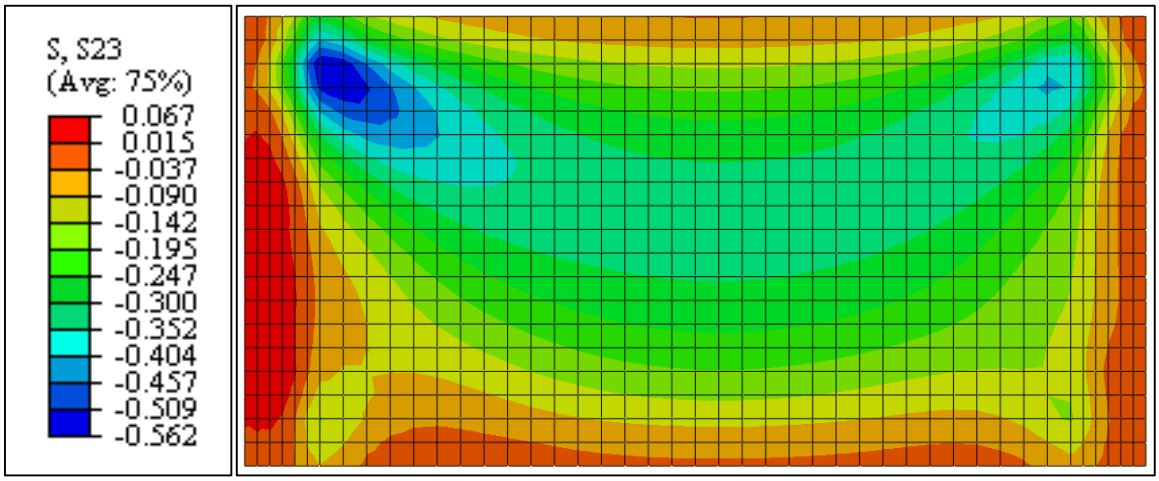

Figure A.40 Contour plot of shear stress in WB2-B of PLP Shore 9

APPENDIX B

Additional Results for Design Modification Shore Models

The figures in this appendix show deformed contour plots of the computed vertical (global y-direction) stress in each shore design modification. The vertical loads and lateral displacements in the images shown herein correspond directly to those imposed on the original shores. Therefore, direct comparison of these values with the computed values for the original shore models is feasible.

B1. DEFORMED SHORE POSITIONS WITH VERTICAL STRESS DISTRIBUTIONS

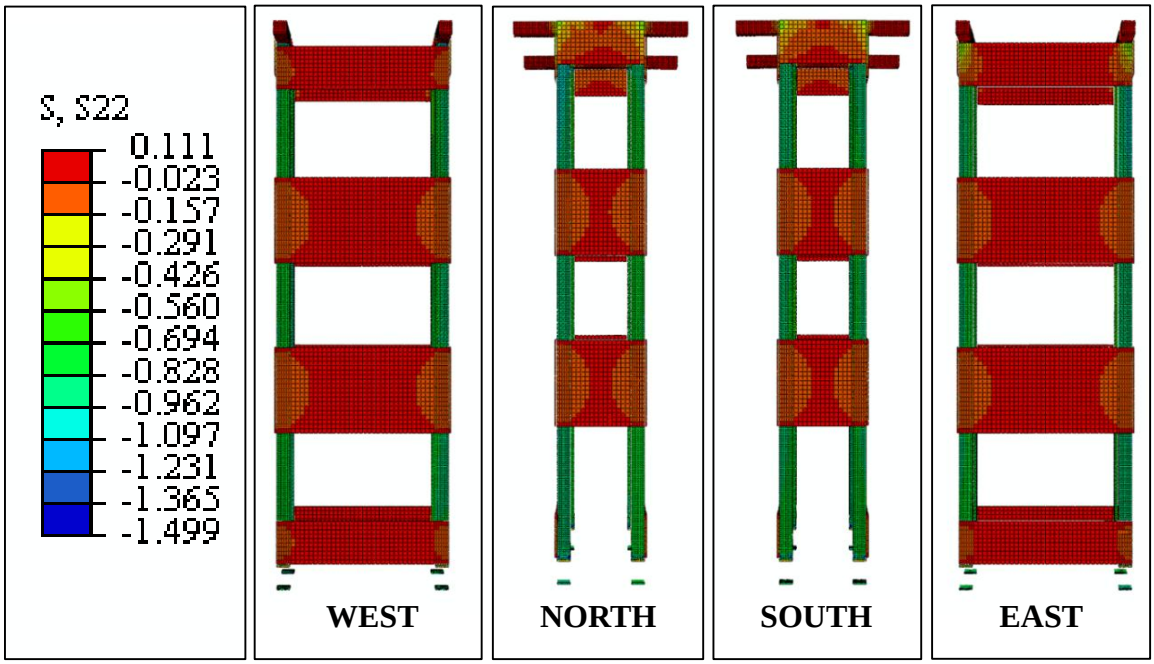

Figure B.1 Contour plots from Abaqus of the vertical stress (y-direction) for PLP Shore 1 MOD1

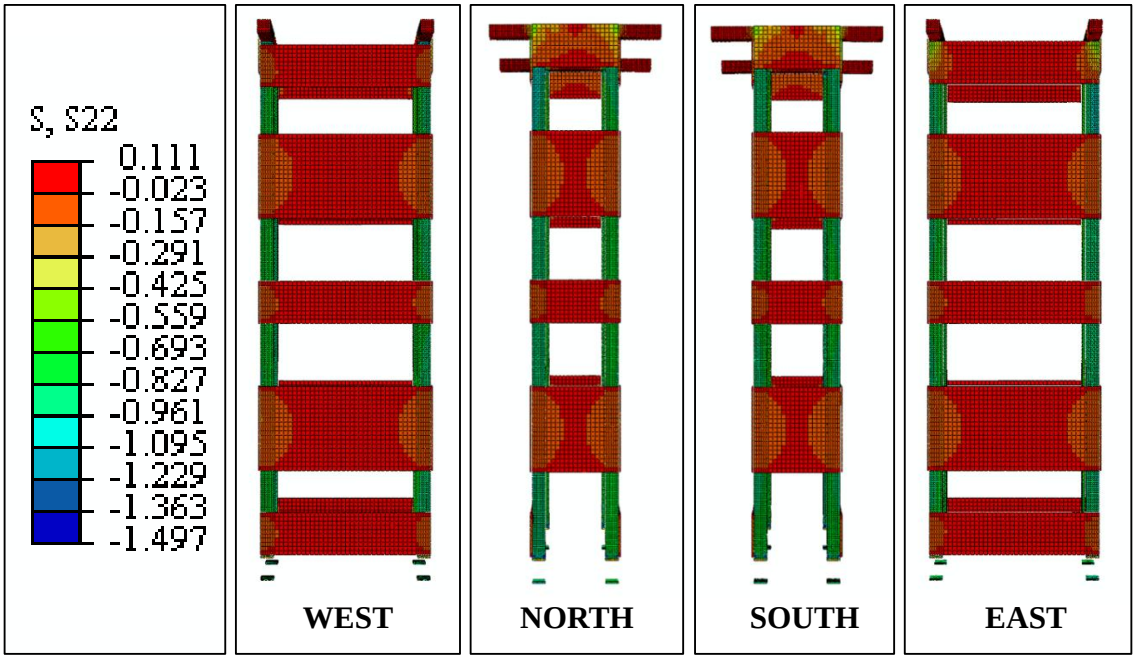

Figure B.2 Contour plots from Abaqus of the vertical stress (y-direction) for PLP Shore 1 MOD2

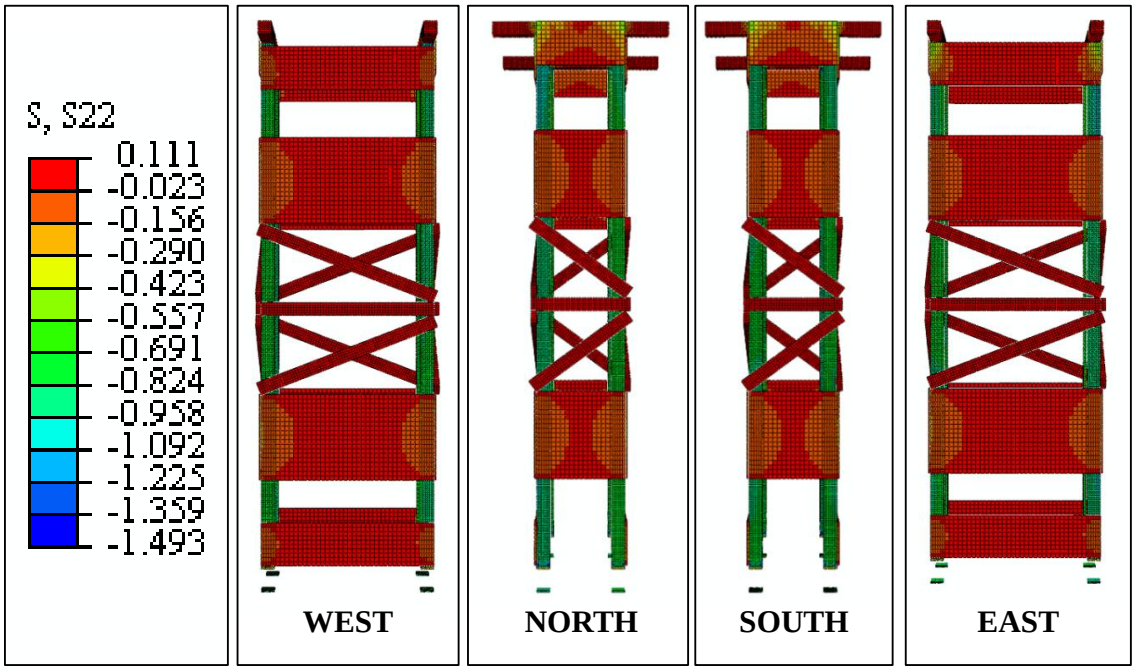

Figure B.3 Contour plots from Abaqus of the vertical stress (y-direction) for PLP Shore 1 MOD3

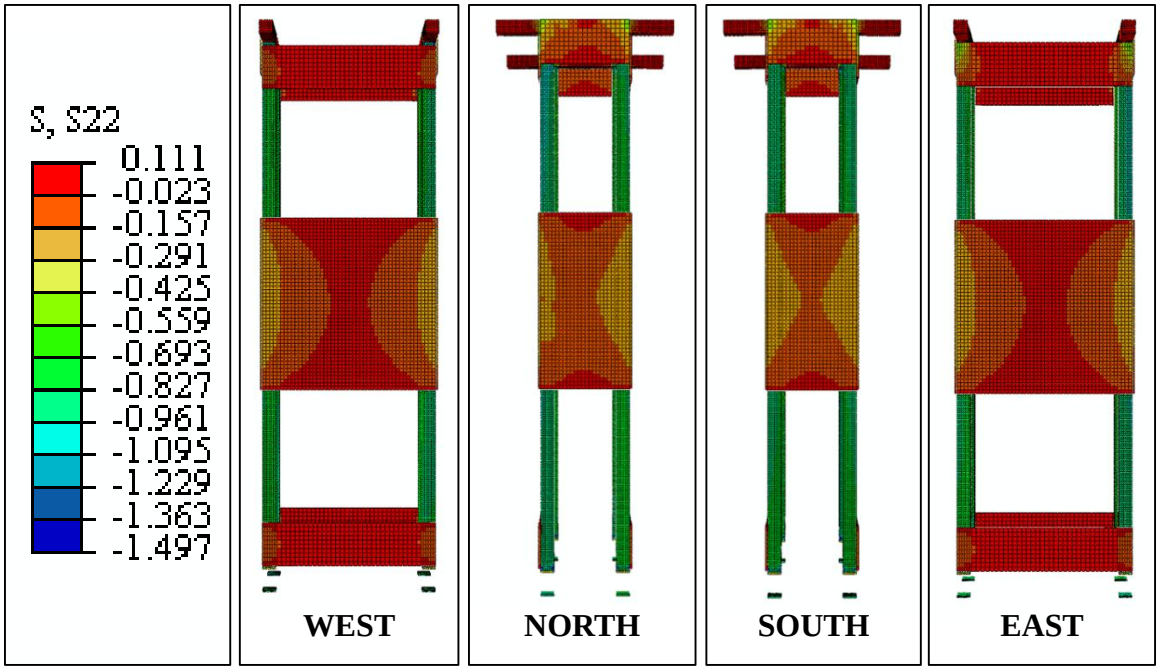

Figure B.4 Contour plots from Abaqus of the vertical stress (y-direction) for PLP Shore 1 MOD4

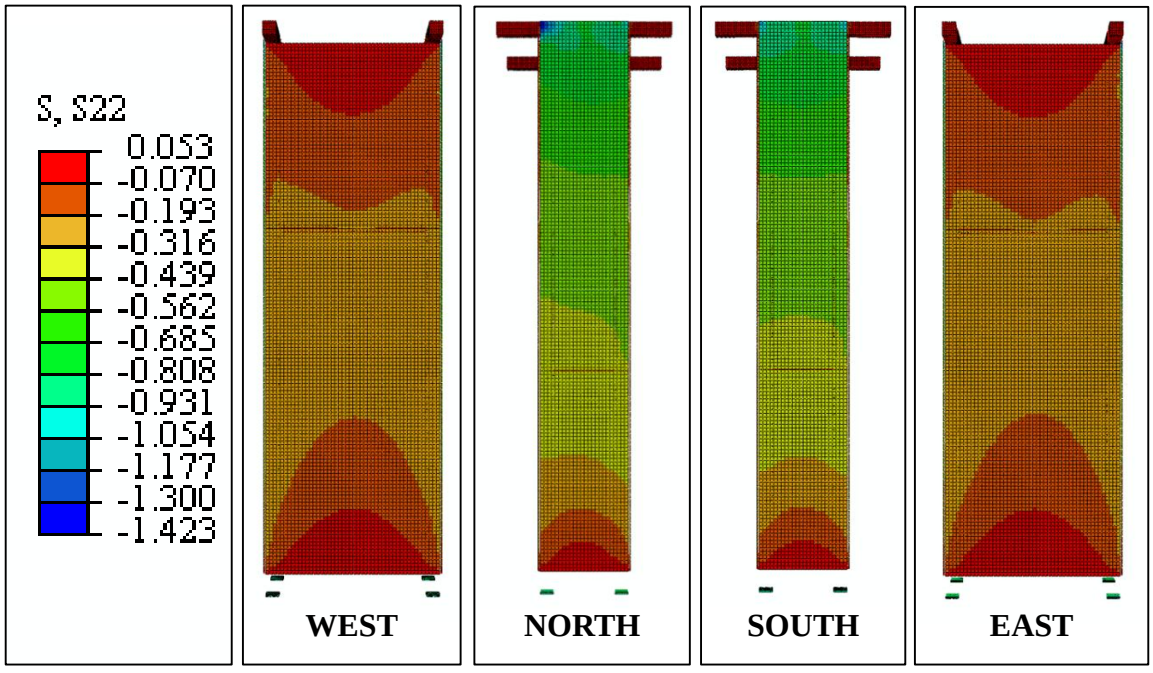

Figure B.5 Contour plots from Abaqus of the vertical stress (y-direction) for PLP Shore 1 MOD5

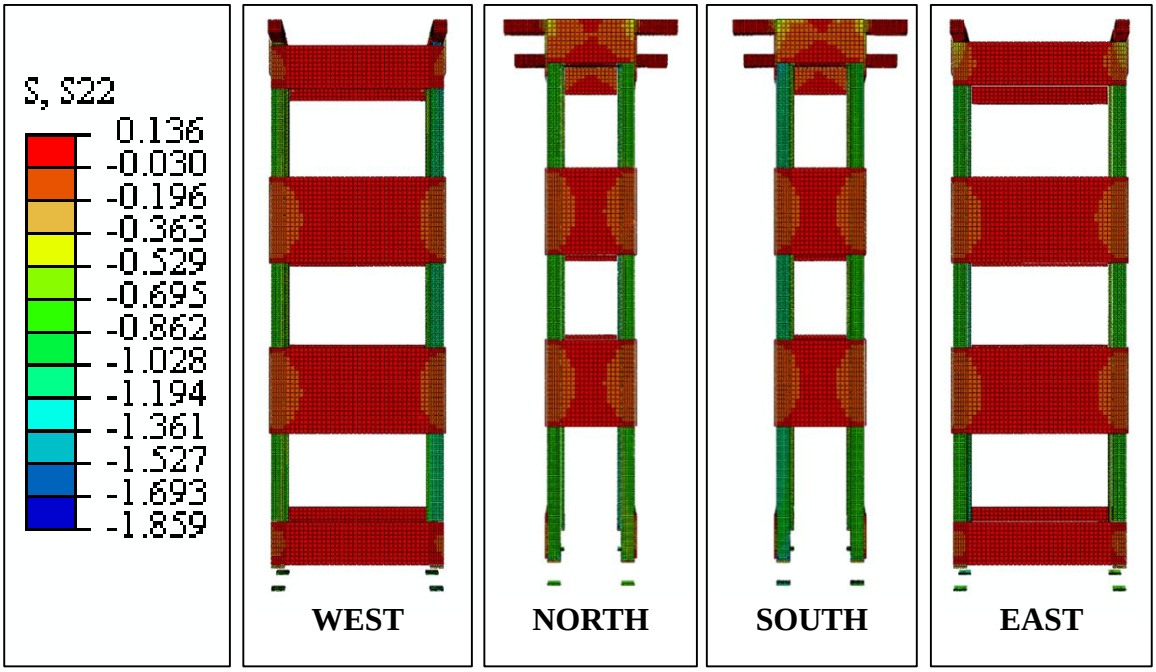

Figure B.6 Contour plots from Abaqus of the vertical stress (y-direction) for PLP Shore 2 MOD1

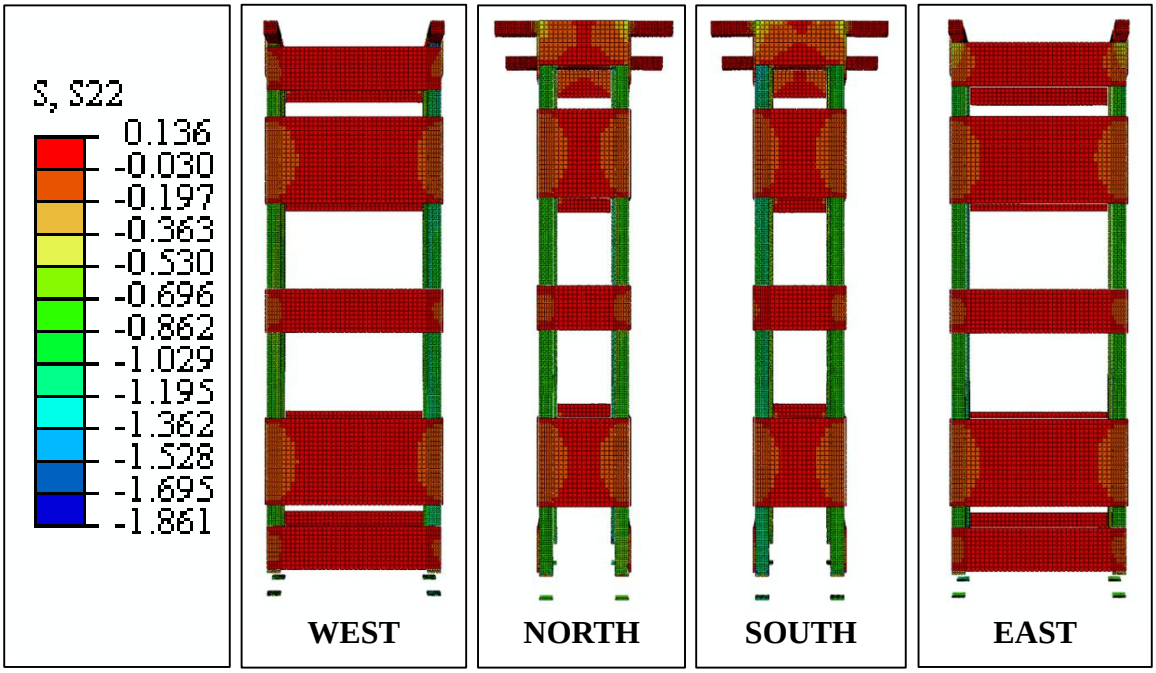

Figure B.7 Contour plots from Abaqus of the vertical stress (y-direction) for PLP Shore 2 MOD2

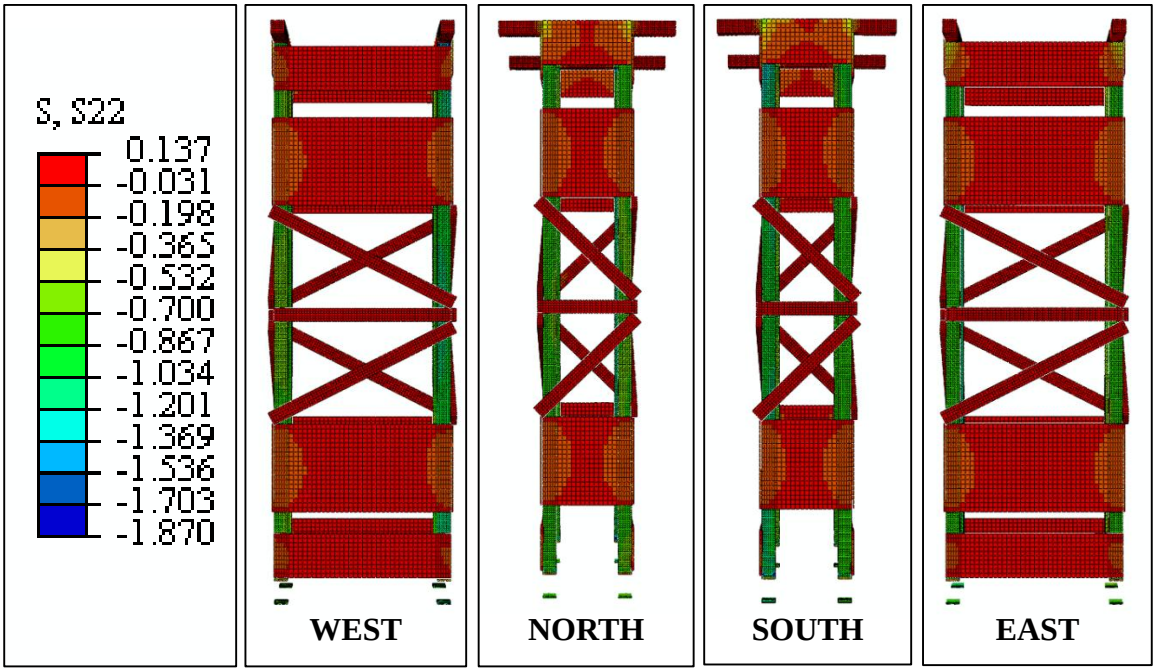

Figure B.8 Contour plots from Abaqus of the vertical stress (y-direction) for PLP Shore 2 MOD3

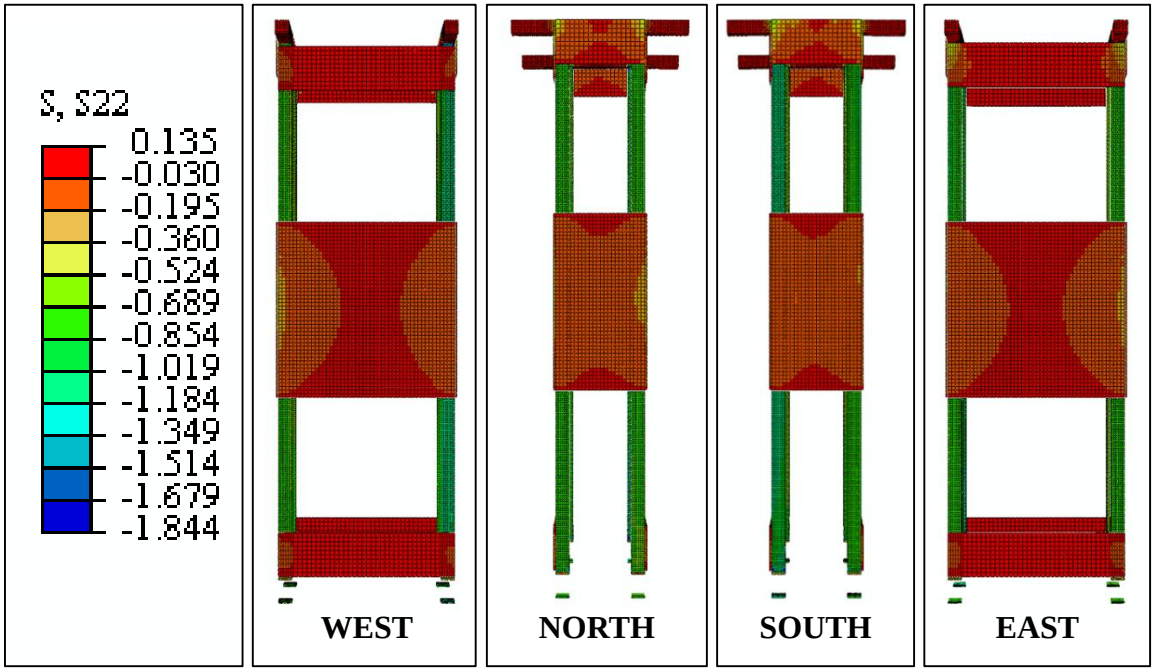

Figure B.9 Contour plots from Abaqus of the vertical stress (y-direction) for PLP Shore 2 MOD4

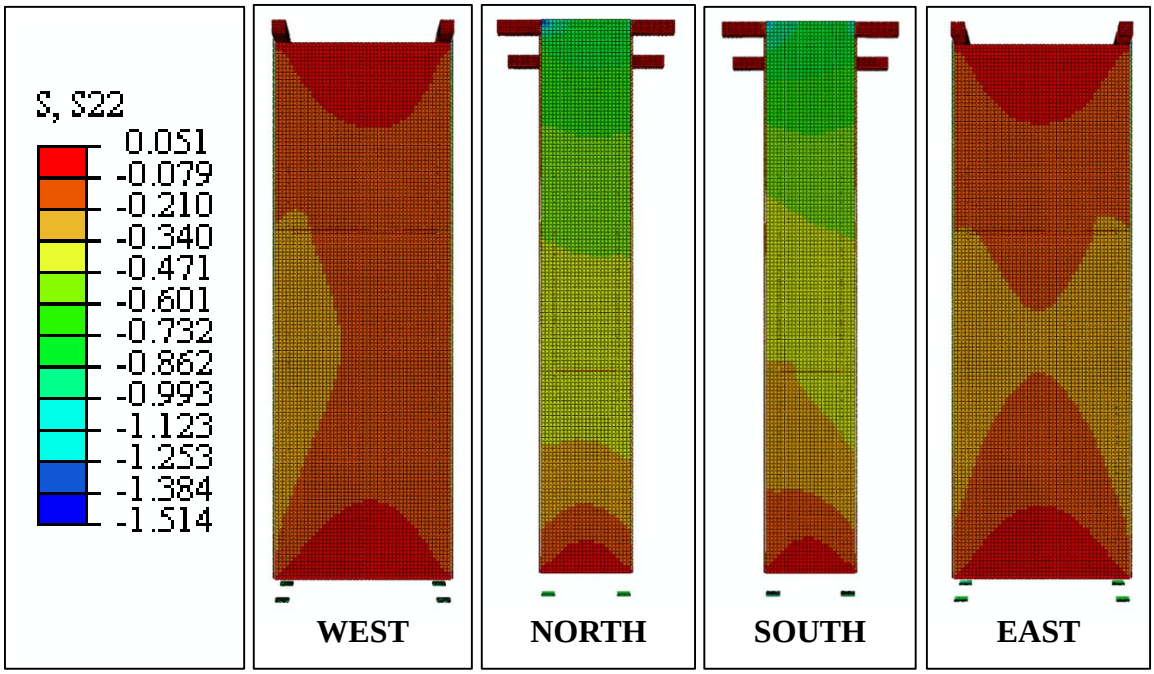

Figure B.10 Contour plots from Abaqus of the vertical stress (y-direction) for PLP Shore 2 MOD5

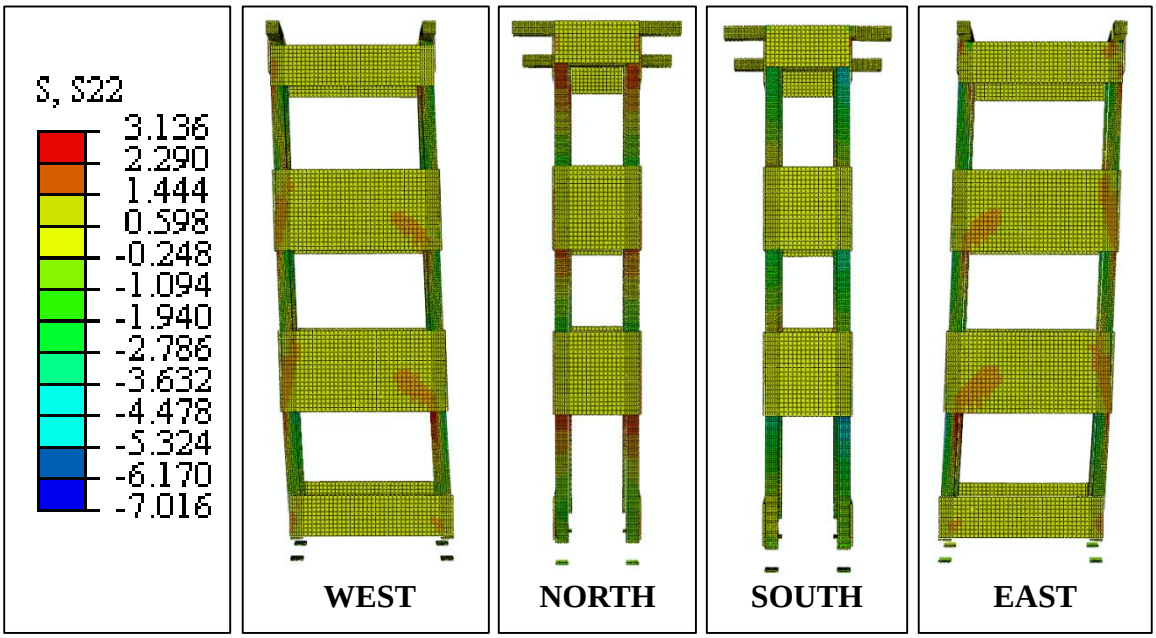

Figure B.11 Contour plots from Abaqus of the vertical stress (y-direction) for PLP Shore 7 MOD1

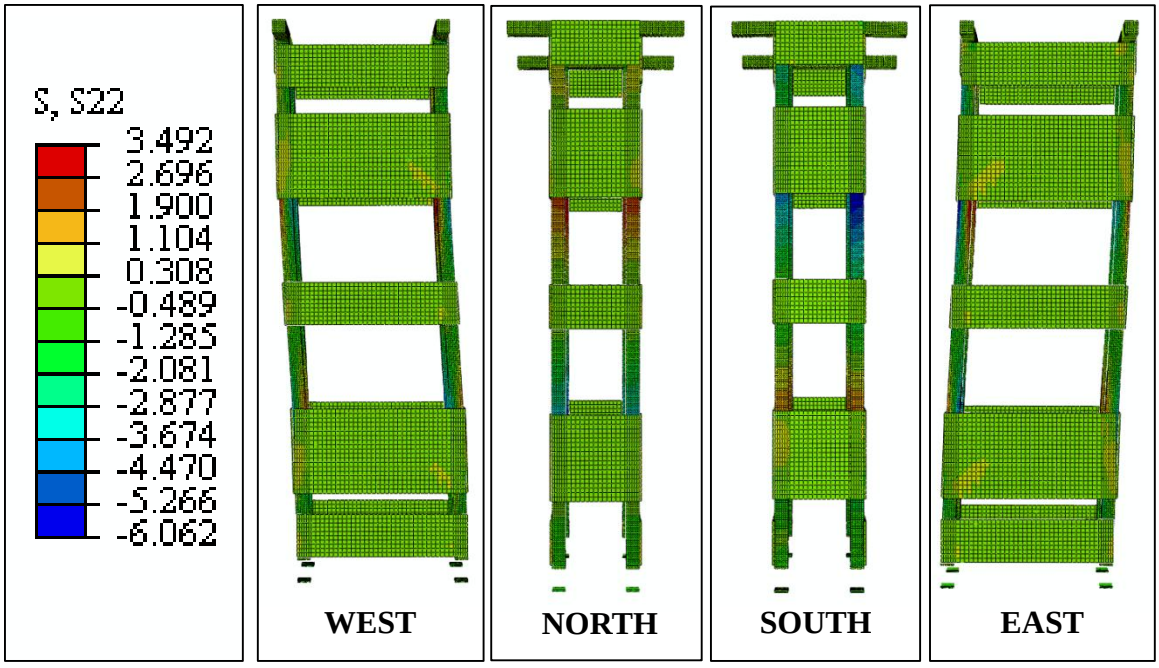

Figure B.12 Contour plots from Abaqus of the vertical stress (y-direction) for PLP Shore 7 MOD2

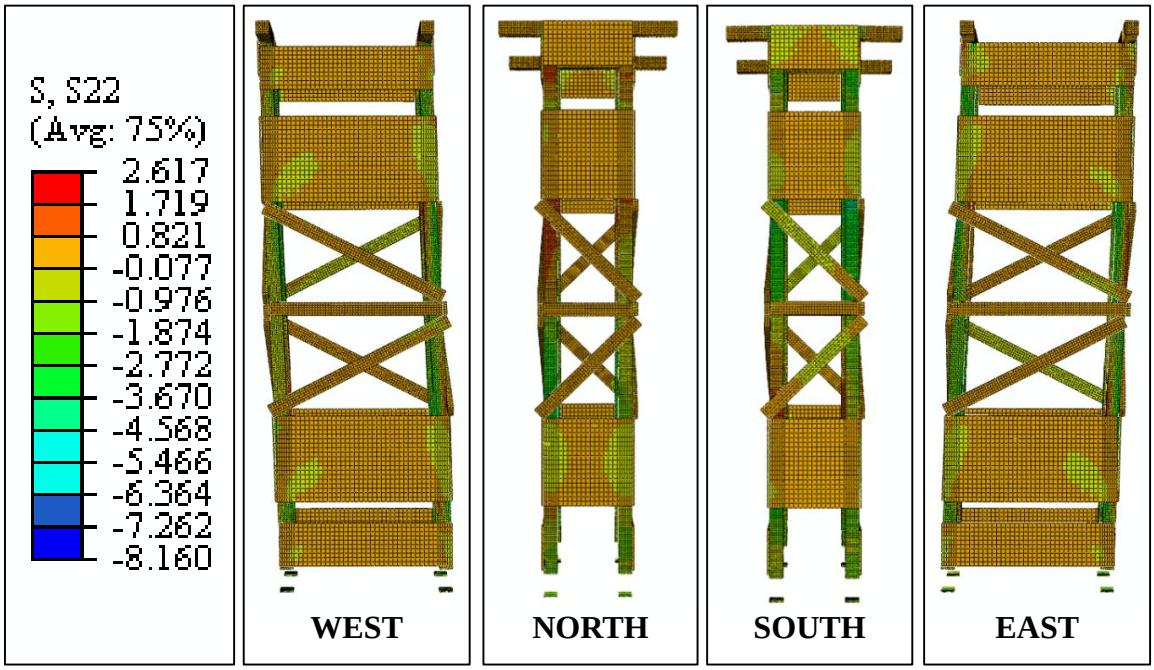

Figure B.13 Contour plots from Abaqus of the vertical stress (y-direction) for PLP Shore 7 MOD3

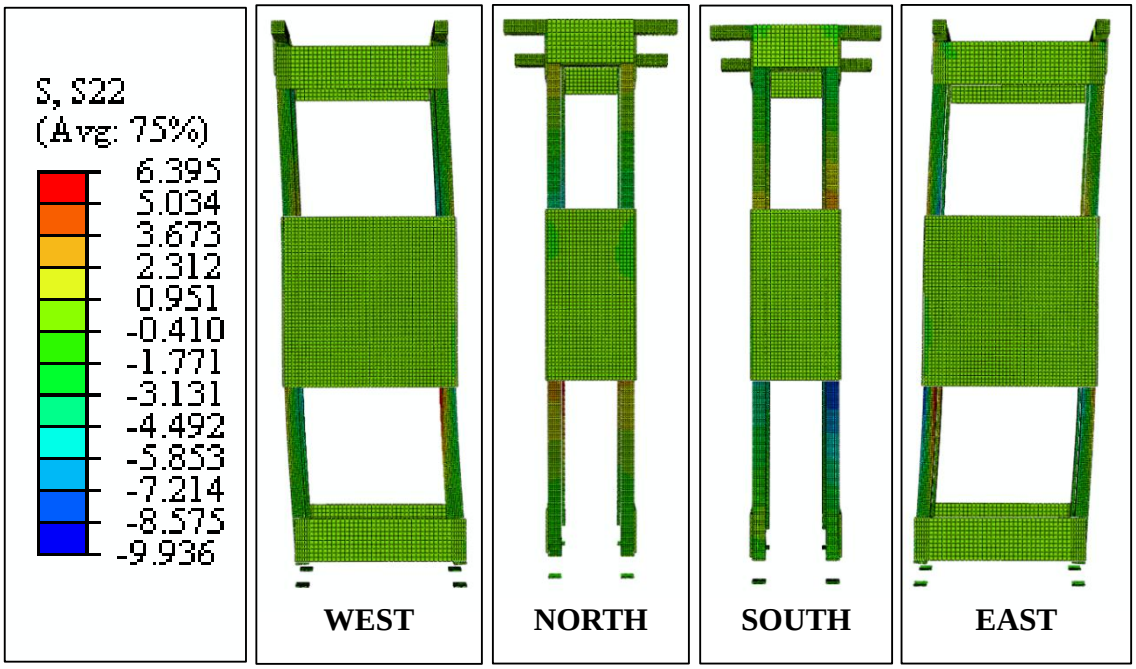

Figure B.14 Contour plots from Abaqus of the vertical stress (y-direction) for PLP Shore 7 MOD4

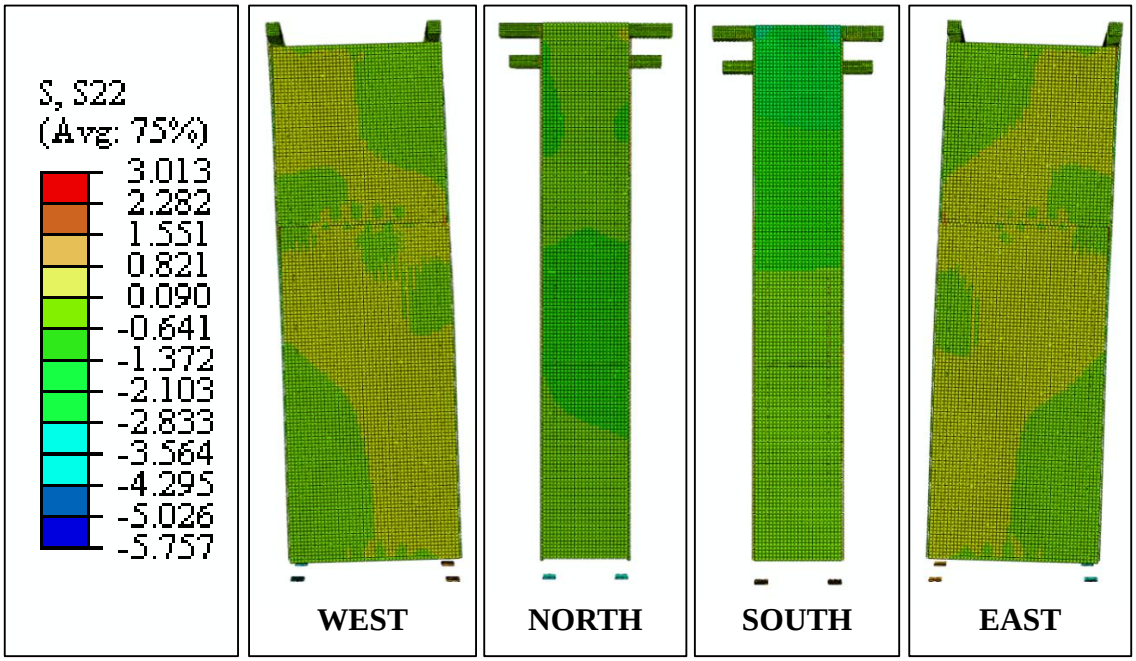

Figure B.15 Contour plots from Abaqus of the vertical stress (y-direction) for PLP Shore 7 MOD5

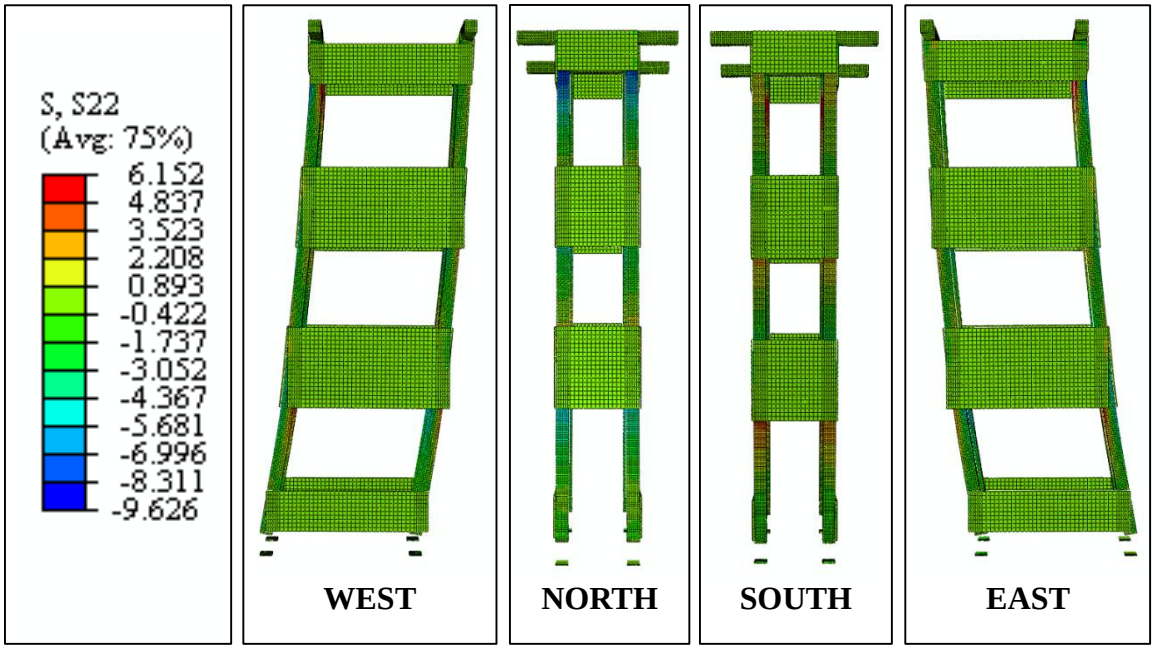

Figure B.16 Contour plots from Abaqus of the vertical stress (y-direction) for PLP Shore 9 MOD1

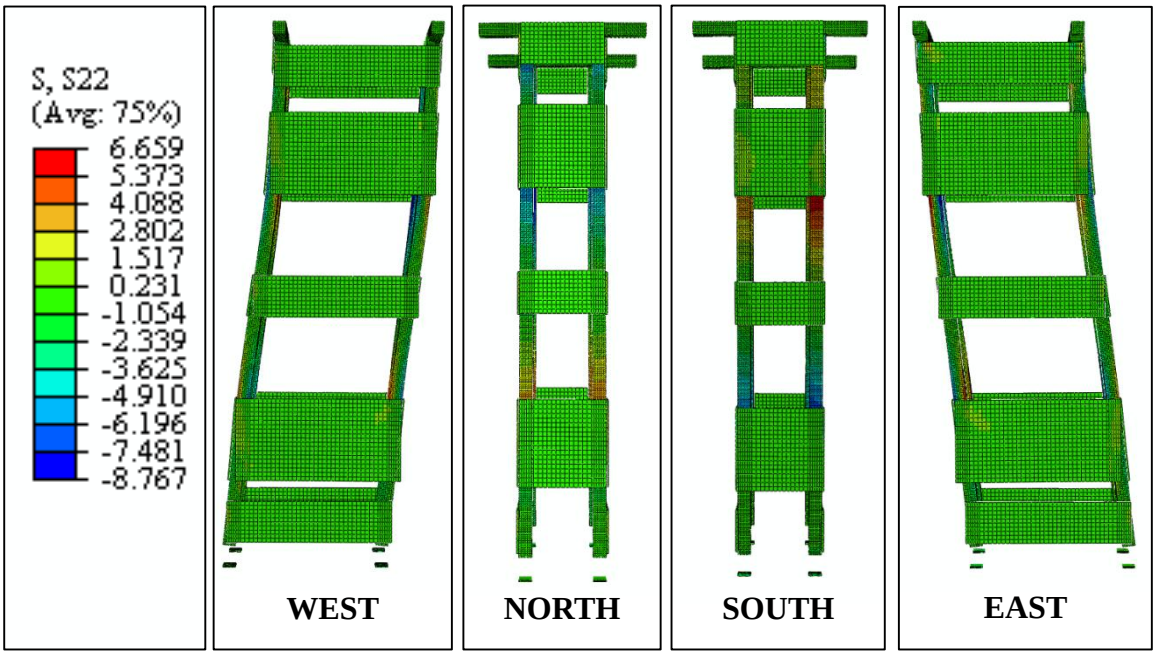

Figure B.17 Contour plots from Abaqus of the vertical stress (y-direction) for PLP Shore 9 MOD2

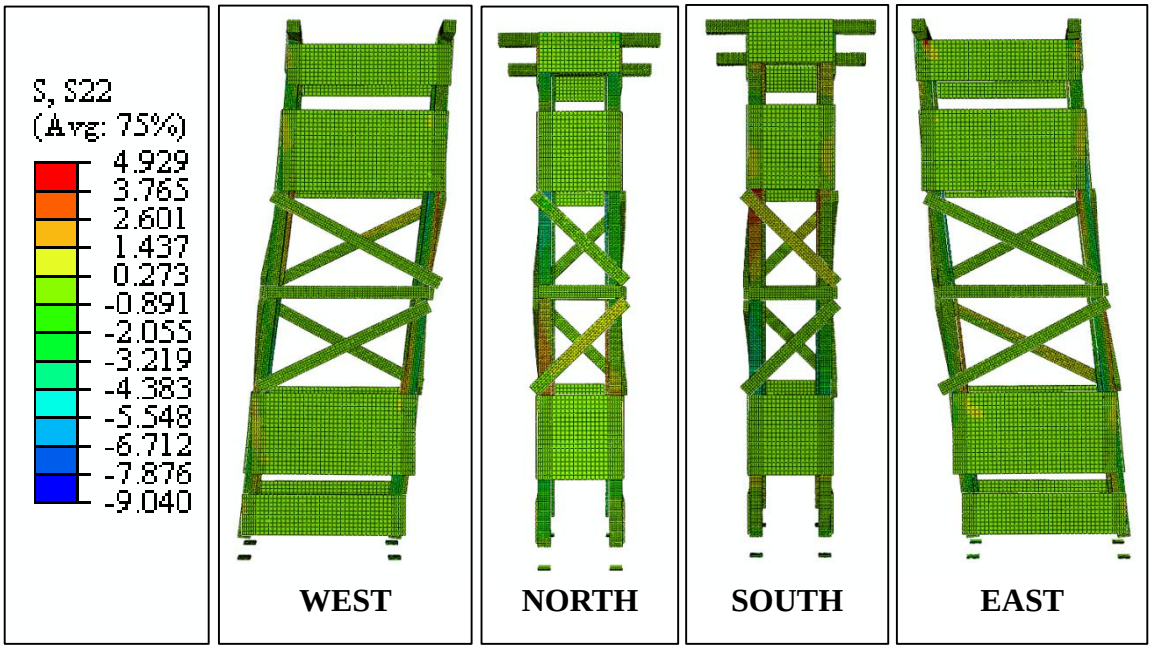

Figure B.18 Contour plots from Abaqus of the vertical stress (y-direction) for PLP Shore 9 MOD3

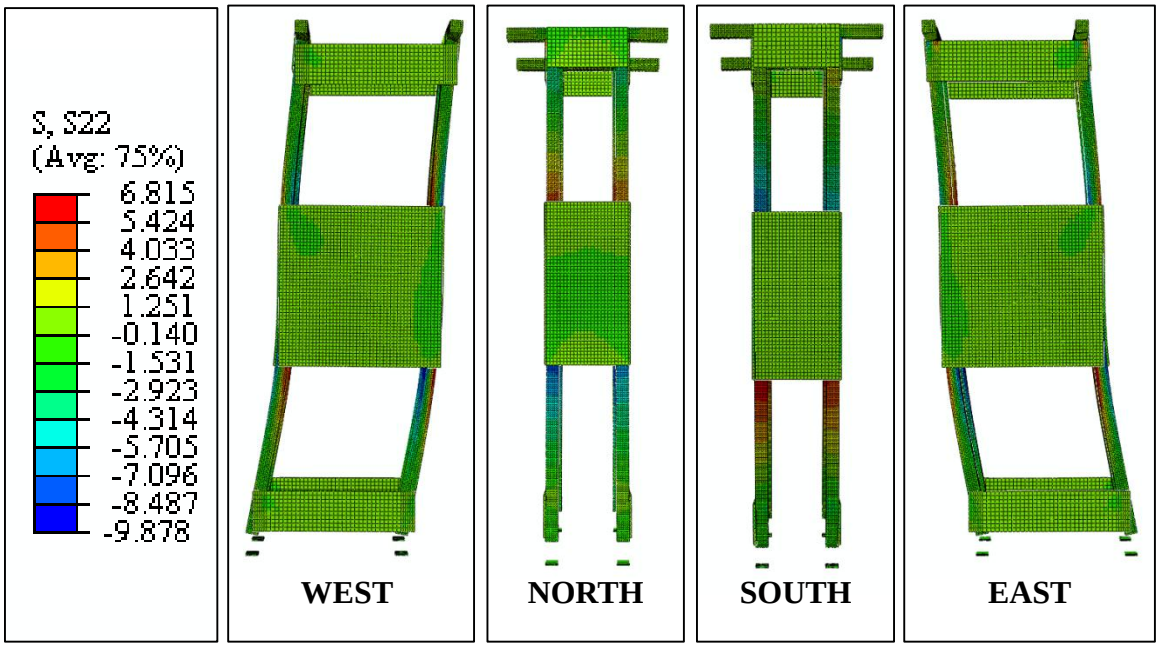

Figure B.19 Contour plots from Abaqus of the vertical stress (y-direction) for PLP Shore 9 MOD4

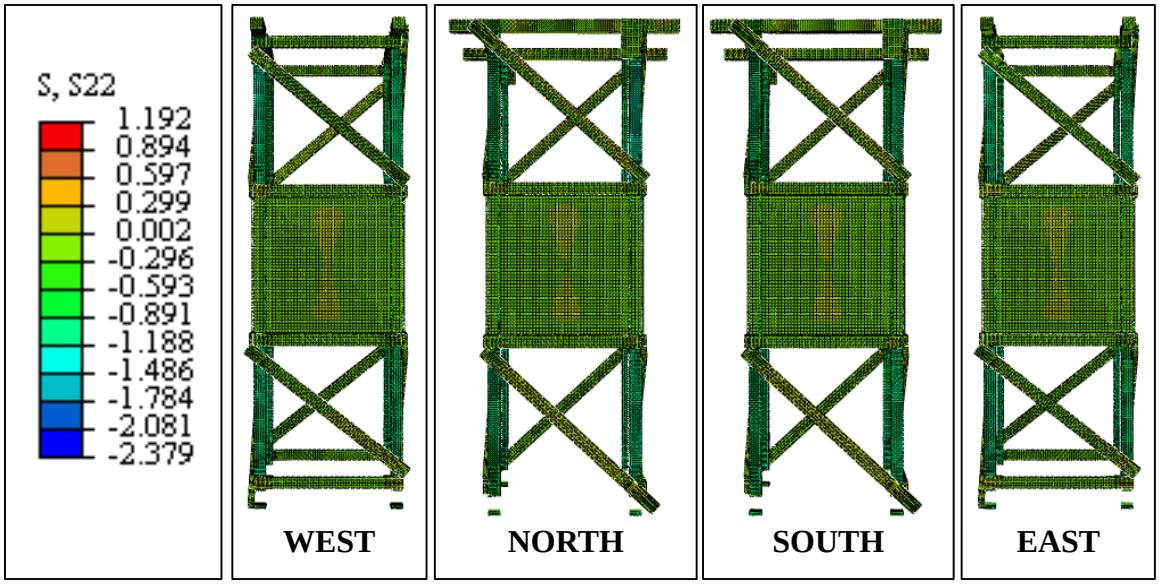

Figure B.20 Contour plots from Abaqus of the vertical stress (y-direction) for LP Shore 3 MOD6

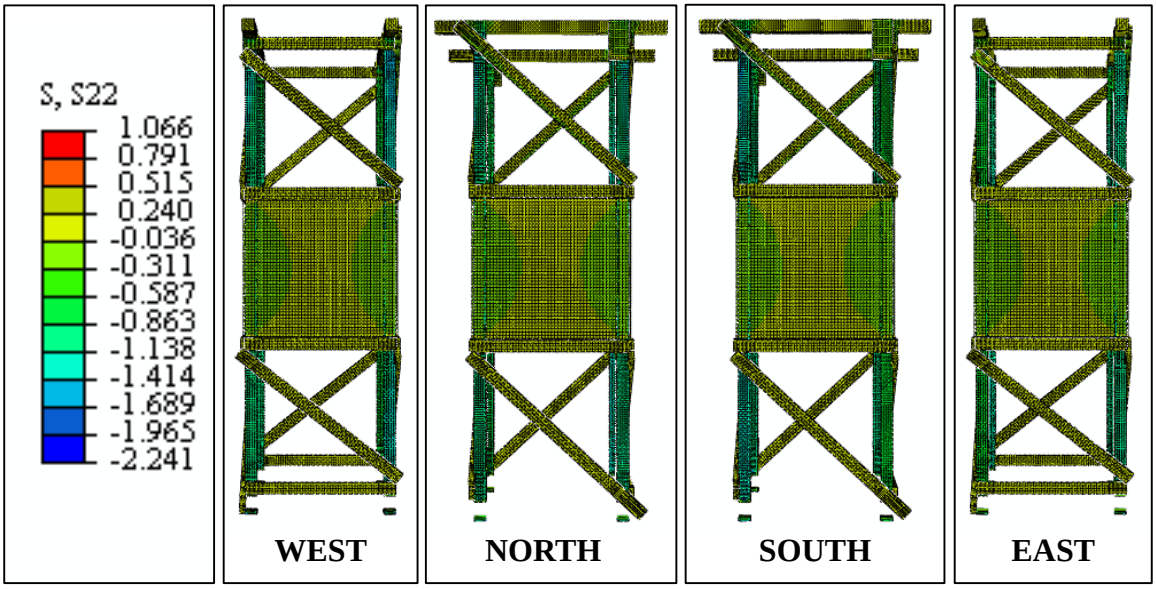

Figure B.21 Contour plots from Abaqus of the vertical stress (y-direction) for LP Shore 4 MOD6

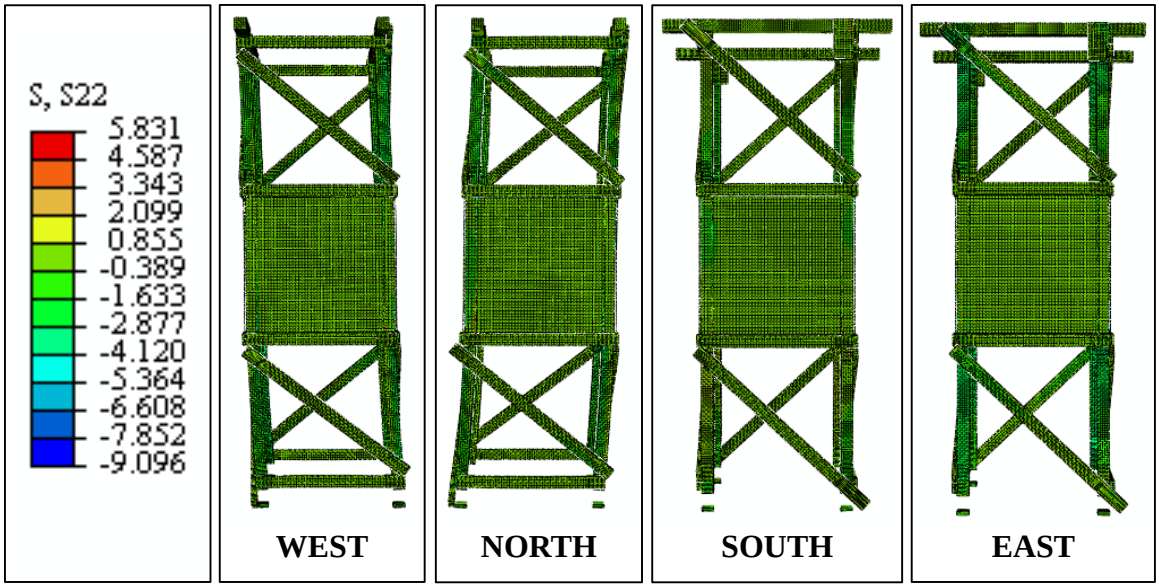

Figure B.22 Contour plots from Abaqus of the vertical stress (y-direction) for LP Shore 6 MOD6

REFERENCES

1. AFPA/ANSI. *National Design Specification for Wood Construction.* American Forest and Paper Association, Washington, D.C. 2005.
2. Dassault Systèmes. *Abaqus/CAE User's Manual 6.11*. 2011.
3. Foschi, Ricardo O. "Load-Slip Characteristics of Nails." Journal of Wood Science, Vol. 7 (1), 1974. 69-76.
4. Foschi, Ricardo O. and Thomas Bonac. "Load-slip Characteristics for Connections with Common Nails." Journal of Wood Science, Vol. 9, January 1977.
5. Hammond, David J. "Engineering the Collapse: Making the Structure Safe." Fire Engineering, Vol. 148 (11), November 1995. 49-61.
6. Hammond, David J. "Wood Shoring Systems: How Do They Perform?" Fire Engineering, September 2011. 49.
7. Hunt, Richard D. and Anthony H. Bryant. "Laterally Loaded Nail Joints in Wood." Journal of Structural Engineering, Vol. 116 (1), January 1990.
8. Judd, Johnn P. and Fernando S. Fonseca. "Analytical Model for Sheathing-to-Framing Connections in Wood Shear Walls and Diaphragms." Journal of Structural Engineering, Vol. 131 (2), February 2005.
9. Kermani, Abdy. "A Study of Semi-rigid and Nonlinear Behaviour of Nailed Joints in Timber Portal Frames." Journal of Forest Engineering, Vol. 7 (2), 1996.
10. Kuenzi, Edward W. "Theoretical Design of a Nailed or Bolted Joint under Lateral Load." Forest Products Laboratory, USDA, Madison, WI, Report No. D1951, 1955.
11. Lee, Whitney. "Determination of Modulus of Elasticity and Modulus of Rupture values for Solid Wood Members used in Tests of Wood Shores." M.S. degree report, Civil, Architectural, and Environmental Engineering Department, the University of Texas at Austin, *in progress*.
12. Mack, J.J. "The Strength and Stiffness of Nailed Joints under Short-Duration Loading." Forest Products Technical Paper, No. 40, 1966.
13. McCord, Scott J. "Testing of Emergency Wood Shoring Towers for use in Urban Search and Rescue Operations." Thesis presented to the University of Texas at Austin, in Austin, TX, in partial fulfillment of the requirements for the degree of Master of Science, 2012.
14. McLain, Thomas Ernest. "Curvilinear Load-slip Relations in Laterally Loaded Nailed Joints." Dissertation presented to the Colorado State University, at Fort Collins, CO, in partial fulfillment of the requirements for the degree of Doctor of Philosophy, 1975.

15. Morris, E.N. "The Application of the Slip Modulus in the Design of Nailed Joints." Journal of Wood Science, Vol.6 (2), 1973. 17-22.
16. Nishiyama, Nobuo and Naoto Ando. "Analysis of load-slip characteristics of nailed wood joints: application of a two-dimensional geometric nonlinear analysis." Journal of Wood Science, Vol. 49, 2003. 505-512.
17. Noren, B. "Nailed Joints – Their Strength and Rigidity under Short Term and Long Term Loading." Statens Institut for Byggnadsfarshing Rapport, 22, Stockholta, 1968.
18. O'Connell, John P. "Supporting a Fractured Building." Fire Engineering, Vol. 148 (11), November 1995. 64-71.
19. O'Connell, John P. *Emergency Rescue Shoring Techniques*. Tulsa: Pennwell, 2005.
20. Pellicane, Patrick J, Jeffrey Stone, and M. Daniel Vanderbilt. "Generalized Model for Lateral Load Slip of Nailed Joints." Journal of Materials in Civil Engineering, Vol. 3 (1), February 1991.
21. Thomas, Babu and Sudershan K. Malhotra. "Behavior of Timber Joints with Multiple Nails." Journal of Structural Engineering, Vol. 111 (973), 1985.
22. Titus, Leo J. "A Review of the Temporary Shoring Used to Stabilize the Pentagon After the Terrorist Attacks of September 11, 2001." Scholarly paper submitted to the University of Maryland Department of Civil Engineering, May 2002.
23. US Army Corps of Engineers. *US&R Structures Specialist Field Operations Guide (FOG).* 6th edition, February 2009.
24. US Army Corps of Engineers. *US&R Structures Specialist Field Operations Guide (FOG).* July 2011.
25. Van Dyer, D.B. "Slip Modulus in Bolted Timber Joints." Canadian Journal of Civil Engineering, Vol. 19, 1992. 960-964.
26. Wheat, Dan L, M. Daniel Vanderbilt, and James R. Goodman. "Wood Floors with Nonlinear Nail Stiffness." Journal of Structural Engineering, Vol. 109 (5), May 1983.
27. Wheat, Dan L. and Jose M. Calixto. "Nonlinear Analysis of Two-Layered Wood Members with Interlayer Slip." Journal of Structural Engineering, Vol. 120 (6), June 1994.
28. Wilkinson, Thomas Lee. "Theoretical Lateral Resistance of Nailed Joints." Journal of the Structural Division, Vol. 97 (5), May 1971. 1381-1398.